Molecular spintronics: from magnetic materials to light emitting spintronic devices

Instituto de Ciencia Molecular
Universitat de València

...

Memoria presentada por Juan Pablo Prieto Ruiz para aspirar al grado de Doctor en Nanociencia y Nanotecnología (programa ref. 3045)

...

Dirigida por el Dr. Eugenio Coronado Miralles y

la Dra. Helena Prima García

D. EUGENIO CORONADO MIRALLES, catedrático del Departamento de Química Inorgánica de la Universitat de València y Dña. HELENA PRIMA GARCÍA, doctora por la Freie Universität von Berlin y actualmente investigadora en el Instituto de Ciencia Molecular de la Universitat de València

CERTIFICAN:

Que la memoria presentada por D. Juan Pablo Prieto Ruiz con título: *"Molecular spintronics: from magnetic materials to light emitting spintronic devices"* corresponde a su Tesis Doctoral y ha sido realizada bajo su dirección en el Instituto de Ciencia Molecular, autorizando mediante este escrito la presentación de la misma para optar al grado de Doctor.

En Paterna, a 14 de Noviembre de 2014

Dr. Eugenio Coronado Miralles Dra. Helena Prima García

Juan Pablo Prieto Ruiz

“The real voyage of discovery

consists not in seeking new landscapes,

but in having new eyes.”

-Marcel Proust-

Agradecimientos

En principio estas líneas podrían considerarse las más sencillas de escribir dentro de una tesis doctoral, teniendo en cuenta todo el esfuerzo ya realizado. Sin embargo, no hemos de caer en el error de pensar que años de experiencias y emociones pueden condensarse sin más en un par de párrafos. Tal vez, si uno escribe sin pausa, poco a poco, la tinta puede ir atrapando esos sentimientos en la hoja, como una cárcel atemporal. Así esas emociones, semillas de un bosque interior que ha crecido durante todo este tiempo, pueden ser compartidas con los seres especiales que las gestaron. La lista de agradecimientos es larga y el papel limitado.

En primer lugar, quisiera darle las gracias a Eugenio por permitirme formar parte de este proyecto que ha desembocado en esta tesis, y por su guía a lo largo de todo este tiempo. Tu visión científica, ambiciosa y en ocasiones semejante a la de un explorador que inicia su viaje sin importar las tormentas que encuentre en el camino, me ha llevado a afrontar una gran cantidad de retos. Y fruto de ese viaje, la recompensa del aprendizaje. No pueden faltar las palabras de agradecimiento para Helena. Te agradezco el haber compartido conmigo toda tu experiencia y el haber estado ahí en todos los momentos buenos y malos que fueron apareciendo en este recorrido. Sin duda, no se puede apreciar la luz si no se ha sufrido la oscuridad. Por todo ello gracias. También me gustaría dedicarle unas palabras a Francisco para agradecerle su apoyo y guía en todo lo referido a la química en mi trabajo.

Tengo que expresar mi gratitud en unas líneas a todos aquellos que aportaron su apoyo a nivel científico, pero sin duda también a nivel personal. Entre estas personas están Chema y Gloria. Gracias por aguantarme preguntando un millón de veces: ¿cuándo es el próximo turno de SQUID? y por estar ahí siempre dispuestos a ayudarme. También he de agradecer a Chimo por apoyarnos en todos esos momentos de “ansia viva”, permitiendo montar muchos de los aparatos que han sido de suma importancia en esta tesis. Muchas gracias Alejandra por tener siempre esa sonrisa y disposición para

echarme una mano; eres una gran persona y profesional. También mi agradecimiento para Jorge, Álex y Eva; coincidimos poco, pero en esas ocasiones siempre estáis ahí para echar un cable. Por supuesto, no pueden faltar mis palabras para Jose el cual es mucho más que un compañero. Con el tiempo se ha convertido en un amigo con el que siempre echar unas risas en mitad de un día ajetreado. Paco, mil gracias por ser como eres; una persona encantadora con esa visión siempre positiva de lo que te rodea. Manuel, te agradezco siempre tu ayuda, no sólo en temas del trabajo sino también por ser mi guía en mis primeros pasos en la fotografía y por compartir charlas tan apasionantes cada vez que nos encontramos. Estela, agradezco enormemente tu disposición para solucionar los problemas y estar siempre pendiente de nosotros. También es fundamental dedicar unas palabras a Marian. Simplemente puedo decir que ha sido una suerte conocerte. Eres una persona increíble que derrocha simpatía y una energía positiva que se contagia. Gracias por toda tu ayuda en la infinita burocracia de la tesis.

Inicio un párrafo nuevo, no por casualidad, sino porque este agradecimiento es muy especial. Estas líneas van dirigidas a Ángel. Compañero, la ayuda que me has proporcionado estos años no se puede pagar ni con todo el oro del mundo. Realmente siento una gran admiración por ti. En primer lugar, a nivel profesional. Nunca pude imaginar que alguien pudiera saber sobre física, química, ingeniería, mecánica, fontanería, fotografía, electrónica, albañilería….y un infinito etcétera, pero te conocí y aprendí que hay gente así. Es increíble las veces que oí por los pasillos: esto no funciona, ¿sabes dónde está Ángel?. En segundo lugar, te admiro como persona. Tienes un corazón enorme y una habilidad natural para estar siempre dispuesto a ayudar. Gracias compañero por estar a mi lado en los buenos y malos momentos. Las risas que nos hemos echado juntos han sido como un bálsamo todo este tiempo.

Cuando llegué al ICMol no podía ni siquiera imaginar la cantidad de gente tan impresionante que iba a conocer. Personas a las que admiro y quiero. Concha, no sabes cuánto echo de menos escucharte diciéndome: Ayy mi Juampiii. Si ese globo con forma de corazón que te compré a regañadientes (vergüenza para mi) te dura tantos años como nuestra amistad creo que lo tendrás para siempre. Julia, gracias por compartir conmigo las penurias de esos momentos duros en

este último tramo. Echo de menos la hora de la merienda cuando nos sentábamos a tomar un té y arreglábamos el mundo. Efrén, compañero, te admiro y mucho. Eres una persona increíble en todos los aspectos y has sido un referente para mí en muchas cosas. Mauri, desde que te fuiste este instituto perdió un trozo importante de su energía y de su alma. Poca gente tan buena como tú llegaré a conocer. Las palabras se quedan cortas cuando me toca hablar de Elena. Todo lo que sé de microscopía te lo debo a ti. Pero además de eso has sido una persona muy importante durante estos años. Siempre ahí para apoyarme, animarme y sentir que había alguien en quien confiar y de quién poder recibir un buen consejo. Mil gracias. También son obligadas unas palabras para Gonzalo; te admiro mucho. En estos años te has convertido en un gran amigo, y sé que eso perdurará mucho más allá de una tesis. Es esencial dedicar unas líneas a María. Hemos compartido un importante tramo en el camino que han supuesto estos años de mi tesis. Muchísimas gracias por todo tu apoyo y amistad. Otras personas que siempre han estado ahí para regalar un consejo y una palabra bonita son Mónica y Guille; gracias chicos. La lista de personas increíbles que esta aventura científica me ha llevado a encontrar es muy larga. Prueba de ello son las páginas que ya llevo escritas. Sin embargo no estaría completa si no tuviera unas palabras para Álex (maestro), José Jaime (sabio), Sergio (profesional), Carlos M. (un gran científico), Alicia (un referente), Álex A. (buena onda), Josep (el consejo exacto), Salva (un artista), Walter (mi eterno compañero), Ramón (con una sonrisa como marca registrada), Samuel (amabilidad sin límites), Marc (siempre una buena palabra), Gustavo (esa onda colombiana), Yan (eterna sonrisa), Jorge (Teruel rules) Michele S. (un caballero italiano; gracias por toda tu ayuda) y Michele M. (ese compañero y amigo que todos quisieran tener). Sara, muchas gracias por nuestras conversaciones y ratos vividos entre experimentos. Eres una persona increíble; muy pronto tus sueños te alcanzarán. También he tenido la suerte de coincidir en mi última etapa con personas encantadoras con las que he compartido momentos muy bonitos. Cristina R., Cris, Lidón, Laura, Enrico, Toni y Dani. Doy gracias de haber tenido la ocasión de conoceros. Espero que nuestra amistad se extienda por mucho tiempo. Si me dejo a gente es por limitación de papel y no por falta de gratitud, pues sois muchos los que habéis contribuido, ya sea científicamente o con una sonrisa a que este barco llegara a buen puerto.

Esta última página de agradecimientos la reservo para todas aquellas personas especiales que se han cruzado en mi vida y me han dado la energía para seguir adelante en los tiempos complicados y con los que he disfrutado los momentos más dulces que recuerdo. Unas líneas en letras doradas están dedicadas para Karo, Patrycja y Diana. Conoceros fue una de las mejores cosas me han sucedido en los últimos años. Fuisteis como una bocanada de aire fresco en el tramo final de mi tesis. Nunca supe que mi corazón llegaría a ser un poquito polaco. Karo, gracias por haber estado estos meses dándome todo tu apoyo, energía y buena onda. Contigo aprendí a ver las cosas siempre con una sonrisa en los ojos. Patraix, ¡ay Patraix! ese lugar donde todo empieza y acaba. Ahí pude conocer a gente extraordinaria; ese tipo de personas que son tan increíbles que encontrarlas es el mejor de los regalos que la vida puede darte. Javi, Juanda, Álvaro, Manolo y Majo. Os adoro. Y punto. Jorge, tuve la infinita suerte de conocerte en la facultad y desde ese día gané a uno de mis mejores amigos. Muchas gracias por ayudarme con los ajustes de datos. Todos vosotros chicos, sois más que amigos; sois mis hermanos. Sólo puedo deciros U.E.E.E. Alan, Luismi y Alicia no me olvido de vosotros. Todos, sin ser conscientes me habéis ayudado a llegar hasta aquí.

Las palabras finales van destinadas a mi familia. Ustedes son lo más valioso que me ha dado la vida. Sin ustedes nunca hubiera llegado hasta este punto. Es difícil resumir en pocas palabras el infinito amor que les tengo y la tremenda gratitud que les debo. A mis padres Cristina y Enrique; les debo todo lo que soy. A mis hermanos Enrique, Rodrigo y Ramiro; desde siempre mis referentes y mis mejores amigos. Yo fui construyendo el camino poco a poco, pero ustedes me alcanzaron las piedras y me ayudaron a caminarlo. Por siempre, gracias.

A mi familia.

El mayor de mis tesoros.

Abstract

The fast development experienced in the fields of molecular electronics and molecular magnetism in the past decade has promoted the interest of these communities in spintronics and the emergence of an exciting research field, named as Molecular Spintronics. The manipulation of the spin degree of freedom of carriers in addition to their charge is the central theme of spintronics. Until now, this research field has been mainly focused on the use of conventional inorganic metals and semiconductors for the fabrication of devices. In this sense, the objective of molecular spintronics is the development of molecular analogues of these materials for their inclusion into spintronic structures. As it has been done for molecular electronics, the field of molecular spintronics can be divided into two main branches: a) molecular-based spintronics or most commonly named as organic spintronics by the physical community and b) unimolecular spintronics. The work in this thesis is focused in the first branch. In this point, it is important to remark that along the discussion of the thesis both terminologies, molecular-based and organic, will be applied depending on the context without supposing any conceptual difference. Thus, in the present work a variety of materials with interest in molecular spintronics is presented. In addition, the fabrication of multifunctional spintronic devices is addressed. The different types of molecular-based or organic materials employed in this thesis are shown in figure 0. This includes molecular-based ferromagnetic materials of the family of Prussian blue analogues (PBAs), organic semiconductors (such as the light emitting polymer F8BT) and dipolar molecules (such as the ruthenium complex N965).

This manuscript is divided in two parts:

The first part deals with the physical characterization of PBA thin films. These magnetic materials can be considered as interesting candidates for their inclusion into molecular spintronic structures. The aim of this thesis is to develop a conceptual background of the properties of these molecular-based materials when ordered as thin films, to check their potential as magnetic

components in new spintronic devices. The first part of the thesis comprises five chapters.

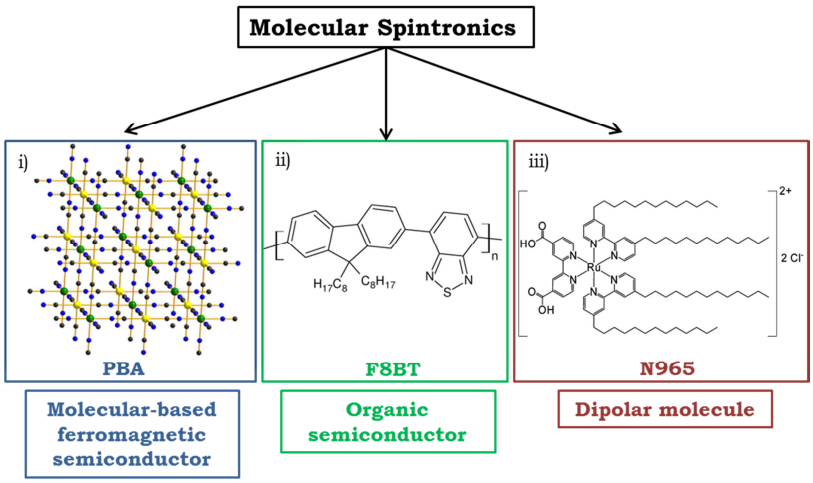

Figure 0- Illustration summarizing the different types of molecular materials studied in this thesis: i)- PBA's with formula $M_x A[B(CN)_6]_z \cdot n\ H_2O$, where A and B are metal centers and M an alkali metal cation. In the image, green and yellow spheres represent the metal centers; blue and black spheres represent the carbon and nitrogen atoms of the cyanide bridge. Water molecules and cations are not included for clarity. ii) Light emitting conjugated polymer: poly(9,9-dioctylfluorene-*co*-benzothidiazole), named as F8BT. iii) Dipolar molecule constituted by an ionic ruthenium complex: bis(4,4'-tridecyl-2,2'-bipyridine)-(4,4'-dicarboxy-2,2'-bipyridine)ruthenium(II)-bis(chloride), named as N965.

In chapter 1 the fundamental aspects regarding the basic concepts and experimental approaches are reviewed.

In chapter 2 a complete physical characterization of thin films of the PBA $Cr_{5.5}(CN)_{12} \cdot 11.5\ H_2O$ is presented. This material will be referred along the thesis as CrCr for a simplified notation. This molecular-based ferrimagnet presents a high critical temperature (240 K), chemical stability and controlled magnetic properties. Due to these properties, this is one of the most promising candidates for applications in molecular spintronics. In this chapter the first

Magneto-Optical Kerr Effect study (MOKE) on a PBA thin film is extensively described.

The unique abilities of the MOKE technique for studying the magnetic properties of PBA thin films, as demonstrated in chapter 2, is also tested in thin films of the ferromagnetic PBA family $Fe_3[Cr(CN)_6]_2 \cdot 15\ H_2O$, named as FeCr along the discussion. This work is extensively described in chapter 3. By means of MOKE it has been possible to identify the presence of a chemical impurity on the surface of these PBA thin films, originated in the electrolyte environment. This impurity escapes completely the SQUID detection. By these studies, MOKE has been established as a powerful complementary technique to SQUID magnetometry for the characterization of thin films of these molecular-based magnetic materials.

In chapter 4, thin films of the two PBA's, CrCr and FeCr characterized in chapter 2 and 3 respectively, are put in intimate contact for obtaining bilayer structures. By means of SQUID it has been detected the evidence of a magnetic coupling between both molecular-based magnetic materials. This result represents the first report of a phenomenon of this nature in an all-molecular based magnetic heterostructure. These studies are of great interest to understand the magnetization reversal processes that take place at the interface between the two PBA layers. This provides a phenomenological framework to control and design all-molecular spintronic structures based on the combination of PBA thin films.

As previously mentioned, CrCr is a very interesting material regarding its possible applications into molecular spintronic structures. In chapter 5 the magnetoresistance characterization of thin films of this PBA is extensively described for the first time. In addition, a prototype spin valve structure employing this chromium cyanide material has been fabricated and characterized for evaluating its potentiality as a spin injector electrode.

The second part of the thesis is devoted to the fabrication of a molecular light emitting spintronic devices exhibiting spin valve magneto-electroluminescence (MEL) effect under the application of external magnetic fields. These

multifunctional molecular devices, showing a coexistence of electroluminescence and organic spin valve performance, are named as spin-OLEDs. In these devices the magnetic modulation of light is achieved by the injection of spin-polarized carriers in the emissive layer. In chapter 6, the fundamental aspects of the basic concepts and experimental techniques employed in this part are reviewed.

In chapter 7, the rational design and fabrication of a spin-OLED device is described. We propose for the first time the implementation of an inverted OLED structure (HyLED) in order to fabricate a multifunctional device. This approach allows the obtaining of robust and stable structures. In this strategy commercially available and non-expensive materials, which are employed as received from the provider without extra chemical processes, are used. In a first example, a device containing Fe and Co as magnetic electrodes and F8BT as the electroluminescent and spin collector layer has demonstrated to exhibit the presence of a spin-polarized current and a good electroluminescence performance. However, both functionalities take place in different ranges of voltage and temperature. Despite this drawback, the proposed structure supposes an interesting prototype for the developing of a light emitting spintronic device fabricated with commercial materials. Indeed, this work has given rise to the creation of a National Patent entitled: “Dispositivo opto-espintrónico y método para su fabricación” (Opto-spintronic device and fabrication method).

The lack of coexistence of both functionalities in the same range of voltage and temperature has been overcome by the substitution of the Fe electrode by a LSMO electrode. This second example is chemically stable in open air, presenting an outstanding performance as an organic spin valve. In this way, it maintains a spin-polarized current at bias voltages as high as 12 V. This value is much higher than that described so far in literature in organic spin valves which work at voltages below 1-2 V. Thanks to this high voltage performance, this hybrid device exhibits a spin valve MEL effect. All this work is described in chapter 8.

List of publications

The publications(*) generated during my PhD thesis are listed below:

[1]-Coronado, E., Makarewicz, M., Prieto-Ruiz, J.P., Prima-García, H., Romero, F.M. "Magneto-optical properties of electrodeposited thin films of the molecule-based magnet $Cr_{5.5}(CN)_{12} \cdot 11.5H_2O$". *Adv. Mater.* **23**, 4323–4326 (2011).

[2]-Prima-Garcia, H., Coronado, E., Prieto-Ruiz, J.P., Romero, F.M. "Tailoring magnetic properties of electrodeposited thin films of the molecule-based magnet $Cr_{5.5}(CN)_{12}$ $11.5H_2O$". *Nanoscale Res. Lett.* **7**, 232–235 (2012).

[3]-Coronado, E., Fitta, M., Prieto-Ruiz, J.P., Prima-García, H. , Romero, F.M., Cros, A. "MOKE magnetometry as a probe of surface magnetic impurities in electropolymerized magnetic thin films of the Prussian blue analogue $Fe_3[Cr(CN)_6]_2 \cdot 15\ H_2O$". *J. Mater. Chem. C* **1**, 6981 (2013).

[4]-Coronado, E., Prieto-Ruiz, J.P., Prima-Garcia, H. "Spin polarization in electrodeposited thin films of the molecule-based magnetic semiconductor $Cr_{5.5}(CN)_{12}$ $11.5H_2O$". *Chem. Commun.* **49**, 10145–10147 (2013).

[5] National patent 201300083: "Dispositivo opto-espintrónico y método para su fabricación". Coronado, E., Prima-García, H., Prieto-Ruiz, J.P. (2013).

[6]-Prieto-Ruiz, J.P., Prima-Garcia, H., Graziosi, P., Riminucci, A., Dediu, V.A., Coronado, E. "Fabrication of robust and low cost spin-OLEDs: evolving to a new generation of optoelectronic devices". *Manuscript to* be s*ubmitted*

[7]-Prieto-Ruiz, J.P., Prima-Garcia, H., Groβmann, N., Cinchetti, M., Coronado, E. "Rational design and fabrication of a light emitting spintronic device with Fe and Co electrodes". *Manuscript to be* s*ubmitted*

[8] Coronado, E., Prieto-Ruiz, J. P. , Prima-Garcia, Romero, F.M., "Fabrication and physical characterization of a Prussian blue analogue bilayer system exhibiting magnetic exchange coupling". *Submitted*

[9]- Abellán, G., Carrasco, J. a., Coronado, E., Prieto-Ruiz, J. P. & Prima-García, H. “In-Situ Growth of Ultrathin Films of NiFe-LDHs: Towards a Hierarchical Synthesis of Bamboo-Like Carbon Nanotubes”. *Adv. Mater. Interfaces* **1,** 1400184 (2014).

(*)- I want to clarify that in papers published only by members of Coronado’s group, due to internal policy, authors of the group appear in alphabetic order. If the paper is fruit of collaboration with other groups, authors from the other groups appear afterwards in the order that they decide. Articles highlighted in black are based on my main research results

Abbreviations

3D	three-dimensional
AF	antiferromagnetic
AFM	atomic force microscopy
AlO_x	alumina
CV	cyclic voltammetry
DOS	density of states
EA	electron affinity
EB	exchange bias
EDAX	energy dispersive X-ray spectroscopy
E_g	band gap
EELS	electron energy loss pectroscopy
EIL	electron injection layer
EL	electroluminescence
EML	emissive layer
et al.	et alii (and others)
FC	field cooled
Fe	zero field cooled
FM	ferromagnetic
FT-IR	Fourier transform Infrared spectroscopy
GMR	giant magnetoresitance
H_C	coercive field
HIL	hole injection layer
HOMO	highest occupied molecular orbital
HyLED	hybrid organic-inorganic light emitting diode
IP	ionization potential
ITO	indium tin oxide
J	current density
LB	Langmuir-Blodgett
LSMO	Lanthanum Strontium Manganite Oxide
Lum	luminance
LUMO	lowest unoccupied molecular orbital
MEL	magneto-electroluminescence

MFM	magnetic force microscopy
MOKE	magneto-optical Kerr effect
MR	magnetoresistance
MTJ	magnetic tunneling junction
OLED	organic light emitting diode
OMAR	organic magnetoresistance
OMEL	organic magneto-electroluminescence
OSC	organic semiconductor
OSV	organic spin valve
PBA	Prussian blue analogue
PCP	π-conjugated polymer
PEM	photo-elastic modulator
PES	photoemission spectroscopy
PPMS	physical properties measurement system
PPs	polaron pairs
R_{ap}	antiparallel resistance
R_p	parallel resistance
S	singlet
S/N	signal-to-noise
SEM	scanning electron microscopy
SQUID	superconducting quantum interference device
STEM	Scanning Transmission Electron Microscopy
T	triplet
T_C	Curie temperature
TEM	transmission electron microscopy
TMR	tunneling magnetoresistance
T_N	Neél temperature
UPS	ultraviolet photoelectron spectroscopy
UV-Vis	ultraviolet-visible spectroscopy
V_{on}	light emission threshold voltage
XRD	x-ray diffraction
Z	atomic number
ZFC	zero-field cool

CONTENTS

PART II

PART I

Chapter 1

Introduction part I

1.1 Fundamental concepts on Molecular spintronics

In the conventional semiconductor electronics, the detection of changes in the electrical current caused by an external stimulus is the operation principle of most of the devices[1]. When the external stimulus is magnetic, the detection is more complicated due the limited effect of a magnetic field on the electron motion (Lorentz force) if compared to an electric field. In consequence, the approach for manipulating charge carriers by magnetic means has to be done relying in an intrinsic property: the spin[1,2]. The active manipulation of spin degrees of freedom of charge carriers, in addition to their electronic charge, is the central issue of a relatively new research field named as spin electronics or spintronics[3–5]. In the field of nanotechnology, spintronics is one of the most emerging branches supposing a very active area within nanomagnetism. This research field started in 1982 with the works of Albert Fert and Peter Grünberg on the giant magnetoresistance (GMR) of metallic multilayers[6,7], being awarded for this reason with the Nobel prize in Physics in 2007[8].

Spintronics has made a significant impact on our daily life by its application in hard drive information storage and magnetic sensing among others[1,9]. Until date, this research field has been mainly using conventional inorganic metals and semiconductors for the fabrication of spintronic devices. However, the fast development experienced in molecular electronics and molecular magnetism in the last decade, with a progressively shift to a nanometer scale scenario, have established the proper conditions for the emerging of a new research field named Molecular Spintronics.[1,2,9]

In the same way, as it was done for molecular electronics, this new field can be divided into two major areas: i) molecular-based spintronics or most commonly named as organic spintronics; ii) single-molecule spintronics.

The main goal of the first area is the design and fabrication of innovative and cheaper spintronic devices by the introduction of molecular materials (also named by the physical community as organic materials). Thus, both terminologies - molecular-based spintronics and organic spintronics - will be used without distinction along this thesis. The molecular world offers several

advantages with respect to conventional inorganic materials. In first instance, organic materials can be designed in an incredibly wide range, with a fine tuning of their properties and high grade of purity[1]. A clear example is the case of conjugated polymers, whose conductivity can be changed in a controlled way by more than fifteen orders of magnitude[10], with the possibility of exhibiting both magnetism[11] and ferroelectricity[2] at room temperature. In second place, most of the molecular materials are made of light elements corresponding to the upper row of the periodic table. Thus, the two principal ways for spins to interact with the medium, spin-orbit coupling (~Z^4) and hyperfine interaction, are weak. As a consequence, the electron spin is preserved for longer time and distances when travelling across these type of materials[12].Finally other outstanding advantages of molecular materials are their low density, flexibility, transparency, chemical versatility and novel added functionalities (photomagnetism, piezomagnetism,…).

The knowledgement accumulated during past decades on the spin–transport phenomena for inorganic systems cannot be directly extrapolated to organic materials. The absence of an extended Fermi surface and the presence of an important electron-phonon coupling in the molecular systems are some of the reasons for this limitation. Thus, it is fundamental to understand how spins can be injected, manipulated and detected in model molecular materials[9]. For this aim the spintronic field offers two types of structures that allow to obtain an accurate scenario of the spin-dependent processes in molecular materials: organic spin valves[13,14] and organic tunneling junctions[12,15].

In the following we will introduce the concepts regarding to these spintronic structures.

1.1.1 Spin valves and magnetic tunneling junctions

In the most simplified situation, the archetypical devices and geometries for the injection/detection of spins are constituted by two ferromagnetic electrodes sandwiching a non-magnetic material[1,9,12,14]. In the context of inorganic spintronics, these structures are named as “spin valve” (SV) or “magnetic tunneling junction” (MTJ) depending on whether there is an effective charge

transport through the spacer or a tunneling between both electrodes, respectively. In these structures, the magnetization of the electrodes can be manipulated by means of an external magnetic field (direct magnetic torque on the local electrode magnetization), or by the effect of a spin-polarized current (via transfer of angular momentum between the spin-polarized carriers and the local ferromagnetic magnetizations)[9]. In the simple case of trilayer nanostructures, two resistive states can be stabilized depending on the relative orientation of the ferromagnetic electrode magnetizations. Thus, high or low resistance configurations are obtained for antiparallel and parallel relative orientations of the electrode magnetizations respectively. This phenomenology is denoted as giant magnetoresistance (GMR) and tunneling magnetoresistance (TMR) when referred to SVs or MTJ, respectively. Based on Mott's two-fluid model[16] the change of the total resistance in these spintronic structures can be described in the context of a simple resistor network model (figure 1.1)[12].

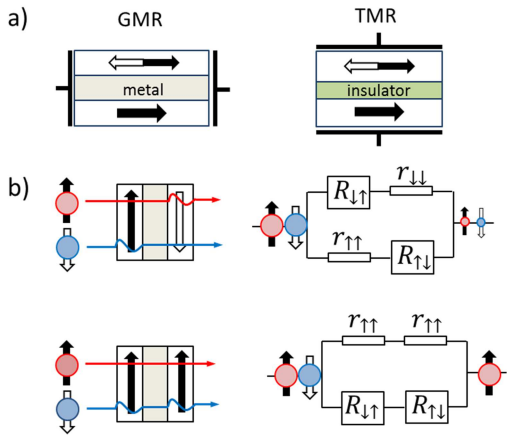

Figure 1.1- a) Basic types of trilayers structures employed in spintronics. b) Simple resistor network model illustration extracted from reference [9].

This model considers the spin current trough the device as composed by two channels corresponding to spin-up and spin-down. The effective resistance experienced by each type of spin channel is directly dependent of the relative orientation of the electrode magnetizations. For the antiparallel orientation both spin channels suffer many scattering processes in some of the ferromagnetic

layers, inducing a high resistance state in the structure. On the contrary, when a parallel alignment is stabilized, only one electron channel will suffer scattering in one of the two ferromagnetic electrodes leading to a low resistance state in the structure.

The spin transport process in each type of spintronic structure is different. In a SV the resistance change is based on the spin-dependent scattering of electrons travelling across thin metallic spacers[5]. On the other hand, in MTJs the electrons tunnel across the insulating spacer, when a bias voltage is applied in the device, preserving the spin information[17].

Moving to the molecular world, the first evidence of spin injection into an organic material was reported in 2002 by V. Dediu *et al.*[18] Sexitiophene (T_6), a rigid conjugated oligomer, was employed as the spin-transport channel situated between two magnetic manganites used as electrodes. So far many groups have reported the spin-dependent transport in organic spintronic spin valves (figure 1.2) and organic tunneling junctions by employing a wide variety of molecules and polymeric materials[12,14,19].

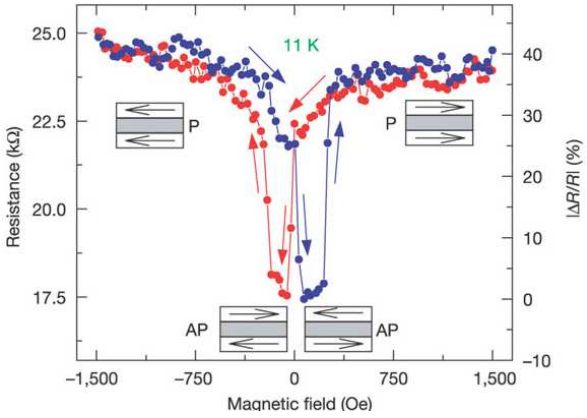

Figure 1.2- First magnetoresistance signal reported by X. Xiong et al.[13] in an organic spin valve structure using LSMO and Co as ferromagnetic electrodes and Alq_3 as organic spacer. Image extracted from reference [13].

However, a lack of a complete understanding of the spin-dependent processes in molecular systems is still present. Severe temperature and bias degradation has

been reported in the magnetoresistance response of organic spintronic structures[1,12,14,19], limiting in this way the future application of this type of devices[9,20]. In all these molecular spintronic structures, the ferromagnetic electrodes employed are conventional inorganic materials (lanthanum strontium manganites (LSMO), Co,…) meanwhile the organic material is only employed as the spacer (spin collector). The understanding and control over the details of the surface engineering processes taking place during the fabrication of these systems are very limited[14,15,21]. A clear example of this point, it is illustrated by the MR sign problem in organic spin valves. The positive spin valve effect is evidenced as a high resistance state for the antiparallel relative orientation of the electrode magnetizations, as expected from a GMR response in the spintronic structure[12]. On the contrary, a negative spin valve effect, translated as a decrease of the resistance in the antiparallel state, has been regularly reported in structures of the type LSMO/Alq_3/Co[14]. Nevertheless, the available knowledge on the spin polarization at both interfaces seriously contradicts this negative-MR data. In this sense, there are many experimental evidences that in the parallel state both electrodes inject spins of the same dominant sign (majority spins)[14]. This situation should lead to a lower resistance state in the parallel configuration respect to the antiparallel one, contrary to the behavior experimentally observed. This point has been addressed by C. Barraud et al.[21] with a model that proposes the formation of spin-hybridization-induced polarized states (SHIPS) at the interface between the electrode and the organic spacer. The presence of these SHIPS would explain the sing inversion detected in the MR of the aforementioned spin valve structures. Thus it is clear that the control and understanding over the physical and chemical processes taking place at the interfaces of this type of devices is not complete.
In addition, one of the main obstacles for an efficient spin injection at the interface between ferromagnetic electrode and the organic material arises from the so-called conductivity mismatch problem[22]. Molecular spintronics proposes the development of molecular-based ferromagnets acting as the spin injector electrodes in molecular spin valves. In principle, the electronic similarities between the spin injector and spin collector materials can reduce the barrier for carrier injection[9]. The semiconducting soft ferrimagnet $V[TCNE]_x$, x~2, is considered one of the most promising candidates for this purpose[23]. This

magnetic molecular-based material, $T_c \approx 380$ K, exhibits a positive MR effects three orders of magnitude higher than its inorganic analogs. The spin injector behavior of $V[TCNE]_x$ has been recently demonstrated in organic spin valves combined with a LSMO electrode[24]. Moreover, an all-molecular spin valve employing two electrodes of $V[TCNE]_x$ with an organic rubrene layer acting as the spacer was reported by A.J. Epstein and coworkers[25] in 2011.

One of the fundamental advantages that can provide the molecular world is the possibility of using multifunctional materials. The organic synthesis toolbox is almost unlimited in terms of design and obtaining of these multifunctional molecular materials respect to their inorganic analogs. Molecular conductors[26] and semiconductors are relevant examples in this context, being hybrid salts typically composed by organic donor layers (responsible of the electrical properties) separated by inorganic magnetic layers. The observation of ferromagnetism and conductivity coexistence[27], non-linear conductivity and negative magnetoresistance[28] are some of the properties found in these molecular systems. However, the application of these materials is limited by the low temperature (below 10 K) at which the mentioned phenomena take place in addition to the fact of being crystalline materials. In consequence one of the main objectives of the molecular spintronics is the application of molecular-based materials exhibiting multifunctional properties at higher temperatures. In addition these materials have to allow their preparation as thin films for the inclusion into spintronic heterostructures. These two requisites are accomplished by one particular type of molecular-based magnetic material: the so-called Prussian blue analogues (PBAs). In the next section we will introduce the main properties of this type of molecular-based materials.

1.2 Prussian blue analogues

The recipe to make a new blue pigment with application for paintings and fabrics was discovered by a Berlin draper named Diesbach in 1704[29]. It was first published in 1710, and its recipe itself described by Woodward and Brown in 1724. Prussian blue (Berlin blue), $Fe^{III}_4\,[Fe^{II}(CN)_6]_3{\cdot}zH_2O$, is often considered as the first synthetic coordination compound[2]. Many centuries later, studies on

this system led to the discovery of its ferromagnetic behavior with an ordering temperature of 5.6 K[30]. Prussian blue and its analogs can be easily synthesized by reacting Lewis bases hexacyanometalates $[B(CN)_6]^{p-}$, with transition metal Lewis acids, A^{q+}, in aqueous solution to give neutral 3D networks $\{A_p[B(CN)_6]_q\}^0 \cdot nH_2O$.[2] Since the 1990s a great variety of PBAs has been synthesized. The most remarkable families of PBAs are those reported to exhibit a high critical temperature with general structure $M_A^{II}[Cr^{III}(CN)_6]_{2/3}\cdot zH_2O$ (M_A=V, Cr, Mn, Ni, Cu)[31,32]. Of particular interest is the system $V^{II}[Cr^{III}(CN)_6]_{0.86}\cdot 2.8H_2O$ obtained by M. Verdaguer et al. with a Curie temperature (T_c) of 315 K[33]. Other examples exhibiting higher critical temperatures have been reported in literature as the crystalline $K^IV^{II}[Cr^{III}(CN)_6]$($T_c$=376K)[34] and the amorphous $K^I_{0.058}V^{II/III}[Cr^{III}(CN)_6]_{0.79}(SO_4)_{0.0058}\cdot 0.93\ H_2O$ with T_c= 372[35].

PBA's are molecular-based materials that accomplish many of the requisites that we have mentioned in the previous section, as potential candidates in spintronic applications. From the point of view of tailoring of magnetic properties, PBA's are interesting systems for two main reasons. Firstly, these molecular-based materials are easily synthesized and in second place, the design of the magnetic properties such as ferromagnetic ordering can be easily achieved by selecting the correct spin sources[36,37].

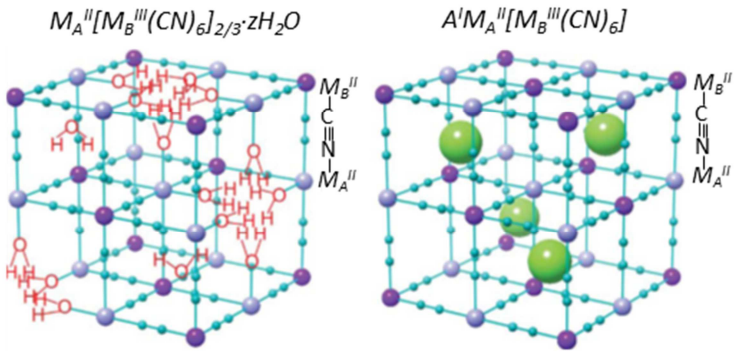

Figure 1.3- Schematic crystal structures for PBAs. Extracted from reference [38].

Two types of cubic crystal structures can be described for PBAs[38] (figure 1.3): i) $A^IM_A^{II}[M_B^{III}(CN)_6]$ being M_A and M_B transition metal ions and A an alkali ion alternatively occupied in the interstitial sites; ii) $A^IM_A^{II}[M_B^{III}(CN)_6]_{2/3}\cdot zH_2O$

containing coordinated and non-coordinated water molecules. Each type of structure will lead to different magnetic and optical functionalities[39,40].

In an ideal scenario, the A and B metal centers are octahedral and connected by nearly A-N≡C-B cyanide bridges. In this context, two types of octahedral sites can be found: strong ligand-field sites $[B(CN)_6]$ and weak ligand field sites $[A(NC)_6]$, since B and A metal centers are surrounded by six carbon or nitrogen atoms of the cyanide bridge, respectively[2,29]. The PBAs structure is closely related to that of perovskites ABO_3, such as $CaTiO_3$ with two main differences. Firstly, instead of oxide ions, in PBA's, metal centers are connected by cyanide bridges forming the 3D framework. In second place, the $[B(CN)_6]^{p-}$ units found in the solid are unaltered from the hexacyanometalate reactant used in the synthesis. This means that, meanwhile the $[Ti^{IV}O_6]^{4-}$ units in perovskite are not stable in water, the $[B(CN)_6]^{p-}$ units remain intact in solution[29]. Due to this situation, PBA's can be considered as molecular-based materials, because they can be directly synthesized from prebuilt molecular precursors[2].

The multifunctionality of these molecular-based materials is another remarkable feature. In a major grade it is determined by the characteristics of the interaction between the metal centers established by the cyano-bridging ligand[38]. These type of materials are classified as mixed-valence compounds arising from the metal-to-metal charge transfer mediated by the cyano ligand[41,42]. The list of scientific literature regarding to the multi-functionalities of PBA's is considerably extensive. In figure 1.4 the main multifunctional characteristics reported for PBA's are summarized. The most remarkable multifunctionalities reported for PBA's are: 1) Charge transfer phase transition[43] 2) Photomagnetism[44,45] 3) Piezomagnetism[46,47] 4) Second harmonic generation (SHG) and magnetization induced SHG (MSHG)[40] 5) Ferroelectricity-ferromagnetism coexistence[48] 6) Humidity-sensitive magnetism[49] 7) Spin ionics[50]. For a complete description of multifunctionalities in PBA's the review published by S. Ohkoshi and H. Tokoro[38] is highly recommended.

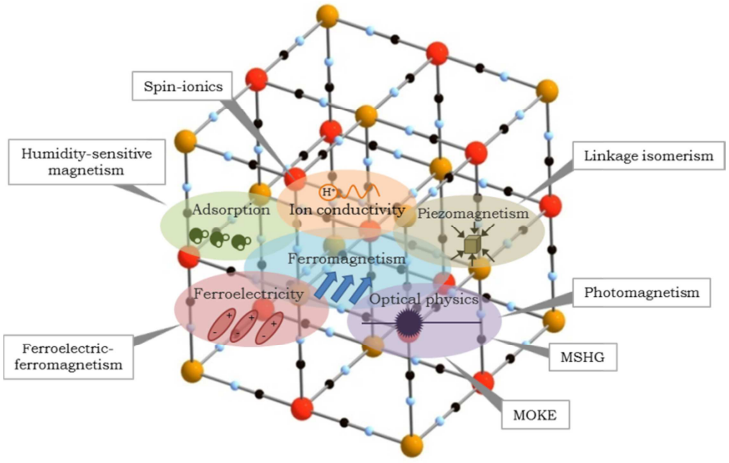

Figure 1.4- Summary of the main multifunctionalities reported in PBA. Base on image of reference [38].

Considering all the information described so far, one can expect that the inclusion of this type of multifunctional materials in spintronic structures could lead to a new generation of devices establishing an almost unlimited playground for physicists and chemists. As it was mentioned in the previous section, one of the challenging points in the molecular approach for spintronics is the organization of molecular-based materials as thin films. This point is completely fulfilled by PBA's. Indeed, several methods for depositing thin films of PBA's have been reported in literature. By far the most applied method has been the electrochemical deposition[51–61]. Other methods for PBA thin film preparation include adsorption onto sol-gel films[62], adsorption at Langmuir monolayers[63] and sequential assembly (layer by layer)[64]. By applying the latter method, Talham *et al.* reported the synthesis of PBA thin films of the family $A_jCo_k[Fe(CN)_6]_l{\cdot}nH_2O$ exhibiting an anisotropic photoinduced effect[64].This fabrication approach is based on the sequential immersion of a substrate on separate solutions containing each of them the A^{q+} cation and the $[B(CN)_6]^{p-}$ anion. As a result of this process, a PBA thin film is formed on the substrate arising from the covalent bonding of the subunits present in each solution. By means of this technique they successfully fabricated heterostructures with the PBA's $Rb_{0.8}Ni_{4.0}[Cr(CN)_6]_{2.9}{\cdot}nH_2O$ and $Rb_{0.7}Co_{4.0}[Fe(CN)_6]_3{\cdot}nH_2O$[65]. Under these

conditions, they could detect interesting cross-properties effects in the materials, leading to photomagnetic effects at higher temperatures than for the isolated systems.

In this thesis we have chosen the electrochemical deposition approach to fabricate PBA's thin films. There are many motivations regarding this strategy with respect to the layer by layer (Lbl) technique. In contrast to the electrochemical method, the Lbl does not need conductive substrates for the growing of the films. Despite this advantageous feature, the Lbl technique has many drawbacks. For the fabrication of a homogenous film, many cycles of the sequential process previously indicated are needed. Thus, Lbl is a slow method in which the control of the growing conditions is difficult to achieve[66]. In addition, many parameters need to be fixed for obtaining reproducible films in terms of morphology and composition (and in consequence, magnetic properties). On the contrary, electrochemical deposition is a fast and reproducible method for the fabrication of homogenous PBA thin films over big substrate areas. A high grade of control on the morphology, composition and magnetic properties of the thin films can be achieved with this strategy[51]. As properly described by K. Hashimoto *et al.*[57], a double motivation is found when using metal cyanides as building blocks for the growing of PBA thin films by an electrochemical approach. Firstly, by means of electrochemical reduction, it is possible to fabricate PBA films formed by mixed-valence transition metals, allowing a control over the structure and potentially raising the critical temperature of the material. In second place, provided by the zeolitic properties of PBA thin films, their magnetic properties can be electrochemically controlled after the synthesis. Another important motivation, regarding the electrochemical approach, is the possibility of synthesizing thin films of PBA's families exhibiting magnetic ordering at high critical temperatures[57,67]. As described in the previous section, this is another important requirement for the application of molecular-based materials in spintronic devices. As an example, we can cite the fabrication of thin films of the system $A_jCr^{II}_x[Cr^{III}(CN)_6]_y \cdot nH_2O$ reported in first instance by K. Hashimoto and co-workers[57]. This PBA exhibit a critical temperature between 100 K and 270K depending on the electrochemically controlled oxidation states[57,68], being this system one of the materials that will

be characterized in the first part of this thesis. In addition, the same authors reported the electrochemical deposition of thin films of vanadium hexacyanochromate derivatives presenting ferromagnetic ordering up to 345 K[67]. Thus, the motivation for the study of these molecular-based materials, as possible candidates for molecular spintronics applications, is supported by all the information presented so far in this chapter.

1.3 Experimental approach

In this section we will explain the experimental techniques employed in the first part of the thesis. The two main aspects to be described are the principles of the PBA thin film fabrication and the characteristics of the Magneto-optical Kerr Effect set-up (MOKE). The last one, as being a self-made set-up, and an important part of the work developed in this thesis, will be more extensively addressed. Finally a short highlight of the rest of techniques applied for the characterization of the PBA systems will be presented.

1.3.1 Fabrication of Prussian blue analogue thin films

In this thesis, the fabrication of PBA' s thin films and heterostructures has been addressed by an electrochemical deposition approach. A Metrohm *AUTOLAB* potentiostat in coulometry mode was employed for depositing PBA thin films onto different type of conductive substrates. The experiment was computer controlled by the software *Autolab 4.8* provided by the same company. A three-electrode cell was charged with an electrolytic solution containing the precursors for the electropolymerization of the material. In figure 1.5 it is shown a picture of the electrochemical cell indicating each element of the set up. A commercial Ag/AgCl (3M NaCl) reference electrode provided by *ALS Co.* was used. As a counter electrode a Pt electrode of 1.5 cm^2 area, provided by *GoodFellow* and adapted to our electrochemical cell, was employed. Different types of working electrodes were used according to the characterization performed on the final samples. The most commonly employed has been a Mylar susbtrate coated with an evaporated gold layer. Mylar is the commercial name for the polyethylene terephthalate, which in our case is provided by *DuPont*

Teijin Films. In other cases, ITO (Indium Tin Oxide) substrates or glass substrates coated with an evaporated gold layer were employed. The evaporation of gold electrodes allowed us to design, by the proper choosing of masks, the geometry of the working electrode. All the electrodes are fixed to the cell containing the electrolytic solution by means of a Teflon holder. This holder is provided with two extra entrances for nitrogen bubbling during the electrochemical process. In addition, the set-up permits a stirring of the solution during the experiments.

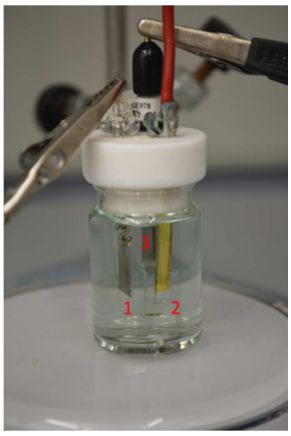

Figure 1.5- Description of the elements in the electrochemical cell: 1) Pt counter electrode, 2) Au working electrode, 3) Ag/AgCl (3M) reference electrode.

As previously indicated, a chronoamperometric method was applied for the electrodeposition of the PBA thin films by electrochemically reducing the precursors for the growing of the material[69]. From the experimental point of view, the PBA electrodeposition by chronoamperometry is relatively simple. Let use consider the synthesis of a mixed-valence PBA of the type $Fe^{II}[Cr^{III}(CN)_6]_{3/2}\cdot nH_2O$ for illustrating the process. Initially, the electrochemical cell is charged with an aqueous solution containing the precursors for the reaction, being $[Fe(H_2O)_6]^{3+}$ species and $[Cr(CN)_6]^{3-}$ anions. By means of the potentiostat, a reduction potential V_R (respect to reference electrode) is applied in the working electrode in order to reduce the $[Fe(H_2O)_6]^{3+}$ entities. With this process, the reduced $[Fe(H_2O)_6]^{2+}$ species formed at the vicinity of the electrode reacts *in situ* with the hexacyanometalate anion forming in this way the PBA

thin film onto the working electrode (figure 1.6). By modifying the electrodeposition time it is possible to tailor the thickness of the films in a highly reproducible way.

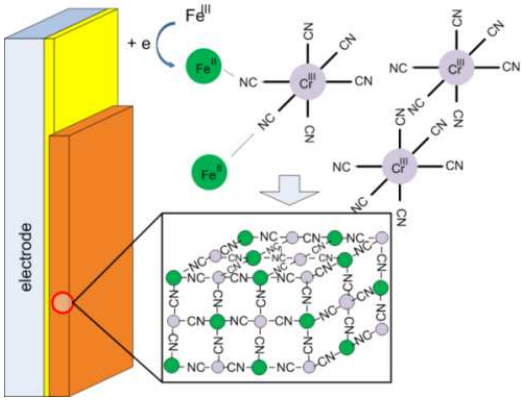

Figure 1.6– Illustration of the electrochemical reduction process taking place in the formation of a PBA thin film.

As it is mentioned along the discussion of the thesis, a chronocoulometry method was chosen for monitoring the electrochemical deposition of the PBA films. In chronoamperometry the monitored response is the current flowing through the electrochemical cell, meanwhile in chronocoulometry is the charge evolution as a function of time. Nevertheless, both methods yield essentially the same information, since the difference between them lies principally in the method of acquisition and treatment of the data[70]. If the chronoamperometric response of a system to a potential perturbation is *i(t)*, then the chronocoulometric response is simply:

$$Q(t) = \int_0^t i(t)dt \quad (eq.\ 1.1)$$

Thus, conceptually both chronomethods are essentially the same respect to the phenomenology taking place. With the set-up previously described, studies of

cyclic voltammetry (CV) can be performed on electrolytic solutions of interest as well as in electrodeposited thin films immersed in an ionic blank solution. A cyclic voltammogram is obtained by measuring the current at the working electrode during the potential scan. From this characterization it is possible to monitor the electrochemical oxidation and reduction processes taking place in the electrolytic solution at the vicinity of the working electrode.

1.3.2 Magneto-Optical Kerr Effect (MOKE) technique

- The magneto-optic effect

The first magneto-optic effect was reported by Michael Faraday in 1845, being the first experimental evidence of the interaction between electromagnetic radiation and a magnetized material[71]. He discovered the rotation of the polarization plane of light when passing through a glass over which a magnetic field in the direction of propagation is applied. This phenomenon is known as Faraday effect. This effect occurs in transmission, being only observed for transparent or semi-transparent systems. It was not until 1876 when John Kerr discovered that the reflected light from a polished surface of an electromagnet pole also suffers a rotation in its polarization plane[72]. This is the so-called magneto-optical Kerr effect (MOKE), in which this rotation angle is known as Kerr angle or Kerr rotation, θ_K. Kerr effect, as occurring in reflection, can be observed in any type of sample with reflective surfaces. Thus Faraday and Kerr effect are physically the same effect, but being the first one taking place in transmittance and the former one in reflectance. The application of MOKE for studying surface magnetism was reported for the first time in 1986 by S. Bader *et al.*[73] on ultrathin Fe films grown epitaxially onto a single crystalline substrate of Au (100). Since that moment MOKE, due to its surface sensitivity and local character, has been extensively applied for the study of surface magnetic properties of ultra-thin films, magnetic heterostructures and a wide variety of low-dimensional magnetic processes. For a more detailed information, a complete description of MOKE applications is nicely reviewed in the works of Z. Q. Qiu and S.D. Bader[74,75]. According to Voigt classification three configurations can be define for Kerr effect, being polar, longitudinal and

transverse, depending on the relative orientation of the magnetization vector of the sample and the light incidence plane[76]. We will briefly describe the two first configurations as being the employed in our set-up (figure 1.7).

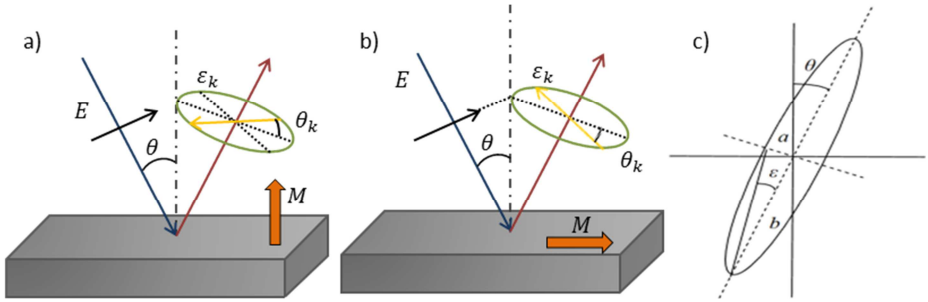

Figure 1.7- a) Polar and b) longitudinal configurations for Kerr effect. c) Polarization ellipse indicating the rotation angle θ_K and ellipticity ε_K.

The *polar configuration* is obtained when the sample magnetization $\vec{M}$ is perpendicular to the film surface and it is contained in the incidence plane. The reflected light, in the direction normal to the surface, experiences a rotation θ_K and acquires an ellipticity ε_k (figure 1.7). In the *longitudinal configuration*, the sample magnetization $\vec{M}$ is parallel to the surface of the film and parallel to the incidence plane of light. As before, the reflected light is elliptically polarized with its polarization plane rotated θ_K and ellipticity ε_k.

Two types of incident linearly polarized light can be defined according to the polarization state: *p-polarized light* (with polarization plane parallel to the plane of incidence) and *s-polarized light* (with polarization plane perpendicular to the incidence one).

- Origin of magneto-optic effect

Magneto-optic effects can be explained in the context of either macroscopic dielectric theory or microscopic quantum theory[77]. Macroscopically, magneto-optic effects arise from the antisymmetric, off-diagonal elements in the dielectric tensor (which is determined by the motion of electrons in the medium). From a microscopic view, spin-orbit interaction will be the responsible for the coupling between the light electric field and electron spin[75]. Thus, a microscopic

description considers the different response of electrons to left- and right-circularly polarized electromagnetic waves. By considering a classical scenario, when a beam of light propagates through a material, the electric field of light will induce a motion of the electrons in the medium[74,75]. In absence of an external magnetic field, the right- and left-circularly polarized light will drive the electrons into respective left and right circular motions with the same radius. Thus no difference between dielectric constant for each type of circularly polarized electromagnetic waves will be detected, since the electric dipole moment is proportional to the radius of the circular orbit[74,75]. No magneto-optic effect will be detected in such situation. However, when an external magnetic field is applied, an additional Lorentz force will act on each electron inducing different radius for each circularly polarized component and in consequence a magneto-optic response. Regarding to a quantum description of the phenomena, in 1932, Hulme gave an explanation of the magneto-optic effect based on the coupling between the electron spin and its motion by means of spin-orbit interaction[78]. Spin-orbit coupling, $\sim(\nabla V \times \vec{p}) \cdot \vec{s}$, is result of the interaction arising between the electron spin and the magnetic field the electron "experiences" when moving through the electric field $-\nabla V$ with momentum $\vec{p}$ inside a medium. Thus, this originates a coupling between the magnetic and optical properties of a ferromagnet. Hulme explained the magneto-optic effect by the difference of refractive index for lift- and right-circularly polarized light in the material, originated by the energy splitting induced by the spin-orbit coupling[78]. Kittel improved the scenario proposed by Hulme, indicating that the change of the wave functions, due to the spin-orbit coupling, gives the right order of magnitude for the difference between both refraction indices in the material[75].

- MOKE set-up

In this last point, we will describe the MOKE set-up employed for the magneto-optical characterization of PBA thin films in this thesis. The equipment described here corresponds to a self-made Kerr magnetometer in which the design, construction and improvement have been developed during the work of this thesis. In particular, this instrument has been systematically evaluated for

the characterization of PBA thin films. Nevertheless, thanks to its surface sensitivity and local character, the application of this instrument has been extended to other materials of interest in the Research Team on Molecular Materials (UIMM). One of the major improvements in the design of this apparatus has been the introduction of a polarization modulation technique[79]. The application of this approach allows sensibilities for the detection of Kerr rotation two orders of magnitude higher than conventional strategies[80]. In figure 1.8 it is depicted a picture of the MOKE set-up, showing the optical elements employed for the characterization of the samples.

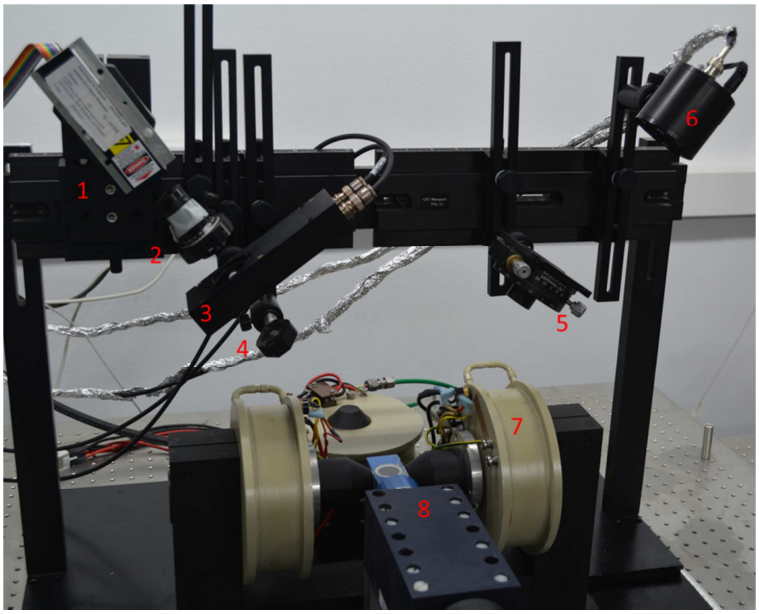

Figure 1.8- Photography of the MOKE set-up indicating some of the most important elements in the set-up: 1) He-Ne laser, 2) Glan-Laser Calcite polarizer, 3) Photoelastic modulator (PEM), 4) Lens, 5) Analyzer, 6) Photodiode, 7) Electromagnets, 8) Cryostat.

A He-Ne laser with a wavelength of 633 nm and an output power of 12 mW is used as the light source, producing a nearly linearly-polarized light beam. This beam is passed through a Glan-Laser Calcite polarizer with an extinction coefficient of 10^{-5}, whose axis is rotated 45º respect to the incidence plane. Subsequently, the polarized light is transmitted through a photo-elastic modulator (*PEM-100, Hinds Instruments*). The PEM consists of a quartz window

which is contracted and expanded in a sinusoidal form along the *s* direction by means of a piezoelectric quartz coupled to one of its extremes[81]. In this way, a modulation of light takes place with a frequency of 50 kHz corresponding to the natural resonant frequency of the modulator optical element. The effect of the modulation is the introduction of a periodic retardation into the electric field of light in the form $\varphi = \varphi_0 \sin(\omega_m t)$, being $\omega_m = 2\pi \cdot 50\ kHz$ the angular frequency of modulation and φ_0 the amplitude of the periodic retardation[81]. If the PEM is set with a retardation of $\lambda/4$, then the element acts as a quarter-wave plate leading to an oscillation in the polarization between left-circularly polarized light, linearly polarized, right-circularly polarized light, repeating constantly this process. The modulation signal is employed as the reference signal in a *lock-in* amplifier (*Stanford Research System, SR830 DSP*). A lens with a focal distance f = 100 mm and a diameter D = 30 mm is used for focalizing, onto the sample the beam of light coming from the PEM. The power density of the beam at the sample position has been determined to be in the order of 6.5 mW·cm^{-2}. After reflection on the sample, the light transmits through an analyzer (which allows working with s- or p-polarized lights) and is finally detected by a photo-sensitive fast responding photodiode (*DET 100*, *Hinds Instruments*) that provides the input signal for the *lock-in* amplifier. The *lock-in* amplifies and analyzes the signal coming from the photodetector. On one side, it takes the value of the continuous signal and on the other hand, it decomposes the signal into Fourier series. By this process, the *lock-in is* able to register the first harmonic with modulation ω_m and second harmonic with modulation $2\omega_m$. The signal corresponding to the first harmonic is proportional to Kerr ellipticity ε_K, while the second harmonic provides information about Kerr rotation θ_K.

Further details about the modulation technique can be found in literature[79,80].Regarding to the magnetic field generation, a bipolar power supply (*Kepco, BOP 50-8M*) provides the ramp current to an electromagnet (*GMW 3470*). The magnetic field is calibrated by means of a Hall sensor (*DTM-133 digital teslameter, Group 3*) in order to get a calibration equation for the conversion between current and magnetic field. With these electromagnets is possible to apply magnetic fields parallel and perpendicular to the film surface. Thus longitudinal and polar Kerr configurations can be achieved in the set-up. Values

magnetic field in the polar configuration range between ±150mT, meanwhile magnetic fields up to ±380 mT can be applied in longitudinal configuration. The sample under analysis is mounted on a cryostat holder (*Oxford Instruments*). By means of a pumping system (*Pfeiffer Vacuum*) a high vacuum in the order of 10^{-6} mbar can be established in the cryostat. In this way, samples can be studied in the temperature range between 10 K and 400 K. All the data acquisition is coordinated by a PC, using a self-made *Labview* program (*National Instruments*).

1.3.3 General characterization instruments and techniques

- *FT-Infra-red spectroscopy*: Infrared spectra of PBA thin films were recorded on a Nicolet 5700 FT-IR spectrometer using a Veemax II Specular Reflectance Accessory.
- *UV-visible spectroscopy*: UV-visible absorption spectra of films of 1 were acquired in a spectroelectrochemical cell using a UV-VIS-NIR DH-2000 Micropack light source and a USB2000 detector (*Ocean Optics*). A slide of ITO-covered quartz was used as the transparent electrode.
- *Elemental analysis*: Carbon, nitrogen and hydrogen contents were determined by micro-analytical procedures using an EA 1110 CHNS-O Elemental Analyzer from CE Instruments.
- *Inductively couple plasma mass spectrometry (ICP-MS)*: Theharacterization was performed on an ICP-MS Agilent 7700x including HMI (high matrix introduction) and He mode ORS as standard. The conditions of measurements were set at the standard values in such a way that a RF power of 1550 W, a carrier of gas of 0.99 L/min and a sample uptake of 0.3ml/min was employed for the characterization. The sampling depth of the apparatus was 8 mm with 100 sweeps and 3 replicates. The dwell time was set at 0.12 seconds with a spray chamber temperature of 2 °C.
- *Thermogravimetric analysis*: TG/ATD curves were registered on a thermogravimetric and differential thermal analyzer model *Mettler Toledo TGA/SDTA 851e* operating in the range 25 -1100 °C with a sensibility of 0.1 µg. Scan rates of 10°C/min under nitrogen

atmosphere were performed. The PBA samples were electrodeposited with the highest electrodeposition time and scratched from the film.

- *Raman characterization*: Raman measurements were performed in collaboration with Prof. Ana Cros from the Material Science Institute (ICMUV) at the University of Valencia. The measurements were done in backscattering geometry by means of a T64000 *Jobin-Yvon* triple spectrometer equipped with gratings of 1800 $gr \cdot mm^{-1}$, a confocal microscope and a liquid-nitrogen cooled charge coupled device detector. The power density was 50 $W \cdot cm^{-2}$ and 100 $W \cdot cm^{-2}$ for blue and red light, respectively.
- *X-Ray diffraction (XRD) experiments*: The XRD characterization was performed using an Agilent SuperNova Atlas Dual Source single crystal diffractometer equipped with a Mo source (λ = 0.711 Å) and a CCD detector. A collection of microcrystals was scraped from the surface of the PBA films and mounted on the sample holder (cryoloop). Four images of diffraction cones were obtained at different angles and the diffraction pattern was obtained by integration using the *CrysAlispro* software. When analyzing a powder sample, it was spread on the cryoloop and characterized using the same protocol.
- *Ellipsometry:* The ellipsometry characterization was performed by means of a *GES5E Variable Angle Spectroscopic Ellipsometer*. This instrument allows the determination of layer thicknesses, homogeneity testing and optical properties of the samples in the range between 250 nm to 1700 nm.
- *EDAX analysis*: Metal analysis of the electrodeposited films was performed on a *Philips XL30* scanning electron microscope equipped with an EDAX DX-4 microsonde.
- *Transmission electron microscopy (TEM)*: A JEM-1010 (*JEOL*) transmission electron microscope operating at 100 kV and equipped with a Digital Camera *MegaView III* was used in the morphological characterization of iron oxide nanoparticles. Solutions containing

nanoparticles were deposited on a TEM grid and dried under vacuum. Images were acquired using the Olympus Image Analysis software.

- *HRTEM-STEM studies*: All high resolution TEM experiments were performed in a *Tecnai F30* (*FEI Company*) operated at 300KV at the Advanced Microscopy Laboratory at the Nanoscience Institute of Aragón. From the High Resolution TEM (HRTEM) images size, morphology and crystalline structure of each of the layers can be obtained. High Angle Annular Dark Field (HAADF) images, Energy Dipersive X-rays Spectra (EDS) and Electron Energy Loss spectra (EELS) were obtained using a HAADF detector, an EDAX detector and a *Tridiem* (*Gatan*) Energy Filter respectively in Scanning Transmission Electron Microscopy mode (STEM): A small probe (diameter around 0.5 nm) is formed and the sample is scanned, obtaining an image and a spectrum in the whole range of Energy simultaneously pixel by pixel. That way we can obtain 1D composition profiles or 2D maps for each of the elements present in the material.

- *Profilometry measurements*: An *Ambios Technology XP-1* profilometer placed on a vibration isolation table was used for determining the thicknesses of the PBA thin films.
- *Atomic Force Microscopy (AFM)*: AFM images were obtained with a *Nanoscope IV* a atomic force microscope from *Veeco*. The images were acquired in tapping-mode in air at room temperature with Si tips (freq. and K of *ca.* 300 kHz and 40 $N \cdot m^{-1}$, respectively). Images were recorded with 512 × 512 pixels and 0.5 – 1 Hz scan rate. RMS roughness and average particle size were analyzed by using *WSxM4 4.0 Develop 13.0* software[82] developed by *Nanotec Electronics S.L.*

- *Magnetic Force Microscopy (MFM): Attocub*e Low Temperature Magnetic Force Microscope (LT-MFM) was employed for the MFM study on PBA thin films. The operating temperature range is 1.8 K - 300 K. External magnetic 2D vector field until 8 T in vertical and 2 T in horizontal direction can be applied.

- *Magnetic characterization:* Variable-temperature and field-dependent dc magnetization measurements were carried out in a SQUID magnetometer model *Quantum Design MPMS* working in the range 2-300 K and ±7T. The same device was used in the ac susceptibility measurements at different frequencies of the oscillating field of 3.95 G amplitude. The PAB films prepared on Mylar were cut in pieces and introduced in the sample holder with the applied magnetic field parallel or perpendicular to the surface. Powder samples were directly measured inside a plastic capsule.
- *Magneto-transport measurements:* The magneto-transport characterization of PBA thin films was performed on a "Physical Properties Measuremet System" Quantum Design PPMS-9 model working between 1.9-400 K and ±9 T. This set-up is designed for low resistance measurements. In order to overcome this limitation, considering the high resistances of PBA films, the system was improved.

1.4 Bibliography

(1) Sanvito, S. *Chem. Soc. Rev.* **2011**, *40*, 3336.

(2) Verdaguer, M, Robert, V. *Compr. Inorg. Chem. II* **2013**, 131.

(3) Prinz, G. a. *Science (80-.).* **1998**, *282*, 1660.

(4) Wolf, S. a; Awschalom, D. D.; Buhrman, R. a; Daughton, J. M.; von Molnár, S.; Roukes, M. L.; Chtchelkanova, a Y.; Treger, D. M. *Science* **2001**, *294*, 1488.

(5) Felser, C.; Fecher, G. H.; Balke, B. *Angew. Chem. Int. Ed. Engl.* **2007**, *46*, 668.

(6) Baibich, M.N., Broto, J.M., Fert, A., Nguyen Van Dau, F., Petroff, F., Eitenne, P., Creuzet, G., Friederich, A., Chazelas, J. *Phys. Rev. Lett.* **1988**, *61*, 2472.

(7) Binasch, G., Grünberg, P., Saurenbach, F., Zinn, W. *Phys. Rev. B* **1989**, *39*, 4828.

(8) Fert, A. *Angew. Chem. Int. Ed. Engl.* **2008**, *47*, 5956.

(9) Camarero, J.; Coronado, E. *J. Mater. Chem.* **2009**, *19*, 1678.

(10) Chiang, C K, Fincher, C R, Park, Y W, Heeger, A J, Shirakawa, H, Louis, E J, Gau, S C, MacDiarmid, A. G. *Phys. Rev. Lett.* **1977**, *39*, 1098.

(11) Manriquez, J. M.; Yee, G. T.; Mclean, R. S.; Epstein, A. J.; Millert, J. S. *Science (80-.).* **1991**, *252*, 1415.

(12) Vardeny, Z. V. *Organic Spintronics*; Taylor & Francis Group: Boca Raton-Florida, 2010.

(13) Xiong, Z. H.; Wu, D.; Vardeny, Z. V.; Shi, J. *Nature* **2004**, *427*, 821.

(14) Dediu, V. A.; Hueso, L. E.; Bergenti, I.; Taliani, C. *Nat. Mater.* **2009**, *8*, 707.

(15) Santos, T.; Lee, J.; Migdal, P.; Lekshmi, I.; Satpati, B.; Moodera, J. *Phys. Rev. Lett.* **2007**, *98*, 016601.

(16) Mott, N. F. *Adv. Phys.* **1964**, *13*, 325.

(17) Moodera, J. S., Kinder, L. R., Terrilyn M. W., M. R. *Phys. Rev. Lett.* **1995**, *74*, 3273.

(18) Dediu, V.; Murgia, M.; Matacotta, F. C.; Taliani, C.; Barbanera, S. *Solid State Commun.* **2002**, *122*, 181.

(19) Ehrenfreund, E.; Valy Vardeny, Z. *Phys. Chem. Chem. Phys.* **2013**, *15*, 7967.

(20) Wang, T. X.; Wei, H. X.; Zeng, Z. M.; Han, X. F.; Hong, Z. M.; Shi, G. Q. *Appl. Phys. Lett.* **2006**, *88*, 242505.

(21) Barraud, C.; Seneor, P.; Mattana, R.; Fusil, S.; Bouzehouane, K.; Deranlot, C.; Graziosi, P.; Hueso, L.; Bergenti, I.; Dediu, V.; Petroff, F.; Fert, A. *Nat. Phys.* **2010**, *6*, 615.

(22) Schmidt, G.; Ferrand, D.; Molenkamp, L.; Filip, a.; van Wees, B. *Phys. Rev. B* **2000**, *62*, R4790.

(23) Prigodin, B. V. N.; Raju, N. P.; Pokhodnya, K. I.; Miller, J. S.; Epstein, A. J. *Adv. Mater.* **2002**, *14*, 1230.

(24) Yoo, J.-W.; Chen, C.-Y.; Jang, H. W.; Bark, C. W.; Prigodin, V. N.; Eom, C. B.; Epstein, a J. *Nat. Mater.* **2010**, *9*, 638.

(25) Li, B.; Kao, C.-Y.; Yoo, J.-W.; Prigodin, V. N.; Epstein, A. J. *Adv. Mater.* **2011**, *23*, 3382.

(26) Coronado, E.; Day, P. *Chem. Rev.* **2004**, *104*, 5419.

(27) Coronado, E., Galán-Mascarós, J.R., Gómez-García, C.J., Laukhin, V. *Nature* **2000**, *408*, 447.

(28) Matsushita, M.; Kawakami, H.; Sugawara, T.; Ogata, M. *Phys. Rev. B* **2008**, *77*, 195208.

(29) Verdaguer, M.; Girolami, G. *Magnetism: Molecules to Materials V- Chapter 9: Magnetic Prussian Blue Analogues*; Wiley, 2005.

(30) Holden, A.N., Matthias, B.T., Anderson, P.W., Lewis, H. W. *Phys. Rev.* **1956**, *102*, 1463.

(31) Verdaguer, M.; Bleuzen, a.; Train, C.; Garde, R.; Fabrizi de Biani, F.; Desplanches, C. *Philos. Trans. R. Soc. A Math. Phys. Eng. Sci.* **1999**, *357*, 2959.

(32) Mallah, T.; Thiébaut, S.; Verdaguer, M.; Veillet, P. *Science* **1993**, *262*, 1554.

(33) S. Ferlay, T. Mallah, R. Ohuaès, P. Veillet, M. V. *Nature* **1995**, *378*, 701.

(34) Holmes, S. M.; Girolami, G. S. *J. Am. Chem. Soc.* **1999**, *121*, 5593.

(35) Hatlevik, B.; Buschmann, W. E.; Zhang, J.; Manson, J. L.; Miller, J. S. *Adv. Mater.* **1999**, *11*, 914.

(36) Ohkoshi, S.; Abe, Y.; Fujishima, A.; Hashimoto, K. *Phys. Rev. Lett.* **1999**, *82*, 1285.

(37) Ohkoshi, S.; Iyoda, T.; Fujishima, A.; Hashimoto, K. *Phys. Rev. B* **1997**, *56*, 11642.

(38) Tokoro, H.; Ohkoshi, S. *Dalton Trans.* **2011**, *40*, 6825.

(39) Nuida, T.; Matsuda, T.; Tokoro, H.; Sakurai, S.; Hashimoto, K.; Ohkoshi, S. *J. Am. Chem. Soc.* **2005**, *127*, 11604.

(40) Ohkoshi, S.; Saito, S.; Matsuda, T.; Nuida, T.; Tokoro, H. *J. Phys. Chem. C* **2008**, *112*, 13095.

(41) Verdaguer, M.; Bleuzen, A.; Marvaud, V.; Vaissermann, J.; Seuleiman, M.; Desplanches, C.; Lomenech, C.; Rosenman, I.; Veillet, P.; Cartier, C. *Coord. Chem. Rev.* **1999**, *190*, 1023.

(42) Robin, M. B.; Day, P. *Adv. Inorg. Chem. Radiochem.* **1968**, *10*, 247.

(43) Ohkoshi, S.; Tokoro, H.; Hashimoto, K. *Coord. Chem. Rev.* **2005**, *249*, 1830.

(44) Escax, V.; Bleuzen, a; Cartier Dit Moulin, C.; Villiam, F.; Goujon, a; Varret, F.; Verdaguer, M. *J. Am. Chem. Soc.* **2001**, *123*, 12536.

(45) Sato, O.; Iyoda, T.; Fujishima, A.; Hashimoto, K. *Science (80-.).* **1996**, *272*, 704.

(46) Coronado, E.; Giménez-López, M. C.; Korzeniak, T.; Levchenko, G.; Romero, F. M.; Segura, A.; García-Baonza, V.; Cezar, J. C.; de Groot, F. M. F.; Milner, A.; Paz-Pasternak, M. *J. Am. Chem. Soc.* **2008**, *130*, 15519.

(47) Coronado, E.; Giménez-López, M. C.; Levchenko, G.; Romero, F. M.; García-Baonza, V.; Milner, A.; Paz-Pasternak, M. *J. Am. Chem. Soc.* **2005**, *127*, 4580.

(48) Ohkoshi, S.; Tokoro, H.; Matsuda, T.; Takahashi, H.; Irie, H.; Hashimoto, K. *Angew. Chem. Int. Ed. Engl.* **2007**, *46*, 3238.

(49) Ohkoshi, S.-I.; Arai, K.-I.; Sato, Y.; Hashimoto, K. *Nat. Mater.* **2004**, *3*, 857.

(50) Ohkoshi, S.; Nakagawa, K.; Tomono, K.; Imoto, K.; Tsunobuchi, Y. *J. Am. Chem. Soc.* **2010**, *132*, 6620.

(51) Coronado, E.; Makarewicz, M.; Prieto-Ruiz, J. P.; Prima-García, H.; Romero, F. M. *Adv. Mater.* **2011**, *23*, 4323.

(52) Coronado, E.; Fitta, M.; Prieto-Ruiz, J. P.; Prima-García, H.; Romero, F. M.; Cros, A. *J. Mater. Chem. C* **2013**, *1*, 6981.

(53) Itaya, K.; Ataka, T.; Toshimaf, S. *J. Am. Chem. Soc.* **1982**, *104*, 4767.

(54) June, I.; Neff, V. D. *J. Electrochem. Soc.* **1978**, *125*, 886.

(55) Kulesza, P. J., Doblhofer, K. *J. Electroanal. Chem.* **1989**, *274*, 95.

(56) Lundgren, C. A.; Murray, R. W. *Inorg. Chem.* **1988**, *27*, 933.

(57) O. Sato, T.Iyoda, A. Fujishima, K. H. *Science (80-.).* **1996**, *271*, 49.

(58) Prima-Garcia, H.; Coronado, E.; Prieto-Ruiz, J. P.; Romero, F. M. *Nanoscale Res. Lett.* **2012**, *7*, 232.

(59) S. Ohkoshi, A. Fujishima, K. H. *J. Am. Chem. Soc.* **1998**, *120*, 5349.

(60) Nuida, T.; Hozumi, T.; Kosaka, W.; Sakurai, S.; Ikeda, S.; Matsuda, T.; Tokoro, H.; Hashimoto, K.; Ohkoshi, S. *Polyhedron* **2005**, *24*, 2901.

(61) Ohkoshi, S.; Einaga, Y.; Fujishima, A.; Hashimoto, K. *J. Electroanal. Chem.* **1999**, *473*, 245.

(62) Guo, Y.; Guadalupe, A. R.; Resto, O.; Fonseca, L. F.; Weisz, S. Z. *Chem. Mater.* **1999**, *11*, 135.

(63) Lafuente, C.; Mingotaud, C.; Delhaes, P. *Chem. Phys. Lett.* **1999**, *302*, 523.

(64) Park, J.-H.; Cižmár, E.; Meisel, M. W.; Huh, Y. D.; Frye, F.; Lane, S.; Talham, D. R. *Appl. Phys. Lett.* **2004**, *85*, 3797.

(65) Pajerowski, D. M.; Andrus, M. J.; Gardner, J. E.; Knowles, E. S.; Meisel, M. W.; Talham, D. R. *J. Am. Chem. Soc.* **2010**, *132*, 4058.

(66) Ariga, K.; Hill, J. P.; Ji, Q. *Phys. Chem. Chem. Phys.* **2007**, *9*, 2319.

(67) Ohkoshi, S.; Mizuno, M.; Hung, G.; Hashimoto, K. *J. Phys. Chem. B* **2000**, *104*, 9365.

(68) Buschmann, W. E.; Paulson, S. C.; Wynn, C. M.; Girtu, M. A.; Epstein, A. J.; White, H. S.; Miller, J. S. *Chem. Mater.* **1998**, *10*, 1386.

(69) Mann, O. *Nanoscale Electrodeposition of Ultrathin Magnetic Ni Films and of the compound semiconductors AlSb and ZnSb from Ionic Liquids*; Cuvillier Verlag: Göttingen (Germany), 2008.

(70) MacDonald, D. D. *Transient Techniques in Electrochemistry*; Plenum Press: New York (USA), 1977.

(71) Faraday, M. *Philos. Trans. R. Soc. London* **1846**, *136*, 1.

(72) Weinberger, P. *Philos. Mag. Lett.* **2008**, *88*, 897.

(73) Bader, S.D., Moog, E.R., Grünberg, P. *J. Magn. Magn. Mater.* **1986**, *53*, L295.

(74) Qiu, Z. Q.; Bader, S. D. *Rev. Sci. Instrum.* **2000**, *71*, 1243.

(75) Qiu, Z. Q.; Bader, S. D. *J. Magn. Magn. Mater.* **1999**, *200*, 664.

(76) Hubert, A., Schäfer, R. *Magnetic Domains: The Analysis of Magnetic Microstructures*; Springer: Germany, 2000.

(77) Landau, L. *Electrodynamics of Continous Media*; Pergamon Press Ltd., 1960; Vol. 9.

(78) Hulme, H. R. *Proc. R. Soc. London Ser. A* **1932**, *135*, 237.

(79) Polisetty, S., Scheffler, J., Sahoo, S., Wang, Y., Mukherjee, T., He, X., Binek, C. *Rev. Sci. Instrum.* **2008**, *79*, 055107.

(80) Sato, K. *Jpn. J. Appl. Phys.* **1981**, *20*, 2403.

(81) *PEM-100 User Manual*; Hinds-Instruments, Ed.

(82) Horcas, I.; Fernández, R.; Gómez-Rodríguez, J. M.; Colchero, J.; Gómez-Herrero, J.; Baro, a M. *Rev. Sci. Instrum.* **2007**, *78*, 013705.

Chapter 2

Fabrication and physical characterization of electrodeposited thin films of the molecular-based magnet $Cr_{5.5}(CN)_{12} \cdot 11.5\ H_2O$

2.1 Introduction

Thin films of PBAs can be interesting materials for the fabrication of future molecular-based spintronic devices[1], combining magneto-optical properties and spin transport. As it was already mentioned in chapter 1, a hot topic in molecular spintronics is that of fabricating spin valves[2] in which either the spin collector layer[3,4], or the ferromagnetic electrodes[5] are based on molecular-based materials. Magnets based on PBA's may exhibit several advantages as compared to other magnets used in spintronics, such as the processability using solution techniques, transparency and new added functionalities (like photomagnetism[6–8], piezomagnetism[9], etc.). In view of these applications, it is necessary to scale down the growth of the PBA films to the nanometer level.

In this chapter of the thesis, a detailed study of the properties of thin films of the PBA $Cr_{5.5}(CN)_{12} \cdot 11.5\ H_2O$, as reducing the film thickness, is going to be described. Four different thicknesses were chosen for the present study being 1500 nm, 450 nm, 250 nm and 80 nm. This range of thicknesses is wide enough for determining any possible change on the properties of the PBA films when moving to values of this parameter with interest for possible applications in spintronic structures.

The chosen material is justified by the high chemical stability and well-known magnetic properties of this system. As previously mentioned, one of the final goals in molecular spintronics is to develop devices working at room temperature in order to have feasible applications. In this sense, the high ordering temperature of this ferrimagnetic material, T_C = 240 K, makes it a good candidate as a first step into the spintronic applications. It is worthy to mention that the family of the vanadium derivatives (VCr) is a class of PBA systems which exhibits higher critical temperatures. These systems present ferromagnetic ordering up to room temperature or even higher[10,11] (T_C=315 K). Nevertheless, the high chemical instability of this type of PBA's makes complicated their manipulation and consequent application into spintronic devices. According to this, the system studied in this chapter supposes a good compromise between high critical temperature and chemical stability.

The synthesis of this PBA was firstly reported by M. Verdaguer and co-workers[12]. By direct precipitation, a light gray powder of the material was obtained by combining $K_3[Cr^{III}(CN)_6]$ and $Cr^{II}Cl_2$ in a deaerated aqueous medium under inert atmosphere. They determined a formula for the compound as $Cr_5(CN)_{12}\cdot H_2O$ according to the elemental analysis. In bulk, this material exhibited a ferrimagnetic ordering with a critical temperature of 240 K.

As it was mentioned in chapter 1, the organization of molecular-based materials in thin films is a key point for their applicability into spintronic structures. The electrochemical deposition provides a useful tool for preparing thin films of this ferrimagnetic material with high critical temperature. Indeed, the synthesis of this material as films was first achieved by electrochemical methods by Hashimoto and co-workers[13]. In this technique, a labile chemical species was generated by electrochemical reduction in an aqueous solution of the substitution-inert $K_3Cr(CN)_6$ and $CrCl_3$. By changing the reduction potential from -840 mV to -760 mV and playing with the presence of CsCl in the structures they were able to obtain films with ordering temperatures ranging from 150 K to 270 K. Further studies on the electrochemical approach for the synthesis of this material were later on performed by Miller and co-workers[14].

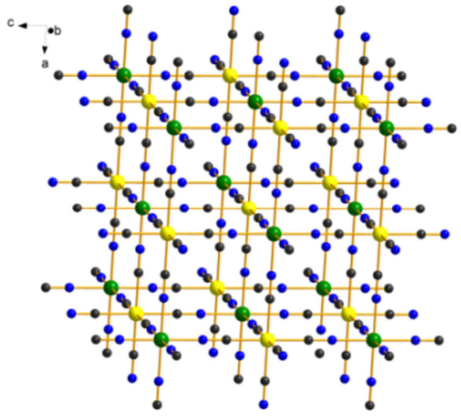

Figure 2.1- PBA unit cell. Cr ions (green and yellow balls) are linked by cyanide bridges (black and blue balls) forming a 3D network. Water molecules and interstitial ions are not included for clarity.

In all the situations, the final system obtained was a crystalline ferrimagnetic material with a high ordering temperature. By X-ray diffraction studies a face-centered-cubic structure was reported, consistent with the typical structure of a three dimensional, mixed-valence transition chromicyanide (figure 2.1).

In those previous reported works[13,14], no systematic characterization of the film properties was performed as a function of the thickness. This is a consequence of the fact that that none of these studies was focused on the possible applications of this molecular-based material into devices. In this chapter, a complete description of the property evolution was monitored by means of different techniques including morphological, optical and magnetic characterizations.

The most outstanding result, regarding the present study, is related to the Magneto-optic Kerr Effect (MOKE) characterization of films of this chromicyanide PBA derivative. In fact, this study represents the first MOKE study of thin films of a PBA with formula $Cr_{5.5}(CN)_{12} \cdot 11.5\ H_2O$ [15,16]. As compared to classical magnets (inorganic metals and most metal oxides), PBAs offer many advantages in the field of magneto-optics. Their transparency in the visible region and their charge-transfer properties are some of them. This is relevant since magneto-optical effects are used in various optoelectronic devices, such as optical memories, optical insulators, etc[17]. The most studied magneto-optical phenomenon in linear optics is the rotation of the plane of polarization of the incident light when passing through a magnetically ordered material (Faraday and magneto-optic Kerr (MOKE) effects for transmitted and reflected light, respectively). Non-linear magneto-optics effects, such as the magnetization-induced second harmonic generation (MSHG), have also been studied[18]. The Faraday effect has been observed in an electrochemically synthesized vanadium hexacyanochromate thin film with a magnetic ordering temperature T_C = 345 K, as well as in other metal hexacyanochromate thin films prepared by the ion exchange method[11,19] .Photoinduced Faraday effects have been evidenced in a cobalt-iron cyanide film[20]. However, to our knowledge, none of these systems has been studied using MOKE despite the fact that, since the early reports on the magnetism of iron surfaces, the technique has been extensively applied to the study of the magnetic behavior of thin films[21–24],

including several properties such as magnetic ordering, spin reorientation transitions and exchange coupling between ferromagnetic layers among others[25,26]. On the other hand, the surface sensitivity and high spatial resolution have promoted MOKE technique as one of the most widely applied for the study of the magnetic properties of ferromagnetic electrodes in spintronic structures[1,27,28]. The proper characterization of the coercive fields of spin injector and spin analyzer electrodes in a spin valve allows determining the feasibility for the stabilization of parallel and antiparallel magnetic configurations in the structure. This is a basic requisite for the correct performance of an organic spin valve (OSV) in order to switch between high and low resistance states[3,29,30].Considering all this information, an evaluation of the applicability of MOKE for the study of the magnetic properties of PBA thin films is of great interest.

Interesting conclusions have been obtained when comparing the information extracted with MOKE from the one registered by SQUID. The latter is a magnetometry technique which measures the bulk magnetic properties of the material without sensitivity respect to the surface characteristics of the films[31]. The differences in the information obtained from each technique have been precisely explained in terms of the surface sensitivity of MOKE which is able to reflect the surface grain structure of these PBA thin films. All the extracted conclusions were corroborated by the study of a supporting material. The family of the ternary metal PBA $(Fe^{II}_{x}Cr^{II}_{1-x})_3$ $[Cr^{III}(CN)_6]_2 \cdot z\ H_2O$ (x = 0.2-0.3), with x = $Fe^{II}/Fe^{II}+Cr^{II}$ a compositional factor, was the chosen one. This factor x can be associated to a grade of substitution of Cr^{II} centers by Fe^{II} centers in the $Cr_{5.5}(CN)_{12} \cdot 11.5\ H_2O$ structure being the latter material resulting from x= 0. The synthesis of films of this material by electrochemical reduction was firstly reported by K. Hashimoto and co-workers[32]. Thin films of this PBA exhibit a mixed ferro-ferrimagnetic behavior with a high ordering temperature of 225 K. Owing to this high critical temperature this system can be also of interest for applications in molecular spintronics. There are previous works reporting the magneto-optical properties of this ternary PBA by means of magnetic second harmonic generation (MSHG)[33,34]. Nevertheless, no MOKE characterization has been performed so far on thin films of this system.

Considering all this information, a powerful technique like MOKE, with high sensitivity down to monolayer detection and a high spatial resolution limited by the laser spot[35], seemed promising in the study of the magnetic properties of such thin films of molecule-based materials and multilayered systems. Indeed, this affirmation was demonstrated by the studies that are going to be described in detail in this chapter of the thesis.

2.2 Results and discussion

2.2.1 Synthesis

All reagents were purchased from Sigma-Aldrich and used without further purification. An electrochemical cell was charged with an aqueous solution (20 mL) containing $K_3[Cr(CN)_6]$ (5 mM) and $CrCl_3$ (7.5 mM).The critical step, for the synthesis of this PBA derivative, is the generation of the substitutionally labile high spins Cr^{II} entities. From the cyclic voltammetry of the electrolytic solution (figure 2.2), it was possible to determine that the deposition of the film was initiated by the quasi-reversible reduction of $[Cr(H_2O)_6]^{3+}$entities taking place at a voltage of -0.83 V[14].

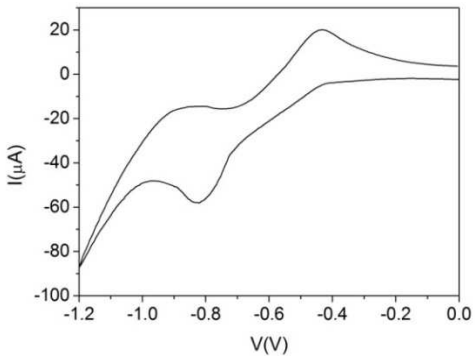

Figure 2.2- Cyclic voltammetry of the electrolyte solution (20mL) containing $K_3[Cr(CN)_6]$ (5 mM) and $CrCl_3$ (7.5 mM). Measurement made at a scan rate of 20 mV/s.

From this information, and considering the previous reported works on this material[13,14], thin films of $Cr_x(CN)_6 \cdot zH_2O$ were obtained by electrochemical reduction (at a fixed potential E = – 0.88 V vs Ag/AgCl reference electrode) of $[Cr(H_2O)_6]^{3+}$ in an aqueous solution containing $[Cr(CN)_6]^{3-}$ anions, as previously described[13,14]. The $[Cr(H_2O)_6]^{2+}$ species formed at the surface of the electrode reacts in situ with the hexacyanometalate anion to give the insoluble PBA, which forms an electroactive transparent film. Electrodeposited films were grown on a substrate of Mylar (dimensions: 5 x 10 mm) coated with an evaporated Au layer of 100 nm thickness acting as the working electrode. A *Metrohm AUTOLAB* potentiostat in coulometry mode was employed for depositing the colorless films. A Pt electrode was used as a counter electrode. After preparation, films were rinsed with mili-Q water and dried at room temperature. The time of electrodeposition was varied to obtain films with different thicknesses, determined by means of profilometry characterization. A nearly linear relationship between the time of deposition and the thickness of the film was found (Table 2.1). Thin films with a thickness of 80 nm were obtained by using very short deposition times (10 s).

Time of deposition [s]	**Thickness [nm]**
10	80±10
25	250±10
50	450±30
100	1500±100

Table 2.1- Relation between film thickness and electrodeposition time.

Elemental analyses performed on films with a several micros thickness are consistent with the formula $Cr_{5.5}(CN)_{12} \cdot 11.5\ H_2O$, that can be expressed as $Cr^{II}_{3.5}[Cr^{III}(CN)_6][Cr^{II}(CN)_6] \cdot 11.5\ H_2O$ from a charge balance.

Anal.calcd for $C_{12}H_{23}Cr_{5.5}N_{12}O_{11.5}$: C 17.90, H 2.88, N 20.87; found: C 17.72, H 2.59, N 20.58.

2.2.2 General characterization

Optical absorption spectra of the PBA films (figure 2.3) were acquired during the electropolymerization on ITO using a spectro-electrochemical cell registering the change in absorption when increasing the electrodeposition time. This characterization was performed with the film inside the electrolytic solution without exposing it to air conditions. In the inset of figure 2.3 it is depicted the comparison of the absorbance curves for the four film corresponding to 100 seconds, 50 seconds, 25 seconds and 10 seconds electrodeposition time, which can be related to thicknesses of 1500 nm, 450 nm, 250 nm and 80 nm respectively as determined by profilometry measurements. It can be observed in all the situations the appearance of a broad band centered around 380 nm corresponding to the intervalence charge transfer process $Cr^{III}-C\equiv N-Cr^{2+} \rightarrow Cr^{II}-C\equiv N-Cr^{3}$.

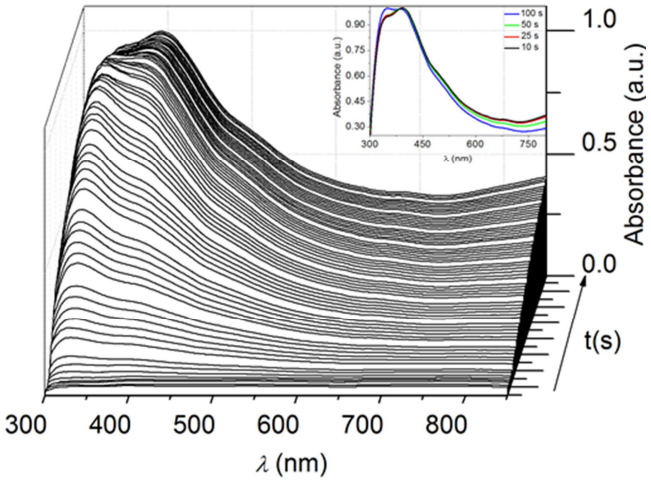

Figure 2.3- Spectro-electrochemical measurement showing the time evolution of the UV-visible absorption spectrum of the chromium cyanide thin film electropolymerized during 350 seconds.

PBA's are materials which exhibit p-type semiconducting behavior with a mechanism of conduction based on hopping between metallic centers[36,37].The electrical characterization of thin films of this chromium cyanide will be more extensively explained in chapter 5 of the present thesis. At this stage, it is

possible to consider this material as a crystalline magnetic semiconductor. From the acquired UV-visible spectra, an estimation of the optical band gap of this material was obtained. The optical absorption near the band edge of this PBA, as being a crystalline semiconductor, follows the formula:

$$Ahv = \alpha(hv - E_g)^{n/2} \qquad (eq.\ 2.1)$$

where A, v , E_g and α are the absorption coefficient, light frequency , band gap energy and a proportionality constant, respectively[38–40]. The value of n is defined according to the type of transition in the semiconductor, being n = 1 for direct transition or n = 4 for indirect transition[39].

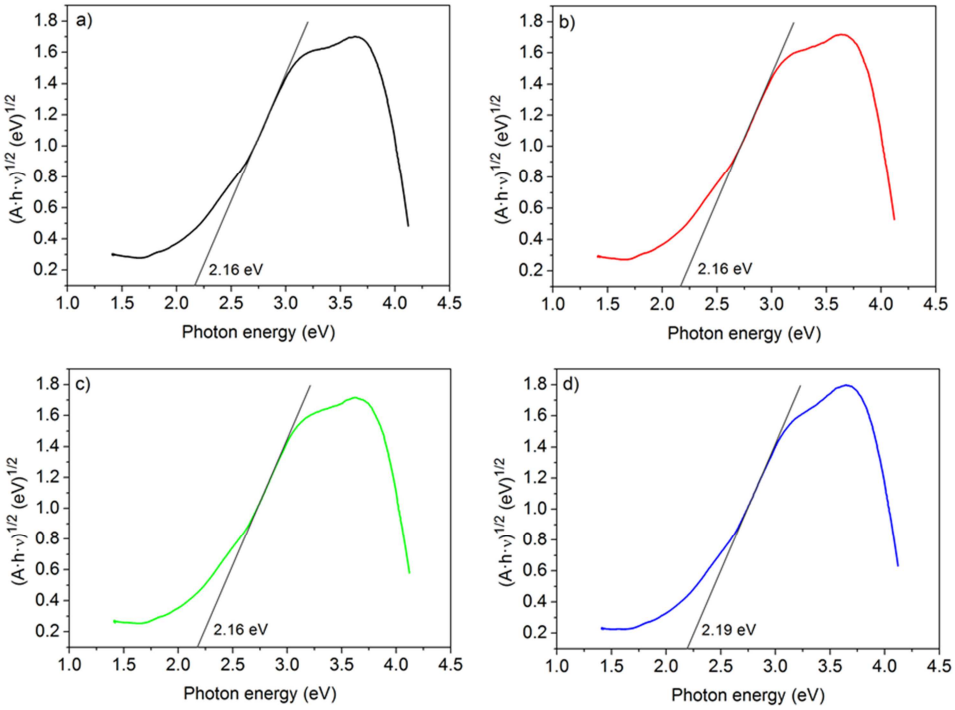

Figure 2.4- Estimation of the optical energy bandgap for chromium cyanide films with thicknesses of a) 80 nm, b) 250 nm, c) 450 nm, d) 1500 nm by employing the plot $(Ahv)^{1/2}$ vs (hv) considering a direct transition.

For the estimation of the optical band gap it has been assumed, as the simplest scenario, a semiconductor with direct band gap between conduction band (CB) and valence band (VB), *i.e.*, n = 1.

In this context, the band gap energy (E_g) has been estimated from the plot $(Ahv)^{1/2}$ versus the photon energy (hv) which is shown in figure 2.4. Plots have been made for the four thicknesses under study in order to elucidate if the estimated value of the band gap energy changes with this parameter. From the intercept of the tangent (grey dashed line) with the x-axis, it has been possible to obtain values of 2.16 eV for the band gap for the film thicknesses of 80 nm, 250 nm and 450 nm. In the case of the thickest film of 1500 nm, the band gap has a negligible difference being 2.19 eV. Thus, an invariance of the estimated direct band gap energy respect to the film thickness has been detected.

As a proof of tolerance in the calculations, a comparison with the value obtained assuming the existence of an indirect band gap on the semiconductor was also performed. A plot based on equation 2.1 but employing in this case n = 4 was applied to the UV-visible spectrum of the 80 nm film. The result is depicted in figure 2.5, where an energy bandgap of 2.39 eV was obtained by applying the same procedure.

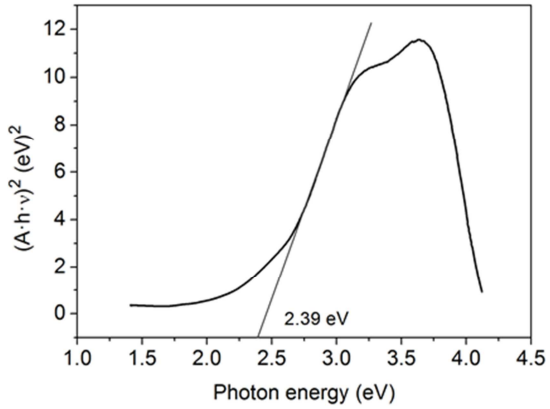

Figure 2.5- Estimation of the indirect optical energy bandgap for the chromium cyanide film with 80 nm thickness by employing the plot $(Ahv)^2$vs (hv).

Thus a difference in energy of 0.23 eV was found in the case of an indirect band gap respect to the situation of considering this chromicyanide PBA as a semiconductor with a direct transition between VB and CB. In all the discussions considering the band gap of this material in this manuscript, a direct transition between CB and VB will be assumed, as being the simplest scenario. Nevertheless, this assumption has to be confirmed by extra characterization on thin films of this material.

An ATR-IR spectroscopy study was performed on thin films in order to elucidate any possible change on the chemical composition of the PBA when decreasing the thickness. When an electrodeposition time of 100 seconds is employed for the electropolymerization, a 1500 nm thickness film is produced with an intense black color meanwhile kept inside the electrolyte. Seconds after being exposed to air, an evident change in color can be observed, evolving to a transparent film. This optical change is clearly indicating a chemical modification under air exposure. This evolution of the chemical identity was monitored by infrared spectroscopy, acquiring spectra of the films as a function of time.

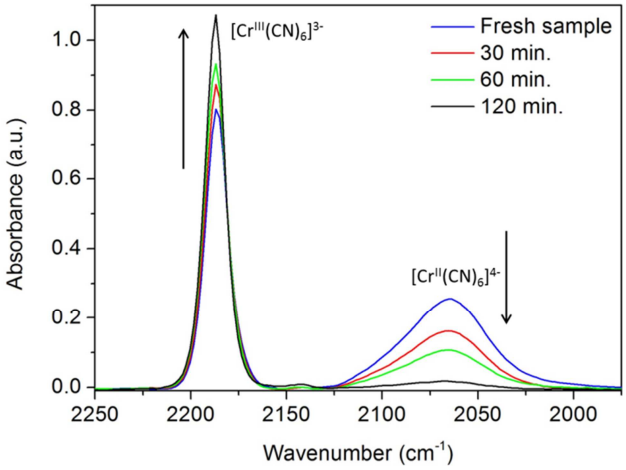

Figure 2.6- Time evolution of the IR spectrum of a chromium cyanide thin film (1500 nm thickness) after air exposure: a) fresh sample (blue curve) b) 30 minutes (red curve) c) 1 hour (green curve) d) 2 hours (black curve).

The ATR-IR spectrum of an electrodeposited thin film of 1500 nm thickness (Figure 2.6), just after being prepared, shows a principal band centered at

2186 cm^{-1}, corresponding to the cyanide stretching vibration of the $[Cr^{III}(CN)_6]^{3-}$ anion, and a secondary band located at 2066 cm^{-1} that can be ascribed to the presence of $[Cr^{II}(CN)_6]^{4-}$ moieties[13,14]. This is an indication that the reduction of the hexaaquachromium species is accompanied by a reduction of the hexacyanometalate anions, a consideration which is supported by the elemental analyses results. However, after air exposure, it can be observed as the intensity of the low-frequency band decreases markedly with exposure time. This effect is faster as the thickness of the film decreases, consistent with an air-oxidation process that converts $[Cr^{II}(CN)_6]^{4-}$ into $[Cr^{III}(CN)_6]^{3-}$.For all the thin films used in this study, the low-frequency band disappears after standing in air for two hours, indicating full conversion to $[Cr^{III}(CN)_6]^{3-}$.

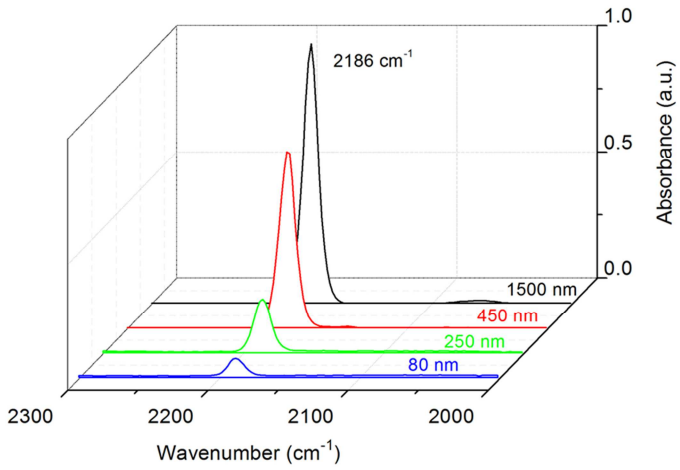

Figure 2.7- IR spectra of chromium cyanide thin films with different thicknesses after air exposure. a) 1500 nm; b) 450 nm; c) 250 nm; d) 80 nm

The IR frequency associated to this species is independent of the film thickness (Figure 2.7), thus the composition of the film is unaltered as the thickness is reduced. After air exposure, only the principal band at 2186 cm^{-1} remains in the IR signal. This is an indication of a complete oxidation of the films independently of the film thickness. As pointed out by Miller and coworkers, the chromium ions in the cationic sites are also in their +3 oxidation state[14], charge

compensation being provided by loss of protons from water molecules. Thus, our study provides evidence that the chemical identity of the PBA is preserved as the film thickness is reduced when moving towards ultra-thin film limit. From now on, in order to simplify the notation along the discussion of the thesis, the thin films of this fully oxidized chromycianide will be referred as CrCr.

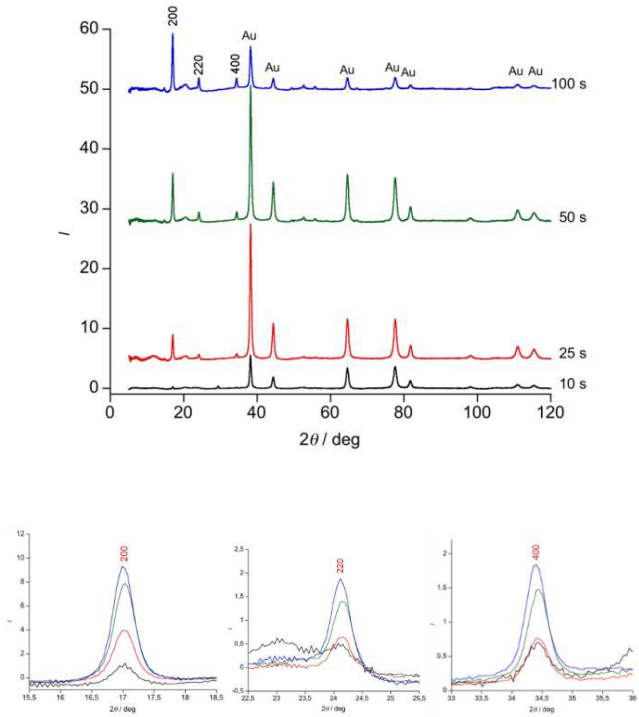

Figure 2.8- *Top:* Powder X-ray diffraction (XRD) patterns of thin films of CrCr synthesized using different electrodeposition times. *Bottom*: Detailed view of the principal peaks corresponding to the Prussian blue type structure.

In principle no change on the crystallographic parameters of the material would be expected as a consequence of the film thickness decrease. This point was clearly confirmed by an XRD study of the system. In this case, a collection of microcrystals was scraped from the surface of the films and mounted on a sample holder (cryoloop). Four images of diffraction cones were obtained at different angles and the diffraction pattern was obtained by integration using

the *CrysAlispro* software. Powder X-ray diffraction of the electrodeposited films (Figure 2.8) shows a typical cubic pattern corresponding to a Prussian blue structure with cell parameter a = 10.42 Å. This pattern is independent of the film thickness as it was expected.

The last point to treat, regarding this general characterization, is the study of the surface morphology of thin films of CrCr. This feature was addressed by means of atomic force microscopy (AFM) (Figure 2.9). Images of 5 x 5 µm scan size were acquired in tapping mode as the deposition time was modified. RMS roughness and average particle size were analyzed by using *WSxM4 4.0 Develop 13.0 software*[41], developed by Nanotec Electronics S.L. The results of the characterization are summarized in Table 2.2.

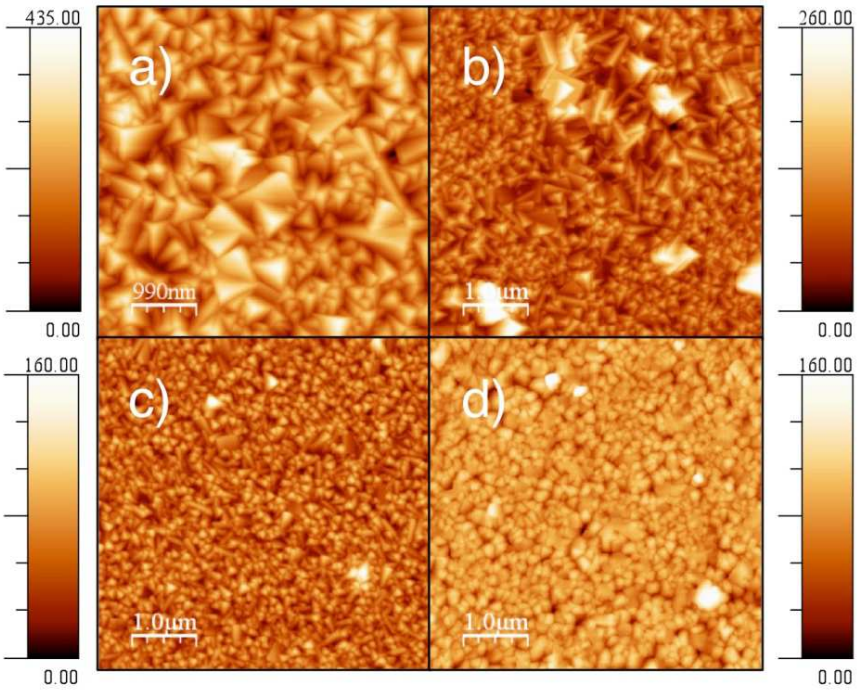

Figure 2.9- AFM topography images of the surface of thin films of CrCr obtained after different times of electrodeposition: a) 100 s (1500 nm thickness); b) 50 s (450 nm thickness); c) 25 s (250 nm thickness); d) 10 s (80 nm thickness). The color scale unit is in [nm].

Time of deposition [s]	Thickness [nm]	Average particle size [nm]	RMS roughness [nm]
100	1500±100	600±100	58
50	450±30	320±80	37
25	250±10	180±30	18
10	80±10	170±40	10

Table 2.2- Morphological parameters of thin films of CrCr determined by means of AFM.

In all the situations, the surface pattern consisted in a collection of pyramidal grains of different sizes. It has been shown that this well-known polycrystalline structure results from the epitaxial electrodeposition of the PBA on a gold surface[42]. The average particle size (Table 2.2) increases from a value of 170 nm (lateral size) for the film prepared after 10 seconds electrodeposition (80 nm thickness) to a value of 600 nm for the thicker film (1500 nm) obtained after 100 s. During the initial (nucleation) stages of the electrodeposition process, the reaction takes place at the naked surface of the electrode and its kinetics is only limited by diffusion of the species, resulting in very small particles that cover homogeneously the electrode surface. At longer deposition times, the intensity of the electrochemical current decreases, indicating a slower electrodeposition kinetics that results in the growth of the particles as pyramidal microcrystals. Consequently, the RMS roughness of the film surface increases with the deposition time, passing from a value of 10 nm for the 80 nm thickness film to a value of 58 nm for the 1500 nm thickness film. This effect is accompanied with the correspondent increase in the average grain size in surface as previously mentioned.

According to this information, a decrease in film thickness induces an improvement in the surface quality. This point has to be considered in possible applications of films of CrCr as electrodes in spintronic structures. In this sense, if CrCr films are employed as spin injector electrodes or spin collector media, the reduction of the thickness would lead to an improvement of the possible interfaces generated in the device. When analyzing the 3D topography

images of the surfaces of films with 80 nm and 1500 nm thicknesses this vision is reinforced (figure 2.10).

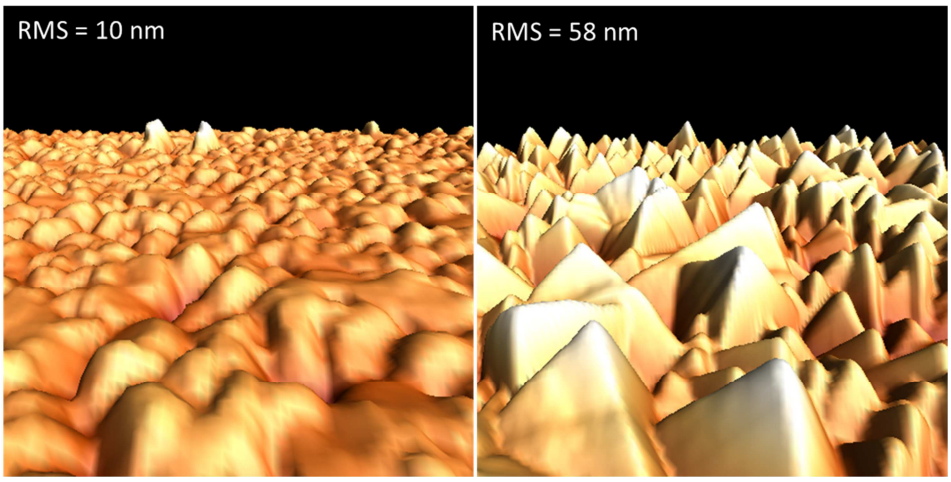

Figure 2.10- 3D topography images of 5x5 μm^2 scan size comparing in detail the surface roughness of a film of CrCr with 80 nm (left) and 1500 nm (right) thicknesses with RMS values of 10 nm and 58 nm respectively.

The fact of decreasing in approximately six times the roughness of the electrode, when passing from 1500 nm to 80 nm thicknesses, makes more feasible the fabrication of devices with a lower probability of pinholes and defects. This improvement in the surface quality of the PBA electrodes can play a major role for avoiding the appearance of shortcuts and malfunction in the fabricated devices.

Note that the influence of interfaces in the performance of spintronic devices such as organic spin valves have been already investigated[43–47].The impact of the roughness in the performance of an OSV was addressed by D.H. Reich et al.[48] in a device employing Co and Fe as spin injector and spin analyzer electrodes respectively. The molecule Alq_3 was chosen as the organic spacer in the structure. From this study it was observed different magnetoresistance (MR) performances for samples fabricated under similar conditions. The discrepancies in MR response were explained in terms of subtle differences in the microstructure of the samples, specially located at the interface between the

ferromagnetic electrode and the organic spacer. In particular, larger MR ratio was associated to smaller structural roughness at the Co/Alq_3 and Alq_3/Fe interfaces and with a magnetically dead region close to the Fe/Alq_3 interface.

2.2.3 Magnetic and magneto-optical characterization of CrCr thin films

A systematic comparison between the magnetic information obtained on thin films of CrCr by means of MOKE and SQUID has been performed in this section. SQUID is a technique in which the magnetic properties of the whole material are evaluated without discrimination between surface, bulk and substrate of the system under study. Thus the magnetic information provided is an average over the whole volume of the sample. On the contrary, MOKE is a magnetometry technique which registers the magneto-optical behavior of the system. This technique, as described in chapter 1, is sensitive to the magnetic processes taking place in the surface of the thin films under study. Considering this, it is of big interest to determine the grade of correspondence between the magnetic information provided by these two experimental approaches when applied to the study of electrodeposited PBA thin films. With this purpose, thin films of CrCr with thicknesses of 1500 nm, 450 nm, 250 nm and 80 nm were analyzed by both techniques.

In first instance, variable-temperature (applied field: 50 Oe) and field-dependent (T = 2 K) DC magnetization measurements were carried out in a SQUID magnetometer. AC susceptibility measurements at different frequencies of the oscillating field of 3.95 G amplitude were performed. Several films of each thickness were cut in many pieces and were introduced in the sample holder with the applied magnetic field parallel to their surface. The magnetic susceptibility of the Au/Mylar substrates was measured independently in the same conditions and subtracted from the signal of the different films.

The magnetic properties of the electrodeposited thin films of CrCr were found to be almost independent of the thickness, in good agreement with previously reported results[13,14].

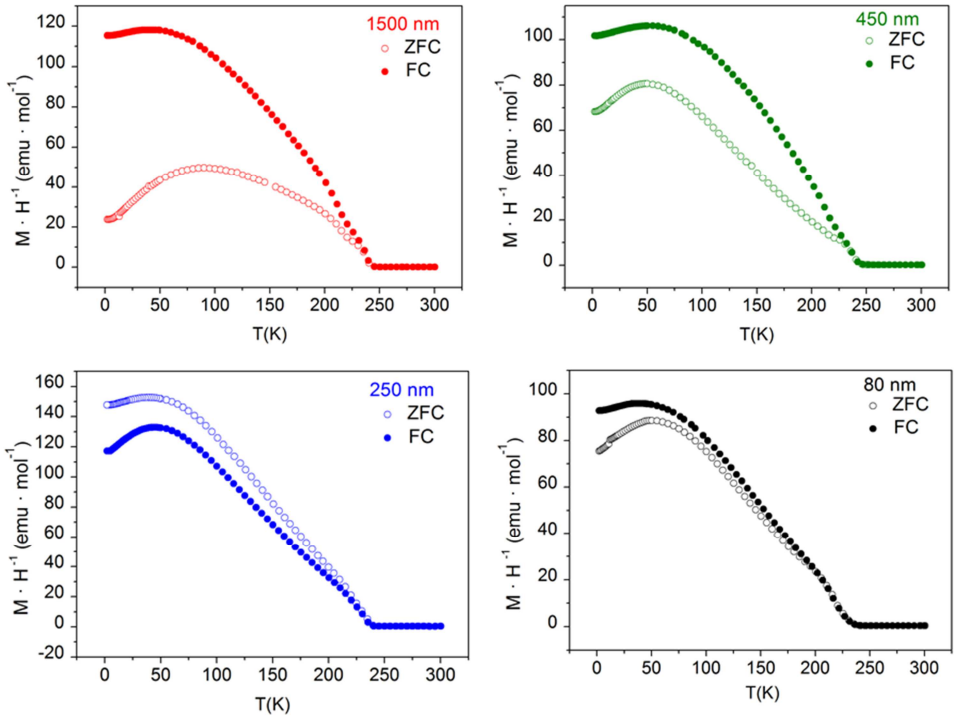

Figure 2.11- Temperature dependence of the susceptibility ($M \cdot H^{-1}$) of four thin films of CrCr with different thicknesses in field-cooled (FC) and zero-field-cooled conditions. The applied magnetic field is 50 Oe.

As observed from figure 2.11, the temperature dependence of the magnetization (expressed as $M \cdot H^{-1} = f(T)$) is almost constant from 300 K to 240 K. Below this temperature, the magnetization shows a steadily increase when cooling to reach a saturation value below 50 K. Below 240 K, a thermomagnetic irreversibility, namely a difference between the field-cooled and zero-field-cooled curves, can be also observed. Interestingly, the temperature at which the two curves diverge (T_{irr}) decreases for the thinner samples.

The reciprocal susceptibility data can be fitted to the Curie-Weiss law by equation (2.2),

$$\chi = \frac{C}{T - T_c} \quad (eq\ 2.2)$$

where, C , T and T_C are the magnetic susceptibility, Curie constant of the material, absolute temperature and Curie temperature, respectively.

The fitting gives as a result C = 10 emu·K·mol^{-1} and θ = –100 K, indicating a large antiferromagnetic interaction between neighboring Cr^{3+} ions through the cyanide bridge. The AC susceptibility measurements performed on thin films of CrCr confirm a transition to a magnetically ordered ferrimagnetic phase at T_C = 240 K (figure 2.12).

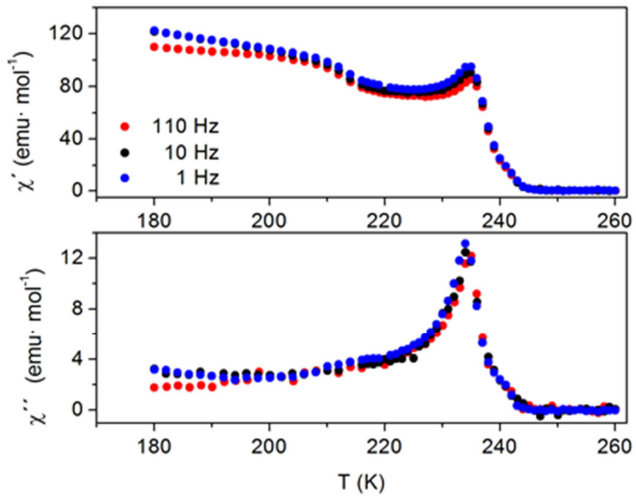

Figure 2.12- Temperature dependence of the ac magnetic susceptibility signal in-phase (*top*) and out-of-phase (*bottom*) for a thin film of CrCr (1500 nm thickness) at different frequencies.

Hysteresis loops for films of CrCr were measured at 2 K as depicted in figure 2.13. The first remarkable feature from this measurement is the independence of coercive fields with film thickness. In all the cases, a coercivity of H_C = 67 Oe (6.7 mT) was obtained with remnant magnetization values all far from saturation (4.5 μB) in agreement with the ferrimagnetic nature of the established state (figure 2.13). The second aspect to highlight from this

characterization is the small value of coercive field determined in all the cases at 2K, defining this material as a soft ferrimagnet. Thus, according to the SQUID characterization, the reduction of film thickness does not change the bulk magnetic properties of the material, such as T_C or H_C.

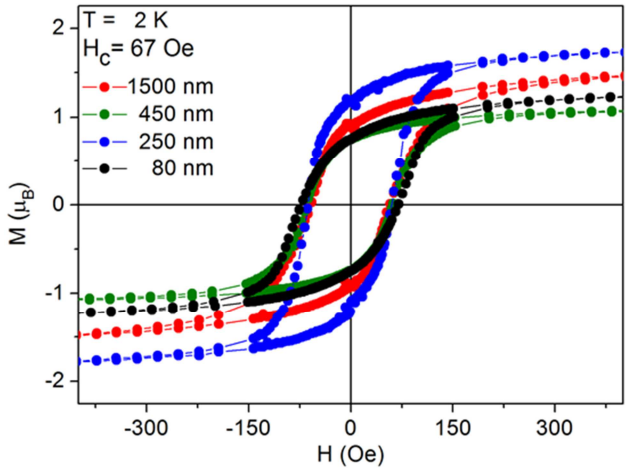

Figure 2.13- Hysteresis plot (T = 2 K) of thin films of CrCr with different thicknesses

MOKE measurements were performed in order to probe directly the surface magnetic properties of the different CrCr thin films described in table 2.2. The magneto-optical characterization[15] was done with a self-made Kerr magnetometer which has been extensively described in chapter 1.

A source of linearly polarized light of high wavelength (λ= 633 nm) and low power (12 mW) was used in order to prevent any photo-magnetic effect. The polarizer was set for employing s-polarized light for probing the sample. The Kerr rotation (θ_k) of the films, directly proportional in first approximation to the magnetization of the samples, as well as Kerr ellipticity (φ_k) were recorded as a function of the applied magnetic field, for different temperatures. Hysteresis loops were observed for all the films measured in polar configuration (magnetic field perpendicular to the surface sample). It should be noted that hysteresis loops were also found in longitudinal configuration but the signal-to-noise (S/N) ratio was extremely low. This is not an indication of anisotropy in the films. It is

rather related to an optical factor that produces a difference in intensity between polar and longitudinal signals (the intensity of the former being typically one order of magnitude higher than the latter)[21]. In the following, for simplifying the discussion, we will restrict our analysis to the hysteresis loops coming from the Kerr rotation (θ_k) as no difference respect to those obtained from the variation of Kerr ellipticity (φ_k) with the external magnetic field was detected (figure 2.14).

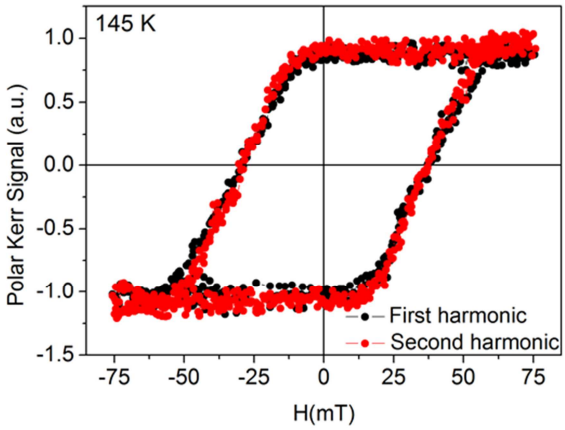

Figure 2.14- Comparison between MOKE hysteresis loops measured in first harmonic (Kerr elipticilty) and second harmonic (Kerr rotation) for a 1500 nm thickness film of CrCr at 145 K. The same magnetic information was obtained in both cases.

In first place, the T_C of the ferrimagnetic ordering on thin films of CrCr was extracted from the thermal evolution of the H_C of the material (figure 2.15). This parameter was found to be 240 K in agreement with SQUID results, being independent of the film thickness. The criterion for defining this value is based on the determination of the temperature at which the Kerr Signal evolves from a diagonal straight line, with zero coercive field and constant slope (diamagnetic contribution of the cryostat window), to a proper S-shaped hysteretic signal. This is an indication of the pass from a paramagnetic state to a ferrimagnetic (or ferromagnetic) ordering in the PBA under study. The intensity of the magneto-optical signal is a key factor in order to determine a precise T_C value for being compared with the SQUID data. From our studies we could observe that a decrease in the thickness of the PBA film was accompanied by a reduction of

the signal-to-noise (S/N) ratio in the measurement. In addition, the Kerr signal was proportional to the grade of magnetic ordering in the material under study, decreasing considerably when approaching to the critical temperature. Thus, if the S/N ratio is very low, a disappearance of the hysteretic shape as a consequence of a "screening effect" induced by the noise in the measurement can appear. This could be confused with a proper loss of the magnetic ordering in the material when passing to a paramagnetic state, introducing an uncertainty in the determination of the T_C. This fact has to be considered in order to choose the proper thicknesses from which extracting the ordering temperature of the PBA under study. In figure 2.15 it is shown the thermal evolution of the coercive field for a 450 nm thickness film of CrCr. The data have been extracted from the hysteresis loops measured in second harmonic for polar configuration and employing s-polarized light for probing the sample. Some examples of the measured hysteresis loops are depicted in the inset of figure 2.15.

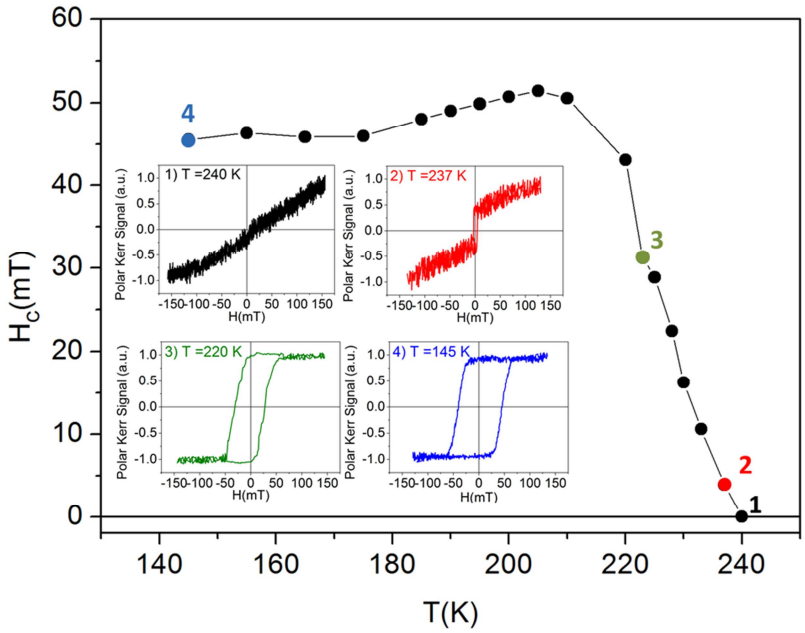

Figure 2.15- Thermal evolution of the coercive field on 450 nm thickness of CrCr measured with MOKE. Inset: Hysteresis loops in polar configuration measured at different temperatures in second harmonic with s-polarized light.

In this case, at 240 K no hysteretic signal is detected and only a straight line with a slope induced by the diamagnetic effect of the cryostat window is measured. When decreasing the temperature, at 237 K the ordering of the material starts to be clear inducing a Kerr effect in the reflected light which allows the registering of a hysteresis loop. At this point, the S/N ratio is still low, but when moving to lower temperatures this ratio is improved in a considerable way. From figure 2.15 it is observed a monotonic increase of the coercive field between 240 K and 205 K, reaching a maximum of 50 mT for this 450 nm thickness film. When reducing the temperature below 205 K the coercive field slightly decreases to 45 mT at 175 K. Below this temperature stabilization in the value of this parameter is detected. The improvement of the S/N ratio is clear when comparing the hysteresis measured at 237 K with the one obtained at 145 K (see inset figure 2.15). From this result it is evident that the most appropriate conditions for the MOKE characterization of PBA thin films, in terms of signal intensity, are located in the range of low temperatures (well below the T_C). In this range of temperatures, a higher ferromagnetic ordering in the material induces a higher Kerr effect on the reflected light. This leads to an improvement in the quality on the magneto-optical response of the PBA. A similar behavior was reproduced for the rest of the film thickness of CrCr studied with MOKE.

The first striking result from this MOKE study is that relatively large hysteresis loops appeared just below T_C for all the films measured in polar configuration. This is in contrast with the SQUID characterization, where an almost negligible value of coercive field (6.7 mT) was obtained even at 2 K. A possible explanation to this discrepancy could be attributed to the different sweeping rates of the magnetic field in the two experiments when acquiring the hysteresis loops (5.5 mT/s in SQUID versus 60 mT/s in MOKE). There are several studies in which the effect of the sweeping rates on the coercive field of a system has been analyzed, showing an important influence of this parameter on the magnetization reversal processes[49].This fact is associated with the competition between domain wall motion and nucleation processes. In the low dynamic regime of magnetic fields, the domain wall motion is dominating. On the contrary, for the high dynamic region, the variations associated to the coercive field are predominately due to nucleation domain processes in the material.

In order to evaluate the influence of the magnetic field dynamics on the coercivity of the material, hysteresis loops on a 1500 nm thickness film where measured with MOKE (figure 2.16) by applying the standard sweeping rate (60 mT/s) and reducing to the minimum sweeping rate (9 mT/s). The latter is on the same order of the magnetic field frequency employed in SQUID. These measurements show that the impact of magnetic field dynamics on the coercivity of the PBA thin films is almost negligible in the range of sweeping rates employed for both techniques. Thus, this point is not explaining the considerable discrepancy in the values determined by the two techniques.

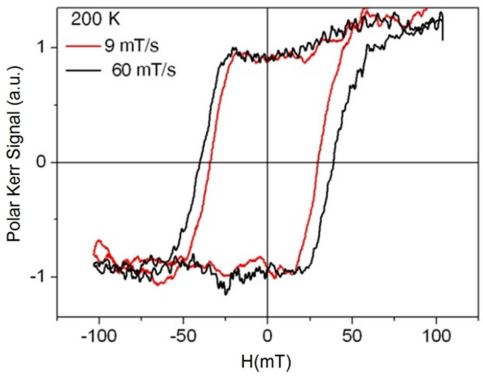

Figure 2.16- MOKE hysteresis loops obtained at 200 K in polar configuration for a thin film of CrCr (1500 nm thickness) at different sweeping rates of the magnetic field.

In this sense, it is proposed that the difference in coercive fields found for the hysteresis loops registered by SQUID and MOKE magnetometers are rather due to the local surface character of the later technique as it will be explained with more detail in the following pages.

A second striking difference respect to SQUID information was detected when comparing the magneto-optical response at a certain temperature for different film thicknesses. In figure 2.17 it is plotted the comparison of the hysteresis loops for films of CrCr with thicknesses of 1500 nm, 450 nm, 250 nm and 80 nm. These hysteresis loops were registered at 200 K in second harmonic and polar configuration with s-polarized light. From this measurement, an increase

of the coercive field when reducing the film thickness is clearly observed. This is in total contrast with the magnetic information provided by SQUID where the coercivity was found to be independent with film thickness.

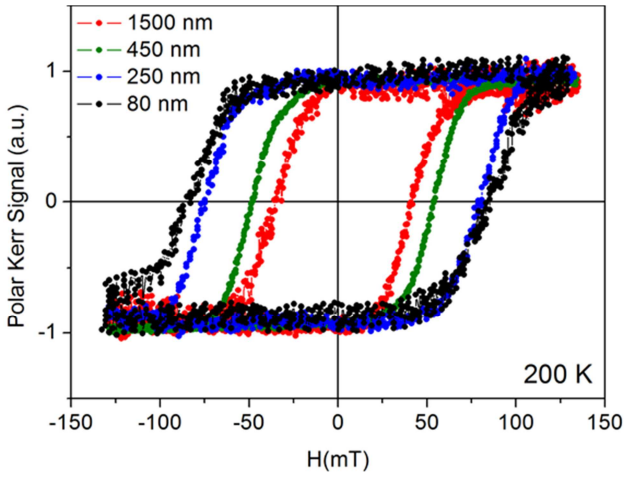

Figure 2.17- Normalized MOKE hysteresis loops obtained in polar configuration for four thin films of CrCr of various thicknesses.

The information described so far is indicating that the differences in the magnetic information registered between both techniques (value of coercive field and dependence of this parameter with thickness) are arising from the ability of MOKE to detect some features of the PBA thin films, with a direct impact on the magnetic properties, which escapes to SQUID magnetometry.

Time of deposition [s]	Thickness [nm]	Average particle size [nm]	Coercive field (mT)
100	1500±100	600±100	38±5
50	450±30	320±80	50±5
25	250±10	180±30	78±5
10	80±10	170±40	85±5

Table 2.3- Summary of the morphological characteristics of films of CrCr compared to the coercive field determined by MOKE.

From the general characterization described in the previous section, it was possible to determine that the surface morphology of the CrCr thin films was the only property affected by the decrease of the thickness. Thus, the discrepancies between the results obtained from SQUID and MOKE can be explained based on the influence of the surface grain structure of the material on the magnetic information registered with the latter technique. In this sense, the increase of coercive field when decreasing the thickness can be correlated with a decrease in the average size of the particles at the film surface. This correlation is more evident from the data presented in table 2.3.

The thicker films consist of relatively large multi-domain magnetic particles whereas in the thinner films the particles approach the single-domain limit, resulting in an increase in coercivity. This behavior will be more extensively explained in the next section. Such a particle-size effect has been previously described in other molecule-based materials[50]. The squareness of the hysteresis loops increases also for the thinner layers. This originates from the more homogeneous distribution of particle size and shape at the thinnest film (80 nm thickness) surface, as evidenced from the AFM study.

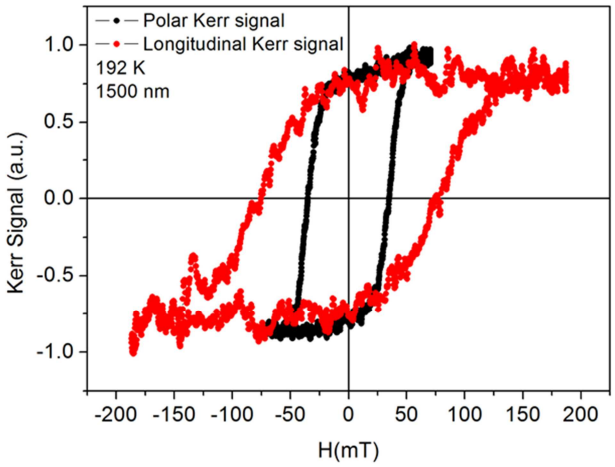

Figure 2.18- MOKE anisotropy measurement at 192 K of a 1500 nm thickness film of CrCr.

The local and surface character of MOKE respect to SQUID is highlighted when measurements are performed for different magnetic field orientations in both cases. For this purpose, hysteresis loops of a 1500 nm thickness film of were recorded both in polar and longitudinal configurations of the magnetic field, i.e., perpendicular and parallel to the film surface respectively. This particular thickness was chosen in order to ensure a proper S/N ratio in the measurement taking into account that, as it was previously mentioned, the longitudinal Kerr signal is one order of magnitude lower in intensity than the polar Kerr signal due to optical factors. The result of this measurement is shown in figure 2.18, where a coercive field of 75 mT is registered in longitudinal configuration with respect to the 38 mT obtained in polar configuration.

As it was shown previously from the IR study of electrodeposited films of CrCr, the full conversion of $[Cr^{II}(CN)_6]^{4-}$ into $[Cr^{III}(CN)_6]^{3-}$ is observed under air exposure. Hence, the time correspondent to an experiment, regarding the magnetic characterization, is long enough to assure that only Cr^{III} ions will be present on these PBA ferrimagnetic films. In this sense, as it was proposed by Miller and co-workers[14] in the case of an octahedral, low-spin d^4, $[Cr^{II}(CN)_6]^{4-}$ a triply degenerate $^3T_{1g}$ ground state is present. However, distortions of the octahedral symmetry around the Cr^{II} ion lead to the removal of the orbital degeneracy and the appearance of single-ion anisotropy. In a similar way, distortions of the octahedral environment break the orbital degeneracy for high-spin Cr^{II}. In contrast, the anisotropy of the Cr^{III} ion is likely negligible considering the non-degenerate $^4A_{2g}$ ground state. Thus the isotropy of the magnetic properties on films of CrCr is expected from regarding their composition. This point was fully proved by the SQUID measurements on a 1500 nm thickness film, corresponding to the same thickness that was analysed with MOKE.

In the work of Pajerowski et al[51] the anisotropic magnetic response of PBA films was studied from magnetization measurements, observing the differences in the FC and ZFC signal of the films in parallel and perpendicular configuration respect to the magnetic field. In our particular case, the study of the film anisotropy was addressed by the comparison of the hysteresis loops measured at 2 K on a 1500 nm thickness film of CrCr when applying a magnetic field

parallel or perpendicular to the surface (figure 2.19). This measurement provides similar information than the one obtained from the FC and ZFC measurements in the works previously mentioned.

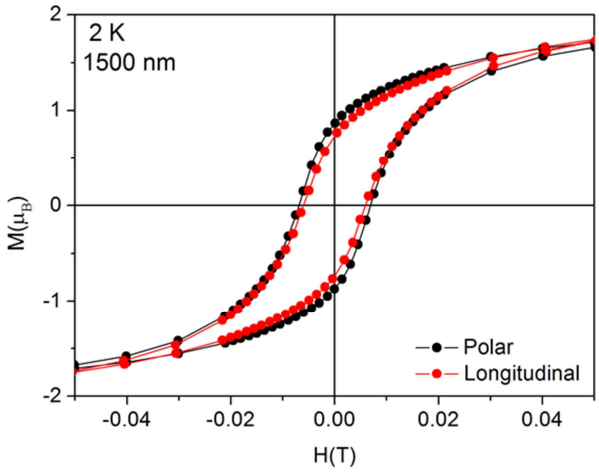

Figure 2.19- Hysteresis plot (T = 2 K) of a 1500 nm thickness film of CrCr in longitudinal (red curve) and polar (black curve) configurations of the magnetic field.

From figure 2.19 it is possible to observe that the magnetization values as well as the coercive fields measured for both configurations (parallel and perpendicular) show a negligible difference (in the order of the experimental error). This can be considered as an absence of magnetic anisotropy in the system under study, as it was expected from the presence of Cr^{III} metal centers in the PBA structure.

On the contrary, there is a clear evidence of anisotropy in the MOKE measurement which is not related to the chemical structure of the material, as demonstrated from the isotropic magnetic signal from SQUID for the same film thickness. This difference in coercivity, which indicates that the magnet is harder when applying a longitudinal magnetic field, demonstrates the influence of the local environment in the volume constricted by the laser spot which is establishing the region under study with MOKE. The characteristics of the region probed by the laser are defined by the morphology of the grains in this

volume of material. In this sense, the coercive field depends on anisotropy, but it is strongly affected by defects, grain size, grain shape and distribution[52]. These differences in the grain parameters are evidenced when applying different orientations of the magnetic fields in MOKE. The surface sensitivity of MOKE over the features of the PBA thin films, as well as its local character, are reinforced by these anisotropy measurements.

At this point, it is important to remark that the PBA thin films under study are transparent materials. This feature is confirmed from ellipsometry studies on CrCr. In figure 2.20 it is shown the measurement of the extinction coefficient and refraction index on a CrCr thin film as a function of the incident light wavelength. Paying attention to the extinction coefficient characteristics of the material, it is possible to observe that the values of this parameter are almost negligible in all the visible range. This can be directly correlated with a transparency of the PBA film over all the wavelengths of the incident light located in the visible range[53].

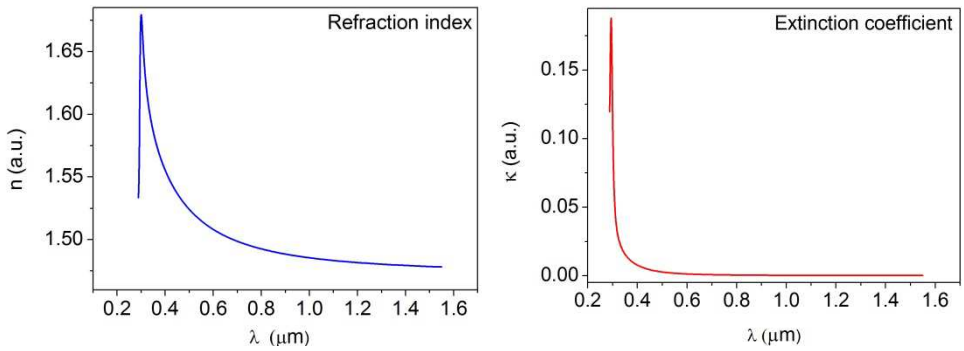

Figure 2.20- Refraction index (left) and extinction coefficient (right) vs light wavelength in a film of CrCr. The negligible values of extinction coefficient denote the high optical transparency of this material in the visible region.

Taking into account the high transparency of the films in the visible light region, it is possible to assume that for all the thicknesses under study the laser travels through the whole material until reaching the gold substrate. Nevertheless, from the registered hysteresis, the Kerr signal is getting

information that comes from the surface layers of the film. Thus, in order to explain the surface character of the magneto-optical properties determined for this transparent polycrystalline material we have proposed a phenomenological model.

As it was mentioned in chapter 1, Kerr effect produces a change in the polarization of the incident light upon reflection on a magnetic material. This change in polarization is directly proportional to the magnetization of the sample. Thus, for registering a hysteresis loop of the material, the reflected light has to preserve the changes in polarization induced by Kerr effect when reaching the photodetector of the set-up. Any depolarization process in the medium will affect the information contained in the reflected light from the film under study. In our model, a scattering-caused depolarization process of light is considered when the laser travels through the volume of the material. Scattering can be produced by different elements in a material such as crystal lattice dislocations, polycrystalline faces, particulate inclusions, heterogeneous composites and anisotropies, among others[54]. Crystalline grains also act as scattering centers inducing depolarization of light in the medium[55]. In particular, an important depolarization is going to take place as result of refraction and reflection of the light beam on the grain boundaries , being this effect enhanced by the inhomogeneity of grain sizes, grain size itself and turbidity[56]. Thus, these crystalline grains are going to be considered as the main source of light depolarization in the PBA films under study. The grade of multiple scattering and depolarization will be directly affected by the grain size.

When photon-traveling distances in a material are at least twice the penetration depth, the multiple scattering will induce a change in the light polarization state. In this context, a considerable depolarization will appear when the penetration depth is greater than the doubled value of the grain size. In consequence, smaller grains will produce higher grades of depolarization[57].

Taking into account a light depolarization effect of the grains composing the polycrystalline PBA films, it is possible to describe the phenomenology taking place in the transparent material under polarized light irradiation. The surface character of the measurement can be understood if we consider a simplified model of the polycrystalline PBA material in which every film of certain

thickness is composed of successive layers, each of them with different grain sizes (figure 2.21).

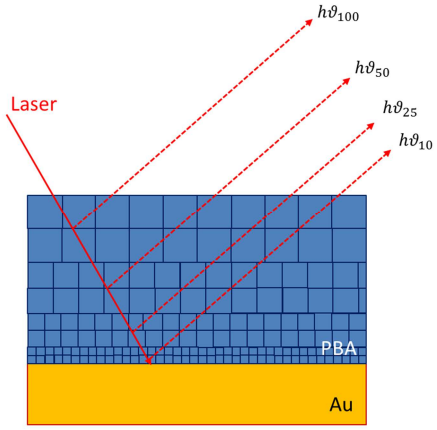

Figure 2.21- Modelled PBA film of 1500 nm thickness (100 seconds electrodeposition time). The incident laser light (solid red line) is transmitted through the whole volume of the film until it reaches the gold substrate. The reflected light (discontinuous red lines) is the result of multiple reflections of the incident laser in each layer corresponding to different deposition times and grain sizes.

In this model, in the particular case of a film of 1500 nm corresponding to the 100 s electrodeposition time, the morphological structure will be formed by the successive layers electropolymerized at 50 seconds, 25 seconds and 10 seconds, with the correspondent grain sizes indicated in Table 2.1. This is a simplified view of the system which only takes into account the film thicknesses studied in this case. Nevertheless, this reasoning can be systematically extended to the successive intermediate film thicknesses resulting from the continuous electrodeposition times from 10 seconds to 100 seconds.

Based on this model, the incident polarized laser beam, denoted as $h\vartheta$ is transmitted through the whole volume of the material until reaching the gold substrate. The reflected light collected by the photodiode will contain the information of each successive layer composing the film, which in figure 2.21 has been denoted as $h\vartheta_{100}, h\vartheta_{50}, h\vartheta_{25}, h\vartheta_{10}$ related to 100 s, 50 s, 25 s and 10 s electrodeposition times respectively. Depolarization effects arising from

grains will produce a loss of the magneto-optical information coming from the deeper layers with progressively smaller grains. According to this, in the considered case of the 1500 nm thickness film, only the reflections from the top layers, $h\vartheta_{100}$, will mainly preserve the changes in polarization induced by the Kerr effect allowing the registering of a hysteresis loop. This scenario can be extended, as well, to the rest of the thicknesses presented in table 2.1.

2.2.4 Characterization of CrCr in the ultra-thin film limit

The effect on the magneto-optical properties of films of CrCr when reducing the film thickness to the ultra-thin limit was also studied. As it was previously described, there is a direct effect of the surface morphology of the film on the coercive field of the hysteresis loops registered with MOKE. The lowest thickness described so far has been 80 nm, corresponding to an electrodeposition time of 10 seconds. As it was demonstrated, the structural, chemical and magnetic properties of the films are preserved when reducing the film thickness. In this sense, following this philosophy, films with shorter electrodeposition times than 10 seconds were electropolymerized, with the same synthetic approach, and studied with MOKE. A set of samples were prepared and systematically analyzed by means of profilometry in order to estimate their thickness. In addition, an AFM study was performed for determining the surface morphology features and the grade of film coverage on the substrate when moving to the ultra-thin film limit. In base of these studies, films of 2 seconds and 1 second electrodeposition time, corresponding to thicknesses of 50±20 nm and 40±20 nm respectively, were analyzed. Shorter deposition times generated an incomplete growing of the film on the substrate, situation that has to be avoided considering the objective of fabricating PBA electrodes for spintronic applications. In this sense, 1 second of electrodeposition time was chosen as the lower limit for study. The 40 nm thickness limit is determined by the mechanism of growing of the material during the electropolymerization, impeding the reduction of this parameter when the coulometry method is used for the fabrication of thin films of CrCr .The morphology of the films was studied by AFM in tapping mode (figure 2.22).

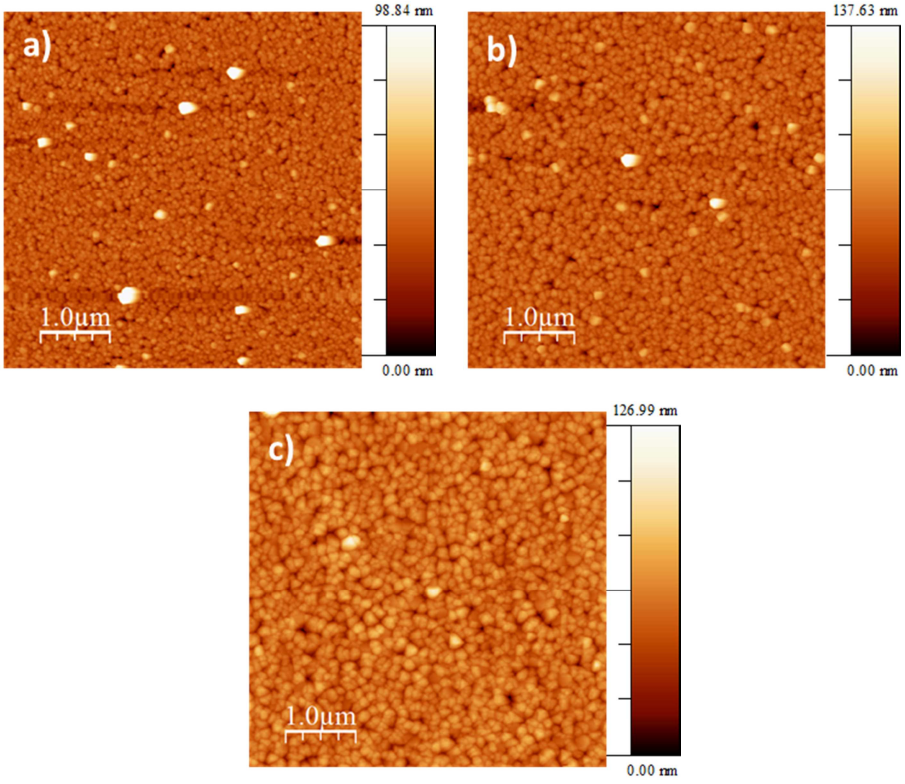

Figure 2.22- AFM topography images for films of CrCr with thicknesses of a) 40 nm (1 second electrodeposition time), b) 50 nm (2 seconds electrodeposition time) and c) 80 nm (10 seconds electrodeposition time).

Compared to the film of 80 nm, the RMS roughness does not appear to be affected when reducing the thickness to 50 nm (RMS~10 nm). Nevertheless, the average grain size is reduced to 120 nm. When the electrodeposition time is decreased down to 1 second, the resulting 40 nm thickness film exhibits a lower RMS roughness of 8 nm, with an average grain size of 90 nm. As conclusion, one can say that the reduction of the film thickness does not affect drastically in the surface roughness of the system but induces a clear reduction in the average grain size. In all the situations, no pyramidal grains have been detected

in surface, something expected taking into account that in these range of time, nucleation prevails over growth[16].

These ultra-thin films were studied with MOKE in polar configuration of the magnetic field employing the same red laser (λ=633 nm) and s-polarized light for comparing with the information obtained for the thicker films. In this situation, the S/N ratio of the measurement was critical taking into account the reduced dimensionality. In each case, an average over 25 cycles was needed in order to obtain a final hysteresis with a proper signal. In figure 2.23 it is depicted the comparison of the hysteresis loops registered at 190 K for the ultra-thin films respect to the 80 nm thickness film.

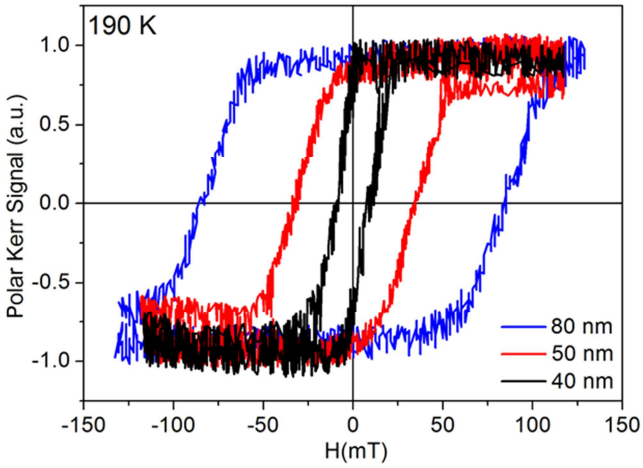

Figure 2.23- MOKE hysteresis loops measured at 190 K for films of CrCr of 80 nm (blue curve), 50 nm (red curve) and 40 nm thickness (black curve) thickness.

From MOKE data, it is observed that for these ultrathin films the H_C is reduced when the thickness decreases. This is again a consequence of the change in the surface morphology when modifying the film thickness.

By considering all the magnetic information obtained with MOKE at 190 K for all the film thicknesses studied in this section, it is possible to construct a

curve of H_C as a function of the average grain size of the surface particles on electrodeposited films of CrCr (figure 2.24).

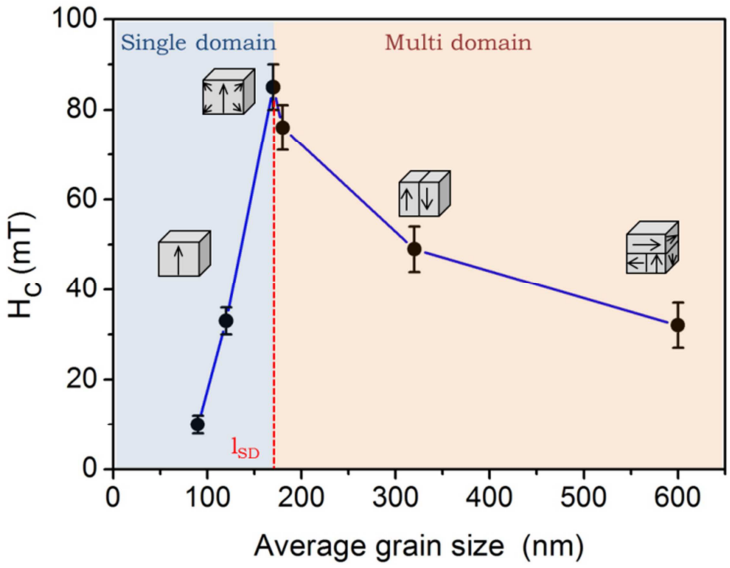

Figure 2.24- Dependence at 190 K of the coercive field determined with MOKE for films of CrCr as a function of the average grain size measured by means of AFM when the film thickness in progressively reduced.

The behavior of the curve in figure 2.24 can be understood by considering the PBA under study as a nanocrystalline ferromagnet composed of multiple PBA interacting particles (dipole interactions) on surface. The sizes of these particles in surface are influenced by the film thickness according to the electropolymerization mechanisms described in section 2.2.2. In this context, the magnetization reversal process taking place for the particles at surface is different in each region of the curve in figure 2.24. For large grain sizes the PBA particles in surface are multi-domain, becoming more bulk-like with increasing the size[58]. For this multi-domain case, the mechanism of magnetization reversal is domain wall nucleation and motion[58]. As the particle size is reduced, the increase of energy due to domain wall formation dominates over the decrease in

energy attributed to the formation of domains. Thus, below a critical PBA particle size, domain walls will no longer form due to energy considerations and single domain particles are stable. This critical size corresponds to the maximum coercivity in the curve of figure 2.24. This peak is defined as the single domain limit (l_{SD}) below which the PBA particles on the surface of the film contain only one magnetic domain[58]. In our particular case, this parameter has determined to be c.a. 170 nm from MOKE measurements. The fact that large coercivity of small particles is the result of single domains was first described by Kittel and co-workers[59] in the 1950s. Typically, in the single-domain regime, the magnetization reversal of the magnetic particles occurs by coherent rotation of the magnetization upon application of a magnetic field. Before application of an external field, the magnetization of a single-domain particle lies along an easy axis direction which is determined by the shape and magneto-crystalline anisotropies. When an external field is applied in the opposite direction, the particle is unable to respond by domain-wall motion, and instead, the magnetization must rotate through the hard direction to the new easy direction. The anisotropy forces which hold the magnetization in an easy direction are strong, and so the coercivity is large. This mechanism is known as the coherent rotation as described by Stoner and Wohlfarth[60]. As the particle size is reduced below l_{SD} the volume of the particle is reduced, thus the energy required for the coherent rotation is smaller leading to a reduction of the coercive field.

In order to confirm the scenario for the single domain particles in surface for the thinner films, a preliminary study with Low Temperature Magnetic Force Microscopy (LT-MFM) was performed in collaboration with Dra. Elena Pinilla. MFM is an imaging technique based on atomic force microscopy in which force gradients between a magnetic tip and the sample are measured to image the magnetic structure of the material under study[61]. It is a very powerful technique for characterizing magnetic domains on surface[62]. In this context, the stray field emanating from the sample generates a force on the MFM tip, inducing a shifting in its oscillation frequency (Δf). A negative frequency shift arising by an attractive sample-tip interaction will lead to a dark contrast in the image. On the contrary, a repulsive interaction will induce a positive frequency shift generating a bright contrast in the image. Thus, the orientation of the magnetic moments of the sample can be distinguished by this technique[63].

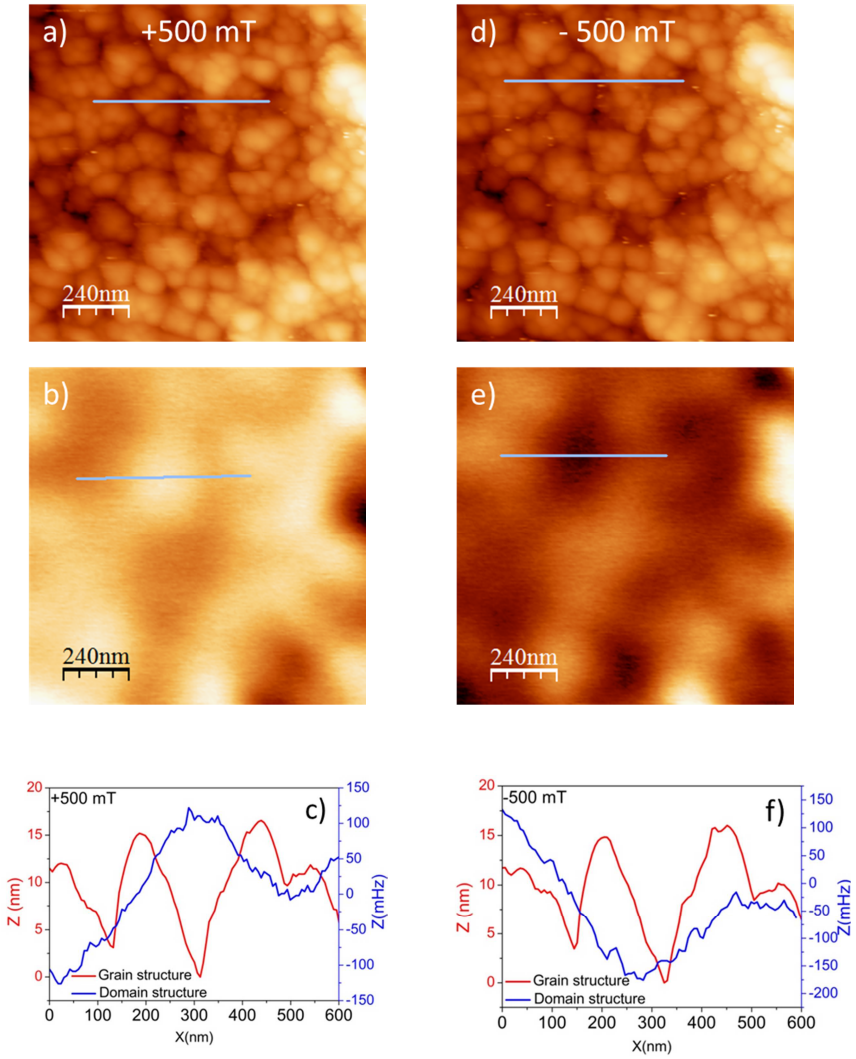

Figure 2.25- LT-MFM study on a 80 nm thickness film of CrCr at 153 K with a polar magnetic field. Initially a magnetic field of +500 mT was applied obtaining the topography (a) and magnetic (b) images in a constant plane mode (Z_{lift}=70 nm). The same procedure was repeated at -500 mT to get the topography (d) and magnetic (e) images of the film. A clear magnetic domain pattern is observed in areas presenting different magnetic contrast which is indicating different magnetization orientations. When the applied magnetic field is reversed this is reflected in a change of the magnetic domain features. Single domain particles are clearly observed, which is more evident from the profile curves (c-f).

Films of CrCr of 80 nm thickness, corresponding to a size of the nanoparticles in the single domain limit (~170 nm) established with MOKE (figure 2.24), were prepared for this preliminary study with LT-MFM. Images were acquired in constant plane mode, in which the tip is first scanned over the surface in close proximity to get the topography image. Subsequently, the tip is retracted by a predefined distance (Z_{lift}) and a second scan is performed, in which the tip follows a constant plane with a constant separation and the frequency shift due to magnetic interaction forces is recorded[63]. In figure 2.25 are depicted the topography and magnetic images (Z_{lift}=70 nm), obtained at 153 K (below the T_C) for a magnetic field perpendicular to the film surface, *i.e*, in polar configuration. These conditions resemble the ones established at the MOKE characterization. Initially, a field of 500 mT was applied to the film, considering the characteristics of MOKE hysteresis loops in which a saturation of the magnetization is detected at these values of magnetic fields. From LT-MFM image (figure 2.25-b) circular domain-like areas up to hundreds of nanometers in size with alternated contrast are observed. When comparing the topography (fig. 2.25-a) and magnetic (fig. 2.25-b) images it can be observed that in one type of magnetic domain many particles are included. This is more evident from the comparison of the profiles (figure 2.25-c) obtained over the topography (red curve) and the magnetic (blue curve) images, corresponding to grain and magnetic domain structures respectively. From this analysis, it can be distinguish that in a certain region of the sample, a domain-like structure of approximately 500 nm wide is measured, meanwhile the grain sizes are determined to be around 150-200 nm. This means that one magnetic domain region is containing several PBA particles in the surface of the film. When the magnetic field is reversed to a -500 mT the magnetic domain-like structure is changed reflecting the magnetization reversal process in the material (figures 2.25-d, 2.25-e, 2.25-f). Similar results have been reported for a two-dimensional cobalt nanoparticle assembly when studied by MFM[64]. In that situation, correlated areas (similar to domains) of parallel magnetization appear as a consequence of interacting particles ordered in a dense assembly. This consideration is coincident with the modeled vision we have proposed for the interacting PBA particles in the surface of the film.

Thus, the establishment of single-domain scenario in figure 2.24, for particles in the order of 170 nm as determined from MOKE coercivity of the PBA particles in surface, is supported by the LT-MFM characterization. The LT-MFM study has to be extended for films with bigger PBA particles in surface (thicker films) in order to analyze the evolution towards a multi-domain situation as established by MOKE measurements.

By considering all the discussion developed so far, regarding the magnetic characterization of thin films of CrCr, interesting conclusions have been extracted when comparing the magnetic information provided by SQUID and MOKE. The main differences were detected in the features of the hysteresis loops registered by each magnetometer. Higher coercive fields, just below the ordering temperature of the PBA, were measured with MOKE. In addition, a value of coercivity clearly dependent on the surface grain structure at surface when changing film thickness was detected by MOKE. Such feature escapes completely the SQUID sensitivity. As shown along the discussion, we have provided many evidences pointing towards the surface sensitivity of MOKE to the magnetic reversal process occurring at the grains in the top layers of the PBA thin film. The observation of these processes is not allowed in SQUID, as it cannot differentiate between bulk and surface in the PBA thin film. For testing the validity of the conclusions extracted for polycrystalline thin films of CrCr, we have extended the same studies to a control system constituted by a new PBA system formulated as $(Fe^{II}_xCr^{II}_{1-x})_3$ $[Cr^{III}(CN)_6]_2 \cdot z\ H_2O$.

2.2.5 Comparison of MOKE and SQUID characterizations on the ternary PBA $(Fe^{II}_xCr^{II}_{1-x})_3$ $[Cr^{III}(CN)_6]_2 \cdot z\ H_2O$

Thin films of a ternary PBA with formula $(Fe^{II}_xCr^{II}_{1-x})_3$ $[Cr^{III}(CN)_6]_2 \cdot z\ H_2O$ were synthesized with the same technique as CrCr, employing the growth conditions previously reported in literature for this material[32,65]. An electrochemical cell was charged with an aqueous solution (20mL) containing $K_3[Cr(CN)_6]$ (5 mM) , $CrCl_3$(6.7 mM) and $FeCl_3$ (1.1 mM). Electrodeposited films were grown at a fixed potential E = – 0.8 V vs Ag/AgCl. For a more simplified notation, from now on, films of $(Fe^{II}_xCr^{II}_{1-x})_3$ $[Cr^{III}(CN)_6]_2 \cdot z\ H_2O$ will be named as FeCrCr. A roughly linear relationship between deposition time and film thickeness was detected for

this system as it was done for films of CrCr. For the study under consideration, films of 1000 seconds and 100 seconds electrodeposition time were synthesized. By means of profilometry, this has been translated into thickness values of 7000 nm and 800 nm respectively (table 2.4).

It is known that the optical and magnetic properties of this PBA are determined by the compositional factor *x*,[32,65] which is mainly established by the mixing ratio (x_{mix} = Fe^{II} / (Fe^{II} + Cr^{II})) of metal ions in the prepared solutions. This ratio is also dependent on the electrochemical potential used in the synthesis procedure. This value of *x* provides an estimation of the grade of substitution of Cr^{II} centers by Fe^{II} in the structure of CrCr. In our case, the same mixing ratio x_{mix}= 0.14 was used in all the experiments and violet films with a compositional factor *x* close to 0.2 were electropolymerized, except for the 7000 nm thick sample, where *x* = 0.3. In both cases the value of *x* was determined by means of EDAX analysis. The difference in *x* can be understood from an increase of resistivity for the thicker sample which leads to a lower negative potential at the film surface. Since the reduction potential of $FeCl_3$ is lower (in absolute value) than that of $CrCl_3$, the increase of resistivity may induce a preferential deposition of iron in the thicker films increasing the Fe/Cr ratio. The compositional parameters as well as thicknesses are summarized in Table 2.4.

Time of deposition [s]	**Thickness [nm]**	**x**	**Average particle size [nm]**	**RMS roughness [nm]**
1000	7000±200	0.3	1100±100	121
100	800±100	0.21	910±90	45

Table 2.4- Compositional and morphological parameters of thin films of FeCrCr.

Prior to the magneto-optical study of FeCrCr with MOKE, a general characterization this ternary PBA films was performed. The optical absorption spectrum of this material is dominated in the visible range by a broad band centered around 520 nm, which corresponds mainly to the intervalence charge

transfer process Cr^{III}–C≡N–Fe^{2+}→Cr^{II}–C≡N–Fe^{3+}. The IR-ATR spectrum of the films (figure 2.26) exhibits a principal band located around 2181 cm^{-1}.

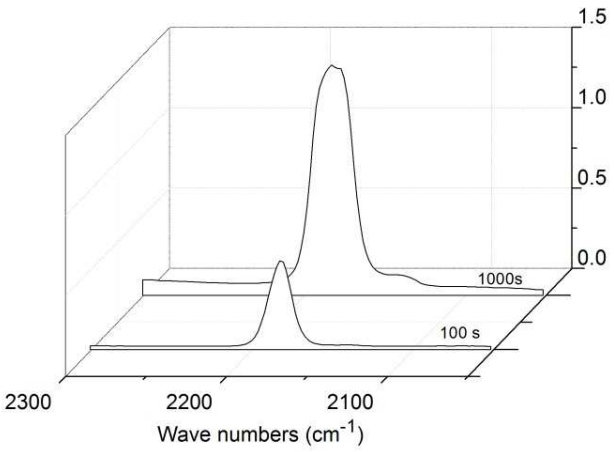

Figure 2.26- IR spectra of the thin films synthesized of FeCrCr with different times of electrodeposition.

This band is assigned to the cyanide stretching vibration of the $[Cr^{III}(CN)_6]^{3-}$ anion. Its position is known to vary along the series of FeCrCr from 2189 cm^{-1} (x = 0) to 2161 cm^{-1} (x = 1)[32]. Thus, the observed band corresponds to an iron molar fraction x close to 0.2 in agreement with the metal analysis. As expected, the intensity of this band increases proportionally to the thickness of the film and a new band located at 2070 cm^{-1} appears for the thicker films. This band corresponds to the presence of $[Cr^{II}(CN)_6]^{4-}$ defects (less than 5 % of total hexacyanometalate).

An XRD characterization (figure 2.27) was performed in films of FeCrCr, showing a typical cubic patter corresponding to a Prussian blue structure with a = 10.45 Å. The inclusion of Fe^{II} centers in the structure does not change the cell parameter of the material respect to the one found for CrCr.

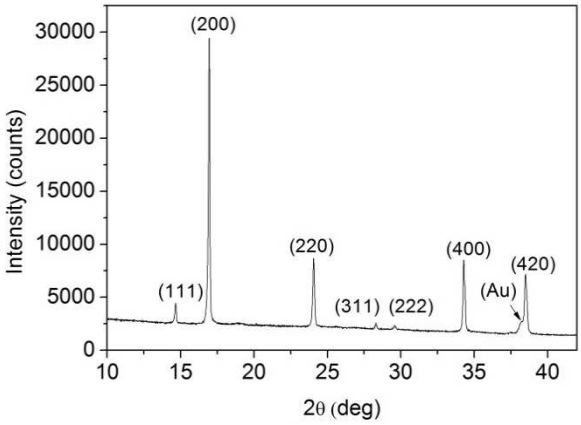

Figure 2.27- XRD diffraction pattern on a 7000 nm thickness film of FeCrCr.

The morphology of thin films of FeCrCr was studied by AFM (figure 2.28). The images were acquired in tapping mode, with a 10 x 10 μm scan size.

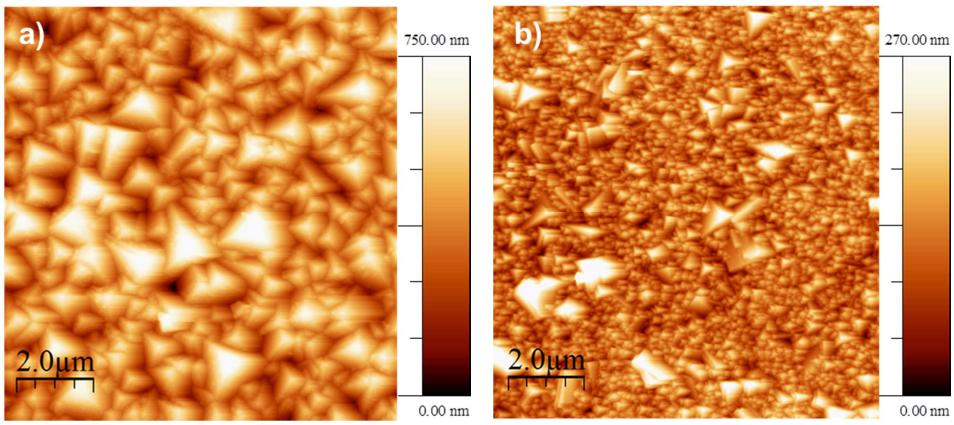

Figure 2.28- AFM image of the surface of the two films a) 1000 s, 7000 nm thickness and b) 100 s, 800 nm thickness of electrodeposition.

From the topography images it is possible to distinguish a polycrystalline structure composed of pyramidal particles of different sizes as it was already described for films of CrCr. The average particle size (Table 2.4) increases from a value of 410 nm for the film of 800 nm thicknesses to a value of 1100 nm for

the thicker film of 7000 nm. The RMS roughness parameter of the film also increases from 41 nm to 121 nm. The increase of the particle size and the RMS roughness parameter with the deposition time is explained under the same mechanisms as described for thin films of CrCr.

The fundamental information, regarding the study presented at this last point of the discussion, comes from the comparison between MOKE and SQUID characterization on thin films of FeCrCr. In figure 2.29 the temperature dependence of the susceptibility at 100 Oe determined by SQUID is depicted, as well as the thermal evolution of coercive field registered with MOKE for the two film thicknesses under study.

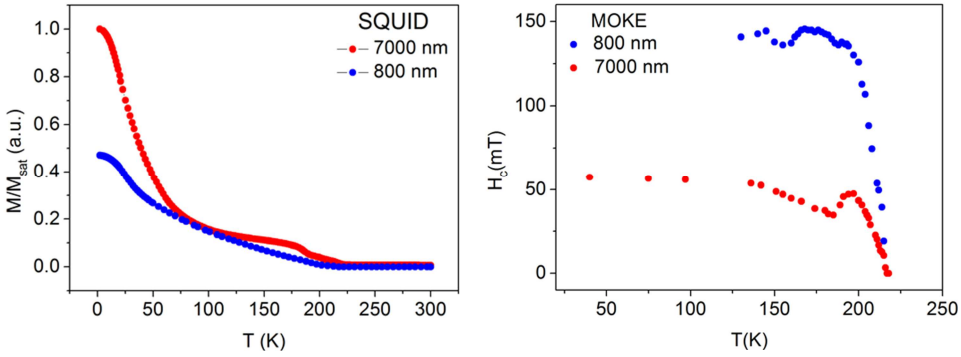

Figure 2.29- Thermal variation of dc magnetic susceptibility at 100 Oe measured with SQUID (left) and thermal evolution of coercivities determined by MOKE (right) for 7000 nm and 800 nm film thicknesses of FeCrCr.

The magnetization increases almost monotonically below a critical value of T_C = 225 K, which can be determined as the critical temperature for this PBA system (figure 2.28) as previously reported in literature[32,65]. A second subphase which orders at around 190 K is observed from the FC curve in the case of the thicker sample under study. The appearance of this second phase ordering at 190 K could be related to a non-totally homogenous distribution of Fe^{II} centers , giving rise to a second chemical environment with a lower *x* value, coexisting with the phase ordered at 225 K (*x*=0.3). This sub-phase is not detected in the

film of 800 nm thickness, thus a more homogenous composition of the material can be assumed.

From the thermal variation of the coercive field registered with MOKE (figure 2.28), it is possible to detect the same critical temperature respect to the one provided by SQUID. In both cases, the T_C (MOKE) value was estimated as the limit of the $H_C = f(T)$ curve for $H_C \rightarrow 0$, as already explained for films of CrCr. For the 800 nm film, the coercive field increases linearly on cooling ($dH_C/dT = -6.7$ mT/K) from 225 K to 200 K; then, it continues increasing more smoothly ($dH_C/dT = -0.46$ mT/K) until it reaches a maximum of 143 mT at 170 K. This maximum is close to the upper limit of applied magnetic fields of the electromagnets in the set-up (150 mT). Below this temperature, the value of coercive field is stabilized when progressively cooling down the system. The coercive field of the thicker film (7000 nm) exhibits roughly the same linear dependence on temperature in the 200–225 K range, reaching a maximum at 190 K. Below 180 K the coercivity increases again to finally reach a plateau with $H_C = 60$ mT below 125 K. This trend is not that clearly observed in the data of the 800 nm thickness film. The maximum detected at 190 K can be correlated with the sub-phase observed in the thermal variation of the magnetic susceptibility at 100 Oe measured with SQUID. Thus, it can be argued that MOKE is sensitive to the presence of regions in the material with defects of Fe^{II} centers, which are evidenced in the thermal response of the coercive field of the material.

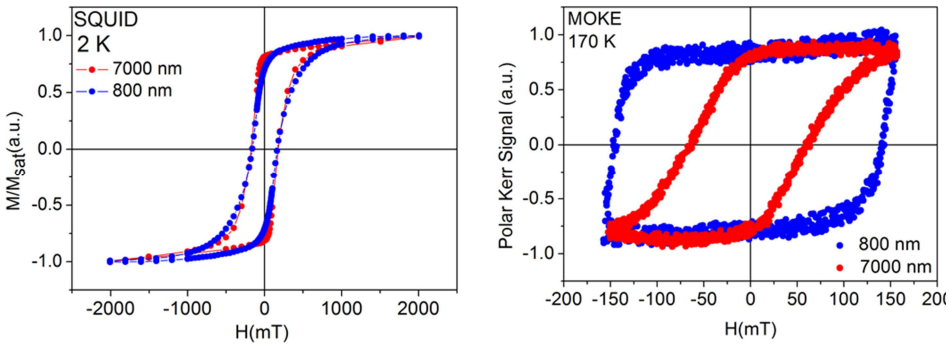

Figure 2.30- Comparison of hysteresis loops measured at 2K with SQUID (left) and at 170 K with MOKE in polar configuration (right) for thin films of FeCrCr.

The same features described with MOKE and SQUID for CrCr, regarding the coercive field dependence with film thicknesses, were also detected for thin films of FeCrCr. In figure 2.30 it is shown the comparison of the hysteresis loops with film thicknes measured with SQUID at 2 K and determined with MOKE in polar configuration at 170 K.

The hysteresis loops determined at 2 K with SQUID for both thicknesses show their behavior as soft magnets with equal coercive fields of H_C= 100 mT. The invariance of the coercive field with thickness for these PBA films is again detected as it was already determined for films of CrCr reinforcing the bulk features of the SQUID characterization in which parameters such as grain size has no effect on the registered magnetic information.

MOKE measurements were performed for linearly polarized incident light (λ = 633 nm), and Kerr rotation and ellipticity of the films, from the first and second harmonic information provided by the *lock-in*, were recorded as a function of the applied magnetic field in polar configuration. Again no difference in coercive fields has been found between first and second harmonic signals as it was expected from these measurements already described for thin films of CrCr.

A comparison of the magnetic behavior determined by MOKE at 170 K (figure 2.30) clearly shows a higher H_C for the thinner PBA film (being 142 mT and 62 mT for the 800 nm and 7000 nm thicknesses respectively). In addition, for both thicknesses the value of coercive field detected at 170 K is considerable high respect to the values obtained by SQUID, considering that in the latter technique the loops are registered at 2K. All this information is an indicative of a particle size effect on the MOKE signal, as already described for thin films of CrCr. This conclusion is again supported by the variations of surface morphology detected by AFM (figure 2.28), which are translated as a reduction of the grain size in surface when reducing the film thickness. The impact of the surface morphology in coercivity is also illustrated from the thermal variation of these parameter depicted in figure 2.29, with a curve for 800 nm thickness evolving above the values of 7000 nm in the low temperature range. The grain morphology in surface for the thinner film leads to an H_C value which at low temperatures is close to the maximum magnetic field allowed for the electromagnets in the MOKE set-up. This point is evidence by the polar MOKE

hysteresis loop in figure 2.30, in which the saturation of the sample is hardly achieved at this film thickness. Thus, based on the relation of surface morphology and magnetic information provided by MOKE, the same explanation to this phenomenology in films of CrCr can be extrapolated to thin films of this ternary PBA.

2.3 Conclusions and perspectives

To summarize, it has been demonstrated in this chapter that it is possible to reduce the thickness of electrodeposited CrCr PBA films to the nanometer range in order to scale down the growth of this material for applications in molecular spintronics. These thin films possess a smoother surface consisting in homogeneous particles of smaller size. This could improve considerably the quality of the interfaces when introducing thin films of this PBA as electrodes in a spintronic structure.

Interestingly, as the thickness of the film is reduced, its magnetic properties are considerably improved (higher coercivity and squareness of the hysteresis loops). It has also been shown that MOKE is a powerful technique for the determination of the magnetic properties of these molecule-based thin films. These materials offer an outstanding magneto-optical response due to the high intensity of the reflected light from the homogeneous transparent film surface, evidencing subtle particle-size effects. In this chapter a model for understanding the origin of the surface sensitivity of MOKE on these transparent materials has been presented and discussed in terms of optical considerations in the context of ellipsometric studies.

The surface characteristics of the magnetic information obtained by MOKE allow the registering of the magnetization reversal processes taking place on the top layers of the PBA thin films. This interfacial region is of great interest, regarding to the possible application of this system as a spin-injector electrode, due to its role defining the interface in a device. A LT-MFM study has been performed on 80 nm thickness films of CrCr. The results from this characterization indicate that the large coercive field observed in these films through MOKE are due to the size of the nanoparticles on the film surface. This information cannot be obtained from the data acquired with SQUID, in which

the measurement is related to the total volume of the material without the possibility of achieving a surface sensitivity.

Further, MOKE yields the possibility of recording magnetic hysteresis loops at relatively high temperatures (just below T_C), a very important fact in terms of future applications. Indeed, the present study shows that it is possible to obtain a magnetic hysteretic signal close to the ordering temperature from a molecular-based magnetic film with a thickness down to 40 nm.

The studies performed on the ternary PBA FeCrCr has been useful to confirm the trends determined for the MOKE response on thin films of CrCr. This situation supports the possibility of extending the study to other PBAs materials with a comprehensive scenario of the physical processes taking place.

As a possible future work to extend the already described studies, it is recommended to perform improvements in the synthesis procedure in order to achieve thinner films of CrCr by electropolymerization in the quest for obtaining higher quality surfaces for the fabrication of devices. A complete characterization of these films in the ultra-thin limit will be also needed to understand their grade of suitability for their application in molecular spintronics.

2.4 Bibliography

(1) Xiong, Z. H.; Wu, D.; Vardeny, Z. V.; Shi, J. *Nature* **2004**, *427*, 821.

(2) Camarero, J.; Coronado, E. *J. Mater. Chem.* **2009**, *19*, 1678.

(3) Dediu, V. A.; Hueso, L. E.; Bergenti, I.; Taliani, C. *Nat. Mater.* **2009**, *8*, 707.

(4) Wang, F.; Vardeny, Z. V. *J. Mater. Chem.* **2009**, *19*, 1685.

(5) Yoo, J.-W.; Chen, C.-Y.; Jang, H. W.; Bark, C. W.; Prigodin, V. N.; Eom, C. B.; Epstein, a J. *Nat. Mater.* **2010**, *9*, 638.

(6) Sato, O.; Iyoda, T.; Fujishima, A.; Hashimoto, K. *Science (80-.).* **1996**, *272*, 704.

(7) Shimamoto, N.; Ohkoshi, S.; Sato, O.; Hashimoto, K. *Inorg. Chem.* **2002**, *41*, 678.

(8) Escax, V.; Bleuzen, a; Cartier Dit Moulin, C.; Villiam, F.; Goujon, a; Varret, F.; Verdaguer, M. *J. Am. Chem. Soc.* **2001**, *123*, 12536.

(9) Coronado, E.; Giménez-López, M. C.; Korzeniak, T.; Levchenko, G.; Romero, F. M.; Segura, A.; García-Baonza, V.; Cezar, J. C.; de Groot, F. M. F.; Milner, A.; Paz-Pasternak, M. *J. Am. Chem. Soc.* **2008**, *130*, 15519.

(10) S. Ferlay, T. Mallah, R. Ohuaès, P. Veillet, M. V. *Nature* **1995**, *378*, 701.

(11) Ohkoshi, S.; Mizuno, M.; Hung, G.; Hashimoto, K. *J. Phys. Chem. B* **2000**, *104*, 9365.

(12) Mallah, T.; Thiébaut, S.; Verdaguer, M.; Veillet, P. *Science* **1993**, *262*, 1554.

(13) O. Sato, T.Iyoda, A. Fujishima, K. H. *Science (80-.).* **1996**, *271*, 49.

(14) Buschmann, W. E.; Paulson, S. C.; Wynn, C. M.; Girtu, M. A.; Epstein, A. J.; White, H. S.; Miller, J. S. *Chem. Mater.* **1998**, *10*, 1386.

(15) Coronado, E.; Makarewicz, M.; Prieto-Ruiz, J. P.; Prima-García, H.; Romero, F. M. *Adv. Mater.* **2011**, *23*, 4323.

(16) Prima-Garcia, H.; Coronado, E.; Prieto-Ruiz, J. P.; Romero, F. M. *Nanoscale Res. Lett.* **2012**, *7*, 232.

(17) Sugano, S.; Tanabe, Y. *Magneto-Optics*; Springer: Berlin, 2000; Vol. 128.

(18) D. Frölich, S. Leute, V.V. Pavlov, R. V. P. *Phys. Rev. Lett.* **1998**, *81*, 3239.

(19) Tozawa, M.; Ohkoshi, S.; Kojima, N.; Hashimoto, K. *Chem. Commun. (Camb).* **2003**, 1204.

(20) Sato, Y.; Ohkoshi, S.; Hashimoto, K. *J. Appl. Phys.* **2002**, *92*, 4834.

(21) Qiu, Z. Q.; Bader, S. D. *Rev. Sci. Instrum.* **2000**, *71*, 1243.

(22) Grimsditch, M.; Hoffmann, a.; Vavassori, P.; Shi, H.; Lederman, D. *Phys. Rev. Lett.* **2003**, *90*, 257201.

(23) R. Miranda, A. Cebollada, J. M. Gallego, S. Ferrer, R. M. *Surf. Sci.* **1989**, *211*, 732.

(24) Albrecht, M.; Hu, G.; Guhr, I. L.; Ulbrich, T. C.; Boneberg, J.; Leiderer, P.; Schatz, G. *Nat. Mater.* **2005**, *4*, 203.

(25) Mewes, T.; Nembach, H.; Rickart, M.; Demokritov, S.; Fassbender, J.; Hillebrands, B. *Phys. Rev. B* **2002**, *65*, 224423.

(26) Stampe, M.; Stoll, P.; Homberg, T.; Lenz, K.; Kuch, W. *Phys. Rev. B* **2010**, *81*, 104420.

(27) Lin, R.; Wang, F.; Rybicki, J.; Wohlgenannt, M.; Hutchinson, K. a. *Phys. Rev. B* **2010**, *81*, 195214.

(28) Riminucci, A.; Bergenti, I.; Hueso, L. E.; Murgia, M.; Taliani, C.; Zhan, Y.; Casoli, F. <*http://arxiv.org/abs/cond-mat/0701603*> **2007**.

(29) Vardeny, Z. V. *Organic Spintronics*; Taylor & Francis Group: Boca Raton-Florida, 2010.

(30) Ehrenfreund, E.; Valy Vardeny, Z. *Phys. Chem. Chem. Phys.* **2013**, *15*, 7967.

(31) Clarke, J.; Braginski, A. I. *The SQUID Handbook: Applications of SQUIDs and SQUID Systems*; Wiley-VCH, 2004.

(32) S. Ohkoshi, A. Fujishima, K. H. *J. Am. Chem. Soc.* **1998**, *120*, 5349.

(33) K. Ikeda, S. Ohkoshi, K. H. *Chem. Phys. Lett.* **2001**, *349*, 371.

(34) Ikeda, K.; Ohkoshi, S.; Hashimoto, K. *J. Appl. Phys.* **2003**, *93*, 1371.

(35) Bader, S. D. *J. Magn. Magn. Mater.* **1991**, *100*, 440.

(36) Behera, J. N.; Alessandro, D. M. D.; Soheilnia, N.; Long, J. R. *Chem. Mater.* **2009**, *21*, 1922.

(37) Coronado, E.; Prieto-Ruiz, J. P.; Prima-Garcia, H. *Chem. Commun. (Camb).* **2013**, *49*, 10145.

(38) Butler, M. a. *J. Appl. Phys.* **1977**, *48*, 1914.

(39) Zhang, X.; Ai, Z.; Jia, F.; Zhang, L. *J. Phys. Chem. C* **2008**, *112*, 747.

(40) Xiao, X.; Liu, C.; Hu, R.; Zuo, X.; Nan, J.; Li, L.; Wang, L. *J. Mater. Chem.* **2012**, *22*, 22840.

(41) Horcas, I.; Fernández, R.; Gómez-Rodríguez, J. M.; Colchero, J.; Gómez-Herrero, J.; Baro, a M. *Rev. Sci. Instrum.* **2007**, *78*, 013705.

(42) Nakanishi, S.; Lu, G.; Kothari, H. M.; Bohannan, E. W.; Switzer, J. a. *J. Am. Chem. Soc.* **2003**, *125*, 14998.

(43) Barraud, C.; Seneor, P.; Mattana, R.; Fusil, S.; Bouzehouane, K.; Deranlot, C.; Graziosi, P.; Hueso, L.; Bergenti, I.; Dediu, V.; Petroff, F.; Fert, A. *Nat. Phys.* **2010**, *6*, 615.

(44) Dediu, V.; Hueso, L.; Bergenti, I.; Riminucci, a.; Borgatti, F.; Graziosi, P.; Newby, C.; Casoli, F.; De Jong, M.; Taliani, C.; Zhan, Y. *Phys. Rev. B* **2008**, *78*, 115203.

(45) Heiliger, C.; Zahn, P.; Mertig, I. *Mater. Today* **2006**, *9*, 46.

(46) Sun, D.; Yin, L.; Sun, C.; Guo, H.; Gai, Z.; Zhang, X.-G.; Ward, T. Z.; Cheng, Z.; Shen, J. *Phys. Rev. Lett.* **2010**, *104*, 236602.

(47) Ruden, P. *Nat. Mater.* **2011**, *10*, 8.

(48) Liu, Y.; Watson, S.; Lee, T.; Gorham, J.; Katz, H.; Borchers, J.; Fairbrother, H.; Reich, D. *Phys. Rev. B* **2009**, *79*, 075312.

(49) Lee, W.; Choi, B.-C.; Xu, Y.; Bland, J. *Phys. Rev. B* **1999**, *60*, 10216.

(50) Kurmoo Mohamedally, C. J. K. *Mol. Cryst. Liq. Cryst.* **1999**, *334*, 632.

(51) Pajerowski, D. M.; Gardner, J. E.; Andrus, M. J.; Datta, S.; Gomez, a.; Kycia, S. W.; Hill, S.; Talham, D. R.; Meisel, M. W. *Phys. Rev. B* **2010**, *82*, 214405.

(52) Valenzuela, R. *Magnetic Ceramics*; Cambridge University Press: Cambridge, 1994.

(53) Tompkins, H. G.; Irene, E. A. *Handbook of Ellipsometry*; William Anderson Publishing-Springer: Heidelberg (Germany), 2005.

(54) Egan, Walter, H. T. *Optical Properties of Inhomogeneous Materials : Applications to Geology , Astronomy , Chemistry and Engineering*; Academic Press, INC: New York, 1979.

(55) Pápa, Z.; Budai, J.; Hanyecz, I.; Csontos, J.; Toth, Z. *Thin Solid Films* **2014**.

(56) Berova, N. *Circular Dichroism : Principles and Applications*; Wiley-VCH, 200AD.

(57) Mamedov, N.; Toyota, H.; Yasunaka, A.; Shim, Y.; Kato, A.; Ashida, A.; Iida, S.; Yamamoto, N. *Phys. Status Solidi* **2003**, *198*, 478.

(58) Sellmyer, D., Skomski, R. *Advanced Magnetic Nanostructures*; Springer: New York-USA, 2006.

(59) C. Kittel, J. Galt, W. C. *Phys. Rev.* **1950**, *77*, 725.

(60) Stoner, E. C.; Wohlfarth, E. P. *Philos. Trans. R. Soc. A Math. Phys. Eng. Sci.* **1948**, *240*, 599.

(61) Martin, Y.; Wickramasinghe, H. K. *Appl. Phys. Lett.* **1987**, *50*, 1455.

(62) Wadas, a.; Moreland, J.; Rice, P.; Katti, R. R. *Appl. Phys. Lett.* **1994**, *64*, 1156.

(63) Pinilla, E. *Characterization and processability of molecular-based magnetic nanoparticles and 2D crystals by scanning probe microscopy-PhD thesis*; University of Valencia, 2014.

(64) Puntes, V. F.; Gorostiza, P.; Aruguete, D. M.; Bastus, N. G.; Alivisatos, a P. *Nat. Mater.* **2004**, *3*, 263.

(65) Nuida, T.; Hozumi, T.; Kosaka, W.; Sakurai, S.; Ikeda, S.; Matsuda, T.; Tokoro, H.; Hashimoto, K.; Ohkoshi, S. *Polyhedron* **2005**, *24*, 2901.

Chapter 3

MOKE magnetometry as a probe of surface magnetic impurities in electropolymerized magnetic thin films of the PBA $Fe_3[Cr(CN)_6]_2 \cdot 15\ H_2O$

3.1 Introduction

In this chapter we present a MOKE study performed on electrodeposited PBA thin films of $Fe_3[Cr(CN)_6]_2 \cdot 15\ H_2O$. This is a molecular-based magnetic material exhibiting ferromagnetic ordering below a critical temperature of 23 K. There have been many previous reports in literature about the possibility of changing the magnetic ordering by external stimuli PBA's. A relevant example is provided by the cobalt-iron cyanide which undergoes a photoinduced magnetization via an electron transfer process[1–3]. A second example is provided by the chromium-iron cyanide. This system can exhibit linkage isomerism in such a way that in the pair $Fe^{2+}–CN–Cr^{3+}$ the CN^- ligand can bridge the Fe^{2+} through the C or through the N: $Fe^{2+}–N{\equiv}C–Cr^{3+} \leftrightarrow Fe^{2+}–C{\equiv}N–Cr^{3+}$.

In this process, the ground spin state of the Fe^{2+} cation undergoes a change from an initial high-spin (HS) configuration where Fe is bonded to N to a final low-spin (LS) state in which the Fe is now bonded to C. This reaction induces a contraction in the material of around 15 % of its volume. Hence, one can take advantage of this feature for controlling this isomerization process by an external pressure. This point has been exploited in the system $K_{0.4}Fe_4[Cr(CN)_6]_{2.8} \cdot\ 16\ H_2O$ to tune its magnetic properties[4,5]. In this case, some of the $Cr^{III}–C{\equiv}N–Fe^{II}$ present in the compound isomerized to the $Cr^{III}–N{\equiv}C–Fe^{II}$ form under an external mechanical perturbation. As a result, there is an increase of the ligand field around the iron (II) centers which undergo spin crossover to the diamagnetic LS state. By increasing the external pressure on the system, the number of paramagnetic centers in the cubic lattice decrease producing a correspondent decrease of the net magnetization and critical temperature of the material.

In addition to the piezomagnetic response of this type of iron-chromium PBA, Ohkoshi and co-workers reported one decade ago the possibility of changing the magnetization of films of $Fe_3[Cr(CN)_6]_2 \cdot\ 7.5\ H_2O$, prepared by electrochemical deposition[6], by an optical mode. They could observe a reduction of 10% in the magnetization of the compound in a photon mode by exciting the intervalence transfer band of the material. This photoinduced magnetization decrease was explained considering the photoexcited state as formed by the mixed-valence

state of Cr^{III}–C≡N–Fe^{II} and Cr^{II}–C≡N–Fe^{III}. This photoexcited state would relax to a metastable state in which the ferromagnetic interaction is not strong enough to maintain the ordering of the spins in the material (figure 3.1). The original ferromagnetic state is recovered when the temperature of the system is increased up to 40 K destroying the metastable state.

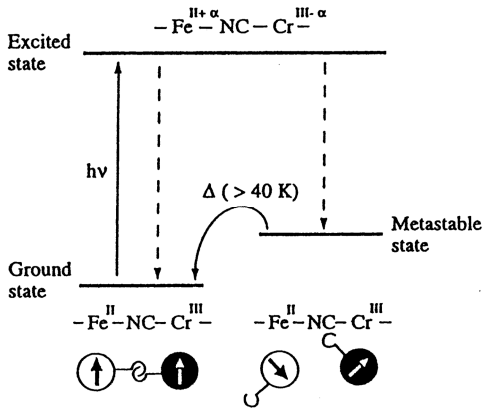

Figure 3.1- Reaction scheme of the photomagnetic process on a electrodeposited film of $Fe_3[Cr(CN)_6]_2 \cdot 7.5\ H_2O$. Image extracted from reference [6].

The ability of this iron-chromium derivative of changing its magnetic properties under the application of external stimuli makes it an interesting candidate in order to design magnetic structures with bistable response. Based on this, the possibility of incorporating this material in future multifunctional spintronic devices has motivated the characterization presented in this chapter.

In the previous chapter, our work regarding to the first MOKE characterization of PBA films reported in literature[7,8] was extensively described. In that case, it was shown that MOKE is a valuable technique for the study of the magnetic properties of electrodeposited ultra-thin films of these molecular-based magnetic materials with interest in molecular spintronics. The technique has a good spatial resolution, it is sensitive to surface properties and thus offers a complementary information as compared to bulk techniques, such as SQUID measurements[9–13]. The key point of the study presented here, relies in the ability of MOKE for giving information about the chemical environment in which

films of this iron-chromium derivative are obtained by electrochemical deposition.

SQUID measurements on these films showed an ordering temperature for the ferromagnetic phase of 23 K, close to that previously reported for this material[6]. In contrast, MOKE measurements revealed a critical temperature located in the range of 60-70 K. Through an extensive characterization study it has been possible to establish that this anomalous T_C is due to the presence of amorphous iron oxide particles that appear during the electrodeposition process of the PBA film. Interestingly, MOKE measurements have made possible the detection of this extra phase that escaped to SQUID detection[14].

3.2 Results and discussion

3.2.1 Synthesis

$K_3[Cr(CN)_6]$ and $FeCl_3$ were purchased from Sigma-Aldrich and used without further purification. An electrochemical cell was charged with an aqueous solution (20 mL) containing $K_3[Cr(CN)_6]$ (5 mM) and $FeCl_3$ (7.5 mM), following the reported procedure[6,14].The pH of the resulting solution was determined to be 2.2. From a cyclic voltammetry study on the electrolyte solution (figure 3.2) it was possible to locate the electrochemical reduction of $[Fe(H_2O)_6]^{3+}$taking place at a voltage of -0.5V.

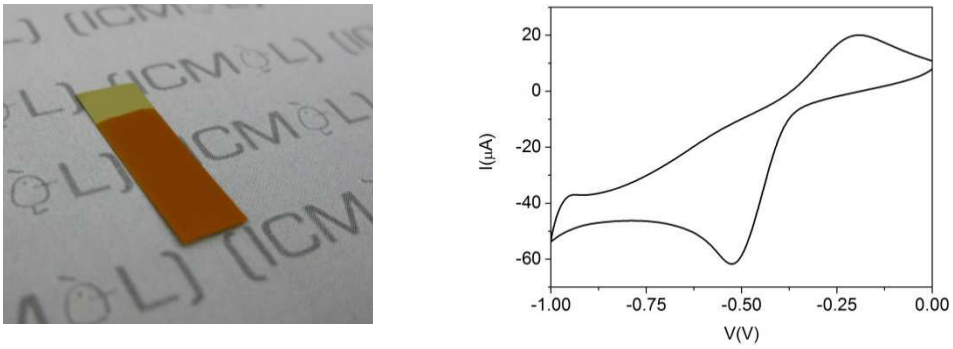

Figure 3.2- *Left*: Image of the electrodeposited film of FeCr after 1000 seconds deposition time. *Right*: Cyclic voltammetry of the electrolytic solution containing $K_3[Cr(CN)_6]$ (5 mM) and $FeCl_3$ (7.5 mM) at an scan rate of 40mV/s.

Electrodeposited films were grown at a fixed potential (E = – 0.5 V vs Ag/AgCl reference electrode) on a substrate of Mylar (dimensions: 5 × 10 mm) coated with an evaporated Au layer of 100 nm thickness acting as the working electrode. A Pt wire was employed as a counter electrode.

In this sense, the electropolymerization of the films takes place by electrochemical reduction of $[Fe(H_2O)_6]^{3+}$ species in an aqueous solution containing $[Cr(CN)_6]^{3-}$ anions. The reduced $[Fe(H_2O)_6]^{2+}$ species formed at the vicinity of the electrode reacts *in situ* with the hexacyanometalate anion to form an orange film of the insoluble PBA on the gold surface (figure 3.2).

After preparation, films were rinsed with water and dried at room temperature.

Time of deposition [s]	**Thickness [nm]**
5	50
20	135
100	300
500	850
750	1300
1000	1450

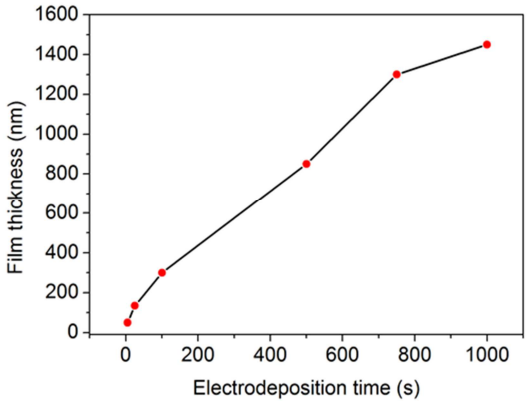

Table 3.1- *Left*: Relation of thicknesses for different electrodeposition times of FeCr. *Right*: Linear relation between thickness of the films and electrodeposition time.

The thickness of the films increases linearly with electrodeposition time, as shown by profilometry measurements (Table 3.1). Through an EDAX analysis it was found a Fe/Cr ratio of 1.53, in comparison with the expected one of 1.5. No presence of potassium in the structure of the material was detected. Thermogravimetric measurements on films obtained using 1000 electrodeposition time were carried out in order to determine the content of water molecules in the structure. In the low temperature range, a first step

centered at around 200 °C, corresponding to desorption of surface and coordinated water molecules, supposed a weight loss of 32 %. This could be translated to the presence of 15 water molecules in the structure of the PBA. In this sense, the formula of the PBA obtained by electrodeposition was determined as $Fe_3[Cr(CN)_6]_2 \cdot 15\ H_2O$. In order to simplify the notation, this compound will be referred from now on as FeCr. As it was mentioned in the introduction of the chapter, the anomaly in T_C determined with MOKE on films of FeCr was found for a thickness of 1450 nm. Thus the study presented on this chapter is mainly related to this film thickness.

3.2.2 General characterization

Powder X-ray diffraction of the electrodeposited films showed a typical cubic pattern corresponding to a Prussian blue structure with a cell parameter a = 10.59 Å (figure 3.3). For this characterization, a collection of microcrystals was scraped from the surface of the film and mounted on the sample holder (cryoloop).

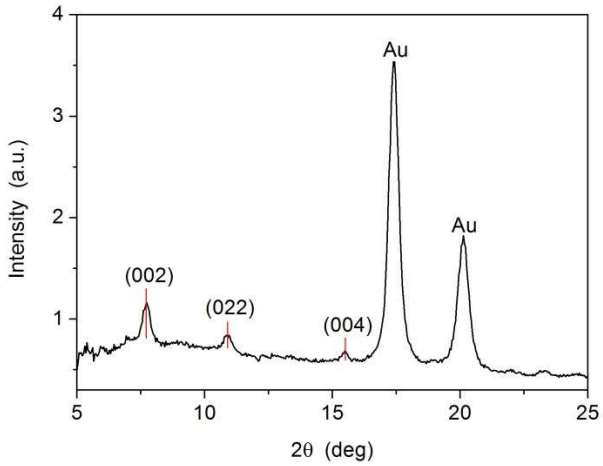

Figure 3.3- X-ray diffractogram of a 1000 seconds electrodeposition time film of FeCr. The lines correspond to the peaks expected for a cubic lattice of parameter a = 10.59 Å.

The ATR-IR spectrum of a film of FeCr exhibits a single band in the cyanide region located at 2165 cm^{-1} as it has been reported previously for this material

(figure 3.4). This band corresponds to the cyanide stretching vibration of $Cr^{III}-C\equiv N-Fe^{2+}$ moieties[6,14].

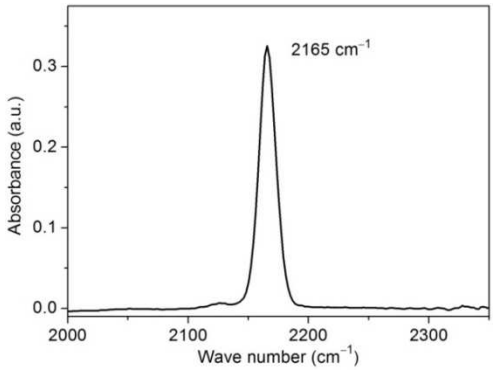

Figure 3.4- ATR-IR spectrum of a thin film of FeCr.

The growth of a thin film of FeCr was monitored *in situ* by means of a spectroelectrochemical cell. The UV-visible spectra recorded during the electrodeposition of the film on ITO and depicted in figure 3.5 exhibits a single absorption band centered around 450 nm.

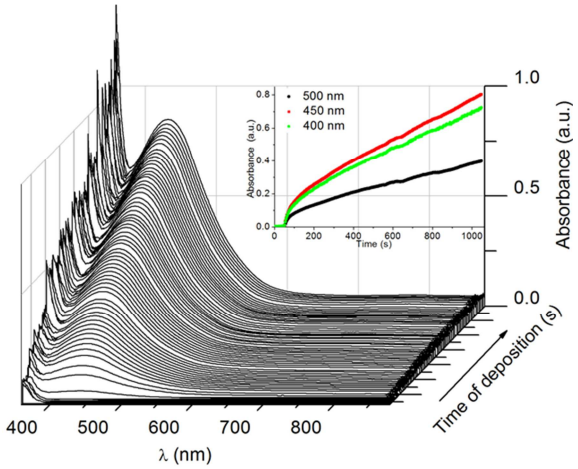

Figure 3.5- UV-visible spectra obtained during 1000 seconds electrodeposition of a thin film of FeCr. *Inset*: Time dependence of the absorbance of the film at different wavelengths.

This band can be assigned to the intervalence charge transfer process $Cr^{III}-C\equiv N-Fe^{2+} \rightarrow Cr^{II}-C\equiv N-Fe^{3+}$. After a few minutes, needed for a

homogeneous covering of the transparent electrode surface, the intensity of this band increases linearly with time. This is not surprising, in view of the linear time dependence of the film thickness.

In the same way as for CrCr films already described in chapter 2, films of FeCr present a semiconducting behavior. From the measured UV-visible spectra it is possible to make an estimation of the optical band gap of this system. The optical absorption near the band edge follows the formula (2.1) , where A, υ , E_g and α are the absorption coefficient, light frequency , band gap energy and a constant respectively, with n=1 or n=4 for direct and indirect band gap respectively[15–17]. As for CrCr, one has assumed for the calculation a direct band gap between the conduction band (CB) and valence band (VB) in the material.

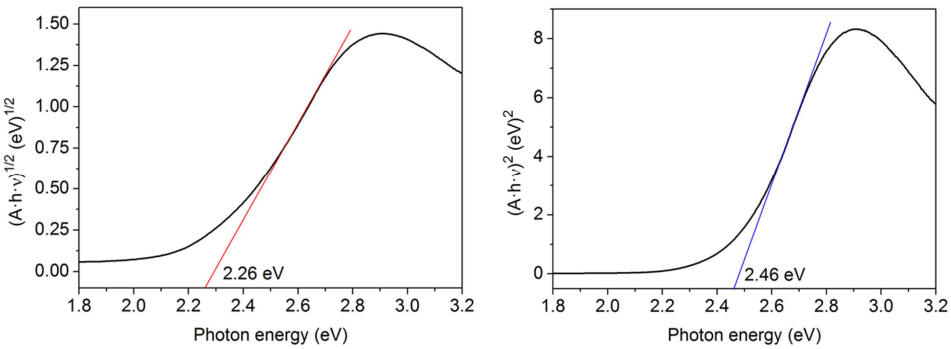

Figure 3.6- *Left: Estimation* of the optical energy bandgap for films of FeCr by employing the plot $(Ahv)^{1/2}$ vs (hv) considering a direct transition. *Right*: Estimation of the indirect optical energy bandgap for a film of FeCr by employing the plot $(Ahv)^2$vs (hv).

The calculation of this parameter was done by plotting $(Ahv)^{1/2}$ versus the photon energy (hv) from the UV-visible data in a film corresponding to 100 seconds electrodeposition time (300 nm thickness). It was possible to make an estimation of the energy band gap (E_g) from the intercept of the tangent (red line) with the *x*-axis obtaining a value of 2.26 eV (figure 3.6) for a direct band gap.

As a proof of tolerance in the calculations, a comparison with the value obtained assuming the existence of an indirect band gap on the semiconductor can be

done. Thus, a plot based on equation (2.1), but employing in this case n = 4, was again applied to the UV-visible spectrum of a 300 nm thickness film of FeCr. The result is depicted in figure 3.6, where an energy bandgap of 2.46 eV was estimated with the same procedure as before.

In order to characterize the morphology of the samples, an atomic force microcopy (AFM) study in tapping mode was performed on a film of 1450 nm thickness. The AFM characterization of the film reveals a polycrystalline structure with the presence of pyramidal grains (Figure 3.7). This well-known pattern results from the epitaxial electrodeposition of the PBA on the gold surface[18], as it was already mentioned in chapter 3 . In the present case, an average crystallite size of 830 nm and a RMS roughness of 125 nm can be measured. This type of morphology has been already described in the previous chapter for the thin films of the PBA's CrCr[7] and FeCrCr.

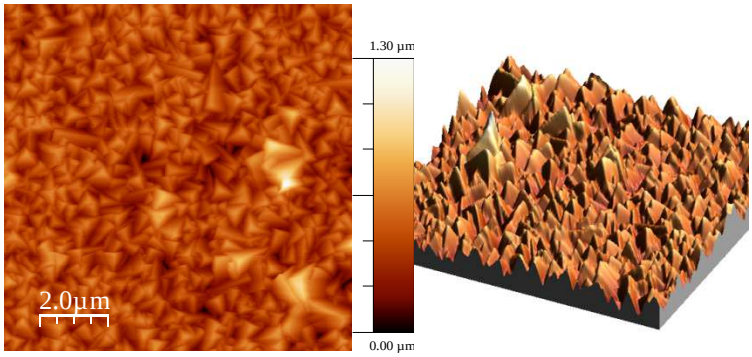

Figure 3.7- *Left*: 100 µm^2 topography image in tapping mode of a 1450 nm thickness film of FeCr. *Right*: 3D representation of the topography (right).

3.2.3 Comparative magnetic study of thin films of FeCr employing SQUID and MOKE techniques

Static magnetic measurements were carried out on a collection of thin films of 1450 nm thickness of FeCr using a SQUID magnetometer. Films were cut in many pieces and introduced in the sample holder with the applied magnetic field parallel to the surface. The temperature dependence of the molar magnetic susceptibility ($x = M \cdot H^{-1}$) in the 2-300 K range was measured under an applied magnetic field of 500 Oe. As depicted in figure 3.8, x increases abruptly at low temperatures, reaching a saturation value of 73.38 emu·K·mol^{-1} below 5 K. This is an indication of a magnetically ordered ground state. The critical temperature of the material obtained from the first derivative of the $x = f(T)$ curve is T_C = 23.5 K. In the high-temperature paramagnetic region (30-300 K range), the data could be fitted to a Curie-Weiss law (equation 3.2), with a positive Weiss constant θ = + 26 K, indicating a ferromagnetic behavior. The Curie constant obtained from this fit (C = 12 emu·K·mol^{-1}) is close to the expected value (12.75 emu·K·mol^{-1}) for three high-spin Fe^{2+} (g = 2) and two Cr^{3+} (g = 2) ions per formula unit.

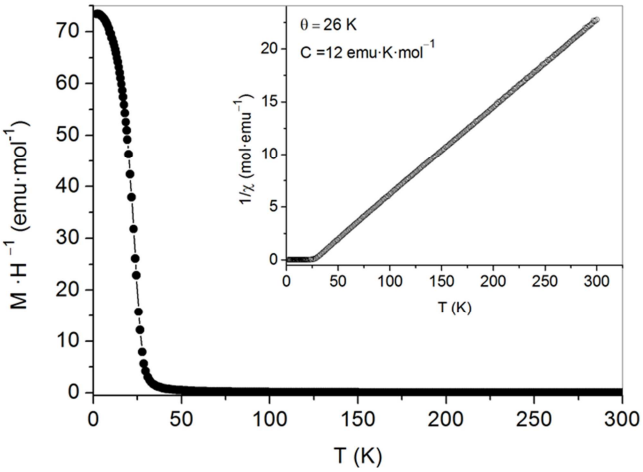

Figure 3.8- Temperature dependence of the molar magnetic susceptibility (x) of a thin film of FeCr.*Inset*: thermal variation of the reciprocal magnetic susceptibility.

The field dependence of the magnetization at 2 K (Figure 3.9) shows a fast increase to reach a value of ca. 10 μ_B in an applied field of 5 kOe. This response is followed by a smooth increase to a value of 11 μ_B at 50 kOe. The value of the magnetization at saturation (M_{sat}= 12.4 μ_B) was calculated from the limit of the $M = f(H^{-1})$ function as $H^{-1} \rightarrow 0$. The value of M_{sat} was much lower than the expected value for ferromagnetic alignment of three high-spin Fe^{2+} and two Cr^{3+} ions (18 μ_B). This fact is well known and is originated by the combination of structural disorder and the anisotropic character of the ferrous ions[5].

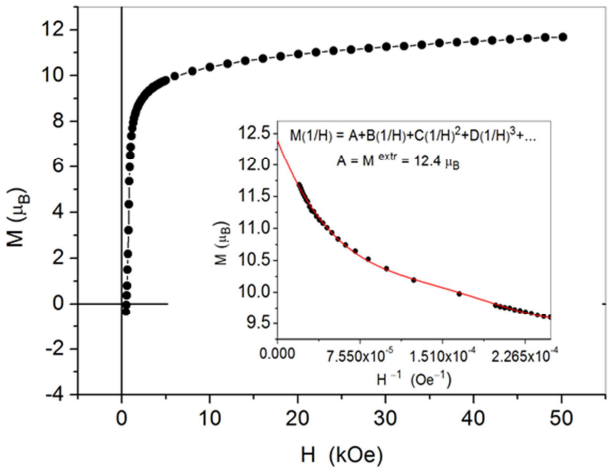

Figure 3.9- Field dependence of the magnetization (M) of a thin film of FeCr at 2 K. *Inset*: $M = f(H^{-1})$ plot. The red line indicates the best fit to a polynomial expansion. The saturated magnetization was calculated from the extrapolation of this curve to $H^{-1} \rightarrow 0$.

Figure 3.10 shows the hysteresis plot of the film in the low-field region. A coercive field of 670 Oe is measured at 2 K, in agreement with previous results concerning polycrystalline samples.

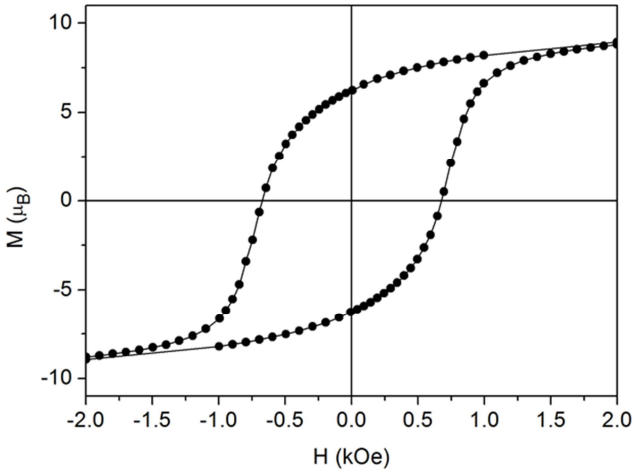

Figure 3.10- Field dependence of the magnetization (*M*) of FeCr at 2 K.

These bulk magnetic properties are very similar to those previously described in other iron(II) hexacyanochromate(III) systems. To our surprise, however, the magneto-optical properties of thin films of FeCr do not correlate with this simple magnetic analysis, as we shall see in the following.

A source of linearly polarized light of high wavelength (λ = 633 nm) and low power (10 mW) was used to irradiate a film of 1450 nm thickness of FeCr. The Kerr rotation (θ_K) of the films was recorded as a function of the applied magnetic field, for different temperatures. Since, in a first approach, θ_K is proportional to the magnetization of the sample on the surface, these measurements are analogous to magnetization $M = f(H)$ curves as it was already described in the previous chapter. Hysteresis loops should then appear below the critical temperature (T_C) of the magnet. An example of hysteresis loop measured at 43 K in polar configuration with s-polarized light is shown in Figure 3.11. No differences in coercivities for the first and second harmonic were found as already observed for thin films of CrCr and FeCrCr and described in chapter 2.

The most remarkable feature of these measurements is that the T_C of the thin films of FeCr, as measured by the onset of a hysteretic signal in the $\theta_K = f(H)$ curve (i.e. the temperature from which the signal evolves from a straight line corresponding to the diamagnetic contribution of the cryostat window to a proper s-shaped hysteretic response), was found in the 60-70 K range.

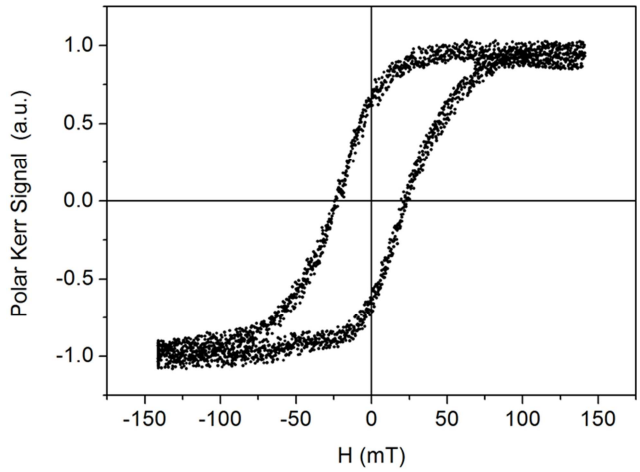

Figure 3.11- MOKE hysteresis loop of a 1450 nm thickness film of FeCr measured at 43 K in polar configuration with s-polarized light.

A proper determination of the T_C obtained from MOKE magnetometry, T_C (MOKE), was made by measuring the thermal evolution of the coercive field (Figure 3.12) as explained with detail in chapter 2. As the temperature increases, the H_C decreases with a slope of –1.12 mT/K. From the extrapolation of this line when $H_C \rightarrow 0$, a value of T_C (MOKE) = 64 ± 2 K was obtained. This is considerably higher than that measured in SQUID (T_C = 23 K)[5,6]. The analysis of DC and AC magnetic measurements with SQUID on films of FeCr with this thickness in the 60-70 K thermal region reveals the lack of any magnetic susceptibility changes that could be related to a magnetic phase transition. This system has been extensively investigated in bulk conditions, but a T_C higher than 27 K has never been reported for this type of material.

In addition, as it was mentioned for films of CrCr and FeCrCr in chapter 3, the correspondence between the critical temperature determined with MOKE and SQUID is complete.

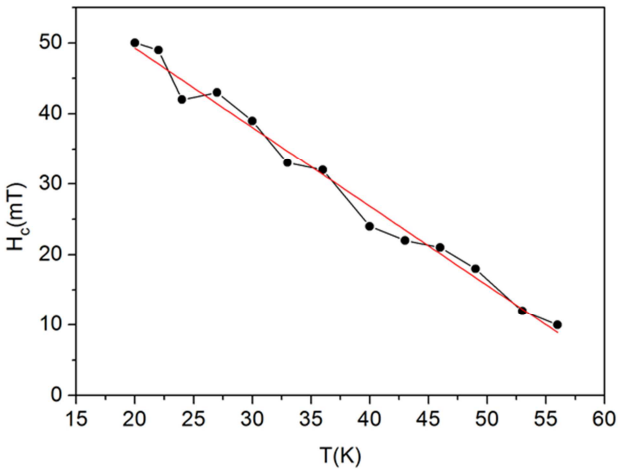

Figure 3.12- Temperature dependence of the coercive field of a thin film of FeCr measured by MOKE magnetometry.

Under this situation, as the MOKE signal is being registered from temperatures well above the ordering one of 23 K, any possible transition observed when going through this critical point is screened by the high temperature signal. Thus, for films of 1450 nm thickness of FeCr it can be observed with MOKE only one ferromagnetic ordering transition located well above the correspondent T_C established with SQUID.

The principles of measurements underlying MOKE and SQUID techniques are quite different: MOKE magnetometry is made by illuminating the sample and detecting the changes in polarization of the reflected light. In contrast, the SQUID characterization is performed in total absence of light. There are many examples in literature concerning the photomagnetic response (i.e., changes in the magnetization of the material under light irradiation) of PBA systems[1]. In addition, as it was described in the introduction of this chapter, a photoinduced effect on the magnetization of electrodeposited films of FeCr has been already described by Ohkoshi and co-workers[6]. Thus, it was necessary to discard the possibility of a light-induced structural change in the films by the MOKE laser. With this aim, a Raman spectroscopy characterization was performed.

3.2.4 Raman study

The Raman spectrum of a thin film of FeCr under red light excitation (λ_{exc} = 647 nm) is shown in figure 3.13. Only one band is observed in the 2000-2200 cm^{-1} frequency region, where the characteristic bands assigned to cyanide stretching vibrations appear. This band is located at 2164 cm^{-1}, in agreement with the IR spectrum.

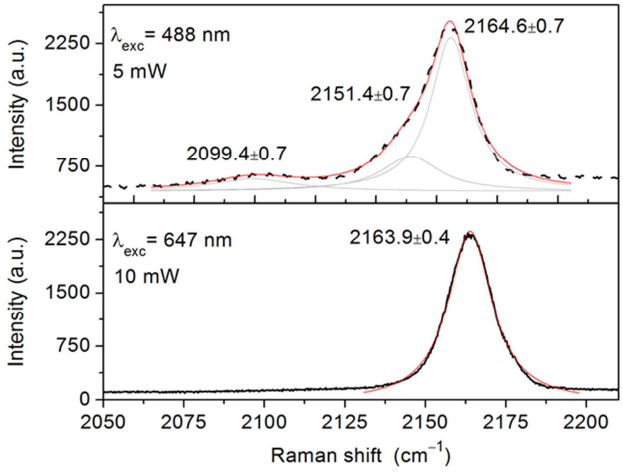

Figure 3.13- Raman spectroscopy measurements of a film of FeCr with a thickness of 1450 nm. Red and grey continuous lines show, respectively, the best-fit of the spectra to a sum of Lorentzian curves and the corresponding deconvolutions.

Under blue light excitation, two extra bands appear centered at 2099.4 cm^{-1} and 2151.4 cm^{-1}. The first new band can be associated to a partial light-induced charge transfer process Cr^{III}–C≡N–Fe^{2+} → Cr^{II}–C≡N–Fe^{3+}. Indeed, the excitation wavelength (λ_{exc} = 488 nm) lies near the maximum of absorption of the intervalence charge transfer band (λ_{exc} = 450 nm). The charge transfer is accompanied by a decrease of the oxidation state of the C-bonded metal ion, leading to a large shift (> 50 cm^{-1}) of the frequency of the C≡N stretching vibration to lower values[5]. The Cr^{II}–C≡N–Fe^{3+} excited state relaxes very fast to a metastable Cr^{III}–C≡N–Fe^{2+} paramagnetic phase[6], as it was explained in the introduction of the chapter, that can be responsible of the band located at

2151.4 cm^{-1}. It is interesting to point out that these states can be assumed as transient states, because in the moment the blue light is again changed to red light the two extra bands disappear.

In any case, these photoinduced effects were produced in blue light and under high power irradiation (laser power density: 100 $W \cdot cm^{-2}$). Under red light, the Raman spectrum of a thin film of FeCr remained unaltered even at laser power densities (50 $W \cdot cm^{-2}$) two orders of magnitude higher than those employed in MOKE measurements (0.4 $W \cdot cm^{-2}$).

From these results, it was possible to discard any photoinduced structural change in the material that would lead to a change in its magnetic properties at the conditions of the MOKE experiment. This prompted us to consider the hypothesis of an exogenous effect originated by traces of a magnetically ordered material that escaped to SQUID detection but could be detected in MOKE magnetometry taking advantage of the surface-sensitive character of this technique.

3.2.5 Identification of surface magnetic impurities in films of FeCr

One hour after completing the electrodeposition process, the resulting electrolyte solution evolved into a colloidal suspension exhibiting Tyndall effect. After 24 h, an orange-brown sediment decanted at the bottom of the electrochemical cell (figure 3.14). The sediment formed was filtered in vacuum through a cellulose nitrate membrane filter. This solid was washed several times with milli-Q water and finally left in vacuum to yield a reddish powder .This sample will be referred from now on as (A).

Figure 3.14- Picture showing the appearance of an orange-brown sediment in the vessel of the electrochemical cell after temporal evolution of the electrolyte. The *right* vessel shows the fresh electrolyte and the *left* vessel the result of 24 hours evolution.

The IR spectrum of (A), shown in figure 3.15, does not exhibit any peak in the frequency range corresponding to the cyanide stretching vibrations.

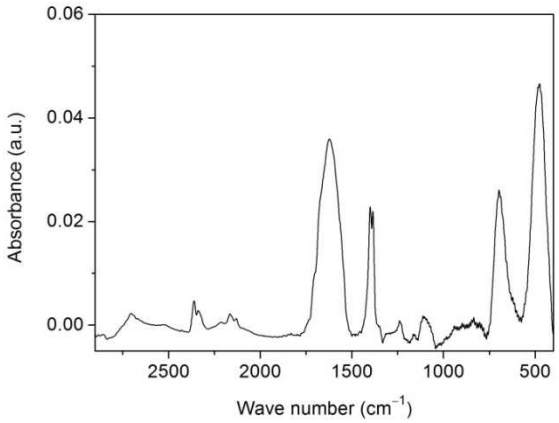

Figure 3.15- IR spectrum of sample (A).

In the low-frequency region, a very broad unresolved band is observed at 473.7 cm^{-1}. This feature has often been ascribed to iron oxide phases[19]. Moreover, EDAX analysis revealed a negligible amount of Cr and N in the material (ratio Fe/Cr = 83.6). These two observations clearly indicated the non-PBA nature of

this solid. Besides, the powder X-ray diffractogram of this sample exhibits a broad band without the presence of any diffraction peak. This is clearly indicating the amorphous nature of this material (Figure 3.16).

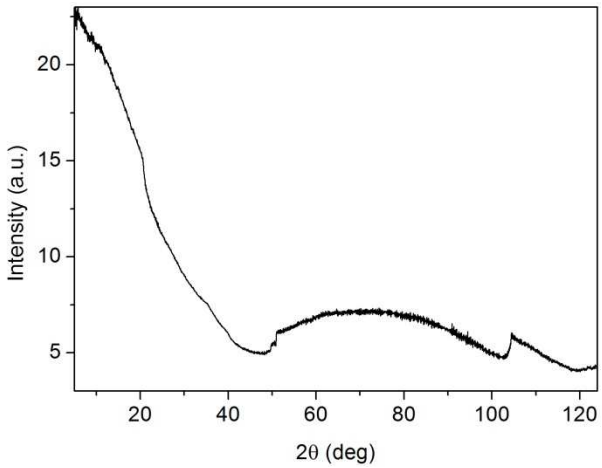

Figure 3.16- XRD pattern of sample (A).

From this characterization we propose that (A) is mainly composed of amorphous iron oxide (Fe_2O_3) or iron oxyhydroxide (FeOOH). The formation of FeOOH resulting from hydrolysis of iron cations in the synthesis of the FeCr PBA system has been reported in a Mössbauer spectroscopy study[20]. At low pH, and independently of concentration and temperature, hydrolysis of $FeCl_3$ yields normally akaganeite (β-FeOOH) instead of the less crystalline ferrihydrite phase[21]. By aging, these phases can transform easily to hematite (α-Fe_2O_3) and this process can be monitored by IR and XRD techniques[22,23]. However, it is known that the presence of complexing ligands can inhibit the formation of crystalline phases[24]. It seems that the $[Cr(CN)_6]^{3-}$ anions play this inhibiting role in the present case and this could explain the lack of crystallinity of the iron oxide sediment. Transmission electron microscopy (TEM) measurements of this iron-containing material reveal the presence of grains of 30-50 nm size (figure 3.17). In general, it is difficult to distinguish from a TEM analysis an amorphous iron oxide material from a collection of aggregates of nanocrystals with very small size. Even the absence of X-ray diffraction peaks or the presence

of broad IR signals cannot be taken as a definitive proof of the amorphous character of the material. Fortunately, the magnetic properties of amorphous and nanocrystalline iron oxide compounds are markedly different[25]. Hematite (a-Fe_2O_3) is a bulk antiferromagnet and the magnetism of a-Fe_2O_3 nanoparticles originates from uncompensated magnetic moments present in the surface, yielding a very low saturated magnetization (M_s = 1-2.5 emu·g^{-1} at 5 K and 10 T). Instead, amorphous iron oxide yields higher M_s values (up to 20 emu·g^{-1} at the same conditions).

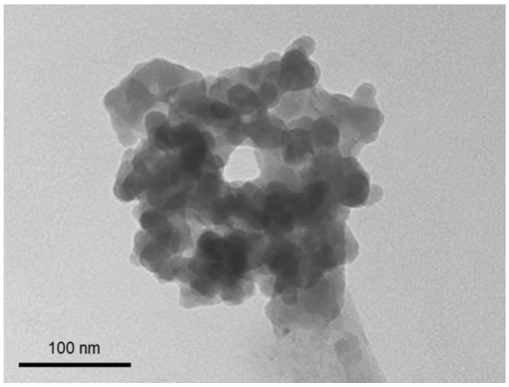

Figure 3.17- TEM image of the solid sediment (A).

DC magnetic characterization was performed on a sample of (A) (figure 3.18). These samples were directly measured in SQUID inside a plastic capsule. Below T_{irr} = 50 K, thermomagnetic irreversibility, namely a difference between the field-cooled (FC) and zero-field-cooled (ZFC) magnetization curves, can be observed. The temperature at which the two curves diverge can be directly associated in a low-field experiment to the blocking temperature of the largest particles in the system.

A maximum in the ZFC curve is seen at T_{max} = 38 K. The small difference between T_{irr} and T_{max} suggests a relatively narrow particle size distribution and/or high degree of interparticle interaction[25]. Similar magnetic behavior has been observed in several amorphous and nanocrystalline iron oxide systems[26] being the clue to distinguish a particular phase, the analysis of the magnetization at saturation.

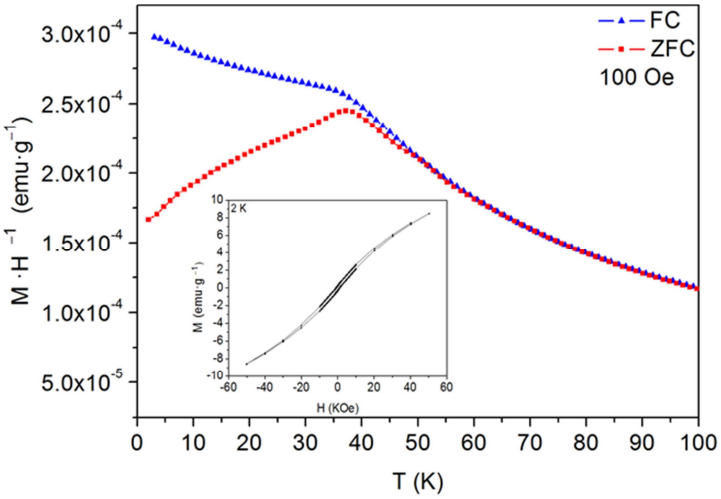

Figure 3.18- Thermal variation of the dc susceptibility ($M{\cdot}H^{-1}$) of (A) in FC and ZFC conditions in an applied field of 100 Oe. *Inset*: Field dependence of the magnetization of (A) at 2 K.

Thus, the field dependence of the magnetization of (A) was measured at 2 K (inset figure 3.18). A hysteretic behavior, with a coercive field of 973 Oe, is detected. The magnetization at the maximum magnetic field of the experiment (5 T) is M_{max} = 8.5 emu·g^{-1}, confirming the amorphous nature of the iron oxide material. A pellet of sample (A) was prepared in order to be characterized by means of MOKE. Nevertheless, the non-reflective nature of the surface of this sample made impossible the magneto-optical characterization of the system.

Once the presence of amorphous iron oxide particles was identified in the chemical environment in which the films of FeCr are grown, it was possible to infer that these particles were also present in the films. Aliquots obtained from the electrolyte solution used in the preparation of the films were analyzed by TEM after 50 min of electrodeposition. The same amorphous structures of variable size were found (figure 3.19), together with cubic nanoparticles of this PBA.

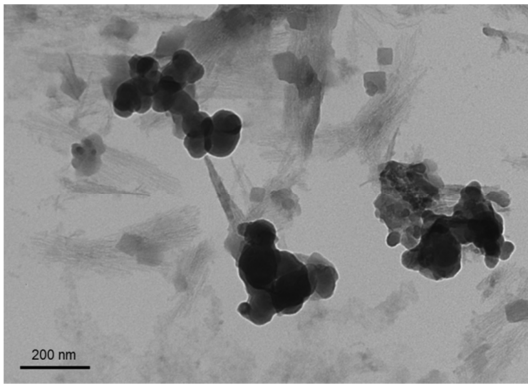

Figure 3.19- TEM micrograph of an aliquot of the electrolyte used in the electrodeposition of a thin film of FeCr.

The proposed scenario in order to explain the anomalous T_C determined by MOKE[14] considers that amorphous iron oxide nanoparticles are produced from the early stages of the electrodeposition process increasing in size and/or aggregation with time. These nanoparticles will precipitate generating the brownish sample (A) when the electrolyte evolves during enough time. In this scenario, the total concentration and size of the iron-based nanoparticles increases with the electrodeposition time (as the film grows). Thus the biggest particles will be present in the films with longer deposition times in which they have reached a proper size and aggregation state. In the electropolymerization process, these nanoparticles might accumulate preferentially near the surface of the film, explaining why the magnetic signal recorded by MOKE in the 60-70 K range is not detected in the SQUID measurements as shown in figure 3.20.

The blocking temperature determined for the solid (A) is different from the T_C (MOKE) values measured for the 1450 nm thickness film of FeCr. This discrepancy could be attributed to the extreme dependence of the magnetic properties of the nanoparticles on factors such as size, shape, orientation and degree of inter-particle interactions[25]. These features can be very different for the nanoparticles embedded in the film with respect to those obtained in the precipitated solid.

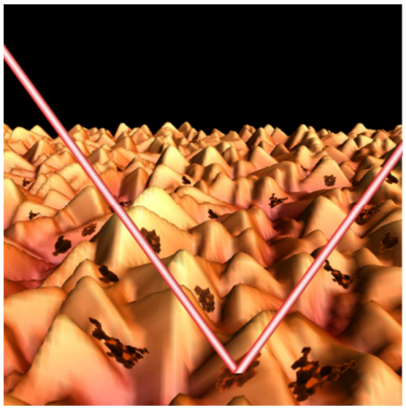

Figure 3.20- Conceptual image of the nanoparticles distribution on the surface of the film of FeCr measured by the laser of the MOKE magnetometer. It is important to remark that the diameter of the laser spot is strictly bigger than the roughness of the film surface. Nevertheless a more simplified view is shown for illustrating the MOKE response.

Taking into account the proposed scenario, films of FeCr with shorter deposition times where prepared and characterized by MOKE. In figure 3.21 it is depicted the MOKE measurements in polar configuration with s-polarized light at 40 K for films of 100 seconds and 20 seconds electrodeposition times corresponding to 300 nm and 135 nm thickness respectively.

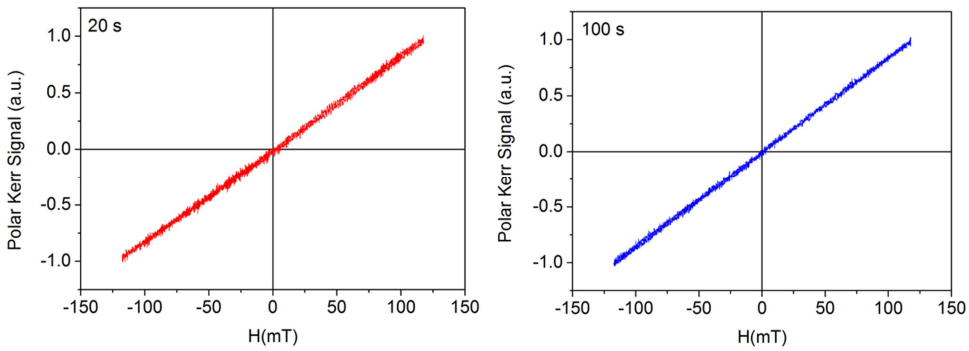

Figure 3.21- MOKE hysteresis loop measured at 40 K for films of FeCr of 20 seconds and 100 seconds electrode time corresponding to a thickness of 125 nm and 300 nm respectively.

As it can be observed from figure 3.21, for shorter electrodeposition times, at 40 K no hysteresis loop with MOKE is registered for these thinner films of FeCr. The only signal detected is the one corresponding to the diamagnetic contribution of the cryostat window. This effect is translated into a straight line with a constant slope. This result supports the idea that at shorter deposition times the electrolyte has not evolve enough to let the appearance of the iron-based nanoparticles. Thus, these nanoparticles are no longer accumulated in the surface of the films ruling out the possibility for being detected with MOKE. These films of 135 nm and 300 nm thickness can be considered exempt from the presence of iron-based nanoparticles. In order to detect the proper magneto-optical signal of these thinner films of FeCr the temperature in the MOKE cryostat was decreased down to the minimum accessible of 10 K. Nevertheless, no hysteretic signal was registered for any of the films as the S/N ratio was too low. This could be understood by the fact that at 10 K the system is still close to its T_C. In consequence, the ferromagnetic ordering achieved in these films of 135 nm and 300 nm thicknesses is not sufficient to generate a detectable magneto-optical signal which can be in turn translated into a MOKE hysteresis loop. It would be necessary to reach lower temperatures in the cryostat in order to check this point, situation which is limited at this stage for the set-up characteristics.

In a previous work[20], it has been shown that the FeOOH impurities present in solid iron(II) hexacyanochromate(III) can be removed by treatment with ozone. We have thus submitted our films to an ozonization experiment in order to confirm that the presence of such an impurity is responsible of the MOKE hysteretic signal observed at temperatures higher than T_C. Films of 1450 nm thickness of FeCr were immersed in Milli-Q water and ozone was bubbled during 1 h through the solution using a Fischer Ozon generator. The EDAX analysis of this sample provided a Fe/Cr ratio of 1.29.

After 1 hour ozonization, the films containing cyanide-bridged Cr^{III}–CN–Fe^{2+} units were completely oxidized to Cr^{III}–CN–Fe^{3+} and this is translated into a shift of the cyanide stretching vibration frequency (Figure 3.22) to higher values.

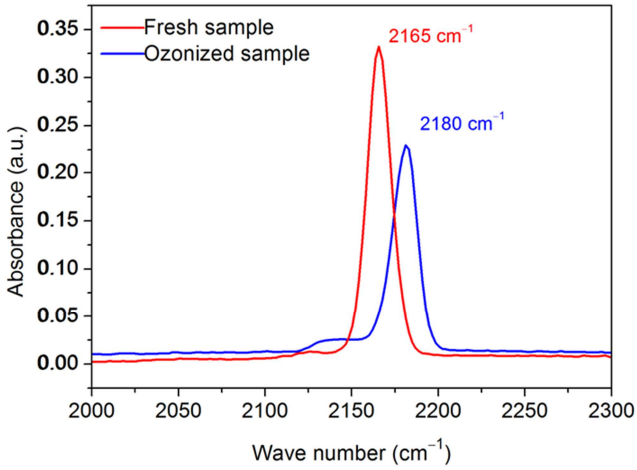

Figure 3.22- IR spectrum of a film of FeCr before (red) and after (blue) ozone treatment during 1 h.

The dc magnetic characterization of the ozonized films FeCr showed an ordering temperature of 20 K (Figure 3.23).

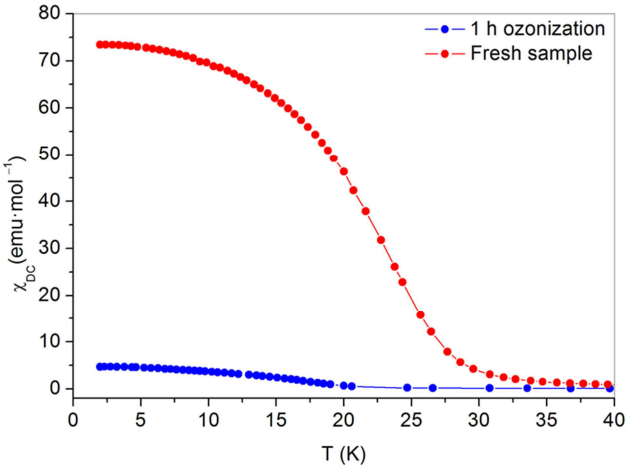

Figure 3.23- DC magnetic measurements of thin films of FeCr before (red circles) and after (blue circles) 1 hour ozone treatment.

Interestingly, no hysteretic signals were observed in MOKE magnetometry above this critical temperature. Figure 3.24 shows a MOKE hysteresis loop at 10K of the fully oxidized film of 1450 nm thickness of FeCr after the ozonization

process. The signal to noise ratio of the measurement was extremely low in this treated material. The high squareness of the plot is in contrast with the S-shaped MOKE hysteresis loop obtained for the pristine film of FeCr shown in figure 3.24. That S-shaped hysteresis loop closely resembles that obtained for sample FeCr using SQUID magnetometry and could originate from the presence of uncompensated magnetic moments in the amorphous iron oxide sediment. It seems then that the amorphous iron oxide impurities were removed after ozone treatment. Ozone produces an oxidation of the Fe^{2+}–OH_2 moieties in the Prussian blue structure to Fe^{3+}–OH, releasing protons that may contribute to the oxide dissolution.

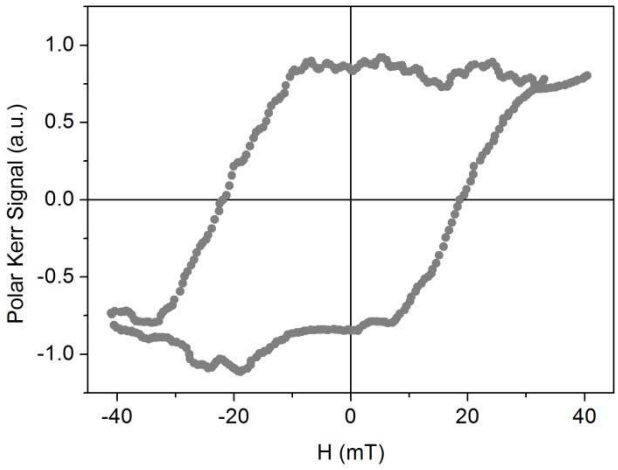

Figure 3.24- MOKE hysteresis loop of a film of FeCr after 1 h ozone treatment. The measurement was performed at 10 K in polar configuration.

3.3 Conclusions

In this chapter a complete characterization of the properties of electrodeposited thin films of $Fe_3[Cr(CN)_6]_2 \cdot 15\ H_2O$ has been performed. As part of this systematic study, MOKE magnetometry was employed in order to elucidate the magnetic properties on surface of this molecular-based ferromagnetic material based on the potential of this technique as previously described in chapter 2.

The anomaly in the T_C determined by MOKE (T_C=60-70K) considerably higher than the one established by SQUID (T_C =20 K) has been explained by the

presence of an amorphous iron oxide phase. This phase appears in the electrolyte environment and it is included in the structure of the PBA during the electrodeposition process.

The Raman study performed on films of FeCr allowed us to discard any photomagnetic effect on the material during MOKE measurements as responsible of this increase in the ordering temperature. This information lead us to consider an exogenous effect arising from the presence of an extra magnetic phase which escaped from the SQUID detection but could be detected by MOKE magnetometry based on the surface characteristics of this technique. By observation of the evolution of the electrolyte solution it was possible to detect the appearance of a precipitate that could be isolated and characterized, magnetically and morphologically, identifying it as an amorphous iron oxide phase. From the analysis of aliquots of the electrolyte solution, by means of TEM,the same type of amorphous structures could be also detected. With this information it was possible to conclude that in the chemical environment in which the electropolymerization of the films takes place, iron-based structures are spontaneously formed. These impurities are included in the structure of the PBA as the electrodeposition process occurs,being accumulated preferentially in the surface of the film, reason why the magnetic signal of this phase is only detected by means of MOKE.

The magneto-optical signal arising from this iron-based phase has been only detected on films prepared during long deposition times, in this case 1000 seconds. For shorter deposition times the lack of detection of these impurities leads us to proposed a scenario in which it is needed a sufficient time of evolution of the electrolytic solution in order to allow the formation and aggregation of these iron oxide nanoparticles which, at the end, will be accumulated at the surface of the film.

This information is important to be taken into account when electrodeposited films of FeCr are prepared, under the synthesis conditions explained in this chapter. Based on the studies developed in chapter 2 for films of $Cr_{5.5}(CN)_{12} \cdot 11.5\ H_2O$, short deposition times and, in consequence, thinner films lead to major quality properties of these systems for being used as elements into

spintronic structures. In this short deposition times the absence of this extra phase can be considered.

The most remarkable result of this study relies on the better sensitivity of MOKE to detect this surface magnetic impurity present in the electropolymerised films with respect to classical bulk magnetic techniques. It has been proved again that MOKE can be used as a powerful complementary technique to SQUID magnetometry in the study of the chemical environment and magnetic properties of PBA films as promising candidates into the molecular spintronics field.

As a future work on this material it is proposed the possibility of changing the electrolyte characteristics in order to avoid the appearance of this iron oxide phase during the electrodeposition process. As it was mentioned in the synthesis section, the pH of the electrolyte was determined to be 2.2. It is already an acid environment but probably by decreasing the pH of the electrolyte the growth of this iron-based nanoparticles can be controlled based on the fact that as more basic the medium the better the conditions for the appearance of oxide phases. In addition, it would be interesting to characterize by MOKE films of FeCr with short deposition times where the presence of the iron oxide phase is avoided. This would allow to measure the intrinsic magneto-optical properties of the pristine material. For this aim, it will be necessary to perform the measurements in a cryostat that allows decreasing the temperature close to 2 K well below the ordering temperature of this ferromagnetic material for having a proper signal to noise ratio in the MOKE measurements.

3.4 Bibliography

(1) Sato, O.; Iyoda, T.; Fujishima, A.; Hashimoto, K. *Science (80-.).* **1996**, *272*, 704.

(2) Shimamoto, N.; Ohkoshi, S.; Sato, O.; Hashimoto, K. *Inorg. Chem.* **2002**, *41*, 678.

(3) Escax, V.; Bleuzen, a; Cartier Dit Moulin, C.; Villiam, F.; Goujon, a; Varret, F.; Verdaguer, M. *J. Am. Chem. Soc.* **2001**, *123*, 12536.

(4) Coronado, E.; Giménez-López, M. C.; Levchenko, G.; Romero, F. M.; García-Baonza, V.; Milner, A.; Paz-Pasternak, M. *J. Am. Chem. Soc.* **2005**, *127*, 4580.

(5) Coronado, E.; Giménez-López, M. C.; Korzeniak, T.; Levchenko, G.; Romero, F. M.; Segura, A.; García-Baonza, V.; Cezar, J. C.; de Groot, F. M. F.; Milner, A.; Paz-Pasternak, M. *J. Am. Chem. Soc.* **2008**, *130*, 15519.

(6) Ohkoshi, S.; Einaga, Y.; Fujishima, A.; Hashimoto, K. *J. Electroanal. Chem.* **1999**, *473*, 245.

(7) Coronado, E.; Makarewicz, M.; Prieto-Ruiz, J. P.; Prima-García, H.; Romero, F. M. *Adv. Mater.* **2011**, *23*, 4323.

(8) Prima-Garcia, H.; Coronado, E.; Prieto-Ruiz, J. P.; Romero, F. M. *Nanoscale Res. Lett.* **2012**, *7*, 232.

(9) Qiu, Z. Q.; Bader, S. D. *Rev. Sci. Instrum.* **2000**, *71*, 1243.

(10) Bader, S. D. *J. Magn. Magn. Mater.* **1991**, *100*, 440.

(11) Grimsditch, M.; Hoffmann, a.; Vavassori, P.; Shi, H.; Lederman, D. *Phys. Rev. Lett.* **2003**, *90*, 257201.

(12) Park, Y.; Shin, S. *J. Korean Phys. Soc.* **2008**, *53*, 2518.

(13) Y.H. Lu, M.H. Cho, J.B. Kim, M.S. Seo, G.J. Lee, Y. P. L. *J. Korean Phys. Soc.* **2008**, *53*, 2442.

(14) Coronado, E.; Fitta, M.; Prieto-Ruiz, J. P.; Prima-García, H.; Romero, F. M.; Cros, A. *J. Mater. Chem. C* **2013**, *1*, 6981.

(15) Butler, M. a. *J. Appl. Phys.* **1977**, *48*, 1914.

(16) Zhang, X.; Ai, Z.; Jia, F.; Zhang, L. *J. Phys. Chem. C* **2008**, *112*, 747.

(17) Xiao, X.; Liu, C.; Hu, R.; Zuo, X.; Nan, J.; Li, L.; Wang, L. *J. Mater. Chem.* **2012**, *22*, 22840.

(18) Nakanishi, S.; Lu, G.; Kothari, H. M.; Bohannan, E. W.; Switzer, J. a. *J. Am. Chem. Soc.* **2003**, *125*, 14998.

(19) Liu, H.; Li, P.; Zhu, M.; Wei, Y.; Sun, Y. *J. Solid State Chem.* **2007**, *180*, 2121.

(20) Reguera, E.; Bertran, J. F.; Nunez, L.; Blue, P. *Polyhedron* **1994**, *13*, 1619.

(21) R.J. Atkinson, A. M. Psoner, J. P. Q. *Clays Clay Miner.* **1977**, *25*, 49.

(22) Lu, B.; Guo, H.; Li, P.; Liu, H.; Wei, Y.; Hou, D. *J. Solid State Chem.* **2011**, *184*, 2139.

(23) S. Kan, S. Yu, X. Peng, X. Zhang, D. Li, L. Xiao, G. Zou, T. L. *J. Colloid Interface Sci.* **1996**, *178*, 673.

(24) Jolivet, J.-P.; Tronc, E.; Chanéac, C. *Comptes Rendus Geosci.* **2006**, *338*, 488.

(25) Machala, L.; Zboril, R.; Gedanken, A. *J. Phys. Chem. B* **2007**, *111*, 4003.

(26) Mukadam, M. D.; Yusuf, S. M.; Sharma, P.; Kulshreshtha, S. K. *J. Magn. Magn. Mater.* **2004**, *269*, 317.

Chapter 4

Fabrication and physical characterization of a PBA bilayer system exhibiting magnetic exchange coupling

4.1 Introduction

One of the final goals in the field of molecular spintronics is the fabrication of structures such as spin valves composed solely of molecular-based materials. The obtaining of these all-molecular systems is a clear motivation for studying the effects arising from the inclusion of PBA's in heterostructures with novel properties.

In this line of work, the most remarkable study reported so far was published by D.R. Talham and et al.[1,2] in which heterostructured thin films consisting of distinct layers of the PBA's $Rb_aCo_b[Fe(CN)_6]_c \cdot mH_2O$ (CoFe PBA) and $Rb_jM_k[Cr(CN)_6]_l \cdot nH_2O$ (MCr PBA, where M= Ni or Co) were fabricated for studying their photomagnetic properties. Films of CoFe PBA have been demonstrated to exhibit photomagnetic properties, displaying light-induced changes in the unit cell size and spin states below temperatures of 150 K and magnetic ordering below 20 K[3–7]. The inclusion of the NiCr and CoCr in these structures, despite not presenting a photomagnetic response, was motivated by their higher ordering temperatures of 70 K and 30 K respectively, as well as for their pressure induced responses. By combining these materials in the heterostructured films they could observe a novel photoinduced magnetism arising from the interactions between layers. The observed photo-effect was manifested as a photoinduced modification of the long-range magnetic order, at temperatures much higher than those reported for the photoactive CoFe isolated compound. This phenomenon has been explained in terms of a photoinduced structural distortion in the CoFe PBA lattice, which induces a random magnetic anisotropy in the MCr PBA component. This effect is a result of the intimate coupling of the two lattices in the heterostructure.

Another example of interaction in a structure composed by a PBA and a spin crossover compound was recently reported also by Talham *et al.*[8]. In this case, a coordination polymer thin film of the PBA $Ni^{II}_b[Cr^{III}(CN)_6]_{0.7}$ was combined with the 3D Hofmann-like spin crossover compound $Fe(azpy)[Pt\text{-}(CN)_4]\cdot xH_2O$ in order to get a heterostructure with novel photomagnetic properties. A decrease on magnetization response of the PBA (T_C = 70 K) upon induction of the LIESST

effect in the Fe^{II} paramagnetic center was detected. This interplay of effects arises, just as in the previous example, from the coupling between the two structurally different materials in the combined system.

By considering the previous works in literature, the study of combined molecular-based materials systems is demonstrated to be of great interest. This situation could induce novel properties and phenomena arising from the coupling between the materials. Taking this into account, we have synthesized by an electrochemical approach, PBA bilayers. The magnetic properties resulting from the coupling between both molecular-based layers in direct contact will be extensively described. The analysis of the magnetic behavior of these two PBA's in intimate contact has allowed us to develop phenomenological scenario regarding the magnetization reversal processes at the interface between both molecular-based materials.

For understanding the physical phenomenology observed in these PBA heterostructures, it is important to remember some basic concepts related to the exchange coupling between magnetic layers.

4.1.1 Exchange Bias

When materials with ferromagnetic (FM)-antiferromagnetic (AF) interfaces are cooled below the Néel temperature (T_N) of the antiferromagnet (with the Curie temperature, T_C, of the FM larger than T_N), an anisotropy ("exchange bias") is induced in the FM[9–15]. In general, the interface coupling between the materials, originated from the exchange anisotropy, is observed when cooling the AF-FM couple in the presence of a static magnetic field from a temperature above T_N, but below T_C to temperatures $T<T_N$. The exchange bias is manifested in the FM material by a shifting of the hysteresis loop, named as exchange field H_E, and an increase in the coercivity H_C. This phenomenon can be understood by means of an intuitive picture of the interaction between both materials (figure 4.1).

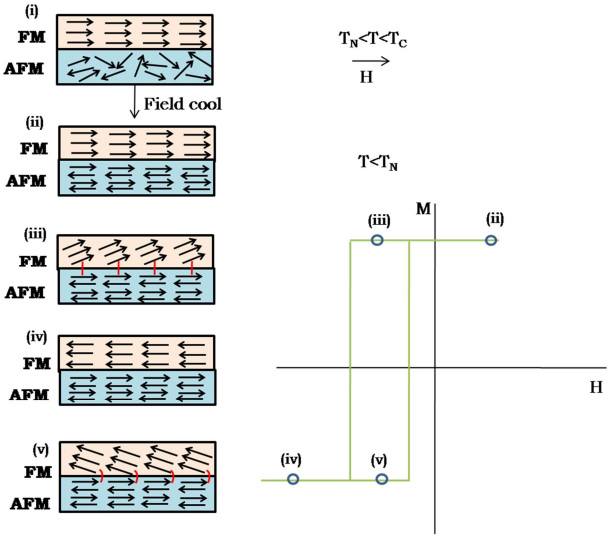

Figure 4.1- Schematic representation of the exchange bias process between a FM and an AF layer.

When a field is applied in the temperature range $T_N<T<T_C$, the FM spins line up with the field, while the AF spins remain random (Fig. 4.1-i). When cooling to $T<T_N$, in the presence of the field, the AF spins next to the FM align ferromagnetically to those of the FM (assuming ferromagnetic interaction) due to the interaction at the interface. The other spin planes in the AF "follow" the AF order to produce a zero net magnetization (figure 4.1-ii). When the field is reversed, the FM spins start to rotate. However, for sufficiently large AF anisotropy, the AF spins remain unchanged (figure 4.1-iii). Therefore, the interfacial interaction between the FM-AF spins, tries to align ferromagnetically the FM spins with the AF spins. In other words, the AF spins at the interface exert a microscopic torque on the FM ones, to keep them in their original position (ferromagnetically aligned at the interface) (figure 4.1-iii). Therefore, the FM spins have one single stable configuration, *i.e.,* the anisotropy is *unidirectional*. Thus, the field needed to reverse completely a FM layer will be larger if it is in contact with an AF, because an extra field is needed to overcome the microscopic torque. However, once the field is rotated back to its original

direction, the FM spins will start to rotate at a smaller field, due to the interaction with the AF spins (which now exert a torque in the same direction as the field) (4.1-v). The material behaves as if there was an extra (internal) biasing field, inducing a shifting in FM hysteresis loop along field axis, i.e. *exchange bias.*

The most general situation is that in which this exchange bias can be found in a FM and an AF in direct contact. Nevertheless, also ferrimagnetic materials can used to study this phenomenon. This produces structures of the type FM-ferri[16], ferri-AF[17], and even ferri-ferri[18]. Due to their magnetic structure, ferrimagnets can play either the role of the AF or FM in bilayer systems. In consequence, an extra complexity for the theoretical understanding appears in the bilayers containing ferrimagnetic materials[19].

4.1.2 Exchange-spring magnets

Classical exchange-spring magnets (ESM) are composed of a two-phase distribution of hard- and soft- magnetic grains that have potential applications as permanent magnets[20]. From a theoretical point of view, composite magnets made from exchange-coupled soft/hard phases are difficult to understand. In contrast, exchange-coupled soft/hard bilayers or multilayers permit the development of ideal modelling systems for understanding the properties of these ESMs. The control over structural or magnetic parameters, such as the thickness of the layers or the interfacial exchange coupling strength, allows a more accurate study of the exchange-spring processes taking place in the system[21].

The switching of the magnetization in a soft-magnet film coupled ferromagnetically to a hard magnetic layer was initially studied in the 1960s by Goto and coworkers[22]. Assuming a scenario in which a hard layer is perfectly rigid with absence of anisotropy in the soft layer (K_s = 0), they solved the magnetization reversal process of the soft layer under an applied field opposite to the magnetization of the hard phase. They could determine that the soft layer remains parallel to the hard layer when the applied fields is smaller than the nucleation field given by

$$H_N = (\pi^2 A_s)/(2M_s\, t_s^2) \qquad \text{(eq. 4.1)}$$

with A_s, M_s and t_s the exchange constant, magnetization and thickness of the soft layer respectively.

The magnetization reversal process in the soft layer takes place as a twisting of the magnetization when the external magnetic field exceeds the nucleation value H_N. This occurs because the soft layer is strongly pinned at the interface with the hard phase. On the contrary, the center of the soft layer is free and follows the external magnetic field. A conceptual view of this phenomenon is shown on figure 4.2.

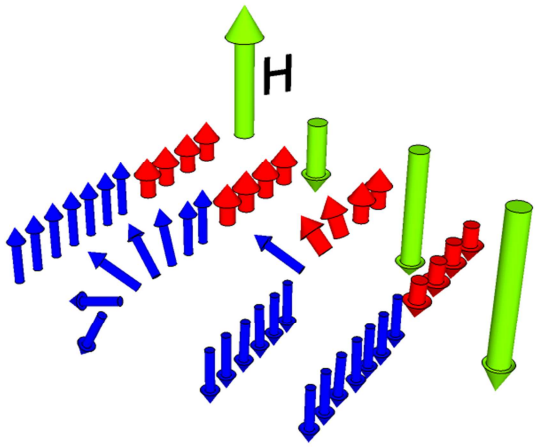

Figure 4.2- Intuitive picture of the reversal process in an ESM. The soft- and hard-magnetic phases are represented by the blue and red arrows, respectively. The external magnetic field is represented by the green arrow. For $H>H_N$ the magnetization reversal process in the soft layer resembles the one taking place on a Bloch wall with an increase in the angle of rotation when going away from the interface. Finally, when the magnetic field is high enough both magnetic phases are completed reversed.

For external magnetic fields $H>H_N$, the spins in the soft layer exhibit a continuous rotation, as in a Bloch wall, with the angle of rotation increasing with the distance to the interface with the hard magnetic layer[23,24]. In the ideal case, this type of magnets exhibit reversible demagnetization curves since the

soft layers rotate back into alignment with the hard phase if the reverse field is removed. This reversing process is often referred to as an exchange-spring process by analogy with the elastic motion of a mechanical spring.

In the ESMs, much of the physics and reversal mechanisms are similar to that observed in exchange biasing systems. In this case, the hard magnetic phase plays the role of the AF layer in the biasing system. Thus, the minor loops obtained in the soft magnetic layers usually resemble exchange-biased loops.

In the present chapter, it is going to be described the complete study performed on a PBA bilayer. By growing films of these molecular-based magnetic materials in the nanometer level with electrochemical methods, it has been possible to observe for the first time a magnetic exchange coupling between both layers. From our knowledge, there is no study reported so far demonstrating such magnetic exchange-coupling phenomena in PBA's bilayers.

4.2 Results and discussion

4.2.1 Fabrication of the bilayer structure

For the fabrication of the PBA bilayer in direct contact, a sequential electrodeposition approach was employed, as depicted schematically in figure 4.3. The bilayer is formed by a first layer of $Cr_{5.5}(CN)_{12} \cdot 11.5\ H_2O$ [25–29] electrodeposited onto a gold substrate. These chromium cyanide thin films suffer a complete oxidation process under air exposure as demonstrated from the characterization in chapter 2, being this material referred as CrCr. Subsequently a film of $Fe_3[Cr(CN)_6]_2 \cdot 15\ H_2O$ [30,31], already described in chapter 3 and named as FeCr, is electropolymerized in direct contact on top of the first layer.. The synthetic procedure in each single step is exactly the same as the one explained previously for the separate films in chapters 2 and 3[25,26,30].

The choice of the order employed for the sequential electrodeposition has been based on the relative value of the hexacyanometallate reduction potentials. As the CrCr layer is electropolymerized with a V=-0.88 V, it guarantees that the

FeCr film synthesized at V=-0.5 V is not producing any chemical change on the first layer.

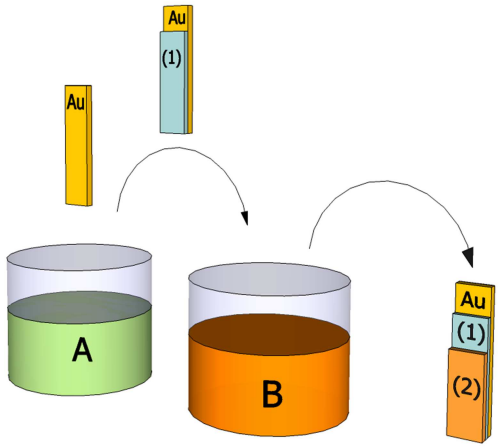

Figure 4.3- Scheme of the sequential electrodeposition method for growing the PBA bilayer system. The Au working electrode is introduced in electrolyte A. The first electrodeposition generates the film of CrCr. Subsequently the first film is transferred to electrolyte B where the second layer of FeCr is electropolymerized in direct contact to produce the final bilayer.

This was confirmed by making the cyclic voltammetry (CV) of a film of 175 nm thickness of CrCr. With this aim the film was electrodeposited in the electrolyte A as depicted in figure 4.3 and subsequently transferred to a blank solution of 0.2 M KCl. In this solution a CV study of this CrCr film was performed at a scan rate of 20 mV/s (figure 4.4). From the CV curve it was possible to observe a quasi-reversible reduction wave scan centered at approximately -0.85 V vs Ag/AgCl, corresponding to the reduction of the Cr anion[29]. Thus, the electroactive region (A) of this of CrCr is located outside the potential window (B) at which the electrodeposition of the FeCr layer is performed (V=-0.5 V), as illustrated in figure 4.4. Thus, by applying the fabrication method mentioned before, the chemical identity of each layer is preserved.

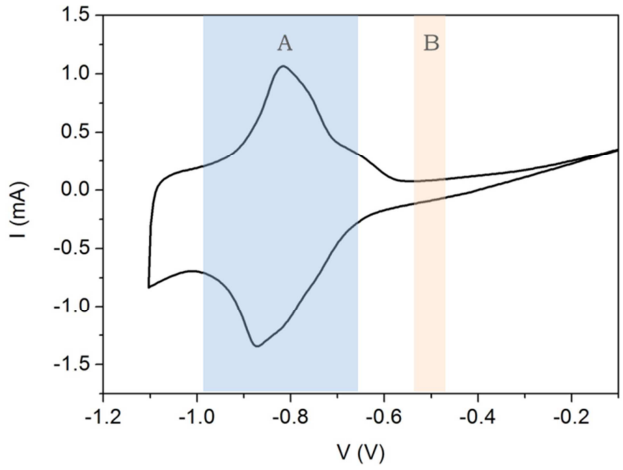

Figure 4.4- Cyclic voltammogram of a 175 nm thickness film of CrCr performed in a blank solution of 0.2 M of KCl at 20mV/s. In blue (A) is indicated the electroactive region of the CrCr film and in red (B) the area corresponding to the window of voltage applied for the electrodeposition of FeCr.

For both the CrCr and FeCr films composing the bilayer, a 20 second electrodeposition time was chosen for the synthesis with the aim of obtaining a proper thickness with sufficient magnetic signal guaranteeing an accurate characterization. As it was explained in chapter 3, long electrodeposition times in the synthesis of FeCr films lead to the appearance of impurities composed by iron oxide particles. These impurities are formed spontaneously in the chemical environment of the electrolyte. For a short electrodeposition time of 20 seconds it has been demonstrated the absence of these impurities in the electropolymerized films by MOKE studies (for more details go to chapter 3). Thus, this consideration has been also taken into account for designing the synthesis conditions of the FeCr films forming part of the bilayer under study.

4.2.2 IR spectroscopy

In figure 4.5 it is depicted the ATR-IR spectrum of a representative PBA bilayer system in direct contact. From this measurement it is possible to identify the presence of the CrCr with a band located at 2186 cm^{-1} corresponding to the cyanide stretching vibration of the $[Cr^{III}(CN)_6]^{3-}$ anion[25]. The presence of the

FeCr electrode directly electrodeposited on top is detected by a shoulder located at 2165 cm^{-1} corresponding to the cyanide stretching vibration of $Cr^{III}–C≡N–Fe^{2+}$ moieties[30].

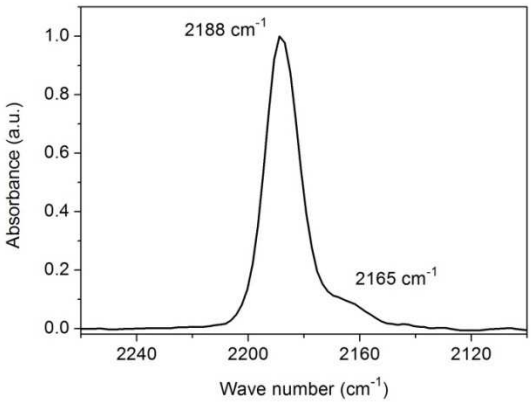

Figure 4.5- ATR-IR spectrum of the bilayer in direct contact showing the presence of the two PBA layers.

4.2.3 Morphological characterization

A morphological characterization by means of atomic force microscopy (AFM) was performed in order to determine the surface features of the films as a result of the growing process. The 3D topography images of 25 μm^2 scan size, obtained in tapping mode for each layer composing the bilayer, are shown in figure 4.6. The deposition of the first layer of CrCr on the gold electrode after 20 seconds leads to the typical surface morphology previously reported for this kind of PBA[25,26] . Pyramidal grains with an average grain size of 180 nm and a surface roughness exhibiting an RMS value of 17 nm are observed. This morphology already described in chapter 2 and 3 can be related to the epitaxial growing of this electrodeposited PBA on the gold electrode[32]. As previously explained, the electroplymerization dynamics of this molecular-based film consists of a fast initial growing on the gold electrode (nucleation process) with a decrease of the electropolymerization rate as the substrate is covered.

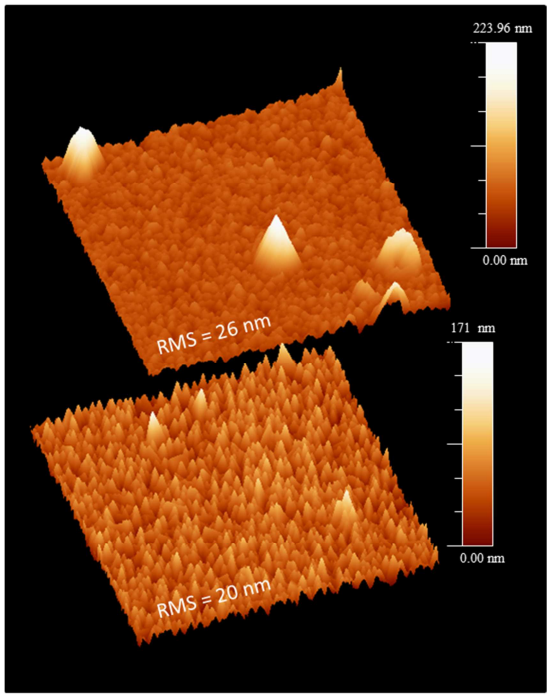

Figure 4.6- AFM 3D topography image 5x5 μm^2. *Bottom*: CrCr 20 seconds electrodeposition time. *Top*: Final bilayer after depositing a 20 seconds FeCr layer.

Then, a crystallization process takes place leading to the formation of bigger grains as the time of deposition is increased[25,26]. When depositing the second layer of FeCr during 20 seconds on top of CrCr, a film with a grain structure in surface can be also observed, exhibiting an RMS roughness of 26 nm and an average grain size of 190 nm. Isolated grains with sizes ranging between 500-600 nm appear in the top layer of FeCr which could be defined as growing defects. In this case, the surface features of the FeCr layer are strongly influenced by the direct deposition onto of the CrCr film, which presents a lower conductivity than the working naked Au electrode. Thus, the initial growing rate is slower, having this situation an impact on parameters of the film such as roughness, average grain size and final thickness. From this morphological characterization, the most important information is the CrCr surface morphology onto which the second film is electrodeposited in direct contact. This bottom layer will define at the end the quality of the interface generated

between both materials. The description of the characteristics and quality of the generated interface is fundamental in order to assess a better understanding of the resulting magnetic coupling between both molecular-based magnetic materials.

For determining the features of the interface between the two PBAs, the morphological analysis of the system was completed by a TEM-STEM characterization performed at the Advanced Microscopy Laboratory-INA. From this study it was also possible to extract a value of thickness for each layer. Having information about any possible interpenetration of the top FeCr on the bottom CrCr film is necessary for understanding the properties of the final bilayer. As the elements composing the two layers (Fe and Cr) have a very similar atomic number, Z, a determination of the interface by direct contrast from TEM images could not be achieved. Nevertheless, the TEM characterization was useful for determining the thickness of each layer in the composed structure. Combining TEM information with the profilometry, the thickness of each layer could be determined.

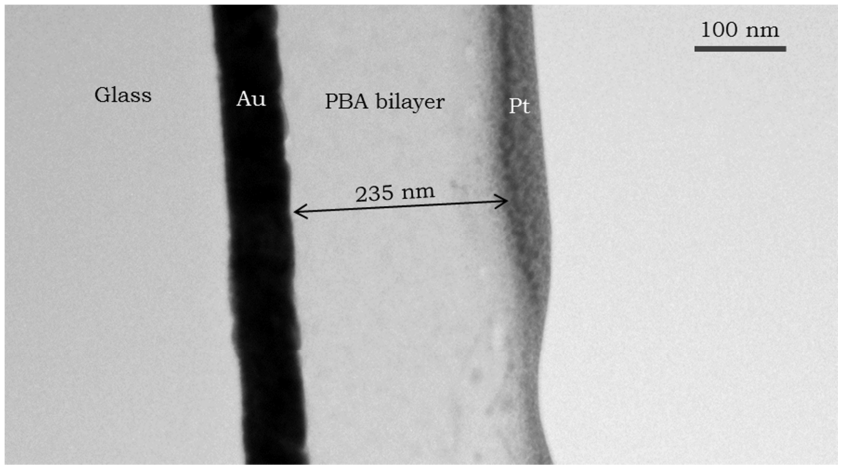

Figure 4.7- TEM image of the lamella of the PBA bilayer in direct contact.

The bilayer structure was submitted to a reduction process by ion milling for obtaining a final ultra-thin cross section of the sample (lamella). This process was performed at low temperatures for preserving the structure of each layer

under the ion attack. In figure 4.7, a representative image of a lamella of the TEM study is shown. It is possible to distinguish the PBA bilayer sandwiched between the bottom Au electrode and the Pt layer which is evaporated on top of the system as part of the lamella. The bilayer for this study was prepared on a glass substrate covered with gold, instead of Mylar, establishing more appropriate conditions for the fabrication of the lamella.

No contrast between both layers of PBA was achieved by means of the TEM image. Nevertheless, a total thickness of 235 nm can be determined. On the other hand, CrCr films of 20 seconds electrodeposition time were prepared and studied with profilometry determining an average thickness of 175 nm. In addition, on top of the first PBA film, another layer of 20 seconds of FeCr was electropolymerized for the study of the final bilayer also with profilometry. By substracting from the total thickness the one corresponding to the CrCr film, a thickness of approximately 50 nm is obtained for the top FeCr layer. This estimation is supported by the TEM image in which also by substracting the 175 nm CrCr layer to the overall thickness of 235 nm for the bilayer, a thickness of approximately 60 nm is obtained for the FeCr. The small discrepancy between both techniques is in the same order of the experimental error for the profilometry measurement. In isolated FeCr films, obtained with 20 seconds electrodeposition time directly onto the Au working electrode, a thickness of 135 nm was determined by profilometry. By calibrating the electrodeposition times it was detected that a thickness of 50-60 nm can be achieved for the FeCr layer with 5 seconds of experiment time. This is a clear indication that the growing process of the top PBA film is limited by the higher resistance of the working electrode after the deposition of the bottom CrCr PBA. As a consequence, a lower thickness is observed in the FeCr film in the bilayer when compared to the direct deposition onto gold.

For overcoming the absence of contrast between both layers in TEM images, an STEM study was performed on the system obtaining a chemical profile of the materials. In this way, a selective view of the region regarding to each element was obtained. In this PBA bilayer, Fe is only present on the top electrode. Thus, this element was employed for determining the point at which the interface between both materials is located. Figure 4.8 shows a representative chemical

profile of the big set of measurements obtained by STEM on the bilayer. The orange curve represents the signal of the K-line of Fe and the blue one is related to the K-line of Cr. In this graph, the position X=0 nm is referred to the point immediately below the Pt layer evaporated for preparing the lamella. It can be clearly observed that the presence of Fe, and in consequence the FeCr layer, is extended in a region of approximately 60 nm from the top Pt. This value is completely in agreement with the thickness obtained by profilometry and TEM. Immediately after this high Fe counts zone, it is detected a region of around 10 nm in which the content of Fe decreases progressively. This region has been associated to the interface between both materials. Below this point, by moving to a deeper region of the bilayer no content of Fe is found, indicating exclusively the presence of the bottom CrCr layer.

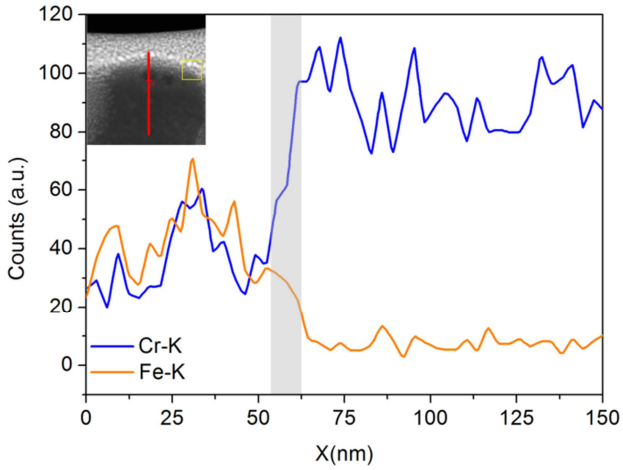

Figure 4.8- STEM profile of the bilayer in direct contact measuring the Fe content (orange curve) and Cr content (blue curve) in the system. The grey region indicates the interface between the two PBA layers.

The presence of a clear interface between the two PBA layers has been demonstrated by the STEM measurement, establishing a value of 10 nm to this particular region. This interface would be directly influenced by the surface morphology of the CrCr film. As it was previously described from AFM measurements, an RMS roughness of 17 nm was established for the surface of

this layer. This value is in the same order than the extension of the region associated to the interface, as determined by STEM (figure 4.9).

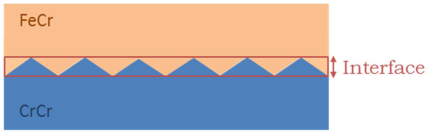

Figure 4.9- Schematic representation of the influence of the CrCr surface roughness on defining the interface region with FeCr.

With all this information, the scenario of an interpenetration of the top FeCr PBA into the bottom CrCr layer can be ruled out. In fact, a clear and defined interface between the both molecular-based materials composing the bilayer has been experimentally determined.

Finally, with the aim of having an alternative estimation of the thickness ratio between both PBA composing the bilayer, a chemical study by inductively couple plasma mass spectrometry (ICP-MS) was performed. A bilayer in direct contact was prepared, as previously described, on a gold evaporated Mylar substrate. Subsequently it was digested in a solution containing HNO_3 and HCl for its analysis. From the ICP analysis it is determined a proportion of 1536.3 mg/Kg of ^{52}Cr and 300.2 mg/Kg of ^{56}Fe. According to the stoichiometry of the compounds, by relating the content of Cr in each layer, a ratio of 3 times more CrCr than FeCr in the bilayer has been determined. Since the density of the two layers is about the same, this mass ratio can be translated into a volume ratio CrCr/FeCr=3, which leads to a thickness of approximately 60 nm for the FeCr PBA film. This value matches the one expected from profilometry and STEM analyses. The agreement indicates a homogeneous covering of the two layers onto the electrode. In this way, from a wide variety of characterization techniques it has been possible to establish thicknesses of 175 nm for the CrCr layer and 60 nm for the FeCr PBA. In both cases this thicknesses are related to 20 second electrodeposition time for the synthesis of each film in the PBA bilayer.

4.2.4 Magnetic characterization of the PBA bilayer

The main objective of the work described in this chapter is the study of the magnetic interactions originated by the direct contact between the two molecular-based magnetic materials. In the bilayer under study, the CrCr layer presents a ferrimagnetic behavior with an ordering temperature of 240 K as previously described in chapter 2.

The hysteresis loop of a 175 nm thickness film of CrCr exhibits a coercive field of 62 Oe as measured at 2K by SQUID magnetometry[25] (figure 4.10).

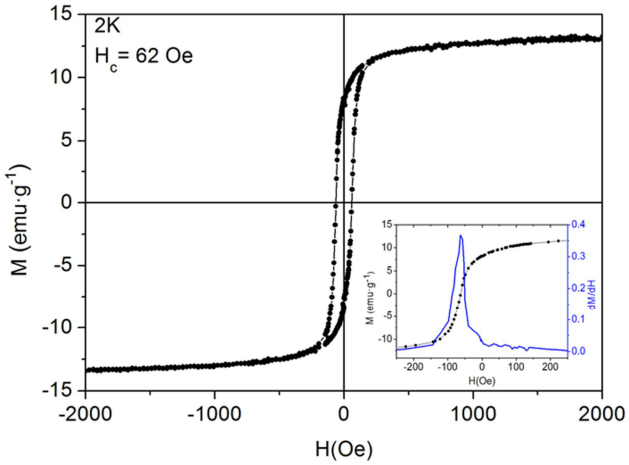

Figure 4.10- Hysteresis loop at 2K of a 175 nm thickness film of CrCr. *Inset*: Derivative (blue curve) of the first branch of the hysteresis loop (black curve) for determining the coercive field of the material.

The inset of figure 4.10 shows the first derivative of the first branch in the hysteresis loop, between 250 Oe and -250 Oe, for a 175 nm thickness film of CrCr. The first derivative was calculated for determining the PBA layer coercive field with more precision. The maximum of the derivative provides the point of maximum change of the magnetization during the reversal process under the application of an external magnetic field. In this case, the maximum of the derivative is located at - 62 Oe defining in this way the coercive field of the layer.

On the other hand, the top FeCr layer is a ferromagnet with a critical temperature of 23 K as explained in chapter 3. The hysteresis loop of a 135 nm thickness film (figure 4.11) exhibits a coercive field of 650 Oe. For this material, the first derivative of the magnetization respect to the field (dM/dH) was also calculated. In the inset of figure 4.1111 it is depicted the dM/dH in the first branch of the hysteresis loop between 2500 Oe and -2500 Oe.

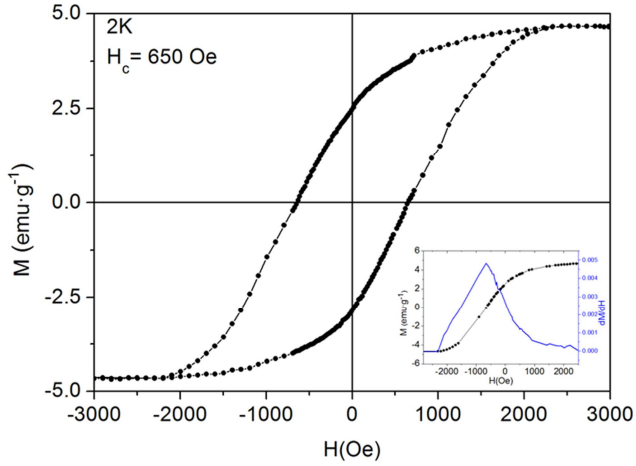

Figure 4.11- Hysteresis loop at 2K of a 135 nm thickness film of FeCr. *Inset*: Derivative (blue curve) of the first branch of the hysteresis loop (black curve).

The coercive field found for the 135 nm thickness film of FeCr is practically identical respect to the value described in chapter 3 for a film of the same material with a thickness of 1450 nm, presenting in that case a value of 670 Oe[30]. This invariance in the coercivity measured by SQUID, when changing the thickness of the PBA, was also observed for films of CrCr and FeCrCr as explained in chapter 2. It is important to remark that the thickness of the FeCr in the bilayer was determined to be 60 nm. By performing a calibration of the synthesis procedure, this thickness was assigned to an electrodeposition time of 5 seconds when deposited directly on the gold electrode. Several trials were made in order to obtain a hysteresis loop for FeCr films of 60 nm thickness. Nevertheless, in all the cases, the quality of the hysteresis was not appropriate (poor signal to noise ratio) for using it as part of the present study. At this respect, the invariance with thickness of the film coercivity determined with

SQUID for all the PBA analyzed in this thesis was considered to overcome this limitation. Thus, the magnetic characterization of an isolated FeCr deposited on gold was performed on the 135 nm thickness film as a reference system. This value is the lowest thickness limit with a good quality in the magnetic signal registered with the SQUID magnetometer. In the following discussion, the information obtained from the 135 nm thickness film of FeCr will be employed for analyzing the effects on this material when putted in direct contact with a CrCr film in the bilayer. Despite being 60 nm the FeCr thickness in the bilayer, by taking into account the coercivity invariance with thickness, the extrapolation of the hysteresis loop information from the 135 nm thickness film to the situation under study, can be done without introducing a significant error in the analysis.

By considering all the information presented so far, it is possible to describe an scenario for the PBA bilayer under study in which the ferrimagnetic CrCr layer, acting as the soft magnetic material (H_C=62 Oe), is in direct contact with the ferromagnetic FeCr layer which plays the role of the hard magnetic phase (H_C= 650 Oe). This situation will define the magnetic behavior of this composed structure, described in the present section.

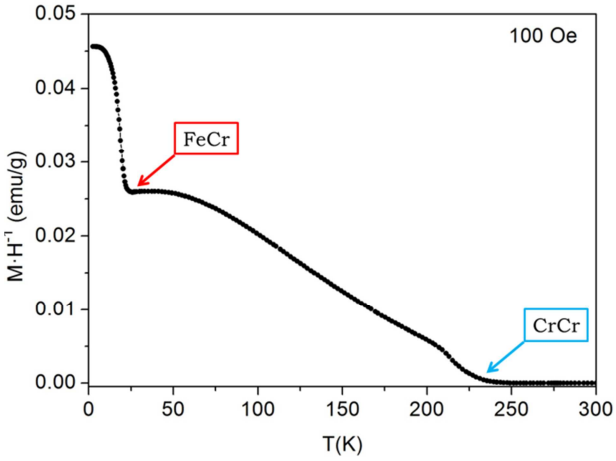

Figure 4.12- Thermal variation of the DC susceptibility ($M \cdot H^{-1}$) of the bilayer in FC conditions in an applied field of 100 Oe.

The thermal dependence of the PBA bilayer DC susceptibility under field-cooled (FC) conditions in an external field of 100 Oe was characterized. From figure 4.12 it is possible to observe a first jump in the susceptibility located at 240 K which to the ferrimagnetic ordering of the CrCr layer. A second jump in the signal is detected at 23 K being referred to the ferromagnetic transition of the FeCr layer. Thus the presence of both PBAs in the bilayer in direct contact is totally demonstrated from this measurement. No other transitions are observed from the FC characterization. This is an indication of the absence of extra magnetic phases in addition to the electropolymerized ones.

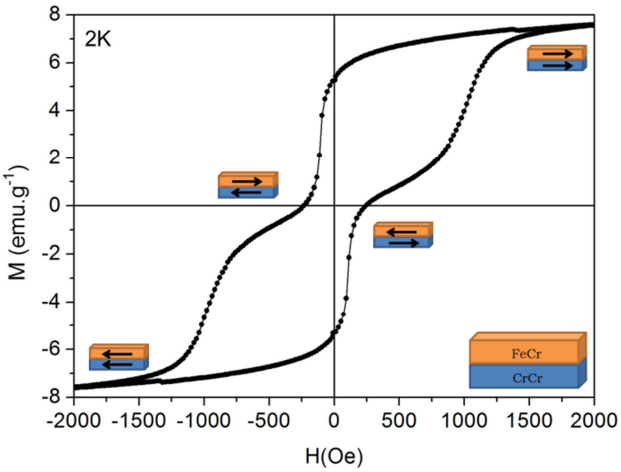

Figure 4.13- Hysteresis loop at 2K of the PBA bilayer in direct contact. In the graph it is indicated the relative orientation of each magnetization layer respect to the magnetic field during the reversal process.

Figure 4.13 shows the SQUID hysteresis loop obtained at 2 K for the PBA bilayer in direct contact. The characterization was done by cutting the samples in many pieces for being introduced into the SQUID sample holder. This measurement, below the T_C of both materials, exhibits two switching events. The magnetic field was applied parallel to the surface, in the same way as done for the characterization of the isolated layers. The hysteresis loop depicted in Figure 4.13 was measured between +60 kOe and -60 kOe, but only the region with interesting magnetic information between +2 kOe and -2 kOe is shown. The hysteresis loop of the bilayer is clearly registering a two-step process, which

can be related to the reversal of each PBA in the composed system. The parameter that will be treated in the discussion is the H_C of each layer composing the structure. As it was done for the isolated PBA films, the coercivities in the bilayer were extracted from the derivative (dM/dH) of the first branch of the hysteresis. The interval of magnetic fields between 1 kOe and -2.5 kOe was the one considered for the analysis of the magnetization data (figure 4.14). All the discussions in this section respect to H_C's will be related to the negative values associated to this branch of the hysteresis corresponding to the second and third quadrants. Nevertheless, the same reasoning can be completely extrapolated to the second branch of the hysteresis loop referred to the magnetization reversal processes in the first and fourth quadrants. From this calculation a first coercive field of -110 Oe corresponding to the CrCr soft layer is determined. On the other hand, the second switching event related to the magnetization reversal process of the FeCr layer can be found -1025 Oe, corresponding to the coercivity of this hard ferromagnetic layer.

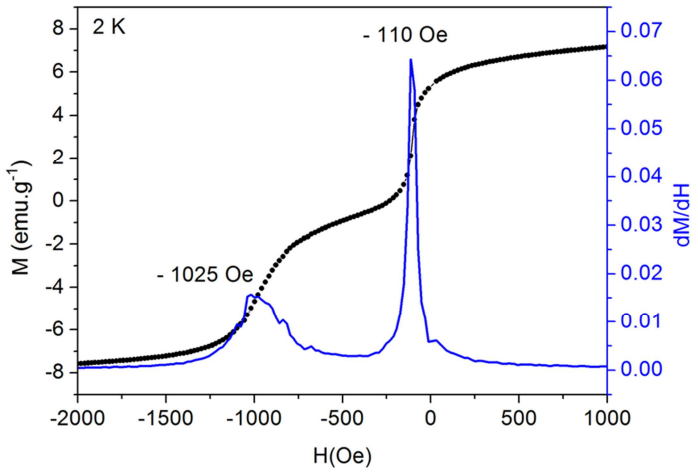

Figure 4.14- Derivative dM/dH of the first branch of the hysteresis loop measured at 2 K for the PBA bilayer in direct contact. Coercive fields of -110 Oe and -1025 Oe were determined for the bottom and top layers respectively

The coercive fields obtained in the PBA bilayer in direct contact are clearly different and much higher than the values calculated for the isolated bottom and top layers, -62 Oe and – 650 Oe respectively.

From these results it is possible to infer that when both molecular-based magnetic materials are put in direct contact, a magnetic coupling between both layers takes place. As a consequence, the magnetization reversal process for each PBA material in the bilayer is modified respect to the one occurring in the isolated films. In particular, the coercivity related to each material is approximately doubled respect to the isolated situation. An analysis of the data was made for discarding the bilayer hysteresis at 2K as arising from the direct combination of the magnetic signals corresponding to the CrCr and FeCr layers. In this way, simulations by linear combinations of the individual hysteresis signals of each material were performed. In this case, the linear combinations were done by employing the hysteresis loops depicted in figure 4.10 and figure 4.11 for the bottom and top layers respectively.

Figure 4.15 shows the comparison of the experimental hysteresis loop (red curve) with the simulation arising from the linear combination the hysteresis of each layer, according to the calculated thickness ratios determined by ICP-MS and STEM (being the same ratio in both cases; 3:1 for CrCr:FeCr). As depicted in figure 4.15 the shape of the experimental hysteresis loop compared to the one obtained by simulation is considerably different. In order to quantify this discrepancy, the switching events of these curves were obtained by calculating the derivative dM/dH of the first branch of the hysteresis as previously described. Only one switching field is detected by the derivative of the simulated curve, with a maximum located at -62 Oe corresponding exactly to the coercive field of the isolated CrCr layer. The second magnetization reversal process located at -1025 Oe for the experimental curve, related to the FeCr layer, is not reflected in the simulation. Thus, from this result it is possible to discard that the experimental loop registered at 2 K for the PBA bilayer is just the result of the addition of the individual magnetic signals of each layer. This point reinforces the idea of a scenario in which there is an effective exchange coupling between the soft ferrimagnetic phase in direct contact with the hard ferromagnetic material.

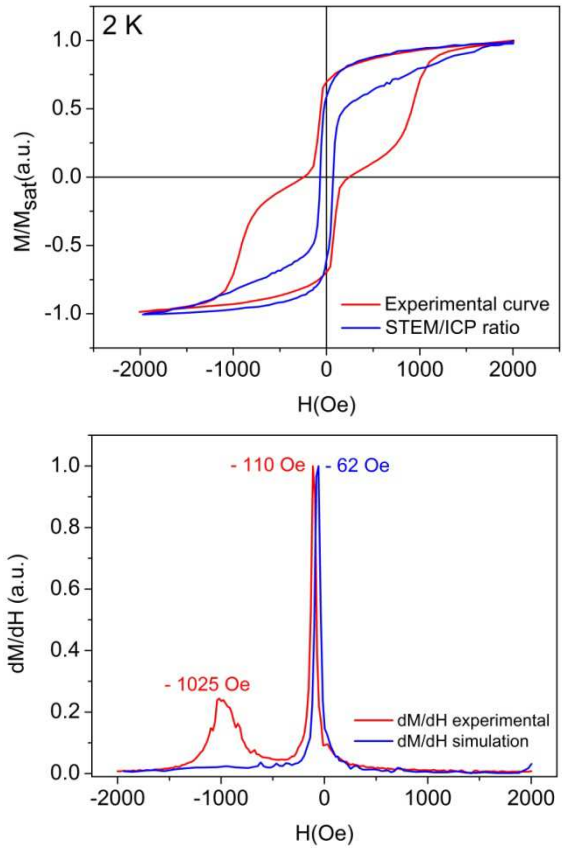

Figure 4.15- *Top*: Comparison of the experimental hysteresis loop (red curve) with the simulated curve employing the thickness ratio of STEM and ICP (blue curve).*Bottom:* Derivative dM/dH of the first branch of the experimental hysteresis loop of the bilayer and the one corresponding to the simulated curve.

There are many examples in literature of bilayers consisting of soft and hard magnetic layers in direct contact[23,24,33–37], being the most common situation the one in which both layers are ferromagnetic. In these cases, the so-called "exchange-spring" magnets are obtained with soft and hard magnetic layers magnetically coupled at the interface as explained at the introduction of the chapter. There is a critical thickness for the soft layer[21] below which both, the soft and hard layers, are rigidly coupled with each other exhibiting a simultaneous reversal process. If the thickness of the soft layer exceeds this

critical value, the magnetization reversal is characterized by a two-step process[21] just like in our situation. The first step involves the creation of an exchange spring magnet in the soft magnetic phase beyond a magnetic field commonly named as bending field[22] or nucleation field, H_N. In this context, the soft layer is strongly pinned to the hard layer at the interface meanwhile the outer region is free to follow the external field. Indeed, the dynamics of the spins in the soft layer resembles the one observed in a Bloch wall, with an increasing angle of rotation as the distance from the interface with the hard layer is increased. The second step in this hysteresis loop arises from the irreversible switching of the hard layer when progressively increasing the external magnetic field. We can extend this scenario to understand the hysteresis loop features of our PBA bilayer (figure 4.13). Starting from a saturated situation in which the magnetizations of both layers are in a parallel state, when the magnetic field reaches the value H_N a nucleation of the magnetization reversal of the softer CrCr layer takes place. The nucleation is produced from the outer surface and the reversal spreads through the whole layer. This process is stopped at the interface by the potential step due to the change of materials. At this stage, the domain wall can be compressed by increasing the field and decompressed by lowering it. This explains why this part of the magnetization is not flat and decreases when the amplitude of the field is increased[34,38].

In order to confirm the spring motion in the PBA bilayer, demagnetization curves in the region associated to the soft ferrimagnet reversal process were measured. Minor loops were registered for confirming the grade of reversibility of the magnetization reversal of the CrCr layer in the exchange spring process as shown in figure 4.16. With this aim, the sample was pole up to +60 kOe well above the saturation field of this material, after which minor loops between + 300 Oe and -650 Oe were traced. It is important to remark that despite the signal in figure 4.16 represents a minor loop for the overall bilayer system, it is actually a major loop for the CrCr ferrimagnetic layer. Indeed, it is obtained by sweeping between extreme magnetic fields which correspond to saturated states of the CrCr magnetization (figure 4.10).

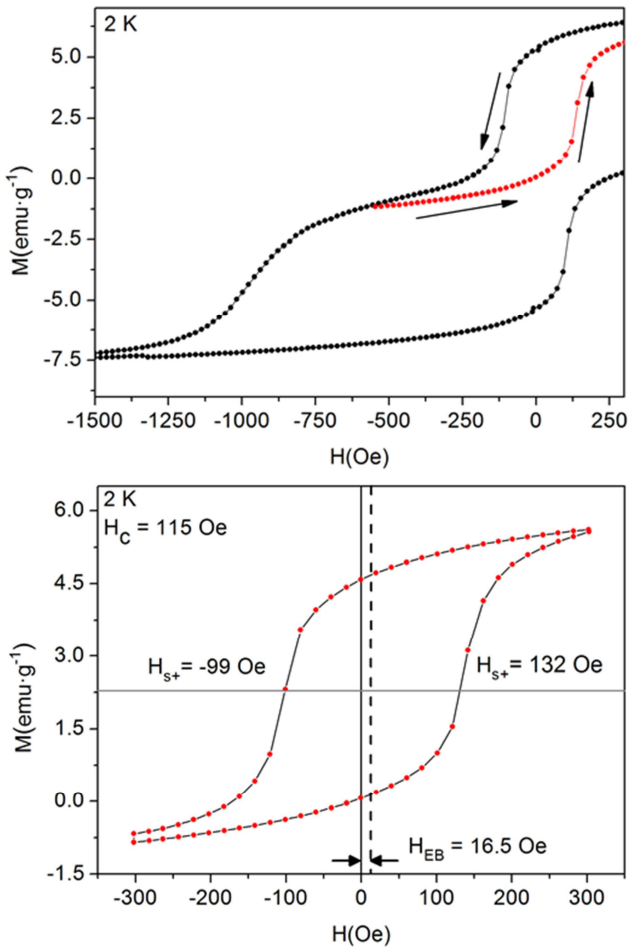

Figure 4.16- *Top*: Demagnetization curve at 2 K of the bilayer indicating the minor loop corresponding to the magnetization reversal process of the CrCr layer. *Bottom:* Exchange biased loop of the soft layer of CrCr. The exchange bias field is illustrated by the dashed line around which the resulting hysteresis is centered.

By performing this protocol, an "exchange-biased" loop is obtained for the CrCr in the bilayer (see figure 4.16), with a positive exchange bias field of 16.5 Oe calculated as[39]:

$$H_{EB} = \frac{|H_{S+} + H_{S-}|}{2} \qquad (eq. 4.2)$$

In addition, a clear enhancement of the coercive field for this layer is detected with a value of H_c = 115 Oe. This coercivity is the double respect to the value corresponding to the isolated situation (H_c= 62 Oe). Thus, the exchange coupling of the soft ferrimagnetic CrCr layer with the adjacent hard ferromagnetic FeCr layer is translated into both, an offset (H_{EB}) and an increase in the coercivity. The reduced value of H_{EB} could be associated to a non-epitaxial growth of the interfaces between both materials. Indeed, exchange interactions are extremely affected by the defects and the quality of the entire interface of a bilayer, being actually more sensitive than any other structural probe[40]. From all the presented information, it is possible to determine that the switching of the CrCr layer is reversible but hysteretic respect to the exchange field H_{EB} = 16.5 Oe, thus confirming in this sense the spring motion of the layer (figure 4.17).

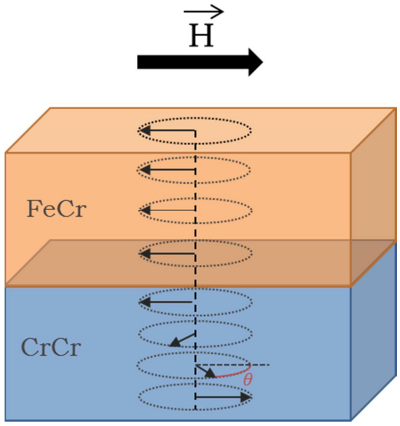

Figure 4.17- Intuitive picture of the exchange-spring process in the CrCr soft ferrimagnetic layer induced by an exchange coupling at the interface with the FeCr hard phase. The magnetization of CrCr is pinned at the interface producing a twisted spiral-spin configuration when the magnetic field is increased, with greater angle θ as moving away from the interfacial region.

Coming from a high magnetic field where both CrCr and FeCr are saturated with their magnetization parallel to the external magnetic field, when the nucleation field in the soft layer is reached the magnetization in this material becomes unstable and a twisted helicoidal spin-configuration is induced. This

spin-configuration in the CrCr layer is a result of the competition between the Zeeman energy that tries to align the spins of this soft ferrrimagnet in the direction of the applied magnetic field and the exchange coupling at the interface with the FeCr, already ordered. The second interaction tends to align the magnetization of the soft layer at the interface in an antiparallel configuration[21].

In previous works on exchange-spring magnets composed by bilayers of SmCo/Co[23], Fe/CoSm and Co/CoSm[35] the hysteretic behavior of the minor loops, as the one observed in our system, was associated mainly to the strength of the magnetic anisotropy in the soft magnetic material. In our particular case, a possible anisotropy in the ferrimagnetic layer of CrCr is discarded as it was explained extensively in chapter 2. From an ATR-IR study on thin films of this chromium cyanide PBA described in chapter 2[25], it was possible to detect a complete oxidation of Cr^{2+} ions to Cr^{3+} under air exposure. The anisotropy of the Cr^{III} ions in the material can be neglected by considering the non-degenerate $^4A_{2g}$ ground state present in this metal ion. Thus, a magnetic anisotropy in these fully oxidized Cr^{III} ferrimagnetic PBA films can be discarded. The isotropy on the magnetic properties of this chromicyanide derivative was confirmed by SQUID measurements on films of this material with magnetic fields applied parallel and perpendicular to the surface. This study showed unaltered values of coercive field and magnetization for each configuration confirming the isotropy in the magnetic properties on this system[41] (for more details go to chapter 2). Discarding the anisotropy in CrCr, the hysteretic behavior in the minor loop of the soft ferrimagnetic layer has to be associated to other phenomenon. In this sense, the already mentioned weak interfacial exchange coupling strength, arising from the interface generated between these two polycrystalline materials[21],has been proposed as a possible explanation. Nevertheless, extra characterization should be performed in order to completely confirm this assessment.

The last point to treat is the effect observed on the hard layer of FeCr. As it was determined previously from the analysis of the bilayer hysteresis loop (figure 4.14), the coercive field associated to the FeCr layer (-1025 Oe) is clearly enhanced respect to the isolated situation (-650 Oe) at the same temperature. In

the majority of the reported exchange spring bilayer systems both layers are ferromagnetic materials and only in few works, one or both materials are ferrimagnets[38,42]. In addition, any of the reported exchange spring bilayers so far include any molecular-based magnetic as part of the structure. When both layers are ferromagnetic, a decrease of the coercive field of the hard magnetic phase is reported as a consequence of an increasing coupling between the two magnetic materials in direct contact. This situation can be explained by the propagation of the domain wall formed in the soft ferromagnet which is compressed against the interface with the hard ferromagnet when the magnetic field is increased. When the field is high enough, the domain wall propagates into the hard ferromagnet initiating the magnetization reversal process at lower magnetic fields, decreasing in this way the coercivity of the material[24].In our case, the effect on the hard ferromagnetic layer is opposite to the commonly observed phenomenology in ferro/ferro exchange-spring magnets. The process taking place on the FeCr layer may be understood by considering the exchange mechanism at the interface. Taking into account the ferrimagnetic nature of CrCr, both ferromagnetic (F) and antiferromagnetic (AF) superexchange interactions paths can be present at the interface. This situation introduces an extra complexity for understanding and explaining the magnetization reversal process of the layers. One possibility, to infer the nature of the interaction at the interface, is the analysis of the shifting in the exchange-biased loops measured in the bilayer. From our characterization, we have been able to obtain information about the shifting on the minor loop related to CrCr as depicted in figure 4.16. The exchange bias field was found to be positive, which can be related to an antiferromagnetic coupling across the interface[43]. For the FeCr layer, the exchange coupling was manifested as an enhancement of the coercive field without the chance of getting information of the shifting in the hysteresis. Thus an incomplete view is present regarding this point.

Another possibility for understanding the nature of the coupling at the interface is through the analysis of the superexchange interactions present in each material composing the bilayer. In the case of the CrCr films, as it was shown in the magnetic characterization of chapter 2, by the least-squares-fitting of χ^{-1} data *vs* temperature a Weiss constant of θ = -100 K was extracted. This is an

indication of a large antiferromagnetic interaction between neighbouring Cr ions through the cyanide bridge. This antiferromagnetic interaction is completely in agreement with the expected behavior from an analysis of the electronic structure of the material[27]. For the ferromagnetic layer of FeCr, the analysis regarding the nature of the magnetic interactions is by far more complex. It has been demonstrated that the exchange interaction for unpaired electrons occupying orbitals of the same symmetry set [t_{2g}(A)-t_{2g}(B) or e_g(A)-e_g(B)] is antiferromagnetic (AF). On the contrary, a ferromagnetic (F) exchange interaction is originated when the unpaired electrons belong to orbitals of different symmetry [t_{2g}(A)-e_g(B) or e_g(A)-t_{2g}(B)]. The sum of the different exchange interaction pathways present in the material defines the sign and strength of the magnetic coupling between the adjacent metal ions[44]. For the FeCr PBA, the Fe^{2+} ion sits in a high-spin environment with a t_{2g}^4 e_g^2 electronic configuration (S=2) interacting with a Cr^{3+} ion which presents a t_{2g}^3 electronic configuration (s=3/2). In this situation, the number of ferromagnetic and antiferromagnetic pathways are equal six for both cases[44]. In general, the AF pathway contributes to spin alignment more effectively than the ferromagnetic one[27,45],thus a global weak antiferromagnetic coupling should be expected in the FeCr. On contrary to this, as it was explained in chapter 3 and reported in many previous works[30,31,44], the fitting of the susceptibility data for films of FeCr leads to a positive Weiss constant of θ = +26 K, indicating a ferromagnetic interaction in the material. It is clear that the theory fails for predicting the magnetic nature of this PBA family, in which a ferrimagnetic ordering should be present. Thus, it seems that a delicate balance between the F and AF contributions are present in this compound[44]. Indeed, the presence of AF pathways in this material cannot be neglected. Taking into account all this information, it is possible to assume an scenario in which an effective AF interaction through the interface of both molecular-based magnetic materials could be present, being this AF coupling the responsible of the enhanced coercive field of the FeCr in the bilayer system.

In the proposed physical scenario, when at a sufficient magnetic field the CrCr layer has been switched, the exchange field in the interface dominates the reversal of the FeCr hard layer. The magnetization in the latter system is stabilized in an antiparallel configuration respect to the external applied field. In

consequence, the strength of the originated exchange field, between both materials, prohibits the reversal of the FeCr in the direction of the external magnetic field by a pinning effect. This process leads to an enhancement in the value of the FeCr coercivity respect to the isolated case. The positive slope between the two switching events on the bilayer (H_{S1} and H_{S2} in figure 4.18) is an indication of the presence of a domain wall in the interface at this range of magnetic fields. This kind of slope was already reported in other exchange coupled bilayer[24,34,38] and it was ascribed to the compression of the interfacial lateral domain wall when the field is increased as previously mentioned.

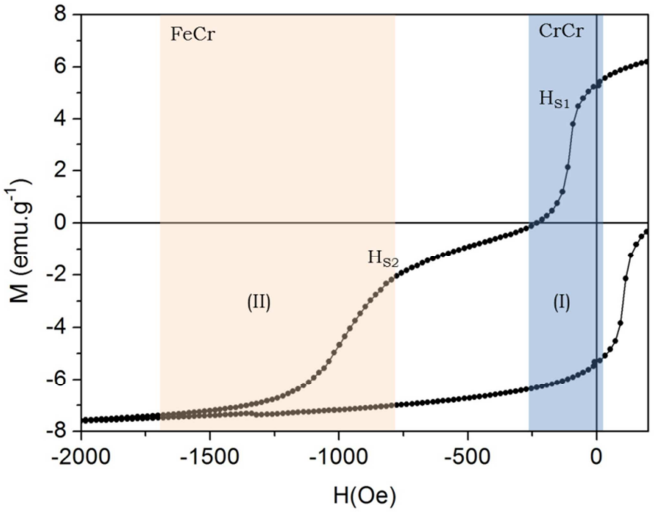

Figure 4.18- Hysteresis loop of the bilayer measured at 2K in which the regions corresponding to each reversal process of the layers are indicated. Region-I corresponds to the exchange-spring reversal process of the CrCr layer. For higher magnetic fields, in region-II the reversal of the FeCr layer is affected by a pinning effect at the interface inducing an enhancement in the coercivity of this material.

Taking into account all the results it is possible to assume a clear exchange coupling between the PBA layers at the interface. The physical phenomenology related to the reversal process of both PBA layers in the bilayer is illustrated in figure 4.18. In the region of lower fields (region-I) the exchange-spring behavior of the soft ferrimagnetic phase takes place. When the field is increased to higher values, the reversal process of the hard layer is affected by a pinning effect at

the interface with the CrCr layer arising from an AF coupling between both materials (region-II). This situation modifies the reversal process in the FeCr with an enhancement of the coercivity of this hard phase. Thus, it is possible to describe a *cross-talking effect* in the magnetic coupling between the layers, with a different physical phenomenology depending on the window of magnetic fields in which the process is studied. An extra characterization, such as polarized neutron reflectivity, should be performed in the bilayer in order to achieve a precise confirmation of the nature of the exchange coupling existing between the two materials, as well as a complete description of the domain wall formation process.

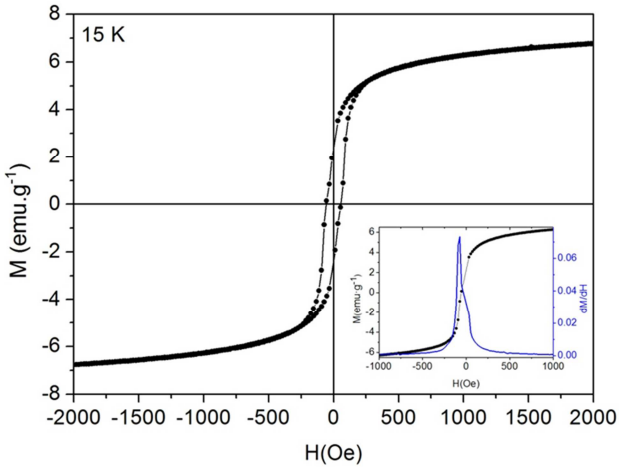

Figure 4.19- Hysteresis loop of the bilayer measured at 15 K. *Inset*: Derivative of the first branch of the hysteresis.

Hysteresis loops of the PBA bilayer were also measured at 15 K as depicted in figure 4.19. This temperature is just below the T_C of the FeCr layer. One observes that the hysteresis presents only one switching event. This is confirmed by the dM/dH of the hysteresis loop (inset figure 4.19) which shows a maximum located at -72 Oe, corresponding to the reversal process of the CrCr layer. From the previous study, the coercive field of the CrCr layer was determined to be -65 Oe and -112 Oe for the isolated case and when forming part of the bilayer respectively. Thus the value of coercivity obtained at 15 K is almost the same than the one found for isolated layer. This can be understood

by considering that the FeCr layer is partially ordered at this temperature being the effect on the soft phase much weaker than at 2 K where the ferromagnetic ordering is complete in the material. When the temperature is increased up to 30 K (figure 4.20), just above the critical temperature of the FeCr but still well below the ordering of the CrCr layer, the measured hysteresis of the bilayer is again reflecting only one magnetization reversal process.

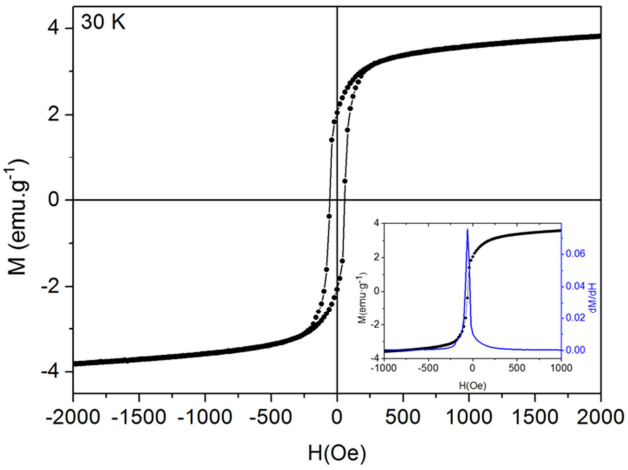

Figure 4.20- Hysteresis loop of the bilayer measured at 30 K. *Inset*: Derivative of the first branch of the hysteresis.

The calculation of the dM/dH (inset figure 4.20) shows a maximum located at – 60 Oe being identical to the coercive field of the isolated CrCr layer. This result is well understood considering that the only material magnetically ordered at 30 K in the bilayer is the soft ferrimagnetic phase. Indeed the magnetization reversal process should reflect the same behavior of the isolated CrCr layer just as it has been extracted from SQUID data. The fact of obtaining this result supports the already considered scenario in which no extra magnetic phase, in addition to the two electropolymerized films, is present in the synthesized PBA bilayer.

4.3 Conclusions and perspectives

In this chapter it has been demonstrated the possibility of fabricating a bilayer of PBA thin magnetic films at the nanometer level. This bilayer exhibits a magnetic coupling between the two magnets. The fabrication of this structure has been achieved by means of a solution process method. Thin films of these molecular-based materials have been electropolymerized in intimate contact materials multiple bath coulometry procedure. With this method we have been able to put a soft ferrimagnetic layer of the CrCr PBA in direct contact with a hard ferromagnetic layer formed by an FeCr layer.

ATR-IR spectroscopy and temperature-dependent susceptibility measurements showed that the chemical identity of the layers is preserved after electrodeposition. This has been achieved by selecting properly the order of electropolymerization of the layers in such a way that the electrodeposition potential for the top film lies outside the electroactive region of the bottom one. By means of a complete morphological study it has been possible to characterize the thickness of the layers and, which is most important, the interface generated between both materials. STEM characterization has shown the formation of a clear interface which extends in a constricted region of approximately 10 nm, evidencing the lack of interpenetration between the two layers.

Through an extensive magnetic characterization of the PBA bilayer, it has been possible to observe an interesting magnetic phenomenology depending on the range of magnetic fields under which the system is studied. When both magnetic materials are put in direct contact a clear enhancement of their coercive fields, with respect to their values when being isolated, is detected. Interestingly by measuring minor loops of the bilayer corresponding to the range of saturation of the ferrimagnetic layer of CrCr, a hysteretic reversible behavior of the magnetization reversal process of this material was observed. This minor loop, being a major loop of the CrCr, showed an exchange-biased response with an enhancement of the coercivity and a positive shifting of the hysteresis. This behavior has been associated to an exchange-spring process in the reversal

mechanism of the CrCr layer induced by the interaction at the interface with the hard ferromagnetic phase of FeCr. The low exchange biasing field (16.5 Oe) and the hysteretic behavior of the magnetic signal in CrCr have been related to the characteristics of the interface between both materials. The lack of epitaxial growth of the successive layers is responsible of a weak coupling between both materials leading to the effects described above. When the magnetic field is increased up to the range of the magnetization reversal of the FeCr layer, the influence of the ferrimagnetic layer of CrCr on this hard magnet is evidenced. An AF interaction between FeCr and CrCr at the interface of both materials is proposed. From this interaction, a pinning effect on the magnetization reversal of the FeCr layer may be induced. This effect accounts for the enhancement in the H_C observed for this hard magnet in the bilayer in comparison with the isolated case. In consequence, from the magnetic characterization of this bilayer structure, composed of two families of PBA's in direct contact, an interesting cross talking effect in terms of magnetic interactions has been described.

The results presented in this chapter open many lines for future work. The thickness of the soft layer has been demonstrated to be an important parameter in the response of the exchange spring magnet. Thus, in first instance other CrCr layer thicknesses need to be studied for understanding the impact of this parameter on the exchange-spring process.

An extra characterization such as polarized neutron reflectivity has to be performed in order to get precise information of the nature of the coupling at the interface of both materials and the process of domain wall creation and propagation.

The intercalation of non-magnetic spacers of different thicknesses (gold or copper films, among others) in these bilayers would allow tuning the exchange coupling between both layers, increasing the information about this process at the interface. For obtaining these spacers, methods such as thermal evaporation or electrochemical techniques are proposed as possible strategies. The latter would present a higher interest due to the fact that the heterostructure could be fabricated from a complete solution-process method. In order to move these PBA heterostructures into the application field, the CrCr

ferrimagnetic layer can be combined with other PBA families with higher critical temperatures such as the vanadium-chromium derivatives which exhibit ferromagnetic ordering up to room temperature. The need to decrease the temperature down to 2 K for characterizing the magnetic properties of the described PBA bilayer, inhibited the possibility of studying the system with MOKE due to technical limitations. The alternative of producing heterostructures of PBA with higher critical temperatures will allow us to make a complementary characterization to SQUID by means of MOKE magnetometry.

Finally, it is important to mention that the study presented in this chapter constitutes the first reported result of a bilayer composed by molecule-based magnetic materials exhibiting an exchange coupling phenomenology. Hence, it has established the bases for the fabrication and characterization of PBA magnetic heterostructures. These systems can be of fundamental interest for achieving a basic understanding of the reversal processes in these molecular-based layers when combined in complex structures. The background acquired in this way could be extended and applied for the fabrication of a new generation of devices with interest in molecular spintronics.

4.4 Bibliography

(1) Pajerowski, D. M.; Andrus, M. J.; Gardner, J. E.; Knowles, E. S.; Meisel, M. W.; Talham, D. R. *J. Am. Chem. Soc.* **2010**, *132*, 4058.

(2) Pajerowski, D. M.; Gardner, J. E.; Frye, F. A.; Andrus, M. J.; Dumont, M. F.; Knowles, E. S.; Meisel, M. W.; Talham, D. R. *Chem. Mater.* **2011**, *23*, 3045.

(3) Sato, O.; Iyoda, T.; Fujishima, A.; Hashimoto, K. *Science (80-.).* **1996**, *272*, 704.

(4) Shimamoto, N.; Ohkoshi, S.; Sato, O.; Hashimoto, K. *Inorg. Chem.* **2002**, *41*, 678.

(5) Escax, V.; Bleuzen, a; Cartier Dit Moulin, C.; Villiam, F.; Goujon, a; Varret, F.; Verdaguer, M. *J. Am. Chem. Soc.* **2001**, *123*, 12536.

(6) Hanawa, M.; Moritomo, Y.; Kuriki, a.; Tateishi, J.; Kato, K.; Takata, M.; Sakata, M. *J. Phys. Soc. Japan* **2003**, *72*, 987.

(7) Sato, O.; Einaga, Y.; Fujishima, a.; Hashimoto, K. *Inorg. Chem.* **1999**, *38*, 4405.

(8) Gros, C. R.; Peprah, M. K.; Hosterman, B. D.; Brinzari, T. V; Quintero, P. a; Sendova, M.; Meisel, M. W.; Talham, D. R. *J. Am. Chem. Soc.* **2014**, *136*, 9846.

(9) Schuller, Ivan K, Nogués, J. *J. Magn. Magn. Mater.* **1999**, *192*, 203.

(10) Meiklejohn, W. H. *J. Appl. Phys.* **1962**, *33*, 1328.

(11) Meiklejohn, W. H., Bean, C. P. *Phys. Rev.* **1957**, *105*, 904.

(12) Search, H.; Journals, C.; Contact, A.; Iopscience, M.; Address, I. P. *J. Phys. DApplied Phys.* **2000**, *33*, R247.

(13) Kiwi, M. *J. Magn. Magn. Mater.* **2001**, *234*, 584.

(14) Camarero, J.; Sort, J.; Hoffmann, A.; García-Martín, J.; Dieny, B.; Miranda, R.; Nogués, J. *Phys. Rev. Lett.* **2005**, *95*, 057204.

(15) Nogués, J.; Sort, J.; Langlais, V.; Skumryev, V.; Suriñach, S.; Muñoz, J. S.; Baró, M. D. *Phys. Rep.* **2005**, *422*, 65.

(16) Romer, S.; Marioni, M. a.; Thorwarth, K.; Joshi, N. R.; Corticelli, C. E.; Hug, H. J.; Oezer, S.; Parlinska-Wojtan, M.; Rohrmann, H. *Appl. Phys. Lett.* **2012**, *101*, 222404.

(17) Ijiri, Y.; Borchers, J. A.; Erwin, R. W.; Lee, S. *Phys. Rev. Lett.* **1998**, *80*, 608.

(18) Radu, F.; Abrudan, R.; Radu, I.; Schmitz, D.; Zabel, H. *Nat. Commun.* **2012**, *3*, 715.

(19) Smith, N.; Cain, W. C. *J. Appl. Phys.* **1991**, *69*, 2471.

(20) Member, E. F. K.; Hawig, R. *IEEE Trans. Magn.* **1991**, *27*, 3588.

(21) Guo, G.; Zhang, G.; Wang, X. *J. Appl. Phys.* **2010**, *108*, 043919.

(22) Goto, E.; Hayashi, N.; Miyashita, T.; Nakagawa, K. *J. Appl. Phys.* **1965**, *36*, 2951.

(23) Fullerton, E. E.; Jiang, J. S.; Grimsditch, M.; Sowers, C. H.; Bader, S. D. *Phys. Rev. B* **1998**, *58*, 193.

(24) Fullerton, E. E.; Jiang, J. S.; Bader, S. D. *J. Magn. Magn. Mater.* **1999**, *200*, 392.

(25) Coronado, E.; Makarewicz, M.; Prieto-Ruiz, J. P.; Prima-García, H.; Romero, F. M. *Adv. Mater.* **2011**, *23*, 4323.

(26) Prima-Garcia, H.; Coronado, E.; Prieto-Ruiz, J. P.; Romero, F. M. *Nanoscale Res. Lett.* **2012**, *7*, 232.

(27) Mallah, T.; Thiébaut, S.; Verdaguer, M.; Veillet, P. *Science* **1993**, *262*, 1554.

(28) O. Sato, T.Iyoda, A. Fujishima, K. H. *Science (80-.).* **1996**, *271*, 49.

(29) Buschmann, W. E.; Paulson, S. C.; Wynn, C. M.; Girtu, M. A.; Epstein, A. J.; White, H. S.; Miller, J. S. *Chem. Mater.* **1998**, *10*, 1386.

(30) Coronado, E.; Fitta, M.; Prieto-Ruiz, J. P.; Prima-García, H.; Romero, F. M.; Cros, A. *J. Mater. Chem. C* **2013**, *1*, 6981.

(31) Ohkoshi, S.; Einaga, Y.; Fujishima, A.; Hashimoto, K. *J. Electroanal. Chem.* **1999**, *473*, 245.

(32) Nakanishi, S.; Lu, G.; Kothari, H. M.; Bohannan, E. W.; Switzer, J. a. *J. Am. Chem. Soc.* **2003**, *125*, 14998.

(33) Zambano, a.; Oguchi, H.; Takeuchi, I.; Choi, Y.; Jiang, J.; Liu, J.; Lofland, S.; Josell, D.; Bendersky, L. *Phys. Rev. B* **2007**, *75*, 144429.

(34) Canet, F.; Bellouard, C.; Joly, L.; Mangin, S. *Phys. Rev. B* **2004**, *69*, 094402.

(35) Nagahama, T., Mibu, K., Shinjo, T. *J. Phys. Chem. C* **1998**, *31*, 43.

(36) Kim, J.; Barmak, K.; De Graef, M.; Lewis, L. H.; Crew, D. C. *J. Appl. Phys.* **2000**, *87*, 6140.

(37) Yan, S.-S.; Elkawni, M.; Li, D. S.; Garmestani, H.; Liu, J. P.; Weston, J. L.; Zangari, G. *J. Appl. Phys.* **2003**, *94*, 4535.

(38) Ramos, a.; Moussy, J.-B.; Guittet, M.-J.; Gautier-Soyer, M.; Gatel, C.; Bayle-Guillemaud, P.; Warot-Fonrose, B.; Snoeck, E. *Phys. Rev. B* **2007**, *75*, 224421.

(39) Ziese, M.; Höhne, R.; Bollero, a.; Semmelhack, H.-C.; Esquinazi, P.; Zimmer, K. *Eur. Phys. J. B* **2005**, *45*, 223.

(40) Suzuki, Y.; van Dover RB; Gyorgy, E.; Phillips, J.; Felder, R. *Phys. Rev. B. Condens. Matter* **1996**, *53*, 14016.

(41) Coronado, E.; Prieto-Ruiz, J. P.; Prima-Garcia, H. *Chem. Commun. (Camb).* **2013**, *49*, 10145.

(42) Demirtas, S.; Hossu, M.; Arikan, M.; Koymen, a.; Salamon, M. *Phys. Rev. B* **2007**, *76*, 214430.

(43) Canet, F., Mangin, S., Bellouard, C., Piecuch, M. *Europhys. Lett.* **2000**, *52*, 592.

(44) Coronado, E.; Giménez-López, M. C.; Korzeniak, T.; Levchenko, G.; Romero, F. M.; Segura, A.; García-Baonza, V.; Cezar, J. C.; de Groot, F. M. F.; Milner, A.; Paz-Pasternak, M. *J. Am. Chem. Soc.* **2008**, *130*, 15519.

(45) Ohkoshi, S.; Iyoda, T.; Fujishima, A.; Hashimoto, K. *Phys. Rev. B* **1997**, *56*, 11642.

Chapter 5

Magnetoresistance measurements on electrodeposited PBA thin films

5.1 Introduction

As mentioned in the previous chapters, molecular spintronics is an emerging field which benefits from the chemical versatility and unique electronic features of the molecules to explore two challenging goals: the development of molecular analogues of the existing inorganic materials used in the construction of spintronic devices, and the evolution towards unimolecular spintronics[1,2]. While the second aspect is strongly limited experimentally by the intrinsic chemical properties of the molecular coordination complexes commonly used for this purpose (reactivity when contacted to electrodes, difficulty in making the contacts, limitations imposed by the use of solution techniques to stabilize the molecule, …), for the first aspect some attempts to develop spintronic devices have already been described. The best example is provided by the so-called molecular spin valves[3–5]. At present the development of these devices is seriously hindered by the very low magnetoresistance (MR) achieved at room temperature. This is a consequence of the poor spin transfer between the inorganic electrodes and the central organic layer. Attempts to improve this transfer involve engineering at the organic/inorganic interface through the insertion of monolayers of dipolar or magnetic molecules[6].

Another possibility that has been much less explored is that of using as ferromagnetic electrode a molecule-based material. The first work in this vein was performed by A. J. Epstein *et al.* on thin films of the $V[TCNE]_x$, x~2 semiconducting soft ferrimagnet[7–10]. This material orders at $T_c \approx 380$ K showing a positive MR of up to 0.7% at 0.6 T at room temperature[7]. Thin films of this material have been successfully included into a hybrid multilayer structure combined with LSMO electrodes showing a suitable behavior as spin injector[11,12].Moreover, two electrodes of this molecule-based magnet have been employed for fabricating an all molecular spin valve structure with an organic rubrene layer acting as spacer[13].

We will describe in this chapter the MR properties of thin films of molecular-based magnets based on Prussian Blue analogues (PBA). In particular, we have chosen the chromium cyanide system extensively described

in chapter 2[14–16]. As mentioned in the previous chapters, the studied system is the resulting material after the air oxidation process of the PBA $Cr_{5.5}(CN)_{12}\cdot 11.5\ H_2O$, that we have denoted as CrCr along all the discussion. The interest for studying thin films of this material is based in its high critical temperature, with a ferrimagnetic ordering below 240 K[14]. In addition, its high chemical stability and well known magnetic properties establish this material as the best candidate for applications among the other PBA systems characterized in this thesis. We took profit of the experience acquired in the fabrication of ultra-thin films of CrCr with controlled properties as described in chapter 2. Indeed, it has been possible to characterize the MR properties of an 80 nm thickness film of CrCr, which supposes the first study of this type on a polycrystalline PBA ultra-thin film[16]. In addition, in this chapter a prototype of a spin valve structure is proposed in order to evaluate the potential applications of this material as a spin injector electrode in a molecular spin valve structure. The preliminary characterization of this spintronics structure will be extensively described in the second part of the chapter.

5.2 Results and discussions

5.2.1 Sample preparation and general characterization

Films of CrCr were synthesized following the same procedure described in chapter 2[14,15]. In order to evaluate the MR properties of this chromium cyanide thin films, the chosen strategy has been the evaporation of a top gold electrode. As a result, the PBA films are sandwiched between a Au working electrode, onto which the electrodeposition takes place, and a top gold layer. It is well known that the conductivity of vacuum-dried PBA films is considerably low[17,18]. In our material, it has been found a critical decrease of conductivity when cooling down the system for film thicknesses above 100 nm impeding a proper characterization. For solving this problem films with 80 nm thickness have been prepared, reducing in this way the influence of temperature on the conductivity. For such small thicknesses the main bottleneck is the physical fragility of the PBA film with respect to the evaporation of a top gold electrode. In consequence, the probability of electrical shortcuts, produced by a direct contact of the top Au

layer with the bottom working electrode, is found to be very high. For solving this important problem, the active areas of the samples have been reduced to 0.0025 cm^2. This considerable reduction of the area under exposure to gold evaporation has led to an important improvement in the statistics of devices without shortcuts.

The device fabrication process consisted of a multiple step procedure combining solution and evaporation techniques. In first instance, two stripes of gold with 0.5 mm width, 1 mm length and 30 nm thicknesses were deposited by thermal evaporation onto a glass substrate, and subsequently employed as working electrodes. The reduced size of the substrates was a limitation for their direct inclusion in the conventional electrochemical cell employed for the fabrication of our PBA films. This set-up has been already described with detail in chapter 1. Thus, it has been necessary the development of a strategy to adapt these substrates to the connector employed for contacting the working electrode in the electrochemical cell. The solution was found in the design and fabrication of a sample adaptor for the electrodeposition of the PBA films.

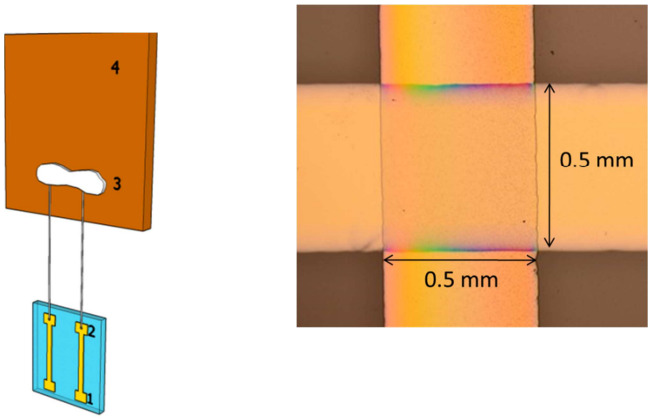

Figure 5.1- *Left:* 3D sketch of the sample adaptor for small substrates:1) Working electrode of Au with 0.5 mm width; 2) indium wildering; 3) Silver contact; 4) Copper covered fiber carbon adaptor. *Right*: Optical image of a cell of the device with an active area of 0.0025 cm^2.

In figure 5.1 it is depicted a 3D sketch of the sample adaptor and the method for contacting the sample. The extremes of two conductive wires were connected to the gold stripes by a cold welding with indium. The other extremes of the conductive wires were contacted with silver painting to the adaptor. A substrate of carbon fiber coated with Cu was employed for fabricating the adaptor. The size of this adaptor allowed the proper connection with the tweezers used in the conventional electrochemical cell, keeping the same reference and counter electrodes described for the set-up in chapter 1. After the electrodeposition of CrCr, the indium welding was removed and the samples transferred to the clean room. By thermal evaporation, a top gold electrode of 20 nm thickness was deposited in a cross bar configuration respect to the stripe of PBA. The evaporation rate was always kept in a rate below 0.01 nm/s during the fabrication process. This was done for minimizing the interpenetration of metal atoms into the molecular-based layer, avoiding in this way electrical shortcuts. At the end of the fabrication process, four cells with an active area of 0.0025 cm^2 were obtained in each sample. In figure 5.1 it is shown the optical image of one of the cells in the final device.

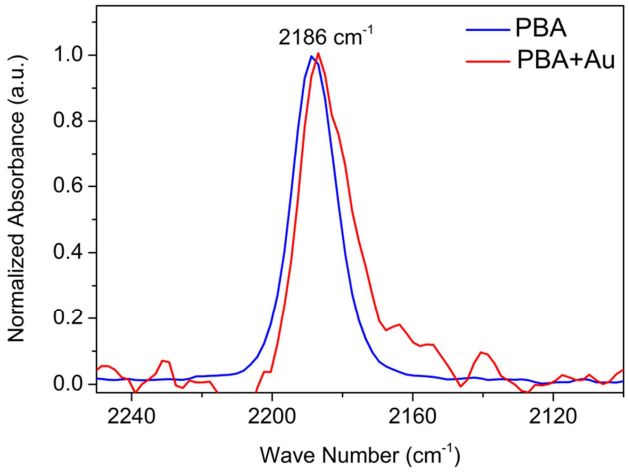

Figure 5.2- Comparison of the ATR-IR spectra of a pristine film of CrCr (blue curve) with the one obtained after the evaporation of a 20 nm thickness gold electrode (red curve).The same band associated to the cyanide stretching vibration of the $[Cr^{III}(CN)_6]^{3-}$ anion is detected.

During the preparation of the device, the PBA layer was exposed to high vacuum conditions and temperatures up to 100 ºC. In order to discard any chemical change or alteration of the magnetic properties of CrCr, a control characterization was performed. In first instance, after the evaporation of the top gold electrode, an ATR-IR study was performed and compared with the pristine material. As depicted in figure 5.2, the IR spectrum the PBA layer covered with 20 nm of gold, exhibits a noisier signal than the pristine film. Only one band is observed at 2186 cm^{-1} in both cases, corresponding to the cyanide stretching vibration of the $[Cr^{III}(CN)_6]^{3-}$ anion[14,15]. Thus the thermal evaporation process was not inducing in principle any chemical change on the ultra-thin film of CrCr by considering the ATR-IR study.

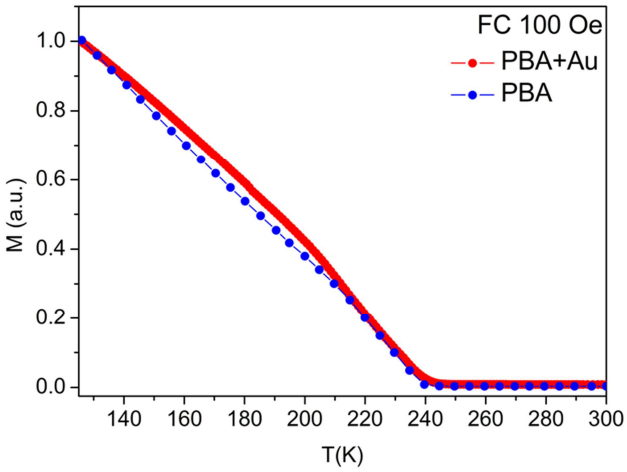

Figure 5.3- Comparative of the FC measurement at 100 Oe of the pristine PBA film (blue curve) and the one covered with 20 nm of gold (red curve). The signal has been normalized to the value of magnetization at 125 K.

As it has been explained in chapter 2, films of CrCr exhibit ferrimagnetic ordering below a T_C of 240 K[14]. After the deposition of a 20 nm gold electrode, a dc magnetic measurement was performed by SQUID magnetometry on the final system. The result, depicted in figure 5.3, shows a preservation of the magnetic character of films of CrCr, with an unaltered T_C for the material. In consequence, it is possible to assume that under the conditions of preparation of the samples the PBA films preserve their chemical integrity.

5.2.2 Magnetoresistance measurements

After the fabrication process, the sample was directly transferred to a PPMS set-up for the MR characterization. Pt wires were employed for connecting the four cells of the device to the PPMS sample holder. By different combinations of the connectors it was possible to evaluate the four cells of the sample. Owing to the high resistance of the films, electrical conductivity measurements were performed using a two-point probe method. In figure 5.4 it is depicted the I-V curve registered at 200 K for an 80 nm thickness films of CrCr. A non-linear behavior at low temperatures was detected in the I-V plots of these samples, in addition to a clear temperature dependence of the curve shape. These two characteristics are an indication of an effective charge injection from the gold electrodes into CrCr and a subsequent transport by hopping in the bulk of the molecular-based semiconductor[19].

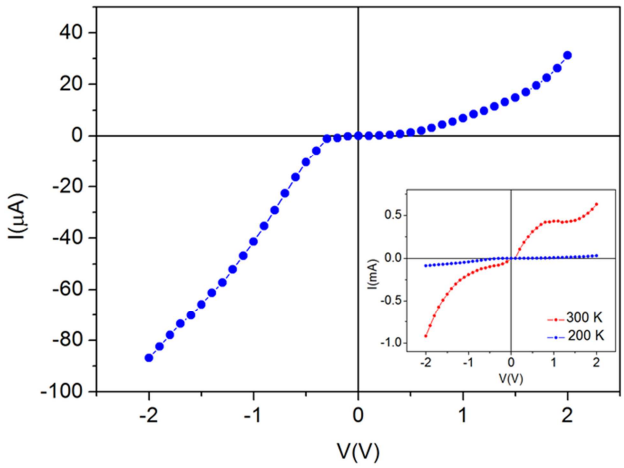

Figure 5.4- IV-trace at 200 K for an 80 nm thickness film of CrCr. *Inset*: Thermal dependence of the I-V traces.

The thermal dependence of conductivity, *σ (T)*, was studied for films of CrCr. As observed from figure 5.5, a drastic reduction of the film conductivity is registered when decreasing the temperature.

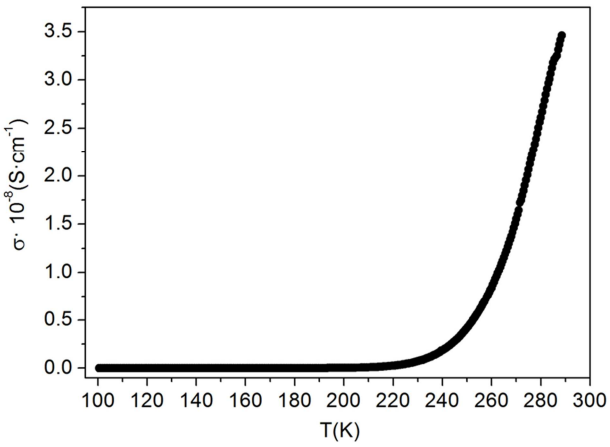

Figure 5.5- Thermal variation of the conductivity of a film of CrCr.

The conductivity is equal to 3.5×10^{-8} S·cm^{-1} at 300 K with an important decrease to 1.25×10^{-13} S·cm^{-1} at 100 K. This reduction in the conductivity of the system is an indication of a semiconducting behavior, as it has been reported for other PBA systems[17,20].The low conductivity values allowed us to rule out both ionic and proton conduction, arising from cations and water molecules respectively, as responsible for the electrical transport in the material[21]. In addition, the absence of an alkali cation in the structure of CrCr, determined by EDAX analysis, discards the scenario of an ionic transport. On the other hand, the proton conductivity related to humidity in a PBA material has been reported to be in the order of 10^{-3} S·cm^{-1} as measured by S. Ohkoshi *et al*[21]. In contraposition, the room temperature conductivity found in our films of CrCr can be associated to a vacuum-dried Prussian blue, free from moisture ($\sigma\sim10^{-9}$ S·cm^{-1})[17,18]. Based on the previous analysis, the electronic transport in CrCr can be described by a hopping conduction mechanism between neighboring metal sites[18,20,22]. The d- electrons of the chromium ion bound to carbon in the cyano-group are supplied to the π^*orbital of the ligand, with a consequent electronic delocalization in the cyano-bridge. In addition, the d-orbital of the chromium ion bound to the nitrogen in the cyano-group partially overlaps the π^* orbital of this ligand[18]. This situation generates a reduction of the activation energy for the electronic conduction, allowing an electron transfer by hopping mechanism between the chromium metal centers[18].

The conductivity data was fitted to a simple activation process. In fact, the $\sigma(T)$ vs T plot follows the Arrhenius law with activation energy of ΔE~0.43 eV (figure 5.6).

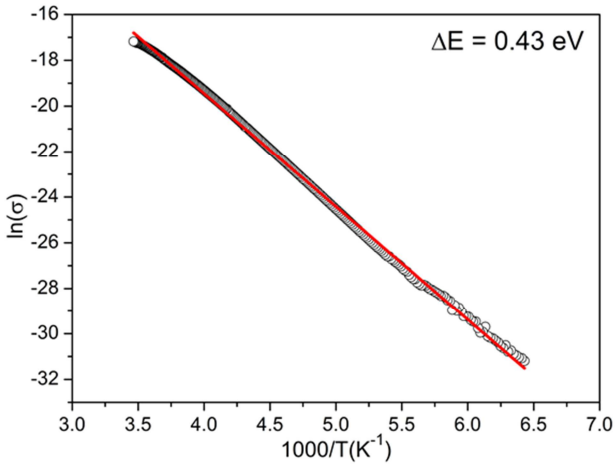

Figure 5.6- Fit of the *σ(T)* to the activated Arrhenius behavior with an estimation of *ΔE* ~ 0.43 eV.

Figure 5.7 shows the MR curves measured in films of CrCr with 80 nm thickness. The measurement was performed by applying a magnetic field parallel to the surface of the sample with a bias voltage of 1V at 200 K and 160 K[16].The MR ratio is calculated according to the formula:

$$MR = \{[\rho(H) - \rho(H=0)]/[\,\rho(H=0)]\} \times 100 \qquad (eq.5.1)$$

These preliminary measurements show a weak and positive MR below the critical temperature of the material. Values of MR at 200 K of 0.5 % and 2 % can be registered at fields of 10 kOe and 60 kOe respectively. In addition, no appreciable difference in the MR values is observed when decreasing the temperature from 200 K to 160 K. In this process of characterization, the study of the thermal variation of the MR was drastically limited by the critical decrease of the conductivity in the film when cooling the system below 150 K. A conductivity reduction of five orders of magnitude with respect to room temperature was observed.

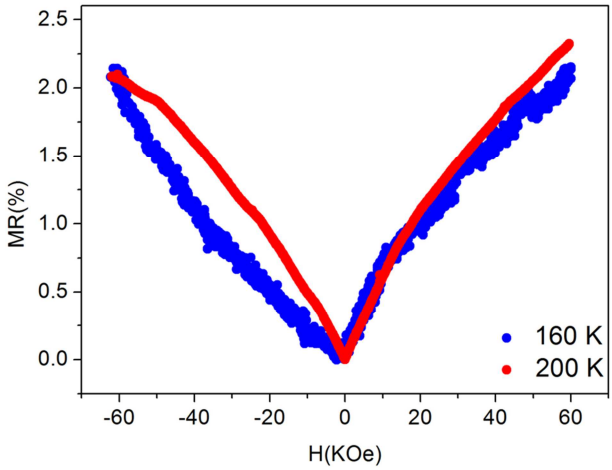

Figure 5.7- MR measured at 200 K and 160 K in an 80 nm thickness film of CrCr for a magnetic field applied parallel to the surface of the sample.

This fact can be distinguished by observing the MR response at 160 K in figure 5.7. A much noisier signal is detected respect to the one obtained at 200 K with an additional shape distortion. The same MR response was found for the measurements with a magnetic field perpendicular to the surface of the film. This is consistent with the isotropy in the magnetic properties in films of CrCr characterized by means of SQUID and extensively described in chapter 2 for this material[16].

A close inspection on the MR dependence with the magnetic field was done with the aim of giving a description of the possible mechanisms behind this property (figure 5.8). As a consequence of the positive MR in the material, an increase in the bulk resistivity was detected when increasing the external magnetic field. From an accurate analysis of the data, it was possible to make a linear fit of the MR data in the range of magnetic fields 0<H<15 kOe. Moreover, for magnetic fields above 15 kOe, a quadratic contribution appears in addition to the linear term in the fitting equation of the MR data. A non-saturating MR was registered in our measurements with a deviation from a pure linear response at high magnetic fields. This last point is illustrated by the presence of the dashed red line in figure 5.8, which serves as a visual reference of this deviation from the linear behavior when going to a high magnetic field limit.

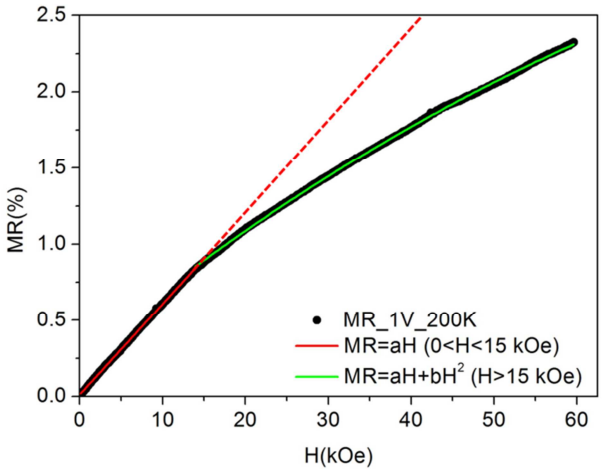

Figure 5.8- Fitting of the positive branch of the MR curve obtained at 1V and 200 K in the 80 nm thickness film of CrCr. The solid red line indicates the linear fitting in the range of 0<H<15 kOe, meanwhile the green solid curve shows the fitting with an extra quadratic term in the region of 15 kOe<H<60 kOe. The red dashed line is a visual reference indicating the divergence of the MR curve from the linear behavior as increasing the magnetic field.

The $V[TCNE]_x$ can be considered as a good reference in order to describe a phenomenological scenario for explaining the linear MR response in our PBA. This material, as in the case of the PBA under study, is a molecular-based ferrimagnet exhibiting a semiconductor behavior. The mechanism responsible for the positive linear MR in $V[TCNE]_x$ has been described in the context of the molecular orbital structure of the material, considering its influence on the propagation of a spin-polarized electron between metal centers[7–9]. This model cannot be directed extrapolated to our PBA, considering the different molecular orbital scenario respect to the $V[TCNE]_x$. The presence of an unpaired electron in the π^* orbital of the $[TCNE]^-$ unit is in major grade the responsible for the behavior of the electronic hopping under the application of an external magnetic field in that material. On the contrary, the CN ligand of the PBA has no unpaired electron in the π^* orbital invalidating the application of the previously indicated model. Despite this important difference, the same philosophy has to be considered in order to develop in the future a model which could include the molecular orbital characteristics of the PBA, in addition to the influence of the

magnetic ordering on the hopping of the charge carriers between Cr centers. It is important to highlight that no MR response was detected for films of CrCr above the T_C of the material[16]. This fact can be considered as an indication of the importance of the AF interaction of the Cr ion sub-lattices in the MR mechanisms in this ferrimagnetic PBA. A complete determination of the energy level diagram of the material would be a key point for understanding the possible scattering mechanisms involved in the electronic hopping through the PBA. This could allow determining the grade of scattering for each electron spin projection (S=±1/2). The preferential scattering of one electron channel could be defined the spin polarization characteristics of this chromium cyanide material. On the other hand, the additional quadratic term which appears in the high magnetic field regime (15 kOe < H <60k Oe) can be associated to an ordinary magnetoresistance (OMR). This is the magnetoresistance that varies as H^2 in half metallic ferromagnets such as CrO_2[23]. The impact of the Lorentz force on the moving charge carriers is the origin of the OMR, in a similar way to the Hall effect[24]. It is interesting to mention that, despite we have a polycrystalline material, the grain effects on the MR have not been considered in our analysis. The low field MR detected in perovskites of the type $La_{1-x}Sr_xMnO_3$ (LSMO) is usually interpreted in terms of spin-polarized tunneling through electronic barriers across the grain boundaries. The nature and size of these grain boundaries play a major role in the low field MR in LSMO samples[24].This mechanism has been described for other systems such as granular magnetic films of Co-Al-O.[25] In this context, a reduction in the resistivity when increasing the magnetic field is observed leading to a negative MR response. This is a consequence of the increase in the spin-dependent tunneling between grains as their magnetizations become parallel. The fact of detecting a positive MR in films of CrCr has moved us to discard, in first instance, the influence of the grain structure in the observed behavior.

The next step in the study described in this chapter is the evaluation of the potential application of films of CrCr as spin injector electrodes in a spin valve structure. With this aim, some preliminary studies have been done which will be described in the following section.

5.2.3 Preliminary studies on the application of CrCr thin films as spin injector electrodes

A complete description of the energy levels of CrCr would allow the proper selection of the rest of materials for building up the interfaces in a molecular spintronic structure. Ultraviolet Photoemission Spectroscopy (UPS) and cyclic voltammetry (CV) are two techniques widely applied for the determination of the absolute energy levels within the band structure of a material[26,27]. By means of the UPS technique it is possible to determine the ionization energy of a material on surface. This energy can be related to the position of the valence band or the HOMO in molecular systems[26]. On the other hand, solution-based CV experiments are able to establish the relative oxidation potentials which are indirectly related to the ionization energy of the material[26]. In principle a characterization with UPS is highly desired, nevertheless the high cost and complexity tends to favor the application of CV for the characterization of the energy features of a material[26]. Preliminary UPS studies on thin films of CrCr were performed in collaboration with the Ultrafast Phenomena at Surfaces research group at the department of Physics and Research Center OPTIMAS (University of Kaiserslautern). It was not possible to extract information of the energy levels of CrCr by means of this technique. This situation could be explained based on the high surface sensitivity of this experimental procedure[28]. In general, the materials studied by UPS are grown in-situ under ultra-high vacuum (UHV) conditions to guarantee the maximum control over the sample composition. Thus the electrodeposition process employed for the fabrication of films of CrCr would not be promoting the proper conditions for the UPS analysis. The chemical control of the surface generated by a solution process method such as electrodeposition, cannot be compared to the one achieved under UHV conditions.

Thus considering this limitation for a proper UPS characterization, we decided to apply the CV technique for getting an estimation of the energy levels in our PBA. CV is a dynamic electrochemical method in which current-potential curves are registered in an electrolyte environment[27]. By this technique, it is possible to correlate the oxidation and reduction potentials of a material with the ionization

potential (IP) and electron affinity (EA), respectively[27,29,30]. In addition, the oxidation and reduction potentials can be related to the energy levels of the valence band (VB) and conduction band (CB) of the material respectively[27].By following the method described by Miller et al.[31], after the electrodeposition of an 80 nm thickness film of CrCr, this system was immersed into a blank solution of 0.2 M of KCl. By employing the same Ag/AgCl reference electrode, used for the electrochemical deposition, CV curves were measured at 20 mV/s scan rate (figure 5.11). Prior to this, the correct calibration of the reference electrode was verified by performing CV measurements in an aqueous solution of 1M KNO_3 and 2 mM $K_3Fe(CN)_6$. The same calibration curve as the one established by the manufacturer was registered for the Ag/AgCl reference electrode. The CV measurement of a 80 nm thickness films of CrCr, depicted in figure 5.9, exhibits a quasi-reversible wave at *ca.* -0.85 V vs Ag/AgCl as reported in literature[31]. The reduction of the Cr anion is associated with the reversible redox at this potential.

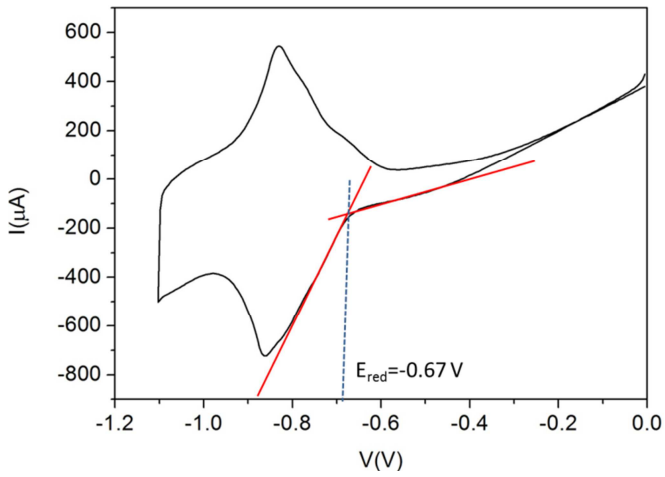

Figure 5.9- CV measurement of an 80 nm thickness film of CrCr at 20 mV/s scan rate in a blank solution of 0.2 M KCl. The quasi-reversible wave at ca. -0.85 V vs Ag/AgCl corresponds to the reduction of the Cr anion. The reduction potential E_{red}=-0.67 V was obtained from the onset of the CV curve.

The electron affinity (EA) can be calculated from the reduction potential E_{red} vs Ag/AgCl applying the expression[29,30]:

$$EA = -(E_{red} + 4.4)\ eV \quad (eq. 5.2)$$

The E_{red} has been determined to be -0.67 V vs Ag/AgCl, from the onset of the CV curve (figure 5.11). With this information an EA of -3.73 eV has been estimated from using equation 5.2. The value of the ionization potential (IP) is calculated from the energy band gap (E_g) of the material determined by UV-visible spectroscopy. In chapter 2, it was extensively explained the calculation of the E_g for thin films of CrCr. Assuming, the most simplified scenario of a direct band gap in the material, an E_g = 2.16 eV was determined. By applying the relation[30]:

$$IP = EA - E_g \quad (eq. 5.3)$$

an IP of -5.9 eV is established for the 80 nm thickness film . As it was previously indicated, the energy of the conduction band (CB) and valence band (VB) can be correlated with the EA and IP of the material respectively. Thus from the CV procedure, the position of the CB band can be located at -3.73 eV respect to the vacuum level, meanwhile the VB is lying deeper in energy at – 5.92 eV.

It is important to remark, that we are aware of the limits established by this technique for a precise estimation of the energy levels in the material. The electron transfer processes taking place during the CV scans are influenced by certain external factors. Possible deviations from the values extracted by UPS characterization can be originated by charge image effects at the film surface and solvation effects introduced by the electrolyte[26]. In addition, extra energetics barriers at the surface of the film can appear in the electron injection process[29]. It has to be considered that, meanwhile the UPS measurement is done under UHV conditions, in the CV an electrolytic solution is present. Thus, charge restructuration events will be locally produced in both the PBA network and the electrolyte environment during the electrochemical reduction of the material. This situation could influence the values obtained from this technique for the energy levels of the material. Despite these limitations associated to the CV, the characterization performed on our films of CrCr is a good starting point

for preliminary studies on the potential application of this molecular-based ferrimagnet in the field of molecular spintronics.

In chapter 1 it has been described the motivation of introducing molecular-based materials in spintronic structures. One of the fundamental objectives in this field is to overcome of the so-called conductivity mismatch problem[1,32]. This is one of the main obstacles for the efficient spin injection from metallic electrodes to organic semiconductors[3,11]. The development of spin injector electrodes based on molecular-based materials provides a possible solution to this problem[1]. In order to evaluate the feasibility for applying ultra-thin films of CrCr, we have made preliminary studies on a spin valve structure containing Co as the spin analyzer electrode. This is one of the most common ferromagnetic electrodes employed for such role in spintronic devices[3].

Up to know, $V[TCNE]_x$ has been the only molecular-based material applied for the fabrication of an all-molecular spin valve[13]. By sandwiching a tunneling barrier of rubrene between two $V[TCNE]_x$ electrodes, a spin valve MR effect was detected by A.J. Epstein et al[13]. Keeping the philosophy of an all-molecular spintronic structure, we wanted to extend this concept taking profit of the solution-process method employed for the preparation of ultra-thin films of CrCr. In this sense, the fabrication of a molecular spin valve from a complete solution-process method would suppose an advantage with respect to other approaches relying in the possibility of scalable, low-cost and large areas deposition. With this concept in mind, we have chosen for the prototype a polymeric spacer deposited by spin-coating as the spin collector medium. This spin collector is composed by the conjugated polymer with formula poly(9,9-dioctylfluorene-*co*-benzothidiazole)named as F8BT[33]. This is a light emitting polymer (LEP) with ambipolar characteristics, capable of transporting both electrons and holes, being for this reason widely applied in the field of organic electronics[33]. In the second part of this thesis, the characteristics of this material will be extensively described, as well as its ability for working as a spin collector layer of a molecular spin valve, which at the same time can act as a light emitting device. A simple hybrid structure has been proposed as the first prototype, which is composed by a spin collector layer of F8BT sandwiched between a spin injector electrode of CrCr and a spin analyzer electrode of Co.

The diagram of energy levels of this device is depicted in figure 5.10 considering the estimation performed by means of CV on films of CrCr.

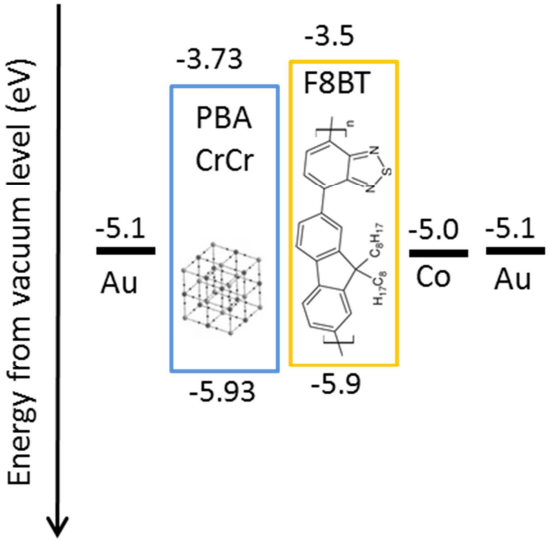

Figure 5.10- Energy level diagram of the prototype device containing layers of CrCr, F8BT[33],Co[34], Au[34].

The prototype device was fabricated by transferring the 80 nm thickness film of CrCr, obtained by electrochemical deposition (according to the method described in section 5.2.1) to a clean room. Then, a 35 nm thickness layer of F8BT was deposited by means of spin-coating from a chlorobenzene solution. The whole system was annealed in a glove box at 100 ºC during 30 minutes to complete the formation of the F8BT layer. Subsequently, the structure was transferred to the metal evaporator for the deposition of the top electrode. Under high-vacuum conditions (base pressure $<10^{-6}$ mbar), a 20 nm film of Co was deposited in a cross-bar configuration respect to the electrodes of CrCr. For this aim, the same mask than the one employed for the fabrication of the working electrodes of gold was used. With this mask and without breaking the vacuum, a final layer of 35 nm thickness of Au was deposited on top of the Co as a protection layer against oxidation. Both layers were evaporated at a very low rate of 0.01 nm/s in order to prevent the diffusion of metal atoms into the organic material, originating the so-called "ill-defined layer"[35]. A more detailed

description of the experimental set-up of the clear room can be found in chapter 6. At the end of the process, a device with four cells with an active area of 0.0025 cm^2 is obtained. The 3D sketch of the prototype spin valve structure is depicted in figure 5.11.

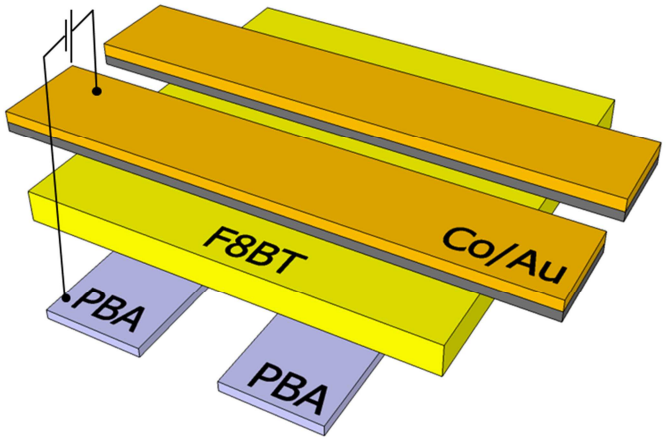

Figure 5.11- 3D sketch of the prototype spin valve indicating the biasing procedure.

As it was indicated in chapter 1, two possible resistance states can be stabilized in a spin valve by modifying the relative alignments of the magnetizations of each electrode. In a conventional spin valve, it is possible to change from a high to low resistance states by passing from an antiparallel (AP) to a parallel (P) alignment of electrode magnetizations by sweeping an external magnetic field[1,3,36]. Thus, for the correct performance of a molecular spin valve it is necessary to have a sufficient difference in the coercive fields of the electrodes for stabilizing P and AP states.

As shown in figure 5.12, from the MOKE characterization of both magnetic electrodes, this point is clearly accomplished. A coercive field of 850 Oe was measured at 200 K for an 80 nm thickness film of CrCr as described in chapter 2, meanwhile a coercivity of 175 Oe was registered for the Co electrode.

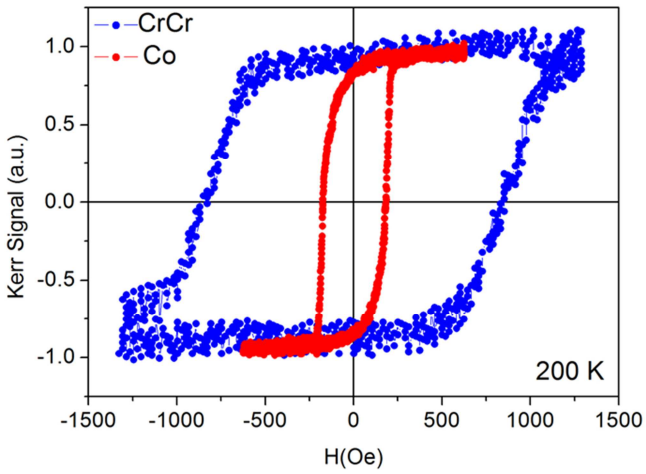

Figure 5.12- Comparative of the MOKE signals of an 80 nm thickness electrode of CrCr (blue curve) with an H_c= 850 Oeand a 20 nm thickness Co electrode protected with gold (red curve) with an H_c= 180 Oe measured at 200K.

After the fabrication process, the device was transferred to the PPMS set-up for evaluating the MR properties. In view of to the high resistivity of the structures, the electrical conductivity measurements were performed using a two-point probe method, in the same way as described for isolated films of CrCr. In first instance, IV-curves of the device were registered according to the biasing procedure indicated in figure 5.11 (positive biasing for the Co electrode).The IV-traces of the device exhibited a highly non-linear behavior in all the temperature range. In addition, an important thermal evolution was detected for these I-V traces (figure 5.13). This is an indication of a charge carrier injection from the magnetic electrodes to the F8BT followed by a hopping in the conjugated polymer[37–39]. Thus, a transport of charge carriers in the OSC can be considered in our device. It is interesting to remark that the sharp decrease in conductivity of the PBA electrode when cooling down the system should be also considered in the important thermal evolution of the IV-trace (figure 5.13 inset). The slight asymmetry detected in the I-V curve for negative and positive biasing can be ascribed to the asymmetry of the device structure.

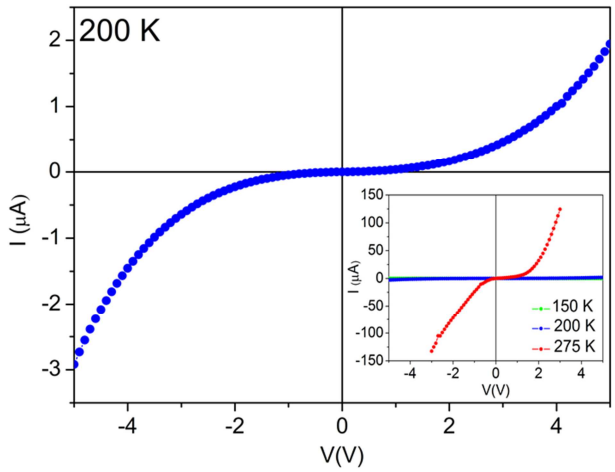

Figure 5.13- I-V curve of the spin valve structure measured at 200 K showing a high non-linear behavior, indication of a carrier injection followed by hopping in the F8BT. *Inset*: Thermal evolution of the I-V traces.

By studying the energy level diagram (figure 5.10), it is possible to observe that the energetic barrier established for carrier injection into the HOMO of the F8BT is considerably lower respect to the one existent for the LUMO of this material for both electrodes. Thus, it is likely that under both biasing signs, the current density in the device is determined by holes as the majority carriers. With respect to the MR measurements, the large temperature dependence of the conductivity of the PBA electrode, has limited considerably the thermal window for evaluating this property. Below 150 K the resistivity of these structures increased drastically, establishing a signal-to-noise ratio out from the sensitivity of our set-up. An in-plane external magnetic field was swept between extreme limits, through the values corresponding to the coercive field of the electrodes, in order to detect the possible resistance switching in the molecular spin valve. The typical MR feature of a spin valve[36] was not detected for any voltage and temperature under analysis. One possible reason for this absence of spin valve MR response could be the screening effect established by the high resistance of CrCr at low temperatures. In the spin valve structures using $V[TCNE]_x$ it has been reported that below a certain temperature, in that case 100 K, the device resistance was dominated by the bulk resistance of the molecular-based ferromagnetic semiconductor[11,13]. In this low temperature range, the bulk

resistance of the $V[TCNE]_x$ was so high that it was not possible to detect any field-dependent interface resistance changes.

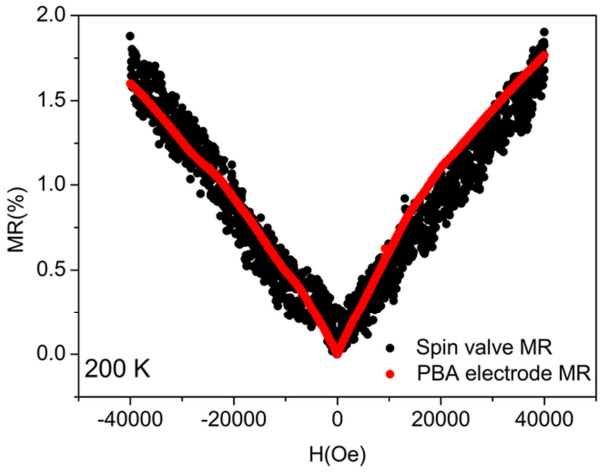

Figure 5.14- Comparative of the MR measured at 1V and 200 K for the spin valve structure and the electrodeposited electrode of CrCr.

Considering this, we evaluated the impact of the bulk resistance of CrCr on the molecular spin valve performance. With this aim, the MR was measured in the same range of magnetic fields than the one employed for the characterization of the isolated PBA electrode. A representative curve obtained at 1V and 200 K in the device is shown in figure 5.14. Compared to the MR signal of the isolated PBA thin film at the same voltage and temperature, one observes that the MR of the whole device resembles quite well the MR response of the PBA electrode both in sign and magnitude. This result indicates that the MR response of CrCr dominates over the MR behavior of the whole structure. In addition, we are confirming a charge flow through the PBA film, discarding possible pinholes in the electrodeposited electrode, which could lead to a direct contact of the F8BT with the Au working electrode[40].

Taking into account all this information, it is very likely that the bulk resistance of the PBA electrode is effectively screening a possible spin valve MR response in the range of voltage and temperature under study. It would be of great interest to evaluate other possible scenarios to explain the absence of a proper spin

valve MR in the device. In this context, it will be of fundamental interest to confirm the effective spin injection from the PBA electrode to the OSC spacer. As possible experiments we propose : i) to study a spin-LED device formed by an interface PBA/AlGaAs in order to optically detect the spin injection across the interface[40], and ii) to perform muon-spin resonance experiments[41].

5.3 Conclusions and perspectives

In this chapter it has been described the procedure for electrodepositing ultra-thin films of CrCr on substrates of reduced size. The design and fabrication of a sample adaptor for these small substrates has allowed depositing 80 nm thickness films of this chromium cyanide by using the conventional electrochemical cell configuration. Devices with active areas of 0.0025 cm^2 have been obtained for a PBA film sandwiched between two gold electrodes in a cross bar configuration. By studying this structure we have measured for the first time the MR properties a polycrystalline thin film based on a PBA. Positive MR signal up to c.a. 2.2 % at 60 kOe and 200 K has been registered. For explaining the linear MR behavior it is needed the development of a model which could include the molecular orbital characteristics of the PBA, in addition to the influence of the magnetic ordering on the hopping of the charge carriers between Cr centers. In this context, the molecular view applied for the development of a MR model in the molecular-based ferrimagnet $V[TCNE]_x$ could be taken into account as a reference for that purpose. On the other hand, the additional quadratic contribution to the MR in the high field region has been explained in terms of an ordinary MR in the material.

It is interesting to compare the MR properties obtained for our molecular-based material with those reported for other magnetoresistive materials. One can first compare with films of $V[TCNE]_x$, x~2,which is a high-T_c molecular-based magnet ($T_c \approx 280K$) showing a similar energy gap $\Delta E \sim 0.5$ eV. This material also exhibits a linear dependence of the MR with H at low fields, with a maximum value of 0.7% around T_c at 0.6 T. This value is slightly higher than the MR value observed in our material at the same field (≈ 0.4%). Another class of systems for comparing with our results is represented by the magnetic metal oxides. The

best MR results have been observed in doped perovskite manganites[24]. Polycrystalline films of these materials can exhibit colossal MR (typically around 30% at low fields), which is two orders of magnitude higher than in our material. Still, other magnetoresistive materials based on metal oxides have shown to exhibit MR ratios which are closer to those observed in our molecular-based material. For example, in films of magnetite, Fe_3O_4, a 7.4% MR has been observed at room temperature and high fields (5 T), which is of the same order of magnitude than that observed in our film in similar conditions (≈ 2%).

Based on the interesting MR properties detected on CrCr a prototype spin valve structure has been fabricated. In addition, an estimation of the energy levels in films of this PBA was done by means of CV technique. With this information a spin valve structure employing the PBA electrode as spin injector and Co as spin collector, sandwiching a layer of the ambipolar conjugated polymer F8BT has been proposed. In the characterization of this device, no spin valve MR effect was detected. Instead, an important influence of the MR response of the PBA electrode on the behavior of the whole structure has been observed. Thus, a "screening effect" of the bulk resistivity of the electrode of CrCr when decreasing the temperature, has been proposed as a possible explanation for the absence of a spin valve effect in the prototype device. Note that we have chosen an OSC that can be deposited by spin coating. This choice is based on our final objective of fabricating an all-molecular spin valve from solution processing methods. In this sense, the proposed study is a first step in this direction.

Several tasks have to be developed in a near future regarding to the characterization of CrCr as a spin injector electrode for its inclusion in molecular spin valve. In first term, the phenomenological model presented in this chapter has to be extended to give a quantitative prediction of the experimental results. This would allow getting a more precise understanding of the MR mechanisms in this material. A study of the spin injection ability of CrCr has to be performed employing extra techniques such as the optical approach described in this chapter or the application of muon-spin resonance experiments. The energy level diagram of this material has to be confirmed by other experimental approaches such as UPS, despite the first attempts in this

direction were not successful. Having a precise description of the energetics of this material will allow the rational design of molecular spin valves with CrCr as an effective spin injector electrode.

The prototype spin valve structure, described in this chapter, has demonstrated the feasibility for fabricating devices with active areas down to 0.0025 cm^2. In this vein, it will be important to test other OSCs as spin collector media keeping the philosophy of fabricating an all-molecular spin valve by using solution processed methods. In the same line, the introduction of molecular barriers in the device deposited from Lagnmuir-Blodgett technique or self-assembling will be considered for the reduction of the charge injection barriers.

In conclusion, in this chapter an important advance has been done in the understanding of the potential application of the CrCr PBA in the field of molecular spintronics. This work has put the first stone of a long road which could lead to the inclusion of other PBA families with interesting functionalities into molecular spin valve structures. In addition, the extension of these studies to the family of vanadium chromium derivatives, with room temperature ferromagnetic ordering, could open the door for the fabrication of a new generation of spintronic devices with a working temperature interesting for feasible applications.

5.4 Bibliography

(1) Camarero, J.; Coronado, E. *J. Mater. Chem.* **2009**, *19*, 1678.

(2) Sanvito, S. *Chem. Soc. Rev.* **2011**, *40*, 3336.

(3) Dediu, V. A.; Hueso, L. E.; Bergenti, I.; Taliani, C. *Nat. Mater.* **2009**, *8*, 707.

(4) Nguyen, T. D.; Ehrenfreund, E.; Vardeny, Z. V. *Science* **2012**, *337*, 204.

(5) Xiong, Z. H.; Wu, D.; Vardeny, Z. V.; Shi, J. *Nature* **2004**, *427*, 821.

(6) Dediu, V. A. *Nat. Phys.* **2013**, *9*, 210.

(7) Prigodin, B. V. N.; Raju, N. P.; Pokhodnya, K. I.; Miller, J. S.; Epstein, A. J. *Adv. Mater.* **2002**, *14*, 1230.

(8) Raju, N. P.; Savrin, T.; Prigodin, V. N.; Pokhodnya, K. I.; Miller, J. S.; Epstein, a. J. *J. Appl. Phys.* **2003**, *93*, 6799.

(9) Prigodin, V. N.; Raju, N. P.; Pokhodnya, K. I.; Miller, J. S.; Epstein, a. J. *Synth. Met.* **2003**, *135-136*, 87.

(10) Raju, N. P.; Prigodin, V. .; Pokhodnya, K. I.; Miller, J. S.; Epstein, a. J. *Synth. Met.* **2010**, *160*, 307.

(11) Yoo, J.-W.; Chen, C.-Y.; Jang, H. W.; Bark, C. W.; Prigodin, V. N.; Eom, C. B.; Epstein, a J. *Nat. Mater.* **2010**, *9*, 638.

(12) Prigodin, V. N.; Yoo, J. W.; Jang, H. W.; Kao, C.; Eom, C. B.; Epstein, a J. *J. Phys. Conf. Ser.* **2011**, *292*, 012001.

(13) Li, B.; Kao, C.-Y.; Yoo, J.-W.; Prigodin, V. N.; Epstein, A. J. *Adv. Mater.* **2011**, *23*, 3382.

(14) Coronado, E.; Makarewicz, M.; Prieto-Ruiz, J. P.; Prima-García, H.; Romero, F. M. *Adv. Mater.* **2011**, *23*, 4323.

(15) Prima-Garcia, H.; Coronado, E.; Prieto-Ruiz, J. P.; Romero, F. M. *Nanoscale Res. Lett.* **2012**, *7*, 232.

(16) Coronado, E.; Prieto-Ruiz, J. P.; Prima-Garcia, H. *Chem. Commun. (Camb).* **2013**, *49*, 10145.

(17) Tennakone, T., Dharmaratne, W. G. D. *J. Phys. CSolid State Phys.* **1983**, *16*, 5633.

(18) Yamada, S.; Kuwara, K.; Koumoto, K. *Mater. Sci. Eng. B* **1997**, *49*, 89.

(19) Wohlgenannt, M. *Phys. status solidi - Rapid Res. Lett.* **2012**, *6*, 229.

(20) Behera, J. N.; Alessandro, D. M. D.; Soheilnia, N.; Long, J. R. *Chem. Mater.* **2009**, *21*, 1922.

(21) Ohkoshi, S.; Nakagawa, K.; Tomono, K.; Imoto, K.; Tsunobuchi, Y. *J. Am. Chem. Soc.* **2010**, *132*, 6620.

(22) Stallinga, P. *Adv. Mater.* **2011**, *23*, 3356.

(23) Yuan, L.; Ovchenkov, Y.; Sokolov, a.; Yang, C.-S.; Doudin, B.; Liou, S. H. *J. Appl. Phys.* **2003**, *93*, 6850.

(24) Siwach, P. K.; Singh, H. K.; Srivastava, O. N. *J. Phys. Condens. matter* **2008**, *20*, 273201.

(25) Inoue, J.; Maekawa, S. **1996**, *53*, R11927.

(26) Dandrade, B.; Datta, S.; Forrest, S.; Djurovich, P.; Polikarpov, E.; Thompson, M. *Org. Electron.* **2005**, *6*, 11.

(27) Kuçur, E.; Bücking, W.; Nann, T. *Microchim. Acta* **2007**, *160*, 299.

(28) Gauglitz, G.; Moore, D. S. *Handbook of spectroscopy*; Wiley-VCH, 2014.

(29) Misra, A.; Kumar, P.; Srivastava, R.; Dhawan, S. K.; Kamalasanan, M. N.; Chandra, S. *Indian J. Pure Appl. Phys.* **2005**, *43*, 921.

(30) Crespilho, F. N.; Zucolotto, V.; Jr, J. R. S.; Carvalho, A. J. F.; Francisco, C.; Paulo, U. D. S.; Carlos, S.; Br-, S. P. *Int. J. Electrochem. Sci.* **2006**, *1*, 151.

(31) Buschmann, W. E.; Paulson, S. C.; Wynn, C. M.; Girtu, M. A.; Epstein, A. J.; White, H. S.; Miller, J. S. *Chem. Mater.* **1998**, *10*, 1386.

(32) Schmidt, G.; Ferrand, D.; Molenkamp, L.; Filip, a.; van Wees, B. *Phys. Rev. B* **2000**, *62*, R4790.

(33) Sessolo, M.; Bolink, H. J. *Adv. Mater.* **2011**, *23*, 1829.

(34) Michaelson, H. B. *J. Appl. Phys.* **1977**, *48*, 4729.

(35) Sun, D.; Yin, L.; Sun, C.; Guo, H.; Gai, Z.; Zhang, X.-G.; Ward, T. Z.; Cheng, Z.; Shen, J. *Phys. Rev. Lett.* **2010**, *104*, 236602.

(36) Vardeny, Z. V. *Organic Spintronics*; Taylor & Francis Group: Boca Raton-Florida, 2010.

(37) Lin, R.; Wang, F.; Rybicki, J.; Wohlgenannt, M.; Hutchinson, K. a. *Phys. Rev. B* **2010**, *81*, 195214.

(38) Yoo, J.-W.; Jang, H. W.; Prigodin, V. N.; Kao, C.; Eom, C. B.; Epstein, a. J. *Phys. Rev. B* **2009**, *80*, 205207.

(39) Sun, X.; Gobbi, M.; Bedoya-Pinto, A.; Txoperena, O.; Golmar, F.; Llopis, R.; Chuvilin, A.; Casanova, F.; Hueso, L. E. *Nat. Commun.* **2013**, *4*, 2794.

(40) Fang, L.; Bozdag, K. D.; Chen, C.-Y.; Truitt, P. a.; Epstein, a. J.; Johnston-Halperin, E. *Phys. Rev. Lett.* **2011**, *106*, 156602.

(41) Drew, a J.; Hoppler, J.; Schulz, L.; Pratt, F. L.; Desai, P.; Shakya, P.; Kreouzis, T.; Gillin, W. P.; Suter, a; Morley, N. a; Malik, V. K.; Dubroka, a; Kim, K. W.; Bouyanfif, H.; Bourqui, F.; Bernhard, C.; Scheuermann, R.; Nieuwenhuys, G. J.; Prokscha, T.; Morenzoni, E. *Nat. Mater.* **2009**, *8*, 109.

PART II

Chapter 6

Introduction part II

6.1 Towards the fabrication of a light emitting spintronic device

The fabrication of robust and reproducible electroluminescent devices showing modulation of light under external magnetic fields will suppose the rise of a new generation of multifunctional spintronic devices, named as spin-OLEDs. The fabrication of these light emitting spintronic devices is a common goal of molecular electronics[1] and molecular spintronics[2,3]. Through the use of organic semiconductors (OSCs) in molecular electronics (either small molecules or polymeric materials) it has been possible to develop a variety of devices such as organic solar cells[4], organic field-effect transistors[5] and organic light-emitting diodes (OLED's)[6], among others. In the particular case of OLEDs, there are several experimental and theoretical studies related to the effect of magnetic fields on this type of devices with non-ferromagnetic electrodes[7–10].These effects are mainly caused by the hyperfine nuclear fields. One can benefit of these effects for modulating the output emission of an OLED with external magnetic fields[11]. In this case, the fringe field of a magnetic electrode is employed for inducing large gradients in the magnitude of the random local field on the OSC allowing a control on the current and electroluminescence of the device.

Another interesting approach for modulating the emitted light of a device, is based on the design and fabrication of structures in which the electroluminescence is sensitive to the spin polarization of the carriers injected in the OSC, the so called spin-OLED[12]. This is precisely the approach in which the second part of this thesis is focused. The key point of this strategy is the presence of a spin polarized current in the device which will lead to a magneto-electroluminescence effect (MEL) under the application of an external magnetic field. The control of the singlet:triplet exciton statistics in the spin collector medium allows the modulation of the device light output. For this aim, molecular spintronics provides the proper structure named as organic spin valve (OSV) constituted by an OSC sandwiched between two spin polarized (SP) electrodes acting as spin injector and detector[13,14]. The OSCs working as spin collectors are expected to possess a large spin-dependent transport (SDT) length

due to their weak spin-orbit coupling and weak hyperfine interaction which allows the preservation of the spin information of the injected carriers[13–16]. It is fundamental to remark that, for the obtaining of a proper spin valve MEL effect, it is mandatory to generate appropriate working conditions for the device, in terms of operation voltage and temperature. This would allow the coexistence of electroluminescence and spin polarized current in the OSC. Let us review some fundamental concepts with interest for this second part of the thesis which is focused on the fabrication of a spin-OLED presenting a spin valve MEL effect.

6.2 Organic semiconductors

Organic semiconductors (OSCs) are mainly classified into two groups, small molecules and polymers according to their molecular weight[17] (figure 6.1). As common feature, both types of OSCs show a π-conjugated chemical structure which leads to the delocalization of their highest energy electrons (π-electrons) over the entire extension of the π-conjugation[17,18].

In general, OSCs materials have an alternating sequence of single and double-bonds along the backbone. The carbons in this sequence show sp^2 hybridizations with three sp^2 orbitals (combination of s, p_x and p_y orbitals) forming a triangle and the p_z orbital located in a perpendicular plane[19]. From the overlap of the sp^2 orbitals, a single σ bond between two carbon atoms can be formed. On the other hand, the unhybridized p_z orbitals form additional π bonds. Under these conditions, a π-electron cloud is formed in the materials delocalized over the conjugation length. The integrity of the organic molecule is established by the σ bonds, which are the responsible of the molecular skeleton[17].

OSCs are materials with filled bonding π-orbitals and unoccupied anti-bonding π^*-orbitals. The highest occupied of these π-orbitals is called HOMO, and the lowest one LUMO. Let us pay a particular attention to the characteristics of π-conjugated polymers, as being the type of OSC employed in this thesis.

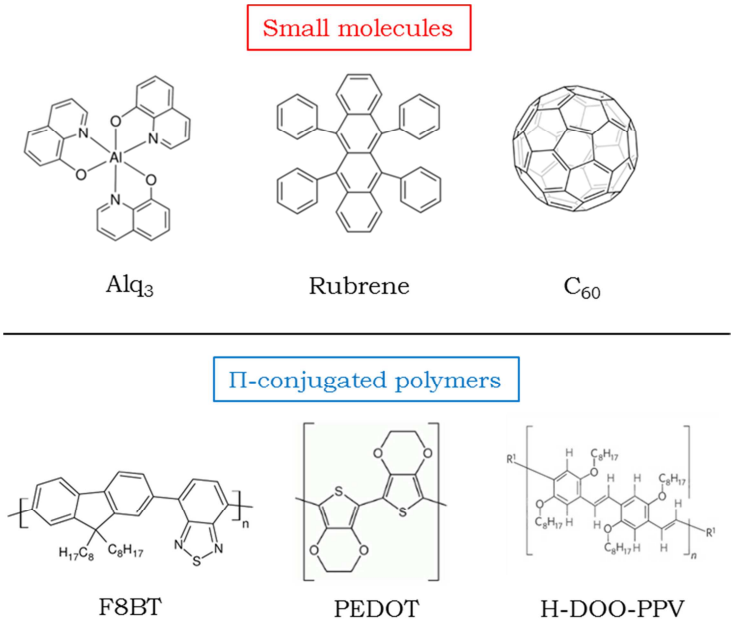

Figure 6.1- Example of the most common employed OSCs classified as small molecules and π-conjugated polymers.

6.2.1 Π-conjugated polymers

A π-conjugated polymer (PCP) is a carbon-based macromolecule in which there is an electron delocalization. It exhibits properties markedly different to those found in inorganic metals or semiconductors[17]. The fact of being quasi-1D systems confers to PCPs these unusual electronic properties, with strong intra-molecular but weak inter-molecular interactions. As a consequence of the low coupling between molecules the charge carriers in these materials are strongly localized on a molecule. The charge transport takes place by incoherent hopping of carriers between localized states. In this case, the site energy is a random variable distributed according to a Gaussian DOS[15]. This charge transport process lead to low mobilities in the material when compared to inorganic semiconductors. In the case of amorphous polymers, mobilities of the order of $\leq 10^{-1}$ cm^2/Vs are present[20], arising from the inter-chain disorder that limits the π-bonding overlapping. Another important factor determining the character of

the electronic states in PCPs is the presence of a strong coupling between charge carriers and lattice. In low dimensional systems, the effects of electron-lattice coupling are enhanced just as it happens with electron-electron interactions. In consequence, charge carriers in these materials are positive or negative polarons, rather than holes and electrons[15].

6.2.2 Primary excited species in organic semiconductors

Two major excitations that are found to be dominant in PCPs are charged or neutral. Under photoexcitation experiments, a photogeneration of neutral spinless excitations is produced. These species can relax to charged excitations or other type of neutral excitations such as spin triplets. On the other hand, under electrical excitation only charge excitations will be injected in the material, being possible their recombination into neutral excitations or other type of charged excitations.[21] In the following items it will be briefly described the different types of possible excitations in the material.

- *Polarons*: As a consequence of the weak intermolecular (van der Waals) forces in OSCs, a propagating charge carrier is able to locally distort the host material. The charge carrier combined with the consequent deformation can be treated as a quasi-particle named as polaron. This presents spin and is considered the primary excitation generated by an electrical stimulus in the non-degenerate ground state of PCPs. When using a PCP as active medium, this species is the major source of current in a device. The charge transport phenomenon is then described by a hopping of the polaron from chain to chain. The polaron is a charged entity that could be negative (P^-) or negative (P^+) having in both cases spin 1/2. In the hopping process two polarons, oppositely charged, can form a polaron pair (PP) if they are in adjacent chains. If the polarons are in the exciton capture distance they can form single or triplet excitons, depending on their spin.[15,17]

- *Polaron Pairs (PPs):* As described by E. Conwell *et al.*[22] two oppositely charged polarons, on two adjacent chains in the polymer, are going to form a PP entity by a Coulombic interaction. In an electrically excited system such as an OLED,

electrons and holes moving in different directions in the active polymer layer capture each other by a Coulombinc binding energy.In thiss way, they establish the precursors for the formation of singlet and triplet excitons, which are intrachain species.

- *Excitons:* The formation of excitonic states is one of the most important spin-dependent processes in OSCs. Excitons in organic materials are the result of very strong exchange-coupled pairs of electron and holes[15]. Indeed, the coupling strength in an exciton is in the order of meV. These species are generated when positive and negative charge carriers encounter each other in the OSC, being able to recombine radiatively, decaying into the uncharged ground state. This radiative decay is the responsible for light generation in OLED structures and display applications. As being the excitons formed from electron and hole polarons, having both a spin S=1/2, they can lead to a system that, according to quantum mechanical rules, can exist in four possible spin eigenstates, namely, one singlet and three triplet states[23]. Only singlet excitons can recombine radiatively in a fast way (fluorescence) with processes in the order of 100 ns, originating the electroluminescence in OLEDs. By spin flop of one of the polaron spins involved in the excitation (due to spin-orbit coupling or hyperfine interaction) an intersystem crossing from singlet to triplet manifolds is possible. The radiative emission from the excited triple state (phosphorescence) is generally weaker in an OSC as the optical transition from the triplet lower state to the ground state is forbidden. The only possibility for this optical transition is by a spin flip of the polaron spins[17]. In π-conjugated polymers this interaction is usually weak, thus the optical transition of the triplet exciton is relatively long (in the order of milliseconds[24]). Considering all this information, the electroluminescence quantum efficiency (η_{EL}) in a OLED is limited by the fraction of singlet excitons (χ_s) formed in the OSC. In the simplest scenario, based on the ratio of triplet to singlet states (3:1), χ_s is only $1/4$, leading to a maximum quantum efficiency of less than 25%. In figure 6.2 it is summarized all the possible processes for generation of the primary excited species in π-conjugated polymers[25].

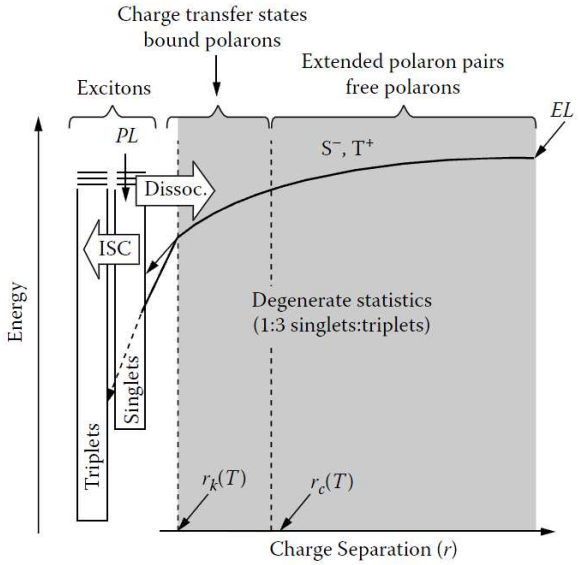

Figure 6.2- Binding energy of electrons and holes as a function of spatial separation. In this plot r_c and r_k describe the distances for which coulombic and exchange interactions become relevant. Image extracted from reference [25].

Once the processes taking place in π-conjugated polymers have been explained, the next step will be to describe some concepts regarding the optoelectronic devices. The understanding of the mechanisms in optoelectronic devices are a key point for the designing of an effective light emitting spintronic structure.

6.3 Basic concepts on optoelectronic devices

6.3.1 Working principles of Organic Light Emitting diodes (OLEDs)

In a typical OLED structure, the device is formed by two organic layers, being one of them selected for hole transport meanwhile the other one being responsible for electron transport and electroluminescence[26–28].Thus, the standard structure for OLEDs is established by an indium tin oxide (ITO) anode, a hole injection layer (HTL), very often PEDOT:PPS, a light emitting layer (or multilayer) acting as the electron transporting layer (ETL), and a metallic cathode[27].

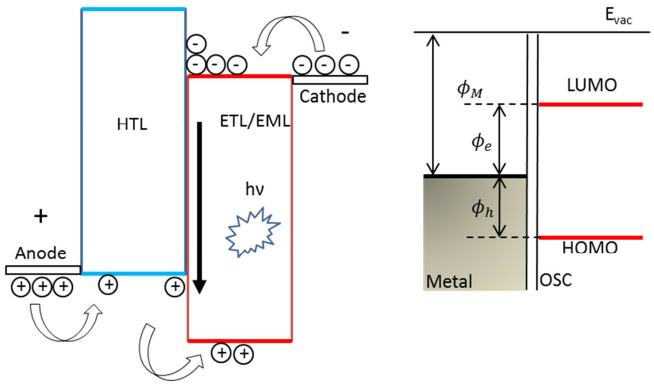

Figure 6.3- *Left:* Simple energy level diagram for a two-layer OLED. The processes of charge injection and recombination are illustrated. *Right*: Electronic structure of a typical OSC-Metal interface.

Upon the application of an external voltage, holes are injected from the anode to the HOMO of the HTL, meanwhile an electron injection takes place from the cathode into the LUMO of the ETL. The electron and holes migrate towards the oppositely charge electrode. The formation of polaron pairs (PPs) take place, being these species precursor excitations to singlet excitons that may recombine radiatively. The recombination process, leading to light emission, occurs near the junction of both organic layers inside the ETL (figure 6.3). The light is released through the transparent anode. The overall efficiency of an OLED is determined by several factors such as charge injection, charge transport, exciton formation, exciton recombination and electroluminescence. The most critical process, to take into account for the fabrication of devices with low operating voltages, is charge injection[28]. The two fundamental parameters determining the charge injection from a metal electrode to an organic material are the electron and hole injection barriers, ϕ_e and ϕ_h respectively (figure 6.3). In the Schottky limit the energy levels of both materials are aligned and the difference between HOMO and LUMO with the electrode workfunction, ϕ_M, can be considered as the barriers for carrier injection. Taking this into account, it is easy to understand that the optimal electron injection into the LUMO of the OSC is achieved for metals with low workfunction, minimizing in this way ϕ_e. This is achieved by employing cathodes of metals like Li, Mg, Ca and Ba. The

inconvenient of these materials is their strong chemical reactivity to atmospheric agents[27]. As a consequence, the device needs to be encapsulated raising considerably the cost of the final structure. An interesting approach for solving this problem is that of using metal oxides as efficient electron injection contacts in inverted OLEDs, the so-called HyLEDs[27].This is the optoelectronic structure that has been employed in this thesis for the design and fabrication of a multifunctional light emitting spintronic device. Thus let us describe briefly the working principles of HyLEDs.

6.3.2 Working principles of an inverted OLED (HyLED).

In a hybrid organic-inorganic light emitting diode (HyLED) the configuration of the device is inverted with respect to OLEDs. These type of devices present an inverse mechanism respect to OLEDs[27]. In this structure a n-type metal oxide thin film (Mox) is deposited onto a transparent ITO electrod (that acts as cathode). The role of the MO_x is to act as electron injection layer (EIL) facilitating the injection of the electron from the ITO to the LUMO of the organic emissive layer (EML). As EML, a widely employed light emitting polymer is the poly(9,9-dioctylfluorene-*co*-benzothidiazole), named as N965. For completing the device, a high work function air-stable metal (like Au, Ag or Pt) is used as the anode, avoiding the use of reactive metals. Between the organic material and the anode, a thin layer of a metal oxide with a very low conduction band (commonly molybdenum oxide, MoO_3) is inserted to facilitate hole injection (HIL)[27,28]. Under these conditions, hole injection takes place from the anode to the HOMO of the organic material through the CB of the metal oxide. A schematic view comparing the mechanism of an OLED and HyLED is depicted in figure 6.4. In a HyLED structure, using F8BT as EML and MoO_3 as HIL, the hole injection interface (F8BT/MoO_3) presents an ohmic behavior due to the effective promotion of holes into the HOMO of the F8BT through the HIL conduction band[27,28]. On the contrary, at the electron injection interface a barrier for electron injection into the LUMO of the EML is established. This situation produces a shift of the recombination towards the non-ohmic contact as a consequence of the unbalanced charge injection.

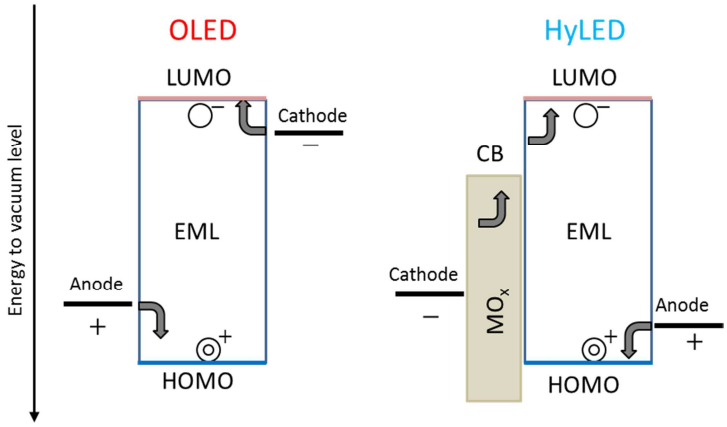

Figure 6.4- Comparative of OLED and HyLED mechanism regarding to charge carrier injection into the emissive layer (EML).

Under the application of a bias voltage, holes are efficiently injected into the HOMO of the F8BT through the conduction band of the HIL. The holes move then across the EML until they are blocked by the valence band of the MO_x (low enough for confine holes into the EML). Some of the most common mechanisms of efficiency lose in HyLEDs are related to the fact of having the recombination zone so close to the electron injection interface. These two mechanisms are exciton quenching at the MO_x acting as EIL and leakage current through this EIL, which are a consequence of the poor electron injection of this type of inverted OLEDs. This constitutes the main bottleneck for improving the efficiency.

6.3.3 Current-Voltage characteristics in OLEDs

The I-V curves for all operating OLEDs are non-linear, independently of the number and configuration of the organic layers. The models commonly reported for carrier injection in a OLED type structure are the Fowler-Nordheim (FN) model of tunneling[29] and the Richardson-Schottky (RS) model for thermoionic emission[30]. As previously described, the transport through the organic layer in the device is by hopping of polarons under the application of an electric field. When the applied electric field is in the order of less than 10^4 V/cm, and the

injected current is less than the intrinsic charge density, the current flowing in the organic is limited by Ohm's law. When the biasing voltage on the device is increased, the injected current density becomes larger than the intrinsic charge density. As a consequence of this, the injected carriers form a space charge layer near the organic/metal interface, due to the limited carrier mobility. The internal electric field is enhanced by this space charge in such a way that the current density flowing in the device is governed by the space charge limited conduction mechanism (SCLC) described by Mott-Gurney law[26,31].

6.4 Spintronics

In chapter 1, the definition and fundamental concepts of spintronics have been extensively described. As mentioned there this thesis focuses on molecular spintronics and, more concretely, on the design of new spintronic devices using molecular-based materials. We have already described the concept of organic spin valve (OSV) and organic tunneling junction in chapter 1[2,3,13,15]. Here we will briefly review a microscopic vision regarding the magnetoconductance in this type of devices.

6.4.1 Model for magneto-conductance in homopolar organic spin valves

We will focus on a homopolar OSV as this is the most common situations one can encounter (i.e., only one type of carrier is injected in the organic semiconductor)[14,32]. If the spin polarization of an electrode is P, then the fraction of injected carriers with a spin parallel to the electrode magnetization is[33]:

$$a = \frac{(1+P)}{2} \quad (eq.6.1)$$

Therefore, the injected carrier density with spin parallel (up;u) and antiparallel (down;d) to the electrode magnetization are respectively $n^u = an_0$ and $n^d = (1-a)n_0$ where $n_0 = n^u + n^p$ the total density of injected carriers. Under the application of an external biasing in the OSV, the charge carriers suffer a drift

between the electrodes, thus the spin selective densities become position dependent with $n^u(x)$ and $n^d(x)$. The position dependent spin polarization function, $S(x)$, is defined as:

$$S(x) = \frac{[n^u(x) - n^d(x)]}{[n^u(x) + (x)]} \quad (eq.\ 6.2)$$

In this model, it is supposed that the carriers are injected from the spin injector electrode (FM_1 at x=0 with magnetic polarization $P_1 = 2a_1 - 1$) and collected at the top spin collector electrode (FM_2 at x=d with magnetic polarization $P_1 = 2a_2 - 1$). In this situation, the total carrier density at the spin collector electrode, $(d) = n^u(d) + n^d(d)$, is independent on the relative orientations of the electrodes and consequently, from the Poison equation, the electric field $F(d)$ is the same for the two magnetization directions. In addition, the carrier mobility (μ) is considered to be independent on the magnetization direction. Thus, the current densities for parallel and antiparallel alignment of electrode magnetizations are expressed as $J^{\pm} = n^d(d)e\mu F(d)$. Under these conditions, a spin-polarized current is stablished in the device with the form:

$$J^{\pm} = \frac{1}{2}[1 \pm P_1 P_2 \bar{S}(d)]\, J \quad (eq.\ 6.3)$$

with $J = e\mu n(d)F(d)$ and $\bar{S}(x) = S(x)/P_1$ the "normalized" ($\bar{S}(0) = 1$) spin polarization. From all this information, the spin valve magneto-conductance can be calculated as:

$$MC_{SV} \equiv \frac{J^+ - J^-}{J^+} = \frac{2P_1 P_2 \bar{S}(d)}{1 + P_1 P_2} \qquad (eq\ 6.4)$$

When a diffusion process controls the decay of spin polarization $S(x)$, the spin polarization is expressed by the steady state (time independent) diffusion equation,

$$\frac{\bar{S}(x)}{\tau_s} = \frac{D\partial^2 \bar{S}(x)}{\partial(x)^2} \quad (eq.6.5)$$

where τ_s and D are the spin relaxation time and spin diffusion length, respectively. By solving eq. 6.5 one obtains $\bar{S}(x) = \exp(-x/\lambda)$, being $\lambda = \sqrt{D\tau_s}$ the spin diffusion length. Thus, the magneto-conductance defined in eq. 6.4 takes the form

$$MC_{SV} = \frac{2P_1P_2e^{-d/\lambda}}{1 + P_1P_2e^{-d/\lambda}} \qquad (eq.6.6)$$

This is a general formula for the GMR (d) of thick OSV devices, considering the decay of the spin polarization inside the organic interlayer (spin collector medium). Formally, it is similar to the famous Julliére expression for tunneling spin valves but modified for including a finite spin diffusion length in the organic material.

6.4.2 Spin relaxation mechanisms in an OSV

In an ideal OSV, the spin could be transported over an arbitrarily long distance. However, in real conditions the spin diffusion length in the OSC is limited by spin relaxation processes. There are two main mechanisms for spin relaxation: spin-orbit coupling and hyperfine interaction[15,34]. Let us describe briefly each mechanism.

- *Spin-orbit coupling:* Spin-orbit coupling is a relativistic effect, describing the interaction between the electron spin and its orbital motion around an atomic nucleus. In a general way, the spin-orbit coupling appears whenever a non-zero spin particle moves within a region in which a finite electric field is present. The electric field can be originated from an atomic nucleus or the band structure of a solid. The spin-orbit coupling has a direct relation with the atomic number, scaling as Z^4.[35] As the organic materials are mainly formed by low-Z atoms (in particular carbon atoms), spin orbit-coupling is usually small. Sulphur, aluminum or platinum atoms could provide an important source of spin-orbit coupling. Nevertheless, these atoms generally play a minor role in the carrier transport by hopping into an OSC.

- *Hyperfine interaction:* This spin relaxation mechanism originates from the interaction of an electron spin with the nuclear spins of the host material, primarily established by the hydrogen atoms of the compounds[15]. The electron-nuclear coupling Hamiltonian is defined as:

$$H_{hyp} = \sum_{i}^{N} A_i \vec{I_i} \cdot \vec{S} \qquad (eq.\ 6.7)$$

In this equation, N is the number of nucleus interacting with the electron spin, $\vec{I_i}$ the spin operator for a nucleus i, and $\vec{S}$ the electron spin. A_i is the hyperfine constant which accounts for the strength of the coupling between both types of spins. In disordered films the carriers spend sufficient time within the molecules (trapping time) leading to the appearance of a strong interaction between the carrier spin and the local hyperfine fields. This relaxation mechanism is considered the major responsible of the organic magnetoresistance (OMAR)[9,11]

6.4.3 Spin valve magneto-electroluminescence effect (MEL)

The obtaining of a light emitting spintronic device with a spin valve magneto-electroluminescence (MEL) effect is the objective of the second part of this thesis. Thus, it is important to briefly describe this effect. As it was already indicated in section 6.2.2 of this chapter, in OLEDs, light generation is usually completely based on singlet exciton decay, causing the fluorescence in the organic material. Radiative triplet exciton (phosphorescence) is negligible in most materials due to mainly three reasons: a) spin-forbidden triple/singlet decay, b) domination of non-radiative processes such as spin-triplet annihilation[36,37] and c) significantly lower wavelength for phosphorescent light arising from the strong exchange interaction with excitonic states[38]. By quantum statistics arguments the singlet:triplet ratio is determined to be 1:3 , in the simplest scenario, leading to a maximum internal quantum efficiency for light emitting devices of 25%[23]. Based on the fact that exciton formation and decay conserves electronic spins, it is clear that the spin of charge carriers (polarons) in an OLED device is very important for the internal quantum

efficiency[15]. In this sense, the injection of spin-polarized carriers could allow the modulation of the exciton statistics and hence the control over light emission in this type of structures[14,23,39]. Thus, for controlling light emission by this mechanism, it is necessary the presence of a proper spin injection in the OSC accompanied by a light emission resulting from this spin-polarized current through the structure. These devices exhibiting a spin valve MEL effect receive the name of spin-OLEDs. This type of structures has to work simultaneously as an OSV and as a light emitting device, in the same ranges of voltages and temperatures. This is the main bottleneck for the successful fabrication of these light emitting spintronic devices, since the OSVs reported so far[14] exhibit a serious degradation of their magnetoresistance performance for voltages at which light illumination takes place in optoelectronic systems.

6.5 Experimental approach

6.5.1 Device fabrication: work at the clean room

The spin-OLED devices described in this second part of the thesis have been prepared in a class 10000 clean room. The clean room is shielded from UV radiation coming from illumination, for protecting the sensitive organic materials during the whole fabrication process. The techniques allowed in the clean room, and employed for the device fabrication can be divided in two types: a) solution methods and b) thermal evaporation.

a) Solution processing methods: For the processing of the organic materials two techniques have been mainly applied: spin-coating and Langmuir-Blodgett technique (figure 6.5).

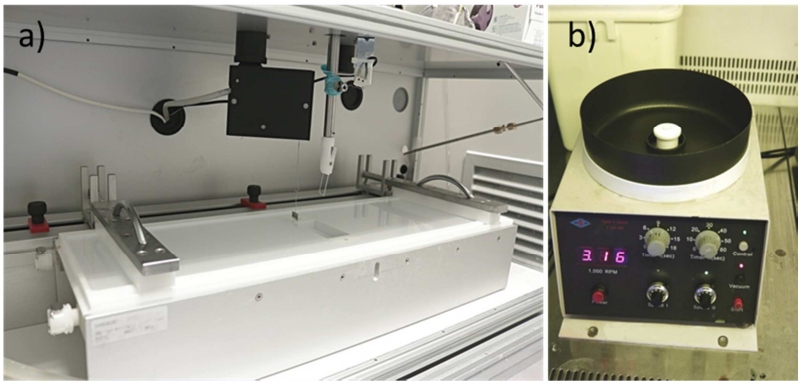

Figure 6.5- a) Langmuir- Blodgett set-up. b) Spin-coating system.

The organic light emitting layer in our spin-OLED is deposited by means of a *Chemat* spin coater (figure 6.5-b). Usually a small amount of the solution containing the precursor of the layer is applied on the center of the substrate. The substrate is then rotated at the desire speed in order to spread the coating material by centrifugal force. Rotation is continued while the fluid spins off the edges of the substrate, until the desired thickness of the film is achieved. The applied solvent is usually volatile, and simultaneously evaporates. So, the higher the angular speed of spinning, the thinner the film. The thickness of the film also depends on the viscosity and concentration of the solution and the solvent[40]. On the other hand, the molecular barriers included from solution method in our spin-OLED structures have been deposited by means of Langmuir-Boldgett (LB) technique. This technique is one of the most widely studied methods for the preparation of ordered monolayer and multilayer thin films[41]. By using this technique, pinhole-free molecular monolayers are assembled at an air-water interface for being subsequently transferred onto a substrate. The stability of the deposited film will be enhanced by the presence of strong interactions. However, they are not essential for the formation of the layers. A correct balance of the interactions between the molecules and between the molecules with the air-water interface is of great importance for the successful formation of molecular monolayers. The molecules employed for the formation of films by LB typically possess a hydrophilic head group and a hydrophobic tail. When these molecules are positioned at the air-water

interface, they spread out with their hydrophilic groups pointing to the water phase, meanwhile the hydrophobic tails orient away from the water. By means of a Teflon or similar barrier, the molecules spread in the water surface are compressed for producing a two-dimensional close-packed molecular array, which can be transferred to a solid support. The steps of this process are summarized in figure 6.6.

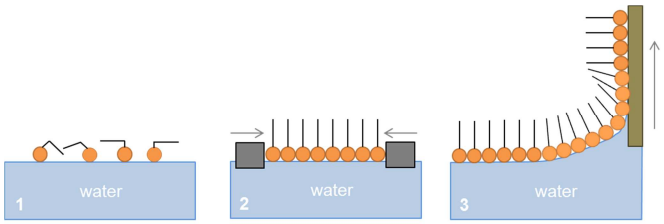

Figure 6.6- Deposition of a LB film: 1) amphiphilic molecules are spread on the air-water interface. 2) The molecules are compressed by a mobile barrier in order to generate a free-pinhole monolayer. 3) The monolayer is transferred to a substrate by dipping through the air-water interface.

If the selected substrate has a hydrophilic character, then the head groups of the molecules will be in contact with the surface and, on the contrary if a hydrophobic character is chosen for the solid substrate the head groups will be far from the surface. The control over the film thickness, orientation, and composition at the molecular levels are some of the advantages that make so interesting this solution process method for the preparation of molecular monolayers[41].

b) *Thermal evaporation techniques*:

The ferromagnetic electrodes fabricated in our laboratory, as well as the metal oxide (MoO_3) employed as the HIL in the spin-OLED have been deposited by means of a metal thermal evaporator.

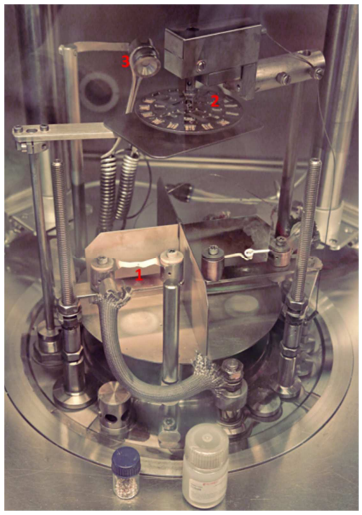

Figure 6.7- Thermal metal evaporator: 1) crucible position, 2) sample holder and masks, 3) quartz crystal microbalance.

This set-up is located inside a globe-box for, for preserving the chemical integrity of the evaporated materials. Inside the evaporator, high vacuum conditions (in the order of 10^{-6} mbar) can be established. Two crucibles allow the deposition of two different materials in the same evaporation processes. The samples are positioned in a rotatory sample holder which can incorporate shadow masks for establishing the desired active areas in the final device. The film thickness evolution is controlled in real time through a quartz crystal microbalance placed close to the substrates.

6.5.2 Magneto-electroluminescence (MEL) set-up

The magneto-electroluminescence (MEL) set-up allows the simultaneous characterization of the electrical transport and electroluminescence of the devices under external magnetic fields (figure 6.8).

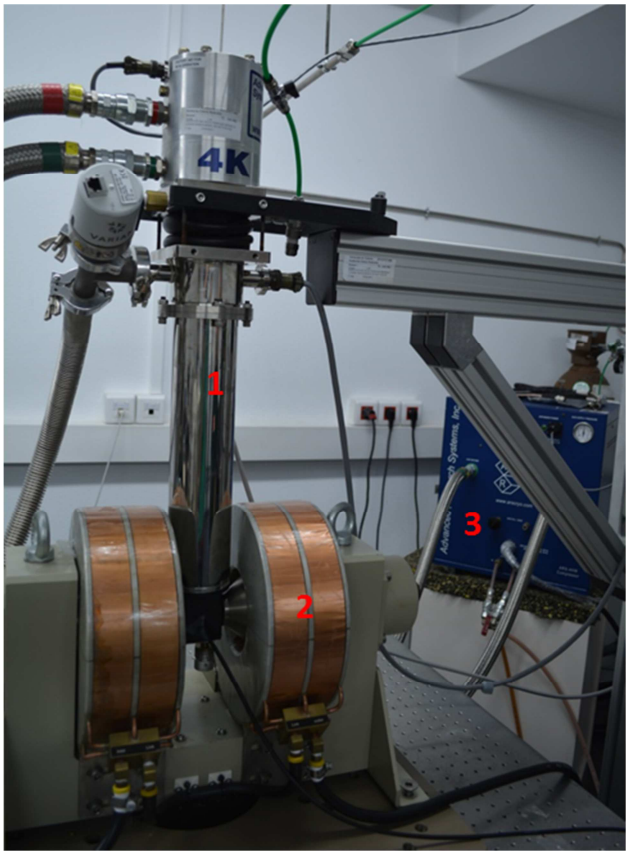

Figure 6.8- Photograph of the MEL set-up: in which it is possible to distinguish the cryostat (1), electromagnet system (2) and He compressor system (3).

This instrument is of fundamental interest in this second part of the thesis regarding the characterization of the magneto-electroluminescence effect in spin-OLEDs structures. The design and setting on of the instrument have been done in our laboratory as part of this thesis.

This set-up has a close loop cryostat (model C52045 F, ARS), which in combination with a He compressor (ARS), allows to cool down the samples under study to minimum temperature of 12 K (figure 6.8-a). By means of Varian pumping system (Mini Task AG81) it is possible to generate high vacuum conditions in the cryostat (10^{-6} mbar), allowing low temperature conditions in the set-up. The temperature in the position of the sample is monitored in real

time by a Cernox sensor which sends the information to a 332 Temperature Controller (Lakeshore). In this context, by means of the temperature controller it is possible perform thermal dependent characterizations from 12 K to 400 K. A high precision in the control of the temperature is achieved thanks to a PID system in the temperature controller which communicates with a heater in the head of the cryostat.

Once the sample is mounted on the sample holder, it is positioned between the poles of two electromagnets which are controlled by a bipolar current source (GMHW 231 HC). Magnetic fields up to ±1 T can be applied in the set-up. The electrical conductivity measurement is done by means of a Keithley 6517 A electrometer, which measures the current through the structure while acting as a voltage source. With this instrument it is possible to apply a maximum voltage of 20 V with a precision of hundreds of pA in the electrical current detection. Thus, under the application of an external magnetic field, magnetoresistance measurements can be done on the devices for a wide range of temperatures and magnetic fields. Simultaneously to the magnetoresistance measurements, the electroluminescence of the device (under external magnetic fields) can be registered. This measurement is done by a Si photodiode coupled to the cryostat window. The information of the photodiode is sent to a Keithley 6485 picoammeter which allows a precision in the order of pA in the registering of the photocurrent. The possible effects on the light measurement (an intrinsic response of the Si photodiode under the influence of external magnetic fields) have been analyzed on reference samples ruling out this situation. The control over the temperature and applied magnetic fields, as well as the registering of the electrical current and electroluminescence of the devices, are coordinated by a self-made Visual Basic PC program.

6.5.3 General characterization techniques

In this last section, we will briefly refer to the rest of techniques exclusively applied in this second part of the thesis.

- *Electroluminescence characterization*: For calibrating the photocurrent of the devices a Minolta LS100 luminance meter was employed. In addition, an Avantes luminance spectrometer was used to measure the EL spectrum of the light emitting devices. For certain situations, the EL properties of the devices were measured in the clean room employing a Si-photodiode coupled to a Keithley 6458 picoamperometer.

- *Raman spectroscopy:* μ-Raman measurements at room temperature were performed with a dispersive Jobin-YvonLabRam HR 800 microscope, working with an excitation line of 532 nm. The scattered light was detected with a thermoelectric cooled (-70 ºC) charge coupled device detector (CCD). It is also equipped with an Olympus BXFM optic microscope. All the measurements were carried out directly over the sample. In the experiments, the power employed over the samples was approximately 0.3 mW, with an exposition time of 60 seconds.
- *UPS characterization:* Photoemission experiments were performed in collaboration with Dr. Mirko Cinchetti from the Ultrafast Phenomena at Surfaces research group at the Department of Physics and research center OPTIMAS (University of Kaiserslautern). The measurements were done inside an ultrahigh vacuum chamber with a base pressure of 2*10^-10 mbar. A Cu(001) single crystal was used as a substrate and cleaned by cycles of argon ion sputtering through a ISE 10 sputter gun and annealing up to 800K. Afterwards a 30 ML (~5.4nm) thick Co thin film was evaporated with an e-beam evaporator (Omicron EFM3) at a rate of 0.25ML/min on top of the copper at room temperature and at a pressure of 5*10^-10 mbar. In the end the substrate was annealed only up to 370K to prevent diffusion of the Cu atoms into the Co film. At this thickness the Co has a fct structure with an easy axis along [110] perpendicular to the surface. The composition and crystalline ordering of the surface has been measured with the help of Auger spectroscopy and Low energy electron diffraction (LEED).The MoO_3 was evaporated on top of the cobalt using an Knudson cell evaporator (Kentax TCE-BSC with 3 cells) at a temperature of ~840 K and a pressure of 5.10^{-9} mbar. The Alq3 was evaporated on top of the MoO_3 using the same Knudson

cell evaporator at a temperature of ~500 K and a pressure of 7.10^{-9} mbar. The photo emission spectra were obtained by an Omicron HIS 13 vacuum ultra-violet lamp (VUV) at room temperature; the HeI line of Helium was used (21,2 eV). The light angle of incidence was 45° and the spectra were recorded with a commercial cylindrical sector analyzer (Focus CSA 300) equipped with a spin detector based on spin polarized low-energy electron diffraction (Focus SPLEED). All measurements were done at room temperature unless otherwise described.

6.6 Bibliography

(1) Koch, N. *Chemphyschem* **2007**, *8*, 1438.

(2) Camarero, J.; Coronado, E. *J. Mater. Chem.* **2009**, *19*, 1678.

(3) Sanvito, S. *Chem. Soc. Rev.* **2011**, *40*, 3336.

(4) Gu, S.; Neugebauer, H.; Sariciftci, N. S. *Chem. Rev.* **2007**, *107*, 1324.

(5) Zaumseil, J.; Sirringhaus, H. *Chem. Rev.* **2007**, *107*, 1296.

(6) Kulkarni, A. P.; Tonzola, C. J.; Babel, A.; Jenekhe, S. A. *Chem. Mater.* **2004**, *16*, 4556.

(7) Kalinowski, J.; Cocchi, M.; Virgili, D.; Di Marco, P.; Fattori, V. *Chem. Phys. Lett.* **2003**, *380*, 710.

(8) Bobbert, P.; Nguyen, T.; van Oost, F.; Koopmans, B.; Wohlgenannt, M. *Phys. Rev. Lett.* **2007**, *99*, 216801.

(9) Francis, T. L.; Mermer, Ö.; Veeraraghavan, G.; Wohlgenannt, M. *New J. Phys.* **2004**, *6*, 185.

(10) Desai, P.; Shakya, P.; Kreouzis, T.; Gillin, W.; Morley, N.; Gibbs, M. *Phys. Rev. B* **2007**, *75*, 094423.

(11) Macià, F.; Wang, F.; Harmon, N. J.; Kent, A. D.; Wohlgenannt, M.; Flatté, M. E. *Nat. Commun.* **2014**, *5*, 3609.

(12) Nguyen, T. D.; Ehrenfreund, E.; Vardeny, Z. V. *Science* **2012**, *337*, 204.

(13) Xiong, Z. H.; Wu, D.; Vardeny, Z. V.; Shi, J. *Nature* **2004**, *427*, 821.

(14) Dediu, V. A.; Hueso, L. E.; Bergenti, I.; Taliani, C. *Nat. Mater.* **2009**, *8*, 707.

(15) Vardeny, Z. V. *Organic Spintronics*; Taylor & Francis Group: Boca Raton-Florida, 2010.

(16) Dediu, V.; Murgia, M.; Matacotta, F. C.; Taliani, C.; Barbanera, S. *Solid State Commun.* **2002**, *122*, 181.

(17) Brütting, W., Adachi, C. *Physics of Organic Semiconductors*; Wiley-VCH: Weinheim (Germany), 2012.

(18) Coropceanu, V.; Demetrio, A.; Filho, S.; Olivier, Y.; Silbey, R.; Bre, J. *Chem. Rev.* **2007**, *107*, 926.

(19) Petrucci, R. H.; Bernardino, S.; Madura, J. D. *General Chemistry : Principles and Modern Applications*; Pearson, 2011; p. 1–.

(20) Sirringhaus, H.; Bird, M.; Zhao, N. *Adv. Mater.* **2010**, *22*, 3893.

(21) Barford, W. *Electronic and Optical Properties of Conjugated Polymers*; Oxford University Press: UK, 2005.

(22) Mizes, H.A., Conwell, E. M. *Phys. Rev. B* **1994**, *50*, 243.

(23) Yunus, M.; Ruden, P. P.; Smith, D. L. *Appl. Phys. Lett.* **2008**, *93*, 123312.

(24) Campbell, D. K.; Bishop, A. R. *Nucl. Phys. B* **1982**, *200*, 297.

(25) Segal, M.; Baldo, M.; Holmes, R.; Forrest, S.; Soos, Z. *Phys. Rev. B* **2003**, *68*, 075211.

(26) Müllen, K., Scherf, U. *Organic Light Emitting Devices: Synthesis, Properties and Applications*; Wiley-VCH: Weinheim (Germany), 2006.

(27) Sessolo, M.; Bolink, H. J. *Adv. Mater.* **2011**, *23*, 1829.

(28) Sessolo, M. *Hybrid organic-inorganic Light Emitting Diodes. PhD Thesis*; University of Valencia, 2010.

(29) Fowler, R. H.; Nordheim, L. *Proc. R. Soc. A Math. Phys. Eng. Sci.* **1928**, *119*, 173.

(30) Crowell, C. R. *Solid. State. Electron.* **1965**, *8*, 395.

(31) Brütting, W., Berleb, S., Mückl, A. G. *Synth. Met.* **2001**, *122*, 99.

(32) Ehrenfreund, E.; Valy Vardeny, Z. *Phys. Chem. Chem. Phys.* **2013**, *15*, 7967.

(33) Julliere, M. *Phys. Lett. A* **1975**, *54*, 225.

(34) Naber, W. J. M.; Faez, S.; Wiel, W. G. Van Der. *J. Phys. D. Appl. Phys.* **2007**, *40*, R205.

(35) Khudyakov, I. V; Serebrennikov, Y. A.; Turro, N. J. *Chem. Rev.* **1993**, *93*, 537.

(36) Dyakonov, V., Rösler, G., Schwoerer, M., Frankevich, E. L. *Phys. Rev. B* **1997**, *56*, 3852.

(37) Partee, J.; Frankevich, E. L.; Uhlhorn, B.; Shinar, J.; Ding, Y.; Barton, T. J. *Phys. Rev. Lett.* **1999**, *82*, 3673.

(38) Reufer, M.; Walter, M. J.; Lagoudakis, P. G.; Hummel, A. B.; Kolb, J. S.; Roskos, H. G.; Scherf, U.; Lupton, J. M. *Nat. Mater.* **2005**, *4*, 340.

(39) Bergenti, I.; Dediu, V.; Arisi, E.; Mertelj, T.; Murgia, M.; Riminucci, a.; Ruani, G.; Solzi, M.; Taliani, C. *Org. Electron.* **2004**, *5*, 309.

(40) Scrive, L. E. *MRS Proc.* **1988**, *121*.

(41) Taylor, R.F., Schultz, J. S. *Handbook of Chemical and Biological sensors*; IOP: Bristol-UK, 1996.

Chapter 7

Rational design and fabrication of a spin-OLED with Fe and Co electrodes

7.1 Introduction

As it has been discussed in the previous introductory chapter, the fabrication of a spin-OLED has been an active research topic in the past decade into the field of organic spintronics. In this type of multifunctional devices, the electroluminescence (EL) is expected to be sensitive to the spin polarization of the injected carriers thus allowing the modulation of the light output. This modulation can be achieved based on a proper control of the exciton statistics in the organic semiconductors by the application of external magnetic fields. For a modulation of the singlet and triplet ratio in a light emitting device it is necessary the presence of a spin-polarized current in the optoelectronic structure. In this sense, it is mandatory the coexistence of EL and spin valve (SV) performance in the device, at the same range of voltages and temperatures[1]. Under these conditions, a proper spin valve magneto-electroluminescence effect can appear in these light emitting spintronic devices. This situation has been the bottleneck for the successful achievement of a device of such characteristics, taking into account that in the range of voltages for light emission in an OLED (V>1V) the organic spin valve (OSV) performance is seriously damaged. Many groups has attempted without success the fabrication of a spin-OLED employing the organic semiconductor (OSC) Alq_3 s with the objective of establishing a spin-polarized current in the structure.[2,3]It was not until 2012 that Vardeny and co-workers[4] reported a spin-OLED fabricated with LSMO and Co, employing the deuterated polymer D-DOOPPV as OSC. They claimed in this work the presence of a spin valve MEL effect of 1% at 10 K and 4.5 V. This work will be analyzed with more detail in the following chapter of the thesis. The main chemical limitation of the strategy proposed by Vardeny et al.[4] is the expensive and complex process of deuteration for obtaining the polymer used as the emitting layer in this spintronic structure.

In this chapter of the thesis we propose an easier and cheaper alternative for the fabrication of a spin-OLED by constructing an OSV with the structure of an inverted OLED (HyLED) employing the green light-emitting conjugated polymer poly(9,9-dioctylfluorene-*co*-benzothidiazole) (F8BT) as spin collector layer. This HyLED device avoids the use of reactive metals such as barium or calcium

employed in conventional OLEDs which, in general, force the encapsulation of the system. By this mean more stable and robust devices can be fabricated.[5]In addition, the F8BT is a commercial material that has been employed just as received from the provider. Thus, along this chapter we will develop the rational design of a spin-OLED fabricated from all commercial non-expensive materials, easily accessible for any research group. The proposed HyLED[5] structure is formed by ferromagnetic electrodes of Fe and Co as cathode and anode, respectively, a barrier of AlO_x as the electron injection layer (EIL), and MoO_3 as a hole injection layer (HIL).

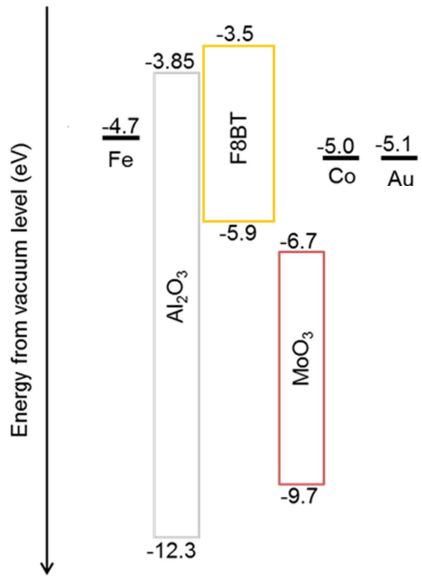

Figure 7.1- Diagram of energy levels for Fe,[6] Al_2O_3,[7] F8BT,[5] MoO_3,[8]Co[6] and Au[6]in the spin-OLED.

By using this approach, we have fabricated an OSV structure including materials such as F8BT and MoO_3, never applied so far in the field of organic spintronics. A schematic representation of the energy levels in this spin-OLED is depicted in figure 7.1. In the next pages, the main concepts regarding these materials and their interest for our purposes will be described.

7.1.1 The light-emitting polymer poly (9,9-dioctylfluorene-*co*-benzothidiazole) (F8BT) for optoelectronic applications

The application of fluorene-based conjugated polymers as light emitting polymers (LEPs) is very attractive in the field of organic electronics relying in their chemical and electroluminescent properties. High quantum efficiencies with thermal stability and photo-oxidation resistance are some of the interesting properties of these materials. In addition, the possibility of tuning by means of chemical modification and copolymerization physical parameters such as solubility and processability, represents an important advantage of this family of LEPs with respect to other polymers.[9]

In the present thesis, the derivative poly(9,9-dioctylfluorene-*co*-benzothidiazole) named as F8BT (figure 1) has been employed as the emissive layer in the spin-OLED.

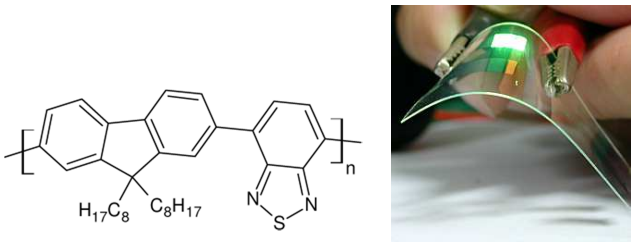

Figure 7.2- *Left*: Chemical structure of the light-emitting polymer F8BT;*Right* : Picture of a flexible OLED fabricated with F8BT as the LEP.

This conjugated polymer is an efficient green light emitter,[5] exhibiting a high photoluminescence quantum yield of up to 75 %. It has been widely applied as an electron transporter layer in polymer blend LEDs[10–12] and in photovoltaic cells[13–15]. In our particular case, F8BT has demonstrated to be a suitable material for its inclusion in HyLED structures.[5] As it was already described in chapter 6, HyLEDs present an inverted working mechanism with respect to OLED structures. As already mentioned, the electron injection process is one of

the main bottlenecks in the performance of HyLEDs[5]. In general, the majority of LEPs present a LUMO level lying between -2.5 eV and -3.0 eV. This supposes a limitation for an efficient device operation, due to the important energy barrier between the conduction band (CB) of the metal oxide and the LUMO of the LEP. In the F8BT the HOMO lies at -5.9 eV with a LUMO located at -3.5 eV (figure 7.1). This value is lower than the LUMO energy reported for other LEPs. This is consequence of the fact that in the LUMO of this conjugated polymer the copolymers electrons are strongly delocalized on the BT unit, which has a LUMO 1.5 eV lower compared to the LUMO of the fluorene unit.[5,16]

In addition, F8BT presents a high electron mobility (of the order of 10^{-3} cm^2 V^{-1} s^{-1}), representing one the few LEPs with such a good electron charge transport.[17,18]The hole mobility in this conjugated material has been reported to be around 40 % smaller with respect to that of electrons.[17] A more recent work provided some lower values for hole mobilities[19] being in in the order of 10^{-6} cm^2 V^{-1} s^{-1}. In any case it is clear the ambipolar nature of this conjugated polymer, being able to transport simultaneously electrons and holes with higher mobilities for the first type of carriers. Thus, the combination of ambipolar character with a low LUMO level has promoted the use of this material for an intensive application in HyLED devices,[20–23] and for instance has motivated us for its application in the present work.

7.1.2 Molybdenum oxide (MoO_3) for efficient hole injection

Molybdenum oxide (MoO_3) has been employed successfully as an anode buffer layer favoring hole injection in plastic solar cells as well as in single and tandems OLED devices[24–26]. The outstanding properties of MoO_3 for injecting holes is due to its deep conduction band, which was found to be at energies ranging between -5.5 eV to - 6.7 eV, depending on the deposition conditions and surface contamination.[8] As a consequence of the high workfunction, an efficient electron transfer can take place from the HOMO of the most common OSCs to the conduction band of the MoO_3. This defines MoO_3 not only as a hole injection layer (HIL), but at the same time as a strong p-type dopant for organic hole injection layers HILs[27]. In particular, with regard to the emitting polymer

employed in our work, the electron transfer from F8BT into MoO_3 was detected by studies of the surface energetics of the interface between both materials[28,29]. In these works, it was demonstrated an effective local reduction of the metal from Mo^{6+} to Mo^{5+} highlighting the hole injecting characteristics of this material.

Regardless its wide application in the field of organic electronics, MoO_3 has not been so far employed into organic spintronic devices. Yet only in very recent reported works of Y. Z. Wang and *et al.*[30,31] this possibility is mentioned. In these works the interface between the oxide and Co was studied by means of photoemission experiments. In first place, a chemical reaction at the interface between both materials with the consequent apparition of an interfacial Co oxide was determined.[30] This point has to be taken into account when inserting this barrier in an organic spintronic structure, as it will be shown in the following sections. In addition, an important enhancement of the workfunction of Co was described, which can be translated into a reduction of the energy barrier for hole injection into the HOMO of an OSC when using this material as a buffer layer[30]. This last statement was demonstrated by an UPS study of the same authors in which it was observed the effect of introducing a buffer layer of MoO_3 between Co and a p-type OSC such as CuPc and pentacene. In both cases an effective reduction of the hole injection barrier was determined.[31]

Despite the interesting potential of MoO_3 for spintronic applications no OSV has been reported so far employing this oxide barrier. The work described here represents the first attempt of using MoO_3 in the construction of an OSV. Taking into account this situation, a spin-resolved ultraviolet photoemission spectroscopy(UPS) characterization was performed for determining the effects of this oxide barrier on the spin polarization of a ferromagnetic electrode.

On the other hand, as previously mentioned, the F8BT has not been applied so far as a spin collector material in an OSV. Thus, there is no information in literature regarding the spin transport properties of this conjugated polymer. With this in mind, by applying a Gaussian disorder model, which includes the hyperfine interaction, the magnetoresistance (MR) curves measured of our spin-OLED were analyzed. By this strategy we have been able to evaluate the spin diffusion length in the F8BT. This analysis has been done in the context of the

model developed by P. A. Bobbert*et al.*[32],whose fundamental ideas will be summarized in the following lines.

7.1.3 Theory for spin diffusion in disordered organic materials

The determination of the key factors influencing the spin transport in OSCs, in particular the spin-diffusion length, is of fundamental interest for understanding the performance of OSVs. The scenario of a hyperfine coupling as the main responsible for spin-relaxation in OSVs has been proposed based on the studies of the OMAR effect, which is supported by recent experiments on deuterated polymers[33]. In this section, the theory of spin diffusion in the presence of a random hyperfine field developed by Bobbert and co-workers will be highlighted[32].The hyperfine coupling can be considered as a classical, quasi-static and random field distributed according to a three-dimensional Gaussian[34] with a standard deviation (B_{hf}). This is based on the fact that typically in the order of 10 (or more) hydrogen nuclear spins couple to the spin charge carrier in an OSC. In addition, this model considers the charge transport in the OSC due to hopping of carriers between localized sites with random energies, distributed according to a Gaussian density of states (GDOS) with standard deviation σ[35].

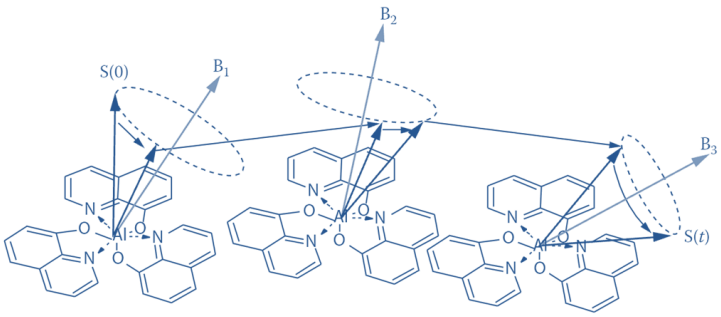

Figure 7.3- Mechanism for spin diffusion in the particular example of Alq_3 as the OSC. Hopping of carriers occurs between neighboring molecules exhibiting a precession of its spin, **S**(t), around the local effective field $\mathbf{B}_i$ while staying on a particular site *i*. Figure adapted from ref. [71].

Considering this, the model describes the spin diffusion in an OSC as a combination of incoherent hopping of carriers in a GDOS combined with a coherent precession of its spin around a local effective magnetic field, as illustrated in figure 7.3. In the model it is considered that a carrier presenting a unit charge, e (electron or hole), and a spin fully polarized in the z-direction is injected by an electrode into the OSC material at $x = 0$, after what moves to the opposite electrode under the influence of the applied electric field, E. One important parameter in this model is the ratio $\equiv \omega_{hop}/\omega_{hf}$, being ω_{hop} the hopping frequency and ω_{hf} the hyperfine precession frequency. If r is large the influence of the hyperfine field on the spin of the carrier is small and large spin diffusion lengths can be expected. For the three dimensional case[32] the authors of the model performed Montecarlo simulations for hopping of single carriers in a homogenous electric field of arbitrary magnitude on a cubic lattice of sites. The spin diffusion length was extracted in this case by considering distances sufficiently far from the electrodes with a exponentially decaying spin polarization $p\ (x)$.

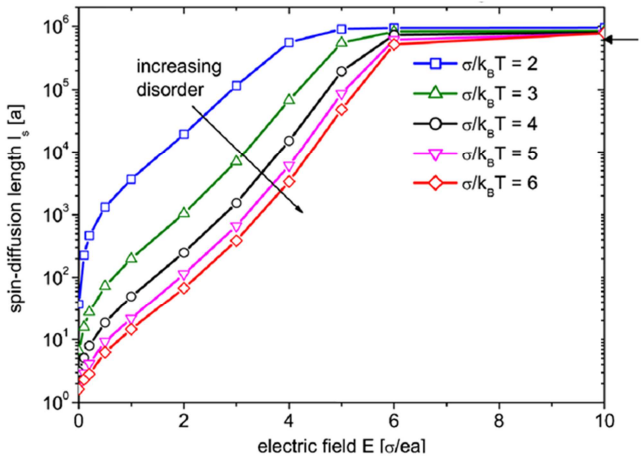

Figure 7.4- Spin-diffusion length l_s [as multiples of the lattice constant] vs electric field E at zero magnetic field, for $r \equiv \omega_{hop}/\omega_{hf} = 1000$ and different $\hat{\sigma} \equiv k_B T$. The arrow at the right axis indicates the result for a one-dimensional chain at large E. Figure extracted from reference [32].

The most important results of this modelling is the relatively weak dependence of l_s on the disorder strength $\hat{\sigma} \equiv \sigma/k_B T$ for strong disorder ($\hat{\sigma} \geq 4$) and, in consequence, with temperature (figure 7.4), in agreement with reported experimental results[36–38].

With respect to the description of Giant Magnetoresistance (GMR) traces of an OSV, the authors performed an analysis in order to obtain information of the spin diffusion length of the OSC, which is based on the observation of the experimental MR traces for OSVs based LSMO and Co electrodes. In these OSVs it has been observed that in the up- and down-field sweeps the resistance as a function of *B* changes considerably already before the magnetization of the soft layer (lower coercivity) is switched. This is an indication that, apart the magnetization reversal of the electrodes, another factor needs to be involved to explain this effect[36,39]. In this context, the hyperfine field is defined as the responsible of this effect.

By a simple phenomenological model, the organic film was described as a reservoir of carriers with spin up and down distributed between two ferromagnetic electrodes exhibiting two spin polarizations P_1 and P_2. The modelling was restricted to low temperatures in order to assume the absence of backscattering from the electrode 1 to the OSC. The spin relaxation arising from the random local hyperfine field was included by defining the spin flip rate α. With all this, by solving the rate equations for the hopping of carriers from electrode 1 into the OSC, the local spin relaxation and the hopping from the OSC to electrode 2, the occupation of up- and down spin carriers was obtained. By considering the spin relaxation in the time domain described by α, the dependence of the spin diffusion length on the magnetic field can be described as:

$$l_s(B) = l_{s,0}\left(\sqrt{1 + (B/B_0)^2}\right)^{3/4} \quad (eq.7.1)$$

with $B = 2.3B_{hf}$ and l_{s0} being the spin diffusion in absence of external magnetic field. With all this, the field dependent magnetoresistance MR (B) traces can be fitted to an equation:

$$MR(B) = MR_{max} \cdot \frac{1}{2}\left(R - sm(B)\right) \exp\left[-\frac{d}{l_s(B)}\right] + MR_0 \qquad (eq\ 7.2)$$

where $m(B) = m_1(B)m_2(B)$ is the product of magnetizations of the electrodes measured along the applied field direction and normalized to the saturation magnetization, being $m = +1\,(-1)$ for P and AP configurations. The characteristics of the spin polarization and the considerations of the carrier transport are included in the parameters R and s. In particular, $R = 1$ corresponds to spin accumulation in the OSC and $R = 0$ to a tunneling situation. The value of $s = +1(-1)$ is defined in a case of equal (opposite) signs of electrode polarizations in parallel alignment of the magnetization, thus determining the positive or negative spin valve effect in the device.

Once the fundamental concepts have been introduced, the rational design and fabrication of a spin-OLED, with Fe and Co electrodes with a HyLED configuration, will be described in the following sections.

7.2 Results and discussions

7.2.1 UPS study of the MoO_3 barrier

Photoemission experiments (PES) have been performed in order to investigate both the electronic structure at the interface of Co/MoO_3 and the effect of this oxide barrier on the spin polarization of the magnetic electrode. This characterization was done by increasing progressively the thickness of the oxide layer with the aim of evaluating the impact of this parameter on the properties previously mentioned. This study was carried out in collaboration with Dr. Mirko Cinchetti from the Ultrafast Phenomena at Surfaces research group at the Department of Physics and Research Center OPTIMAS (University of Kaiserslautern).

Despite the several reported works of the effect on the hole injection barrier of this oxide, there is no study so far regarding on the impact of this oxide on spin polarization.

At the initial stage of the study, a thick Co film of 30 ML (~5.4 nm) was evaporated onto a Cu (100) single crystal which was employed as the substrate. This substrate was annealed only up to 370K to prevent diffusion of the Cu atoms into the Co film. At this thickness the Co exhibits an *fct* structure with an easy axis along [110] perpendicular to the surface[40]. The same MoO_3 material employed for the fabrication of the spin-OLED device was evaporated directly on top of the Co by progressively increasing from 0 to 9 nm the thickness of the oxide barrier.

In figure 7.5 are depicted the ultraviolet photoemission spectra (UPS) for the stepwise deposition of MoO_3 on a Co electrode. In figure 7.5-*top* it is shown the UPS spectra of the Co/MoO_3 system in which the secondary electron background has been removed for a more accurate determination of peak positions. From these spectra it is possible to detect a decrease of the Co-*3d* bulk peak, located at -0.4 eV (in agreement with the findings in Ref [40]), as the thickness of the MoO_3 is progressively increased. The valence band structure of the MoO_3 is clearly resolved above a nominal thickness of 1 nm. The different states located between -3 eV and -10 eV are mainly related to the O-*2p* derived states[30,41,42].

The first result to highlight from these measurements is the effect of the MoO_3 on the workfunction of Co. The evolution of the workfunction can be directly determined by monitoring the position of the low-energy cutoff of the UPS spectra shown in figure 7.5-*bottom*. The figure shows a clear shift of the low-energy cutoff towards the Fermi energy for increasing thickness of the oxide barrier. This can be translated into an increase of the workfunction of the Co/MO_3 system, which is up to 1.37 eV for the 9 nm thick MoO_3 barrier with respect to the pristine Co. This effect is in total accordance with previously reported works on UPS studies of this particular system[30,31,41,42]. The formation of an interface dipole with its negative terminal pointing to the MoO_3 can be ascribed to this overall vacuum level shifting[30]. From the perspective of the

device, this important upward shifting in the vacuum level is translated into a reduction of the hole injection barrier, Δ_h, when using this oxide as a buffer layer.

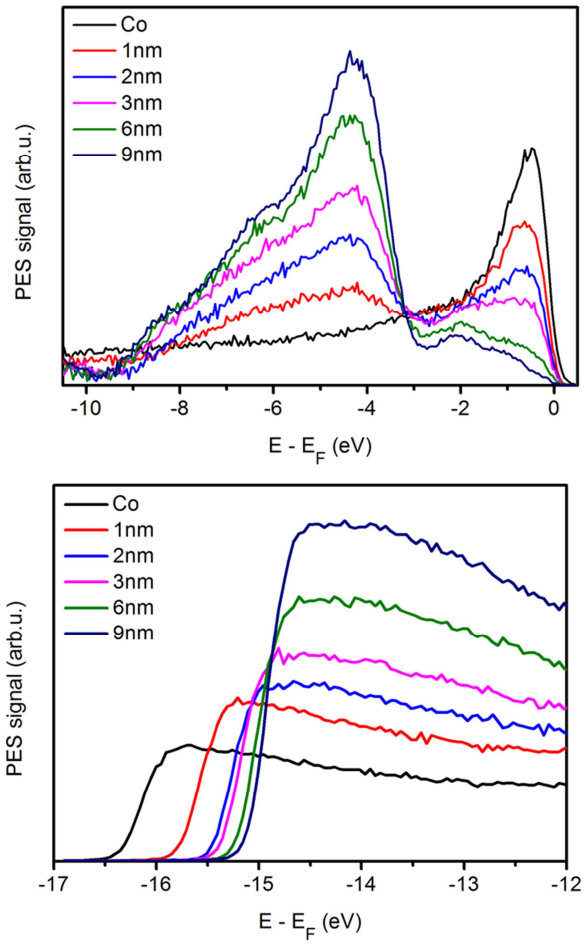

Figure 7.5- *Top*: UPS spectra of the Co/MoO_3 system recorded for different MoO_3 thickness (from 0nm to 9nm), in which the secondary electron background has been subtracted. *Bottom:* Low-energy cutoff of the UPS spectra without subtraction of the secondary electron background. An evolution of the Co workfunction when increasing the MoO_3 thickness is observed.

In the field of optoelectronics there are many works focused on the understanding of the interface between MoO_3 and organic semiconductors as it

has been mentioned in the introduction of this chapter[24,27–29,43]. It has been shown how, thanks to its deep work function (between -5.7 eV and -6.7 eV depending on the deposition conditions), MoO_3 interacts via the formation of charge transfer states by accepting electrons from the HOMO of the organic material. This mechanism creates a doped injection layer that is responsible for the enhanced hole injection properties of MoO_3 in organic electronic devices.

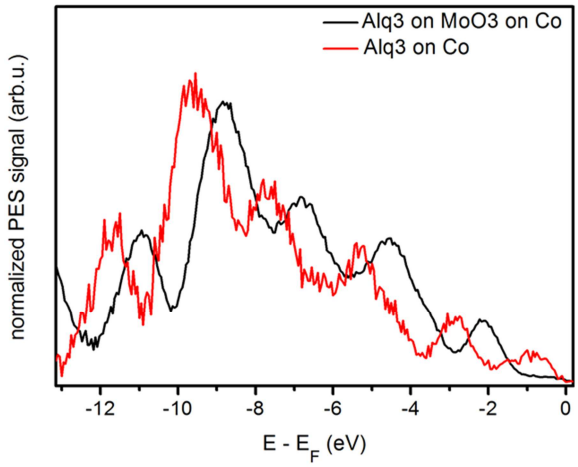

Figure 7.6- Comparison of the UPS spectra of Alq_3 on Co (red curve) and Alq_3 on Co/MoO_3 (black curve).

We have confirmed this effect of the oxide buffer layer on the interface with an organic semiconductor by comparing the PES signal of an Alq_3 layer on top of pristine Co and onto Co/MoO_3. In figure 7.6 it is depicted the UPS spectra for this system in which the secondary electron background has been removed. It is possible to observe that no interface states are formed directly at the Fermi level in any case. Nevertheless, when Alq_3 is deposited on MoO_3/Co, there is a clear shift of 0.75 eV towards the Fermi level of all molecular orbitals if compared to Alq_3 deposited on clean Co. Thus the presence of the MoO_3 at the interface is reducing the hole injection barrier from Co to Alq_3 which is translated into a shifting of all organic states towards the Fermi level as described for other OSCs in contact with this oxide barrier[31].

As it was previously mentioned, UPS measurements with spin resolution were performed with the aim of analyzing the effect of the MoO_3 layer on the spin polarization of the Co electrode. In figure 7.7 it is shown the results from the spin-resolved UPS characterization arising from the stepwise deposition of MoO_3 from a nominal thickness of 0 nm to 9 nm. By using spin-resolved photoemission it is possible to determine the number of majority (minority) photoemitted electrons N^{up} (N^{down}) for which the projection of the spin along a defined in-plane direction and along the sample normal is +1/2 (-1/2). The spin polarization P of an electron with binding energy E* is then calculated as:

$$P(E^*) = \frac{N^{up}(E^*) - N^{down}(E^*)}{N^{up}(E^*) + N^{down}(E^*)} \qquad (eq.7.3)$$

The shape and value of the measured spin polarization give information about the changes of this quantity at the Co surface as the MoO_3 layer is deposited on top[44].

From the information depicted in figure 7.7 it is possible to detect an identical spin polarization directly at the Fermi level for the Co/MoO_3 respect to the pristine magnetic electrode for nominal thicknesses of the oxide barrier up to 3 nm. By increasing the thickness of the barrier above this limit the spin polarization directly at the Fermi level is affected. For a 9 nm thickness oxide layer, the measurements exhibit a very poor signal-to-noise ratio from -1 eV to 0 eV, thus no conclusion can be extracted in this case. On the other hand, it is also possible to observe a decrease of the spin polarization of Co for energies below -1 eV for all the oxide thicknesses under study. Both these experimental facts are mainly due to photoemission-related effects, like spin-dependent scattering of the photoelectrons in the progressively thicker MoO_3 layer.

These measurements are clearly indicating that a device with a Co/MoO_3 interface should keep the magnetic properties of the Co electrode and could utilize the organic states located near to the Fermi level. In particular by employing a barrier of 3 nm thickness of MoO_3 the spin polarization of the magnetic electrode is unaffected at the Fermi level and a certain grade of depolarization is only present for energies below -1 eV. Thus this result is

supporting the choice of a 3 nm MoO_3 barrier in a spintronic device as a good compromise in order to preserve the spin information in the resulting interface.

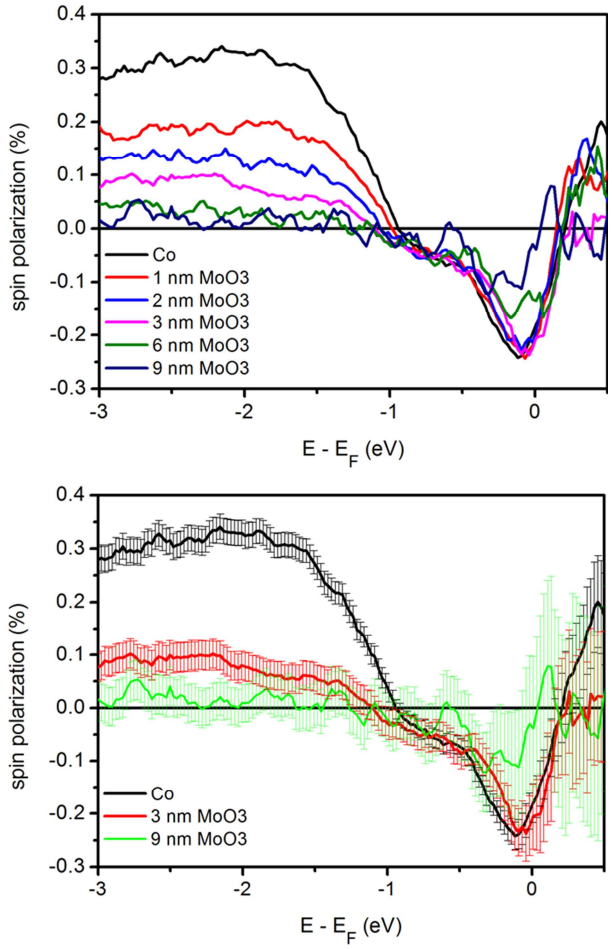

Figure 7.7- *Top*: Spin polarization measurements of the Co electrode as a result of the stepwise deposition of MoO_3. Error bars are omitted for clarity. *Bottom*: Comparison of spin polarizations for pristine Co and after the deposition of 3 nm and 9 nm of MoO_3. No effect on spin polarization of Co at the Fermi level is detected for nominal thicknesses of MoO_3 up to 3 nm.

7.2.2 Device fabrication

In order to fabricate the spin-OLED, the strategy was focused on the incorporation of ferromagnetic electrodes into a typical HyLED structure[5]. Thus, the rational design of the device was based on the obtaining of a HyLED exhibiting simultaneously an OSV performance, in order to generate a spin polarized current in the.

With this aim, starting from a 100 nm indium tin oxide (ITO, In_2O_3:Sn) electrode on glass (*Naranjo Substrates*), an initial layer of 4.5 nm of Fe was thermally evaporated on top (base pressure < 10^{-6} mbar), establishing the cathode device. Prior to the Fe evaporation the ITO substrate was cleaned following a standard procedure. In first instance the substrates were rubbed with gloves employing a solution of alkaline detergent (Mucasol, from Sigma-Aldrich) in distillated water. Immediately after that, the substrates were immersed in the detergent solution and placed in a sonication bath during 10 minutes. The same procedure was repeated in pure distillated water and finally in isopropanol after which the substrates were completely dried under an N_2 gas flow. This cleaning process guarantees a good quality surface for the growing of the rest of the layers in the device. Thus, the appearance of defects due to organic residues which can lead to shortcuts or anomalous device performance is avoided.
The thickness of the Fe electrode was chosen based on a study of the transmittance of the film as a function of this parameter. In our spin-OLED the light is emitted through the transparent glass/ITO substrate. The incorporation of the Fe layer was done minimizing the absorbance and recovering the maximum of light produced in the LEP volume. In figure 7.8 it is depicted the curve of transmittance in function of Fe thickness obtained for a light wavelength of 700 nm. A4.5 nm thickness exhibits a transmittance of 70 %, meanwhile it goes down to 35 % when increasing the Fe thickness up to 10 nm. For higher thicknesses the transmittance of the layer is drastically reduced. Thus in order to have a maximum amount of recovered light as well as an appropriate amount of material on the electrode, the thickness of 4.5 nm was finally selected as a good compromise.

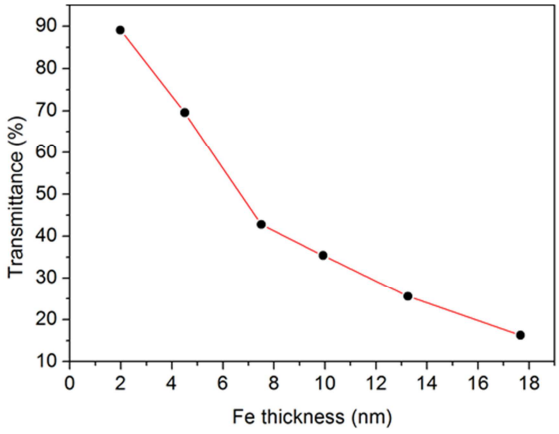

Figure 7.8- Curve of transmittance vs Fe electrode thickness.

Employing the same technique for depositing the Fe electrode, an aluminum layer was subsequently evaporated using the same mask. By exposing to air this electrode an alumina barrier (AlO_x) was fabricated. In previous reported works, by means of XPS studies it was shown that meanwhile the thickness of the Al film is not higher than 1.5 nm a completely oxidized amorphous film of alumina is obtained after 5 minutes to air exposure.[45]In addition, based on the extremely large bandgap of the alumina (8.45-9.9 eV), it is crucial an optimal selection of the thickness of the barrier for minimizing the series resistance. However, the thickness have to be enough for the barrier to effectively act as an EIL.[46]Having all this information in mind, a 1.5 nm layer of Al was evaporated on top of the Fe and subsequently transferred out of the glove box, where the evaporator is located, in order to get the AlO_x barrier after ten minutes of air exposure.

The good performance of the AlO_x barrier as an EIL has been demonstrated in OLED devices[45,47]as well as recently in HyLED structures[46]. On the other hand, from the spintronic point of view, the AlO_x barrier has been successfully adopted as a tunneling barrier in OSVs, significantly improving the device performance,[48,49] by reducing the "conductivity mismatch" between the ferromagnetic electrode and the OSC[50–52]. In the context of our work, the employment of this oxide barrier on top of the Fe electrode has a double motivation regarding both the spintronic and optoelectronic performances of the structure under fabrication. In addition, the AlO_x barrier is going to play the

role of protecting layer, retarding the oxidation process of the Fe electrode when exposed to atmospheric conditions during the fabrication.

After the cathode evaporation process was accomplished, a 100 nm layer of the light emitting polymer F8BT was deposited by spin coating from a chlorobenzene solution. An annealing at 100 °C during 30 minutes inside the glove box was subsequently performed for completing the fabrication of the emissive layer. In order to characterize the chemical environment of the polymer employed in the spin-OLED, a Raman study on a layer of F8BT was performed.

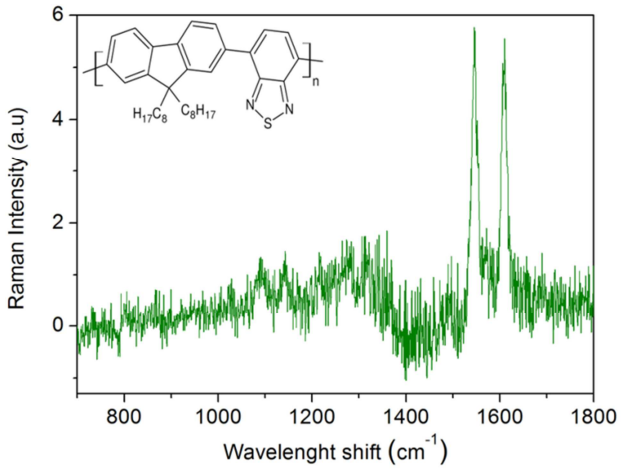

Figure 7.9- Raman spectrum of a F8BT layer with 100 nm thickness.

The Raman spectrum is shown in figure 7.9. From this spectrum it is possible to observe a prominent peak at a Raman shift of 1610 cm^{-1}. Peaks in this spectral region have also been observed in the conjugated polymer PPV. They have been attributed to C=C stretching of the phenyl ring, C–C stretching of the phenyl ring, and C=C stretching of the vinyl group,[53]. The same peaks have been also reported for the conjugated polymer poly(9,9dioctyl flourene), where it was attributed to a mode of the fluorene group (see inset figure 7.9 for the chemical structures). The F8BT layers also exhibits a Raman peak at 1548 cm^{-1}, probably due to the presence of the five-member ring containing two nitrogen and one sulphur atoms.

After the polymer deposition, the device was transferred again to the thermal evaporator in order to deposit a MoO_3 layer of 3 nm thickness (base pressure <

10^{-6} mbar) over the whole substrate. This strategy guarantees a complete covering, avoiding any edge effect induced by the masks which could affect the performance of the device. The evaporation was performed at an average ratio of 0.1 Å/s for reducing any possible interpenetration in the F8BT. As the spin-OLED has to exhibit simultaneously EL and a good performance as an OSV, the thickness of this oxide barrier acting as HIL has to present a positive impact in both functionalities. In the context of the spintronic properties the interfaces are critical as it has been extensively described in literature[1,54]. In our particular case, based on a systematic variation of the MoO_3 barrier thickness, it was found that 3 nm was the lowest limit for a good EL performance in the device in terms of turn on voltage (V_{on}) for light emission. Below this value, the hole injection from the anode to the HOMO of the F8BT was seriously damaged. This is reflected in the shifting of the V_{on} to higher values, degrading in this way the EL properties of the spin-OLED. On the other hand, the spin-resolved UPS studies of section 7.2.1 confirmed the good choice of 3 nm for the MoO_3 as exhibiting this thickness a null impact on the spin polarization of Co at the Fermi level.

On the other hand, the MoO_3 barrier was included in the structure in order to prevent the metal interpenetration from the top magnetic electrode into the soft organic layer of F8BT. By this strategy it is possible to avoid the appearance of the so-called "ill-defined organic spacer layer". Depending on the materials, the thickness of this layer can vary from 50 to 100 nm preventing the realization of devices with well-defined geometry[36,38,55–57].

After depositing the MoO_3 barrier, the anode of the spin-OLED was thermally evaporated (base pressure $<10^{-6}$ mbar). The anode is constituted by a Co layer of 18 nm thickness with a protective layer of Au with 35 nm thickness. Both layers were deposited in a cross bar configuration respect to the ITO/Fe/AlO_x electrode with a different mask, obtaining two cells per device with an active area of $2mm^2$. Both metal layers, forming the anode, were evaporated with a ratio of 0.1 Å/s for improving the quality of the interface generated with the F8BT through the MoO_3 barrier. In this way, Co inclusions or defects on the F8BT and, in consequence, the appearance of an ill-defined layer in the device are avoided. For testing the quality of the top interface, an HRTEM study of the

sample was performed at the Advanced Microscopy Laboratory (LMA) at the Nanoscience Institute of Aragon (INA). In figure 7.10, it is shown a representative HRTEM image of a lamella of the device prepared under cryogenic conditions to avoid the damage of the organic layer. As it can be observed from this study, the oxide barrier efficiently prevents the penetration of Co atoms into the organic spacer preventing from the appearance of an ill-defined layer in the device. As a consequence, smooth and homogenous interfaces were fabricated.

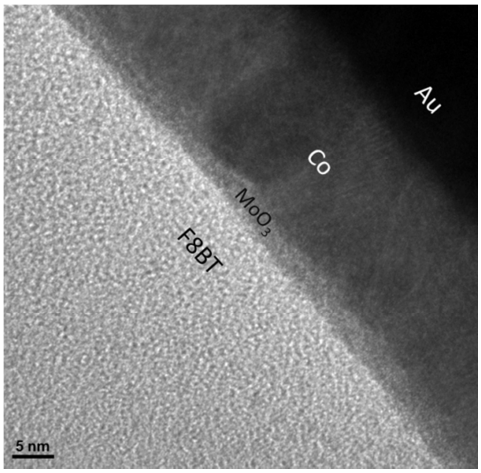

Figure 7.10- HRTEM image of a lamella of the device showing the Co/MoO_3/F8BT interface.

It is important to note that all the materials employed for the fabrication of the spin-OLED were commercially available and were used directly as received from the provider. The polymer employed was purchased from *American Dye Source* and used without any further chemical treatment. The rest of the materials were purchased to *Sigma-Aldrich*.

In figure 7.11 it is shown the schematic diagram of the layers: ITO[100nm]/Fe[4.5nm]/AlO_x[1.5nm]/F8BT[100nm]/MoO_3[3nm]/Co[18nm]/ Au[25nm]. The light produced by the recombination of the injected carriers in the F8BT is emitted through the transparent Fe cathode.

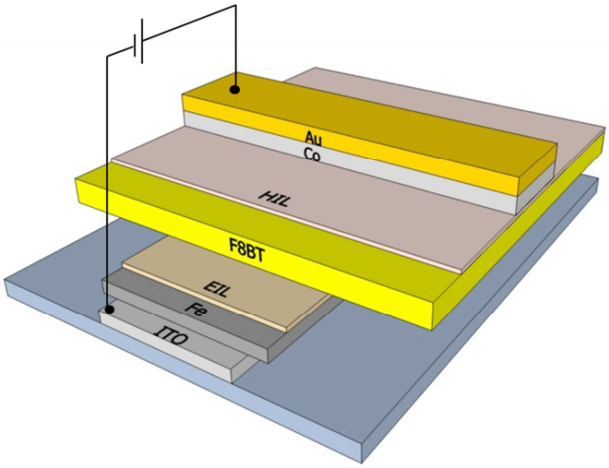

Figure 7.11- Schematic sketch of the layers composing the spin-OLED with AlO_x and MoO_3 barriers as EIL and HIL layers respectively.

The study of the surface morphology of the layers composing the device was performed by means of atomic force microscopy (AFM). Images of 25μm^2 scan size were acquired in tapping mode for the layers after each deposition in the same order as the one established for the preparation of the device (figure 7.12). The surface generated by the deposition onto ITO of 4.5 nm of Fe and 1.5 nm of AlO_x has to be sufficiently smooth to prevent the appearance of defects which can lead to shortcuts or malfunctions in the device. This requisite was accomplished as can be observed from the AFM characterization of this surface, which exhibits a RMS roughness of 1.81 nm. Taking into account the low thickness of these layers, the surface morphology of the Fe/AlO_x is clearly influenced by the ITO surface features. According to this information, the generated cathode is sufficiently homogenous and smooth in order to guarantee a correct deposition and coverage by the LEP. This analysis also showed a smooth surface for the F8BT layer and the MoO_3 barrier deposited on top with RMS roughness of 0.91 nm and 0.97 nm respectively. These conditions establish the basis for the good quality of the interfaces in the device, as it was confirmed by the HRTEM study of the F8BT/MoO_3/Co interface.

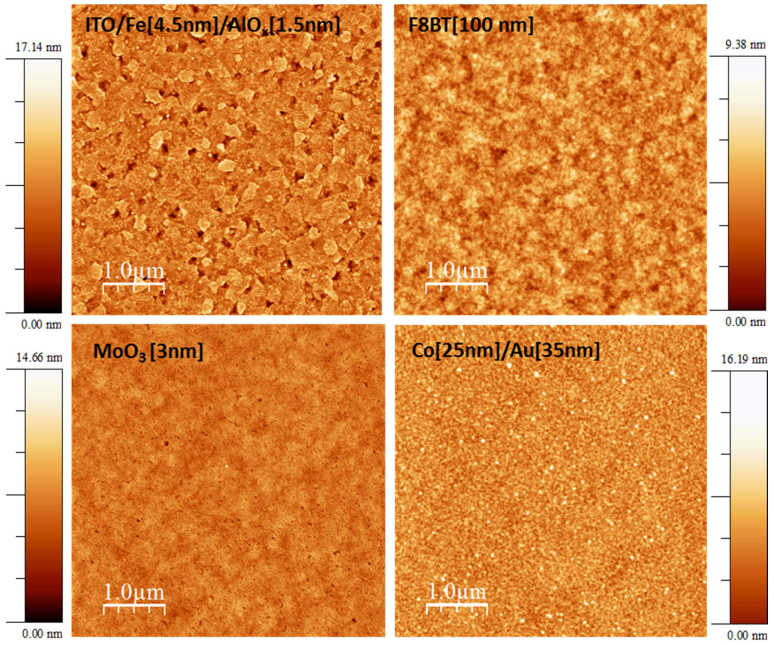

Figure 7.12- AFM images of 25µm^2 scan size in tapping mode for the layers of the spin-OLED after each deposition in the same order as the one established for the device.

The properties of the magnetic electrodes are fundamental for getting a good performance of this device as OSV. In particular, the coercive fields of the magnetic electrodes have to be sufficiently different in order to allow the establishment of parallel (P) and antiparallel (AP) configurations of their respective magnetizations. The achievement of these configurations can lead to high and low resistance states as already explained in the introductory chapters of this thesis. A low temperature MOKE characterization was performed after the deposition of all the layers. In this way, the coercivity of the ferromagnetic electrodes when sweeping the external magnetic field was established. As it can be observed from figure 7.13, coercive fields of 90 Oe and 190 Oe for the layers of Fe/AlO_x and Co/Au respectively were measured by this technique. This difference in coercivity is enough to guarantee the stabilization of an AP state of the electrode magnetizations in the spin-OLED structure.

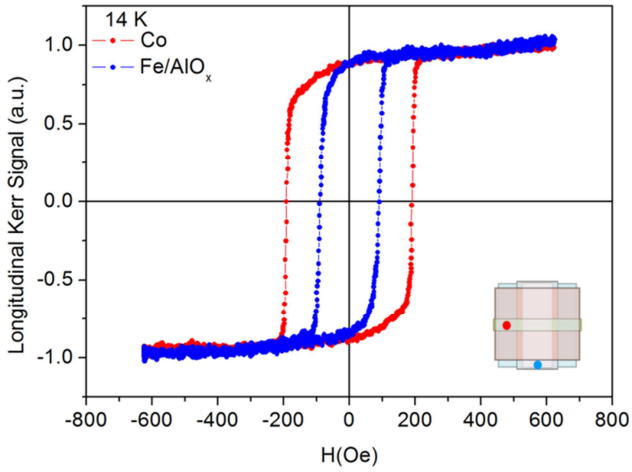

Figure 7.13- MOKE signal at low temperature of the ferromagnetic electrodes in the spin-OLED. *Inset*: Scheme of the spot laser position of MOKE in the measurements.

7.2.3 Electroluminescence properties

In figure 7.14 it is shown the current density and luminance versus voltage measured at room temperature for the spin-OLED. The measurement was done in forward bias, with a positive biasing for the Co/Au anode as depicted in the inset of figure 7.14. The J-V and Lum-V curves are represented in logarithmic scale as it is normally reported in literature for this type of devices. The spin-OLED showed a low turn on voltage of about 1.8 V for current injection followed by a steep raise in the current density that reaches a value of 105 A/m^2 at 6V. The electroluminescence (EL) in the device appeared at a slightly higher turn on voltage (V_{on}) of 2 V reaching a value of 2.25 Cd/m^2 at 6 V. The delay observed in the V_{on} of the current density respect to the one of luminance is related to the preferential injection of one type of carriers. In particular, holes are more efficiently injected in the polymer promoted by the presence of the MoO_3, followed by the injection of electrons as it was already explained in chapter 6. Thus, the delay has been ascribed in literature to the evolution from a mainly unipolar charge transport regime to a properly bipolar regime in the F8BT[21,58]. In this bipolar regime, polaron pairs (PPs) are generated by the presence of the two types of carriers in the OSC. These PPs are the precursors for singlet and

triplet excitons in the emissive layer. Only the singlet excitons will contribute to the light emission of the device as explained in chapter 6.

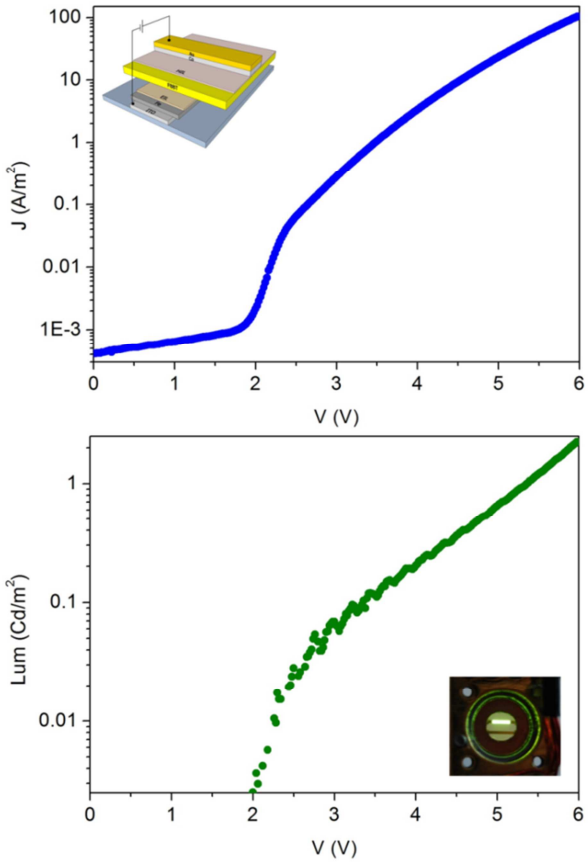

Figure 7.14- *Top:* Current density (J)*vs* voltage (*inset*: biasing procedure); *Bottom*: luminance (Lum)*vs* voltage (*inset*: light emission of the device) for the spin-OLED measured at room temperature.

The active area of the device exhibited a uniform yellow-green luminescence, with an EL spectrum (figure 7.15) at room temperature presenting a maximum

at a wavelength of 560 nm. This spectrum is coincident with the emission of the F8BT polymer.

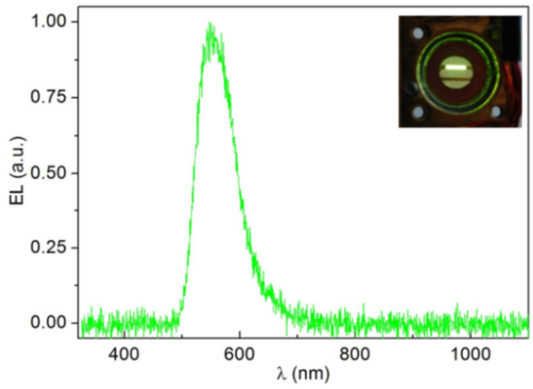

Figure 7.15- Electroluminescence spectrum of the spin-OLED at room temperature.

The electronic mechanisms behind the operation of our spin-OLED regarding to light emission, can be understood and described taking into account all the information in literature respect to this type of inverted OLEDs[5,58].In the EL performance of a HyLED structure, the charge injection barriers, both the EIL and the HIL, play a fundamental role. As it was previously described in many reported works[28,29,42,43] and showed by the UPS measurements in section 7.2.1, the MoO_3 layer deposited between the Co anode and the F8BT has the ability to reduce the energy barrier for hole injection. Although there is an important energetic difference between the workfunction of Co and the HOMO of the F8BT (figure 7.1), the low conduction band of the MoO_3 layer is capable of decreasing the barrier for hole injection into the LEP. As a consequence, an ohmic contact is established at the F8BT/MoO_3 interface. In opposite way, a considerable energetic barrier is present for the injection of electrons in the electron injecting contact of the spin-OLED. In our case, the injection barrier for electrons from Fe to the F8BT LUMO is around 1.2 eV (figure 7.1). In this context, the injection of electrons into the polymer is assisted by two processes taking place at the electron injecting interface that we are going to explain in the following lines.

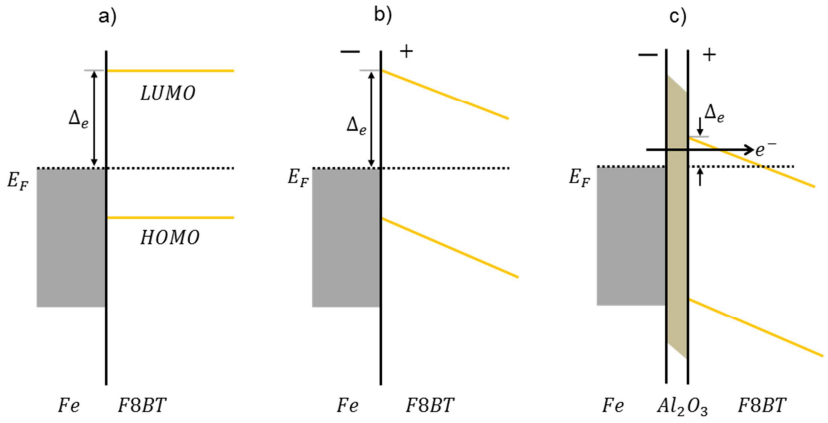

Figure 7.16- Schematic band diagram: a) without EIL under no bias, b) without EIL in a forward bias, c) with the presence of the alumina under forward bias showing the decrease of the electron injection barrier, Δ_e, in the polymer.

As described in previously reported works on OLEDs with AlO_x as the EIL[45], the improvement in the performance of the device is ascribed to the promotion of charge injection by a Fowler-Nordheim tunneling mechanism at the ultrathin oxide barrier. The same mechanism has been described in devices employing other insulating oxides such as MgO[59,60]. In this scenario, due to the presence of the insulating oxide layer, when the spin-OLED is forward biased, an important voltage can be dropped across the AlO_x barrier. This situation leads to a reduction of the electron injection barrier from the Fe cathode to the F8BT as dipoles are formed at this interface. In consequence, an alignment of the LUMO level of the F8BT with the Fermi level of the Fe is produced allowing a direct tunneling of electrons through the EIL of AlO_x (figure 7.16)[60].

The second process that favors the electronic injection in the spin-OLED is the hole accumulation at the electron injection interface[5,58]. Despite this mechanism has been explained in chapter 6, it will be particularized for the spin-OLED under study. When holes are injected into the F8BT from the MoO_3/Co interface, they migrate across the active material under the application of a forward bias in the device. This migration takes place until the

holes reach the interface with the AlO_x barrier being blocked. This process is responsible of a hole accumulation on the electron injecting contact, from the side of the F8BT, leading to a strong interfacial field resulting from the charge accumulation in a very thin region.[58]This interfacial field enhances the injection of electrons from the Fe to the LUMO of the F8BT through the AlO_x, promoting the exciton formation with light emission. In addition, this mechanism raises the hole concentration in the device with a consequent increase of the current density as a result of a lowering of the space charge limitation for the hole current. In this context, an effective hole blocking by the EIL plays an important role in the EL performance of the device. This point has been analyzed in HyLEDs employing a wide band gap insulating layer such as HfO_2 and MgO[22] as EIL. In our particular case, the AlO_x has a wide band gap between 8.45 and 9.9 eV[7,46] with a deep valence band (figure 7.1). These characteristics promote a better confinement of holes in the active layer improving the EL performance of the spin-OLED.

Thus, at this point it has been demonstrated that the proposed spin-OLED exhibits a good EL performance with a V_{on} for light of 2 V at room temperature. As the characterization of the OSV performance of the light emitting structure is done at low temperature, it is fundamental to study the evolution of V_{on} with temperature. This information is of great interest to evaluate the potentiality of our spin-OLED for exhibiting MEL effect. The V_{on} of the device was measured when decreasing the temperature from 300 K to 2K. As it is depicted in figure 7.17, the thermal evolution of V_{on} shows a light emission in the spin-OLED for all the range of temperatures. However, there is a drastic increase of the V_{on} for light when cooling down the system, which is reflected in an evolution from 2 V at room temperature to 11 V at 8 K. The temperature influence on the V_{on} of light can be ascribed to the thermal dependence of the processes related to charge injection and carrier mobilities in the OSC.

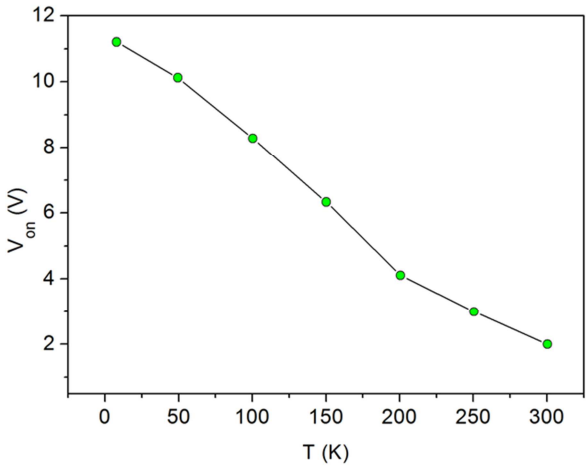

Figure 7.17- Thermal evolution of the turn on voltage (V_{on}) for light when cooling down the spin-OLED.

At lower forward bias, Fowler-Nordheim tunneling contributes to the device current. For higher bias voltages, the space charge limited current (SCLC) governs the current density in the structure[61]. In bipolar devices, in absence of traps and with a field dependent mobility, the current density is a direct function of the product and the sum of the mobilitites of electrons and holes[62].Thus, the current flowing throw the device is governed by SCLC conduction described by the Mott-Gurney law modified for bipolar injection:

$$J = \left(\frac{9\pi}{8}\right)^{1/2} \varepsilon_0 \varepsilon_r \left(\frac{2q\mu_p\mu_n(\mu_p + \mu_n)}{\varepsilon_0 \varepsilon_r B}\right)^{1/2} \frac{V^2}{L^3} \qquad (eq.\ 7.4)$$

where$\varepsilon_0\varepsilon_r$, μ_p,μ_n,B, q,V and L are the polymer permittivity, hole mobility, electron mobility, bimolecular recombination constant, electron charge, bias voltage and polymer thickness respectively.

The mobilities at lower temperatures are considerably decreased, which is translated in an increase of the V_{on}. Indeed the carrier transport in this device is considerably dependent on temperature, which explains that when cooling down a higher voltage is needed for activating the mechanisms necessary for light emission[61].

Taking into account all the information presented so far, it is possible to claim a good EL performance in the spin-OLED for all the temperature range. This demonstrates the appropriate approach considered for the design and fabrication of this multifunctional device in terms of light emission. The next step of the study is the analysis of the spintronic properties of the device.

7.2.4 Spin transport properties

The device was transferred to a Physical Properties Measurement System (PPMS). In this set-up, a complete magnetoresistance (MR) characterization was done employing a standard two-probe method.

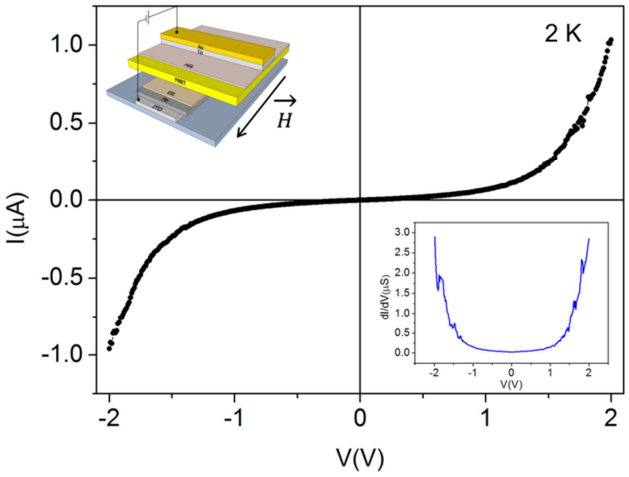

Figure 7.18- Current versus voltage curve at 2 K for the spin-OLED. *Inset up:* Biasing of the spin-OLED and configuration of the external magnetic field. *Inset down*: Differential conductance (dI/dV) versus voltage at 2K.

The MR measurements were performed by applying a constant biasing voltage across the electrodes, while measuring the resulting current in the device. In this way, it was registered the changes of resistance (R) of the device as a function of an external magnetic field (H) applied parallel to the surface of the sample. In this case, the spin-OLED was biased in the same way as done for the J-V and Lum-V measurements in the previous section. That is, a positive and negative biasing for the Co anode and Fe cathode, respectively. The current-

voltage curve of the device at 2 K is depicted in figure 7.18. This curve exhibits a behavior presenting an onset voltage below which hardly any current flows. Above this onset voltage, the current increases with a highly non-linear behavior. Thus, as it was expected, our device exhibits at 2 K the typical I-V of an OLED structure, which can be directly correlated to a carrier injection followed by a hopping process in the OSC[63,64].

This statement is supported by the voltage dependence of the differential conductance at 2 K of the device (inset figure 18). The dI/dV shows a clear non-parabolic trace which can be directly related to the absence of a tunneling process through the OSC as being the responsible of the conductivity in the system[63,64]. Nevertheless, the fundamental proof of carrier injection followed by a hopping process in the F8BT as the conduction mechanism of the OSV performance in the spin-OLED is the presence of light emission in the system. The light emission of the spin-OLED at 8 K, as shown in the previous section, is clearly evidencing the carrier injection and transport through the F8BT spacer. The EL in the spin-OLED can take place only by the formation of polaron pairs in the F8BT that lead to singlet excitons which in terms recombine radiatively. This is a clear advantage of this type of OSVs presenting light emission because the transport mechanisms can be unambiguously determined.

The MR curves for the spin-OLED were acquired at 2 K with the magnetic field applied parallel to the surface of the sample, *i.e.*, perpendicular to the electrical current direction. The MR was calculated by using the expression:

$$\frac{\Delta R}{R_{ap}} = \left[\frac{\left(R_p - R_{ap}\right)}{R_{ap}}\right] \cdot 100 \ (\%) \qquad (eq.\ 7.5)$$

where R_p and R_{ap} are the resistances of the device for parallel and antiparallel configuration of the electrode magnetizations respectively. The MR traces of the device for some of the voltages in forward and reverse biasing are shown in figure 7.19. This measurement shows that a sizeable MR at 2K can be detected

reaching values up to 14 % for biasing voltages of ±10 mV with resistances in the order of megaohms. The resistance is higher for the antiparallel (AP) relative orientation of the electrode magnetizations. Thus, our spin-OLED presents a positive MR effect as observed in many other reported OSVs[55,65–67]. It is important to remark that the definition of "positive" or "negative" MR is not assigned directly to the sign of the calculated MR, being this sign directly determined by how this value is calculated as in equation 7.5. In fact, the "positive" or "negative" character of the MR is related to a higher or lower value respectively of the resistance at the antiparallel configuration of the electrode magnetizations in the OSV performance.

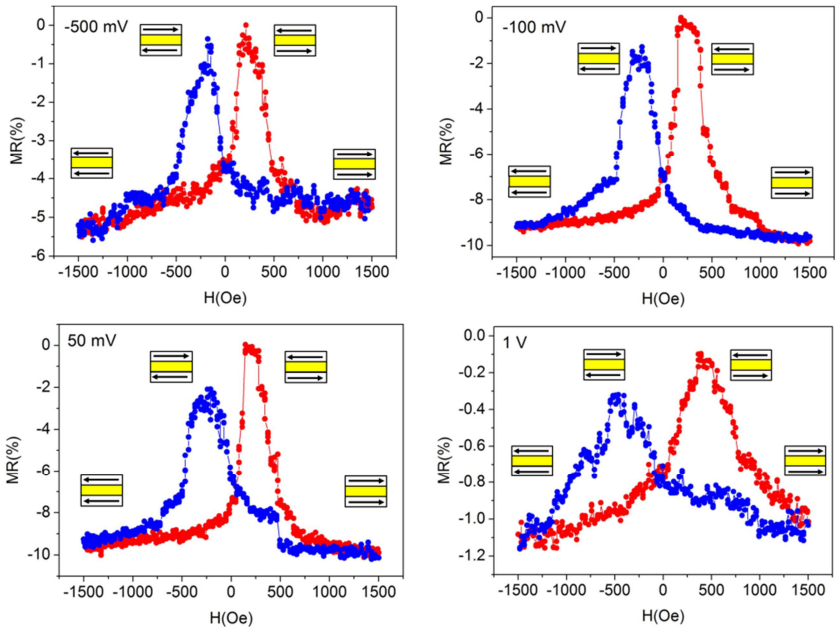

Figure 7.19- MR curves at 2K of the spin-OLED measured with a magnetic field parallel to the surface of the sample. Up- and down-sweeps of the magnetic field are indicated by the red and blue curves respectively. The arrows indicate the relative orientation of Fe and Co respect to the external magnetic field.

In literature, the positive MR has been directly related to an equal sign of the spin polarization of the electrodes[68].As reported for other OSVs, the spin

polarization sign of the electrodes has been found to be very dependent of the employed barriers[48,69]. In addition, this sign depends on the possible spin-hybridization-induced polarized states (SHIPS) in the first molecular layer at the electrode interface, as described by C. Barraud *et al.*[68]. Nevertheless, in the field of organic spintronics, considering the existent works, the spin polarization for transition metals such as Fe, Ni, Py and Co have been considered to be positive[48,69]. Thus, in principle it is possible to assume that in our spin-OLED the spin polarization of both Fe and Co are positive, without any sign inversion due to the barriers,. This would lead to a positive MR response of the device as it is confirmed by our measurements.

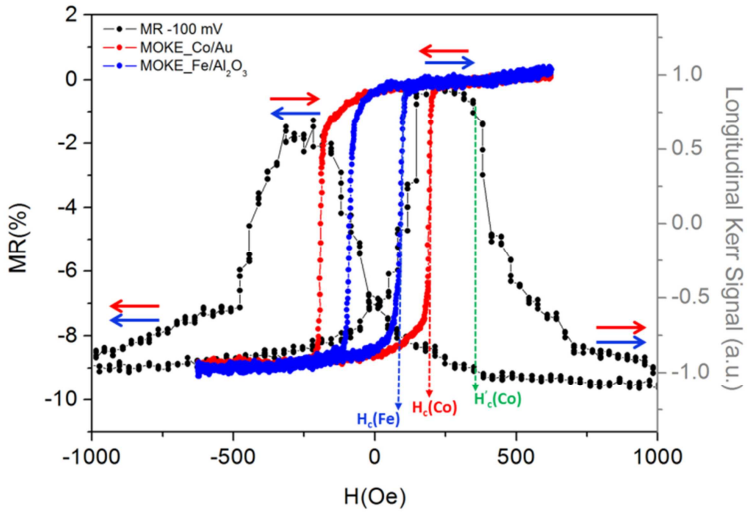

Figure 7.20- Comparison of the MR curve at -100 mV of the spin-OLED (black curve) with the MOKE hysteresis for Fe (blue curve) and Co (red curve) electrodes. The blue and red arrow indicates the relative magnetization orientations of Fe and Co respectively.

An interesting point to treat is the analysis of the switching fields at which the high and low resistances states are achieved. In first approach, the transition of the MR curves between both resistance states should reflect the coercivities of each ferromagnetic electrode. In a general way, the coercive fields of the ferromagnetic electrodes in OSVs are characterized by means of MOKE magnetometry thanks to the spatial resolution and surface sensitivity of this

technique. In section 7.2.2 it has been shown the MOKE study on our system (figure 7.13) establishing coercivites of 90 Oe and 190 Oe at 14 K for the Fe cathode and Co anode, respectively. The limited thermal evolution of the coercivity in these materials allows comparing these values at 14 K with the switching fields of the MR curves at 2 K. In figure 7.20 the MR curve for a -100 mV bias (black curve) is compared with the MOKE hysteresis loop (blue and red curves for Fe and Co electrodes respectively).The first switching event of the MR curve located at around 90 Oe matches properly with the MOKE coercive field of the Fe, denoted as H_c (Fe). Nevertheless the second swithching event is not taking place at the MOKE coercive field H_c (Co) =190 Oe for the Co electrode. On the contrary, the transition from antiparallel to a parallel magnetization states is occurring at a higher magnetic field value of around 330 Oe, denoted as H'_c (Co). Thus, it is evident that the MOKE measurement on the Co electrode in the device is not reflecting the real magnetization reversal process taking place at the interface created by this electrode and the MoO_3 barrier with the F8BT. The same type of discrepancy has been observed in previously reported works regarding the MR behavior of OSVs employing different types of OSCs[63,64,70]. In all the situations the explanation of this discrepancy was related to the fact that the magnetic behavior of the ferromagnetic electrode at the interface with the OSC is different to that of the top surface, which is the region studied by MOKE. In our case, this affirmation was fully confirmed by measuring the bulk magnetization reversal process with SQUID of a spin-OLED employing LSMO and Co as cathode and anode respectively. This measurement will be shown in the discussion of chapter 8.

In figure 7.21 it is shown the bias voltage dependence of the absolute value of the MR at 2 K for the spin-OLED. From this study it is observed a monotonically decrease in MR when increasing the bias voltage of the device. This feature has been described in other organic spin valves[36,37,63]. In our particular case for voltages above ± 1V the MR curves were considerably degraded without the possibility of registering sizeable MR values.

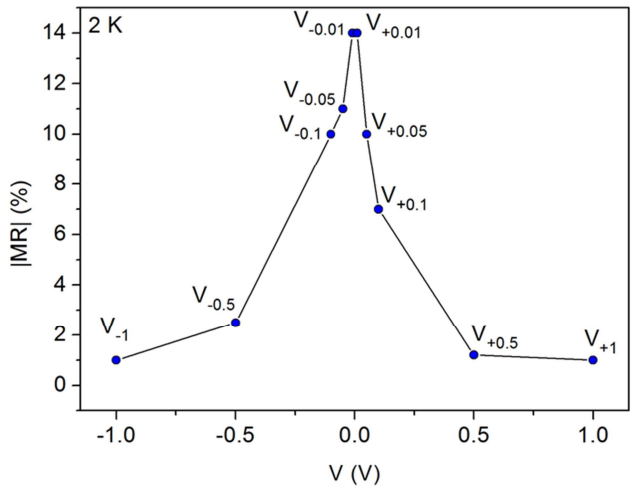

Figure 7.21- Absolute value of MR versus bias voltage for the spin-OLED measured at 2 K.

In our spin-OLED, by employing a bipolar polymer with the ability of transporting both type of carriers (electrons and holes), as described in the introduction, we have set the basis for fabricating an OSV that can work in a bipolar charge transport regime. The low temperature OSV performance for the spin-OLED explained so far, has been found at voltages well below the light emission of the device. This is an indication that in the window of considered voltages, the OSV performance of the spin-OLED is mainly determined by a unipolar charge transport regime. In this context, as it has been explained in the previous section, the injection of holes from the Co/Au anode into the F8BT through the CB of the MoO_3 is more efficient than the electron injection from the cathode. Thus, the latter charge carriers constitute the minority carriers in the device. According to this, for the voltages in which a sizeable MR at low temperature is detected, the spin-polarized current trough the spin-OLED is mainly determined by the charge transport of holes in the F8BT spin collector.

The MR *vs* voltage curve in figure 7.21 shows an asymmetry in the response of the OSV performance which depends on the sign of the biasing. When the spin-OLED is biased in a reverse way, which means an electron injection from the Co anode, the MR values are slightly higher. This asymmetry in the MR *vs* V curves

has been related to the asymmetry of the device structure established by the two different magnetic electrodes as reported for other OSVs with the same feature[36,37,71].

A proper characterization of the thermal evolution of the MR in our spin-OLED has not been possible to perform. In general, for spin-OLEDs with these electrodes, we have observed a fast degradation of the measured MR when increasing the temperature. This behavior has impeded a proper analysis of the impact of this parameter on the OSV performance. In OSVs with Alq_3, employing the LSMO as the spin injection electrode, the decreased of the MR with temperature was determined to follow the thermal evolution of the LSMO magnetization[37,38]. This was indicating that the thermal dependence of the MR was completely dominated by the spin injection process instead of the possible losses on the spin transport in the OSC with temperature[1]. For our spin-OLED, we propose as a possible scenario, a rapid degradation of the MR with temperature promoted by the degradation of spin injection from the Fe electrode for progressively higher temperatures. The quality of the ferromagnetic cathode is in certain grade technically limited regarding to the fabrication process. In addition, the deposition of the F8BT layer on the Fe electrode is done under ambient conditions. Despite the electrode is protected with an alumina barrier, this could have a direct influence on the properties of spin injection. Nevertheless this point has to be studied in more detail for giving a complete explanation of this phenomenology. The most straightforward solution to this problem would be the inclusion of a more stable cathode such as the magnetic oxide LSMO as it will be shown in the next chapter of the thesis.

The last point to be treated in this section is the estimation of the spin diffusion length for the conjugated polymer F8BT employed as the spin collector in our spin-OLED. As it was previously mentioned during the discussion of this chapter there is no previous reported works regarding the application of this OSC in spintronic structures. Taking this into account, in order to get an estimation of the spin diffusion length in the F8BT, we have applied the model developed by P.A. Bobbert and *et al.*[32] which consider the spin transport in a disordered organic material under the influence of a random hyperfine field. As it is well known, the spin-orbit coupling is weak in the OSCs. In the context of

photoinduced spectroscopy experiments, the discussions about the responsible mechanisms on the intersystem crossing (ISC) of singlets and triplets in F8BT totally neglect the spin-orbit coupling in the material based in the weakness of this interaction[72]. In general an important factor ascribed to the spin mixing in OSCs is the hyperfine coupling[33,73,74]. Thus considering all this information, we can treat the spin carrier transport in our conjugated polymer considering the hyperfine interaction as one of the determining factors on the spin diffusion length. This allows us to estimate of the spin diffusion length parameter in the context of the model developed by P. A. Bobbert et al[32]. In this context, there is no information concerning the hopping frequency of carriers in F8BT. Nevertheless, taking into account that the carrier mobilities in this conjugated polymer are higher than those of the PPV-derivatives studied by P. A. Bobbert et al[32,75] it is possible to infer a ratio r >1000 just as it was considered for Alq_3[32]. Values of $\sigma = 0.1\,eV$ for electrons[76] and $\sigma = 0.15\,eV$ for holes[19] have been reported in literature for F8BT at room temperature. This leads to values of disorder strength $\hat{\sigma} \approx 4$ and $\hat{\sigma} \approx 6$, for electrons and holes respectively. This is clearly indicating that our conjugated polymer is in the strong disorder limit (being this limit established for $\hat{\sigma} \geq 4$). In this sense, let us consider the information in figure 7.4 which summarizes the results of the Monte Carlo simulations in a 3D situation for the model under consideration. By assuming an average neighbor distance $a \approx 1.2\,nm$ in F8BT[19] and in the range of $E \ll \sigma/ea$ corresponding to the experiment conditions, a spin diffusion length in the order of hundreds of nanometers could be expected for our conjugated polymer.

The MR traces obtained for our spin-OLED were fitted to the equation 7.2. For our situation in which the system exhibits a positive MR the fitting equation is defined as:

$$MR(B) = MR_{max} \cdot \frac{1}{2}(1 - m_1(B)m_2(B))\exp[-d/l_s(B)] \quad (eq.7.6)$$

with $l_s(B) = l_{s,0}\left(\sqrt{1 + (B/B_0)^2}\right)^{3/4}$

In the equation 7.6, $m_{1,2}(B)$ stand for the normalized magnetizations of the ferromagnetic electrodes. In this case, for defining these magnetizations, we

have employed an error function centered at the correspondent coercive fields. This was made for matching the rounded switching of the electrodes in the MR trace as it was performed by P.A. Bobbert et al[32]. In figure 7.22 it is shown the result of a representative fitting on the data corresponding to the MR curve of the spin-OLED measured at -50 mV at 2K. The fitting procedure of the MR trace to equation 7.6 yields $l_{s,0}/d$ ≈3.6 and $B_0 \equiv 2.3\, B_{hf} \approx 23{,}7$ mT which supposes $B_{hf} \approx$ 10.3 mT. As pointed out by S. Sanvito *et al.*[77] the hyperfine interaction may be represented by a field of the order 10 mT, which causes the electron spin to precess. Thus, the value obtained from the fitting is in concordance with this expectation.

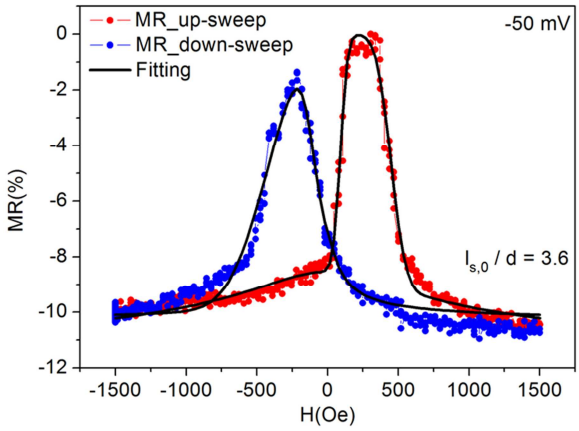

Figure 7.22- Fitting of the MR trace of the spin-OLED measured at -50 mV and 2K employing the model developed by Bobbert and co-workers in the framework of a spin diffusion in disordered organic materials under the influence of a random hyperfine field.

In table 1 it is compared the $l_{s,0}/d$ obtained by the application of this model for fitting the MR traces of OSVs with other OSCs respect to the one extracted from the fitting on our spin-OLED employing F8BT. In all the cases under comparison, the fitting procedure was applied to MR curves measured in the same range of low voltages. From table 1 it is possible to observe that the ratio $l_{s,0}/d$ for F8BT is very similar, even slightly higher, to the one determined for the deuterated polymer D-DOO-PPV studied by Z. V. Vardeny and co-workers[33] . This material was applied in the first reported structure of a

spin-OLED claiming to present a control of light emission with a spin valve MEL effect[4].On the other hand, the $l_{s,0}/d$ for F8BT is approximately double than the one obtained from the fittings for Alq3[32] and C60[65]. This fitting procedure has allowed us to get an idea of the spin diffusion on our conjugated polymer related to other materials analyzed in the framework of the model of Bobbert *et al.*[32] Nevertheless, for the obtaining of an exact value of the spin diffusion length of the F8BT, an extra characterization is needed such as muon spin-resonance experiments[78].

OSC	**Structure**	$l_{s,0}/d$
F8BT	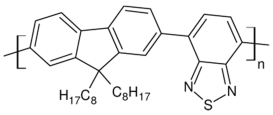	3.6
D-DOO-PPV[33]	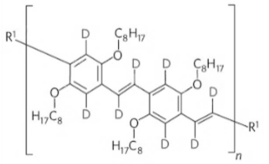	3
Alq3[32]	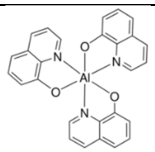	1.7
C60[65]		1.7
H-DOO-PPV[33]	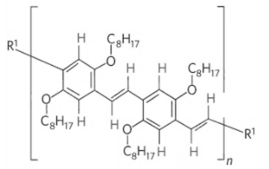	1

Table 1- Comparison of the fitting parameter $l_{s,0}/d$ for different OSCs applying the model of spin transport in disordered materials with hyperfine field contribution[32].

7.3 Conclusions and perspectives

In this chapter of the thesis we have described the design and fabrication of a spin-OLED prototype employing Fe and Co as ferromagnetic electrodes. This work responds to the interest of developing light emitting spintronic devices presenting a modulation of electroluminescence by a spin valve magneto-electroluminescence (MEL) effect. We have proposed for the first time the implementation of an inverted OLED structure (HyLED) in order to fabricate such a multifunctional device. This approach allows the obtaining of more robust and stable structures. The key point of our strategy is the application of commercially available and non-expensive materials, which are employed as received from the provider without extra chemical processes. This contrasts with approaches proposed so far for the fabrication of spin-OLEDs as the one presented by Z.V Vardeny *et al.*[4]. In that case, an expensive and complex deuteration process is needed for the obtaining of the OSC used as the active media in the device. By this means we have applied for the first time in the field of organic spintronics materials such as F8BT and MoO_3 extensively used for optoelectronics.

As explained many times in this chapter, there is a fundamental condition for light modulation under magnetic fields based on a spin valve MEL effect. This is the coexistence of electroluminescence (EL) and spin-polarized current in the device for the same range of voltages and temperatures. It has been shown the presence of a good EL performance in the spin-OLED for all the temperature range under study. In addition, an OSV performance has been described for this structure at low temperatures, which is an indication of the presence of a spin-polarized current in the system. However, these functionalities take place at a different range of voltage and temperatures. Despite this drawback, the proposed structure supposes an interesting prototype for the developing of a light emitting spintronic device fabricated with commercial materials. This work this work has led to the creation of a national patent nº 201300083 entitled: "Dispositivo opto-espintrónico y método para su fabricación"[79].

7.4 Bibliography

(1) Dediu, V. A.; Hueso, L. E.; Bergenti, I.; Taliani, C. *Nat. Mater.* **2009**, *8*, 707.

(2) Davis, a. H.; Bussmann, K. *J. Appl. Phys.* **2003**, *93*, 7358.

(3) Salis, G.; Alvarado, S.; Tschudy, M.; Brunschwiler, T.; Allenspach, R. *Phys. Rev. B* **2004**, *70*, 085203.

(4) Nguyen, T. D.; Ehrenfreund, E.; Vardeny, Z. V. *Science* **2012**, *337*, 204.

(5) Sessolo, M.; Bolink, H. J. *Adv. Mater.* **2011**, *23*, 1829.

(6) Michaelson, H. B. *J. Appl. Phys.* **1977**, *48*, 4729.

(7) Palomares, E.; Clifford, J. N.; Haque, S. a; Lutz, T.; Durrant, J. R. *J. Am. Chem. Soc.* **2003**, *125*, 475.

(8) Meyer, J.; Shu, a.; Kröger, M.; Kahn, a. *Appl. Phys. Lett.* **2010**, *96*, 133308.

(9) Zhang, Y.; Blom, P. W. M. *Appl. Phys. Lett.* **2011**, *98*, 143504.

(10) Xia, Y.; Friend, R. H. *Macromolecules* **2005**, *38*, 6466.

(11) Kim, J.-S.; Ho, P. K. H.; Murphy, C. E.; Friend, R. H. *Macromolecules* **2004**, *37*, 2861.

(12) Corcoran, N.; Arias, a. C.; Kim, J. S.; MacKenzie, J. D.; Friend, R. H. *Appl. Phys. Lett.* **2003**, *82*, 299.

(13) Arias, a. C.; Corcoran, N.; Banach, M.; Friend, R. H.; MacKenzie, J. D.; Huck, W. T. S. *Appl. Phys. Lett.* **2002**, *80*, 1695.

(14) Kim, Y.; Cook, S.; Choulis, S. A.; Nelson, J.; Durrant, J. R.; Bradley, D. D. C. *Chem. Mater.* **2004**, *16*, 4812.

(15) Snaith, H. J.; Arias, A. C.; Morteani, A. C.; Silva, C.; Friend, R. H. *Nano Lett.* **2002**, *2*, 1353.

(16) Cornil, J.; Gueli, I.; Dkhissi, a.; Sancho-Garcia, J. C.; Hennebicq, E.; Calbert, J. P.; Lemaur, V.; Beljonne, D.; Brédas, J. L. *J. Chem. Phys.* **2003**, *118*, 6615.

(17) Zaumseil, J.; Donley, C. L.; Kim, J.-S.; Friend, R. H.; Sirringhaus, H. *Adv. Mater.* **2006**, *18*, 2708.

(18) Chua, L.; Zaumseil, J.; Chang, J.; Ou, E. C. *Nature* **2005**, *434*, 194.

(19) Zhang, Y.; Blom, P. W. M. *Appl. Phys. Lett.* **2011**, *98*, 143504.

(20) Morii, K.; Ishida, M.; Takashima, T.; Shimoda, T.; Wang, Q.; Nazeeruddin, M. K.; Grätzel, M. *Appl. Phys. Lett.* **2006**, *89*, 183510.

(21) Bolink, H. J.; Coronado, E.; Repetto, D.; Sessolo, M.; Barea, E. M.; Bisquert, J.; Garcia-Belmonte, G.; Prochazka, J.; Kavan, L. *Adv. Funct. Mater.* **2008**, *18*, 145.

(22) Bolink, H. J.; Brine, H.; Coronado, E.; Sessolo, M. *J. Mater. Chem.* **2010**, *20*, 4047.

(23) Haque, S. a.; Koops, S.; Tokmoldin, N.; Durrant, J. R.; Huang, J.; Bradley, D. D. C.; Palomares, E. *Adv. Mater.* **2007**, *19*, 683.

(24) Matsushima, T.; Kinoshita, Y.; Murata, H. *Appl. Phys. Lett.* **2007**, *91*, 253504.

(25) Tokito, S.; Noda, K.; Taga, Y. *J. Phys. D. Appl. Phys.* **1996**, *29*, 2750.

(26) Shrotriya, V.; Li, G.; Yao, Y.; Chu, C.-W.; Yang, Y. *Appl. Phys. Lett.* **2006**, *88*, 073508.

(27) Kröger, M.; Hamwi, S.; Meyer, J.; Riedl, T.; Kowalsky, W.; Kahn, A. *Org. Electron.* **2009**, *10*, 932.

(28) Morii, K.; Omoto, M.; Ishida, M.; Graetzel, M. *Jpn. J. Appl. Phys.* **2008**, *47*, 7366.

(29) Nakayama, Y.; Morii, K.; Suzuki, Y.; Machida, H.; Kera, S.; Ueno, N.; Kitagawa, H.; Noguchi, Y.; Ishii, H. *Adv. Funct. Mater.* **2009**, *19*, 3746.

(30) Wang, Y.-Z.; Yang, M.; Qi, D.-C.; Chen, S.; Chen, W.; Wee, A. T. S.; Gao, X.-Y. *J. Chem. Phys.* **2011**, *134*, 034706.

(31) Wang, Y.-Z.; Cao, L.; Qi, D.-C.; Chen, W.; Wee, A. T. S.; Gao, X.-Y. *J. Appl. Phys.* **2012**, *112*, 033704.

(32) Bobbert, P.; Wagemans, W.; van Oost, F.; Koopmans, B.; Wohlgenannt, M. *Phys. Rev. Lett.* **2009**, *102*, 156604.

(33) Nguyen, T. D.; Hukic-Markosian, G.; Wang, F.; Wojcik, L.; Li, X.-G.; Ehrenfreund, E.; Vardeny, Z. V. *Nat. Mater.* **2010**, *9*, 345.

(34) Schulten, K.; Wolynes, P. G. *J. Chem. Phys.* **1978**, *68*, 3292.

(35) Bassler, H. *Pshysica Status Solidi B* **1993**, *175*, 15.

(36) Xiong, Z. H.; Wu, D.; Vardeny, Z. V.; Shi, J. *Nature* **2004**, *427*, 821.

(37) Wang, F.; Yang, C.; Vardeny, Z.; Li, X. *Phys. Rev. B* **2007**, *75*, 245324.

(38) Dediu, V.; Hueso, L.; Bergenti, I.; Riminucci, a.; Borgatti, F.; Graziosi, P.; Newby, C.; Casoli, F.; De Jong, M.; Taliani, C.; Zhan, Y. *Phys. Rev. B* **2008**, *78*, 115203.

(39) Majumdar, S.; Laiho, R.; Laukkanen, P.; Vaÿrynen, I. J.; Majumdar, H. S.; Oˆsterbacka, R. *Appl. Phys. Lett.* **2006**, *89*, 122114.

(40) Andreyev, O.; Koroteev, Y. M.; Sánchez Albaneda, M.; Cinchetti, M.; Bihlmayer, G.; Chulkov, E. V.; Lange, J.; Steeb, F.; Bauer, M.; Echenique, P. M.; Blügel, S.; Aeschlimann, M. *Phys. Rev. B* **2006**, *74*, 195416.

(41) Fleisch, T. H., M. G. J. *J. Chem. Phys.* **1982**, *76*, 780.

(42) Wu, C.-I.; Lin, C.-T.; Lee, G.-R.; Cho, T.-Y.; Wu, C.-C.; Pi, T.-W. *J. Appl. Phys.* **2009**, *105*, 033717.

(43) Matsushima, T.; Jin, G.-H.; Murata, H. *J. Appl. Phys.* **2008**, *104*, 054501.

(44) Droghetti, A.; Steil, S.; Großmann, N.; Haag, N.; Zhang, H.; Willis, M.; Gillin, W. P.; Drew, A. J.; Aeschlimann, M.; Sanvito, S.; Cinchetti, M. *Phys. Rev. B* **2014**, *89*, 094412.

(45) Li, F.; Tang, H.; Anderegg, J.; Shinar, J. *Appl. Phys. Lett.* **1997**, *70*, 1233.

(46) Peng, J.; Wang, X.; Liu, J.; Huang, X.; Xiao, J.; Wang, S.-D.; Wang, H.-Q.; Ma, W. *J. Mater. Chem. C* **2014**, *2*, 864.

(47) Tang, H.; Li, F.; Shinar, J. *Appl. Phys. Lett.* **1997**, *71*, 2560.

(48) Santos, T.; Lee, J.; Migdal, P.; Lekshmi, I.; Satpati, B.; Moodera, J. *Phys. Rev. Lett.* **2007**, *98*, 016601.

(49) Li, K.-S.; Chang, Y.-M.; Agilan, S.; Hong, J.-Y.; Tai, J.-C.; Chiang, W.-C.; Fukutani, K.; Dowben, P. a.; Lin, M.-T. *Phys. Rev. B* **2011**, *83*, 172404.

(50) Schmidt, G.; Ferrand, D.; Molenkamp, L.; Filip, a.; van Wees, B. *Phys. Rev. B* **2000**, *62*, R4790.

(51) Rashba, E. *Phys. Rev. B* **2000**, *62*, R16267.

(52) Smith, D.; Silver, R. *Phys. Rev. B* **2001**, *64*, 045323.

(53) Mulazzi, E.; Ripamonti, a.; Wery, J.; Dulieu, B.; Lefrant, S. *Phys. Rev. B* **1999**, *60*, 16519.

(54) Ruden, P. *Nat. Mater.* **2011**, *10*, 8.

(55) Shim, J.; Raman, K.; Park, Y.; Santos, T.; Miao, G.; Satpati, B.; Moodera, J. *Phys. Rev. Lett.* **2008**, *100*, 226603.

(56) Sun, D.; Yin, L.; Sun, C.; Guo, H.; Gai, Z.; Zhang, X.-G.; Ward, T. Z.; Cheng, Z.; Shen, J. *Phys. Rev. Lett.* **2010**, *104*, 236602.

(57) Wang, F. J.; Xiong, Z. H.; Wu, D.; Shi, J.; Vardeny, Z. V. *Synth. Met.* **2005**, *155*, 172.

(58) Sessolo, M. *Hybrid organic-inorganic Light Emitting Diodes. PhD Thesis*; University of Valencia, 2010.

(59) Choi, H. W.; Kim, S. Y.; Kim, W.-K.; Hong, K.; Lee, J.-L. *J. Appl. Phys.* **2006**, *100*, 064106.

(60) Choi, H. W.; Kim, S. Y.; Kim, W.-K.; Lee, J.-L. *Appl. Phys. Lett.* **2005**, *87*, 082102.

(61) Predeep, P. *Optoelectronics: Devices and Applications*; Intech: Rijeka-Croatia, 2011.

(62) Blom, P. W. M.; De Jong, M. J. M. *IEEE J. Sel. Top. Quantum Electron.* **1998**, *4*, 105.

(63) Lin, R.; Wang, F.; Rybicki, J.; Wohlgenannt, M.; Hutchinson, K. a. *Phys. Rev. B* **2010**, *81*, 195214.

(64) Wohlgenannt, M. *Phys. status solidi - Rapid Res. Lett.* **2012**, *6*, 229.

(65) Zhang, X.; Mizukami, S.; Kubota, T.; Ma, Q.; Oogane, M.; Naganuma, H.; Ando, Y.; Miyazaki, T. *Nat. Commun.* **2013**, *4*, 1392.

(66) Liu, Y.; Watson, S.; Lee, T.; Gorham, J.; Katz, H.; Borchers, J.; Fairbrother, H.; Reich, D. *Phys. Rev. B* **2009**, *79*, 075312.

(67) Kawasugi, Y.; Ujino, T.; Tada, H. *Org. Electron.* **2013**, *14*, 3186.

(68) Barraud, C.; Seneor, P.; Mattana, R.; Fusil, S.; Bouzehouane, K.; Deranlot, C.; Graziosi, P.; Hueso, L.; Bergenti, I.; Dediu, V.; Petroff, F.; Fert, A. *Nat. Phys.* **2010**, *6*, 615.

(69) Alam, K. M., Pramanik, S. *http://arxiv.org/ftp/arxiv/papers/1005/1005.1118* **2012**.

(70) Riminucci, A.; Bergenti, I.; Hueso, L. E.; Murgia, M.; Taliani, C.; Zhan, Y.; Casoli, F. <*http://arxiv.org/abs/cond-mat/0701603*> **2007**.

(71) Vardeny, Z. V. *Organic Spintronics*; Taylor & Francis Group: Boca Raton-Florida, 2010.

(72) Ford, T.; Avilov, I.; Beljonne, D.; Greenham, N. *Phys. Rev. B* **2005**, *71*, 125212.

(73) Lee, S.; Paik, S.; Mccamey, D. R.; Yu, J.; Burn, P. L.; Lupton, J. M.; Boehme, C. *J. Am. Chem. Soc.* **2011**, *133*, 2019.

(74) Wang, J.; Chepelianskii, A.; Gao, F.; Greenham, N. C. *Nat. Commun.* **2012**, *3*, 1191.

(75) Pasveer, W.; Cottaar, J.; Tanase, C.; Coehoorn, R.; Bobbert, P.; Blom, P.; de Leeuw, D.; Michels, M. *Phys. Rev. Lett.* **2005**, *94*, 206601.

(76) Blakesley, J. C.; Clubb, H. S.; Greenham, N. C. *Phys. Rev. B* **2010**, *81*, 045210.

(77) Szulczewski, G.; Sanvito, S.; Coey, M. *Nat. Mater.* **2009**, *8*, 693.

(78) Drew, a J.; Hoppler, J.; Schulz, L.; Pratt, F. L.; Desai, P.; Shakya, P.; Kreouzis, T.; Gillin, W. P.; Suter, a; Morley, N. a; Malik, V. K.; Dubroka, a; Kim, K. W.; Bouyanfif, H.; Bourqui, F.; Bernhard, C.; Scheuermann, R.; Nieuwenhuys, G. J.; Prokscha, T.; Morenzoni, E. *Nat. Mater.* **2009**, *8*, 109.

(79) Coronado, E., Prima-García, H., Prieto-Ruiz, J. P. *National Patent 201300083: "Dispositivo opto-espintrónico y método para su fabricación"*; 2013.

Chapter 8

Observation of spin valve magneto-electroluminescence effect on a spin-OLED with LSMO and Co electrodes

8.1 Introduction

From the results presented in the previous chapter, it was clear that for having light modulation by a spin valve magneto-electroluminescence (MEL) effect in the spin-OLED structures, it was necessary to drive the EL and the OSV performances to the same range of voltages and temperatures. A fast degradation of the MR with temperature was detected in the Fe/Co device described in chapter 7. This is likely due to the degradation of the spin injection properties of the Fe electrode as a consequence of the fabrication conditions. Thus, a feasible strategy for improving the performance of the spin-OLED is the substitution of this transition metal electrode by other more stable one. The magnetic oxide Lanthanum Strontium Manganite Oxide, $La_{1-x}Sr_xMnO_3$ (LSMO) constitutes a good option for this purpose. The LSMO is a material exhibiting a half-metallic ferromagnetic behavior with near 100 % spin polarization[1,2] (nearly one spin direction in the Fermi level). This property combined with an outstanding resistance against air oxidation[2,3] has promoted the wide application of this electrode in the field of organic spintronics[4–10]. Considering the fabrication process of our spin-OLED device, in which in certain step the cathode is exposed to ambience conditions, the chemical stability of the LSMO would promote the preservation of the spin injection properties. In addition, the important chemical stability of this material allows the incorporation of new barriers, respect to the conventional ones, by applying wet solution methods. This approach has been recently demonstrated by the growth of dodecylphosphonic acid self-assembling monolayers (SAMs) on LSMO electrodes for the obtaining of spintronic structures[9,10].

Thus, by starting from the spin-OLED prototype presented in chapter 7, the Fe electrode was substituted by a LSMO one, using a molecular barrier as the EIL in the structure. The energy level diagram of the layers composing the final device proposed in this chapter is shown in figure 8.1

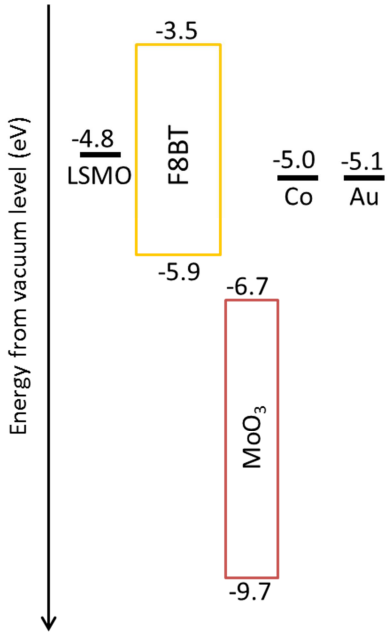

Figure 8.1- Diagram of energy levels for LSMO[5], F8BT[11], MoO_3[12], Co[13] and Au[13] composing the spin-OLED.

8.2 Results and discussion

8.2.1 Device fabrication and general characterization

The philosophy underlying the design and fabrication of the device described in this chapter is the same respect to the spin-OLED prototype fabricated with Fe and Co as cathode and anode respectively. In the present spin-OLED, the hole injection layer (HIL), the emissive layer and the anode were maintained as part of the structure. Nevertheless, the severe degradation with temperature of the MR signal spin-OLED prototype with a Fe cathode, as detailed in the introduction of the chapter, has motivated its substitution by the LSMO as the spin injection electrode in the light emitting spintronic device.

The LSMO electrodes were grown with a thickness of 20 nm on (100) oriented transparent $SrTiO_3$ (STO) substrates by Channel-Spark ablation (CSA) from polycrystalline targets[14]. The STO double side polished substrates were purchased from MaTeck, and the epitaxial LSMO thin film was deposited with a shadow mask forming a stripe of 1 mm width on the substrate. The LSMO electrodes were fabricated at the *Instituto per lo Studio dei Materiali Nanostrutturati (ISMN-CNR)* at Bologna and provided by Dr. V.A. Dediu and Dr. P. Graziosi. A morphological characterization was performed by means of atomic force microscopy (AFM) for determining the surface quality of the electrodes. Topography images of 1 μm^2 scan size were acquired in tapping mode as shown in figure 8.2. The LSMO surface presents a value of 0.2 nm for the RMS roughness. This clearly supports the excellent morphology of this electrode and establishes the proper initial conditions for depositing the subsequent layers of the devices.

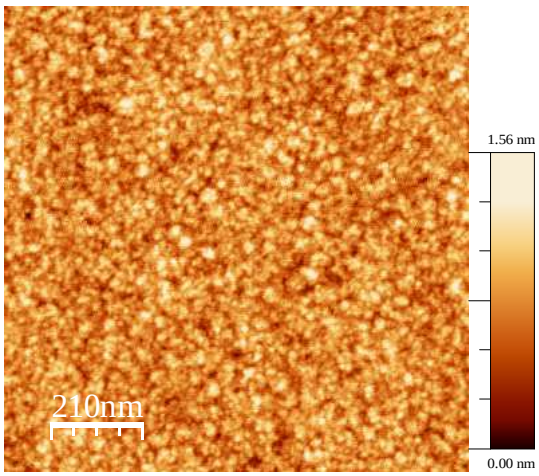

Figure8.2- 1μm^2 scan size AFM topography image in tapping mode of a LSMO substrate employed in the fabrication of the spin-OLED.

The MR of the LSMO in the range of ±3000 Oe was measured and calculated with the formula:

$$\frac{\Delta R}{R(0)} = \frac{R - R(0)}{R(0)} \cdot 100\ (\%) \qquad (eq.\quad 8.1)$$

Absolute values of MR of 0.36 % and 4.3 % were found for this electrode when measured by a two point standard method at 42 K and 292 K respectively under a bias voltage of 1V (figure 8.3) when sweeping an in-plane external magnetic field. The low MR values determined at fields of ± 1000 Oe are totally correspondent with the previous reported values for these LSMO electrodes fabricated by the CSA technique[14]. In general, this is an indication of high epitaxial quality of the electrode, based on the fact that presence of grain boundaries would increase the MR up to several percents[15]. Thus, the measured MR signal of the LSMO confirms the good quality of the electrode for its inclusion as the spin injection electrode in the structure.

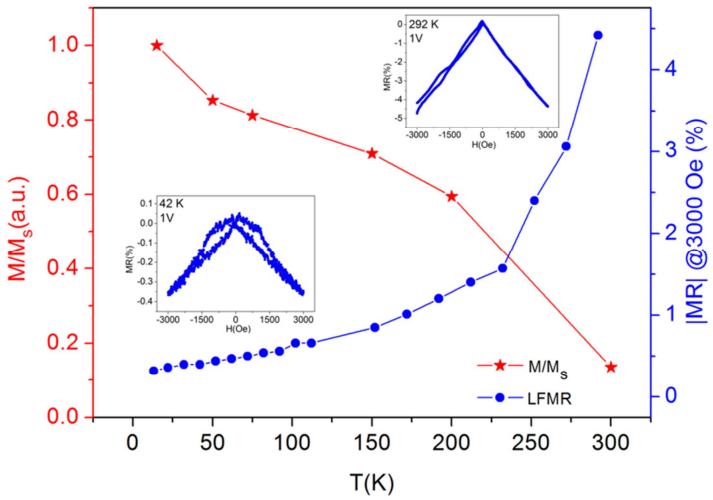

Figure 8.3- Thermal dependence of the absolute value of the MR (blue curve) and bulk magnetization (M/M_s) of the LSMO electrode (red curve). *Inset*: MR signals at 42 K and 292 K measured at 1V.

The thermal dependence of the MR in the LSMO was evaluated as well as the evolution of the bulk magnetization with temperature (figure 8.3). From this study an increase in the MR values was observed when increasing the temperature with a simultaneously decrease in the bulk magnetization, resembling the same tendency reported for these LSMO grown by CSA onto STO subtrates[14].

After stablishing the good quality of the LSMO as the cathode of the spin-OLED, the next step is the inclusion of a proper electron injection layer (EIL). As it was previously mentioned in the two previous chapters, the electron injection in a HyLED structure is the main bottleneck for optimal performance of this type of devices. Thus by solving this problem an important improvement of the EL properties can be achieved.

The outstanding chemical stability of the LSMO against air oxidation allowed us to include a new type of barrier not only from conventional evaporation methods. In most of the spintronic structures reported so far evaporated barriers of Al_2O_3 or MgO[16–18] have been included. On the contrary, we propose a more innovative approach by the application chemical solution processes. The philosophy underlying our strategy is based on the fact that the designing of a device with striking properties such as a spin-OLED requires from challenging approaches which can lead to new functionalities.

In the field of organic electronics, a wide variety of strategies focused in decreasing the gap between energy levels of metals and OSCs have been developed for enhancing the charge injection between both materials[19]. The surface modification of the metal or semiconductor by self-assembling molecules with the ability of forming highly ordered, 2D layers with a dipole in the desire direction has been extensively applied. In this context, carboxylic acid[20,21], phosphonic acid[22], and silane derivatives[23] have been used to functionalize ITO, commonly used as an anode in OLED devices. For noble metal electrodes such as Au[24] monolayers of thiol derivatives have been applied[24].

On the other hand, in the field of molecular spintronics, the application of self-assembling monolayers (SAMs) to functionalize spin injection electrodes has been demonstrated by the preparation of tunneling nanojuctions by the grafting of a octanethiol SAMs on Ni[25,26] and recently by the functionalization of LSMO electrodes with a phosphonic acid derivative[9,10]. In this last work[9], tunneling nanojunctions with LSMO and Co as electrodes and phosphic acid as a tunneling barrier, showed a tunneling magneto-resistance (TMR) up to 2V. This supposes an important improvement respect to the performance of large-

area organic spin valves reported so far[5–8,27–33]. The new functionalities acquired from the molecular engineering approach, with the application of molecules and SAMs for the electrode functionalization, are quite evident from the point of view of the organic electronics and more recently from the perspective of organic spintronics. With this background in mind, we wanted to take profit of this molecular engineering approach for fabricating a more efficient electron injection interface in our spin-OLED structure employing LSMO as the cathode.

For this aim we have based our strategy of cathode functionalization on the work published by H. J. Bolink and co-workers[19]. In this work a molecular ionic junction was fabricated by depositing a monolayer of a charged ruthenium complex on TiO_2 using the Langmuir-Boldgett (LB) technique. The inclusion of this ionic molecule in the HyLED induced an important improvement in the EL performance of the device. In particular, a reduction of the light emission turn on voltage (V_{on}) of approximately 1V respect to the device without the ionic complex was reported. The same ruthenium complex as the one employed in the previous described work, with formula bis(4,4'-tridecyl-2,2'-bipyridine)-(4,4'-dicarboxy-2,2'-bipyridine) ruthenium(II)-bis(chloride) and named as N965 (figure 8.4), has been included in our spin-OLED. The synthesis of this ionic ruthenium complex, performed by Md. K. Nazeeruddin at the Laboratory of Photonics and Interfaces (EPFL) , is described elsewhere[19].

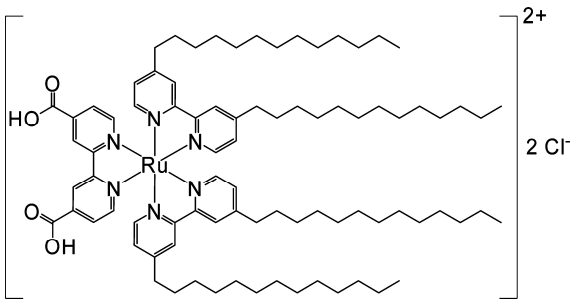

Figure 8.4- Structure of the ionic ruthenium complex bis(4,4'-tridecyl-2,2'-bipyridine)-(4,4'-dicarboxy-2,2'-bipyridine)ruthenium(II)-bis(chloride) (N965).

One important characteristic of this ionic charged complex is the ability to anchor via covalent bonds to an oxide surface, as it has been demonstrated in the functionalization of TiO_2 surfaces[19]. Considering this property, the possibility of transferring by means of LB this ionic molecule to the surface of a magnetic oxide such as LSMO is guaranteed. In this sense, the formation of a monolayer of N965 on the LSMO electrode by LB is promoted by two aspects: the amphiphilic character of the ionic complex and the presence of carboxylic groups which can bond covalently to the magnetic oxide surface. For the fabrication of this ionic molecular junction on LSMO with LB, a solution of the chloride salt of the N965 complex was prepared on chloroform ($CHCl_3$) and employed as a spreading solution. Certain amount of this solution was subsequently spread on an aqueous subphase of KPF_6, and the $CHCl_3$ solvent was let to evaporate after 10 minutes. A compression of the monolayer was done, with a transferring to the substrate at 27 mN/m controlled by the evolution of the compression isotherm of the process (figure 8.5).

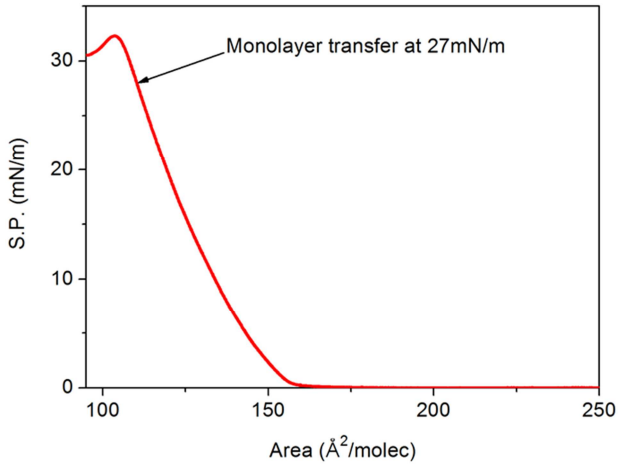

Figure 8.5- Compression isotherm of the N965 complex on a KPF_6 subphase.

The assembling of the monolayer on the LSMO substrate was done by a vertical lifting method consisting on an immersion and a subsequent withdrawal of the substrate through the interface containing the ionic molecular complex. The transferring of the monolayer takes place on the withdrawal step due to the amphiphilic nature of the Ru complex. In all this process, there is an effective

adsorption of the PF_6^- anions, present in the aqueous subphase, on the Ru complex monolayer. This is accomplished by a substitution of the Cl^- anions of the Ru salt employed for the preparation of the spreading solution. The substitution of the Cl^- by the PF_6^- anion is promoted by the latter higher mobility of the latter one. This higher mobility arises from the bigger size of the anion which reduces the electrostatic interaction with the counterion.

The correct formation of the Ru complex monolayer on LSMO was tested by measurements of contact angle. This technique has been extensively employed for monitoring the growing of molecular monolayers and multilayers by self-assembling or LB[34–37]. The evolution of the wettability of the surface under water exposure is the tool we have used for characterizing the correct formation of the molecular monolayer on top of the transferring substrate. The contact angle measurements, before and after the deposition of the Ru complex monolayer, are shown in figure 8.6.

Figure 8.6- Contact angle measurement of a water droplet on the clean LSMO substrate (*left*) and after the LB deposition of the molecular monolayer of N965 (*right*).

The contact angle evolved from an average value of 27° for a clean LSMO substrate, to a contact angle of 95° after the deposition of N965. The evolution of the wettability of the surface evolving to a more hydrophobic character after the LB deposition can be explained by the presence of the molecular complex. While the LSMO substrate is hydrophilic, after the deposition of N965 the surface becomes hydrophobic due to the long aliphatic chains of the molecule. The monolayer of N965 is strongly anchored to the LSMO surface through its hydrophilic part composed by the bipyridine (bpy) ligand functionalized with two

carboxylate groups. On the other hand, the hydrophobic part, composed by the bpy ligand functionalized with long alkyl chains, is oriented away from the magnetic oxide surface. The advantage of the contact angle technique relies in the big areas under analysis, determined by the size of the water droplet deposited with the set-up. Regions in the order of several microns to millimeters are characterized, demonstrating in this way the good coverage of the manganite substrate by the monolayer of N965.

In addition, a morphological analysis of the monolayer growth was done by means of AFM. In figure 8.7 it is shown the topography image in tapping mode of a 1 μm^2 scan size area of the functionalized LSMO electrode. From this study it is possible to observe a slight evolution of the RMS roughness from 0.2 nm in the clean LSMO (figure 8.2) to a value of 0.4 nm after the deposition of the N965 monolayer. This is a proof of the homogenous growth of the molecular layer. In this sense, an inhomogeneous growing, translated into incomplete covering or aggregate formation, would induce a greater roughness considering the size of the Ru complex (~2 nm)[19].

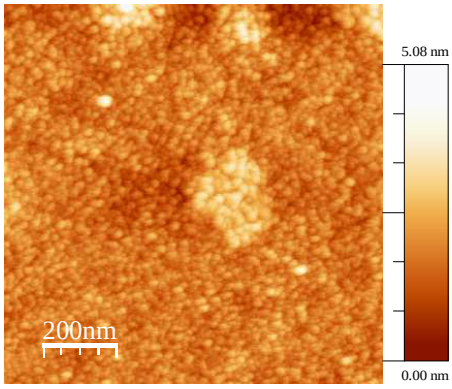

Figure 8.7- AFM topography image in tapping mode of 1μm^2 scan size of the N965 monolayer growth by LB onto a LSMO electrode.

At this point, the good quality of the LSMO for its inclusion as a cathode in our spin-OLED device, as well as the correct growing of a monolayer of the Ru complex N965 has been proved. Based on this, the substitution of the Fe cathode with an AlO_x EIL, described in chapter 7, by the LSMO electrode with

the N965 monolayer acting as the new EIL in the device is straightforward. The rest of the elements composing the spin-OLED as the light emitting polymer (LEP), the HIL and the Co/Au anode are maintained in the structure.

After being received from Bologna and prior to the fabrication of the device, the 20 nm thickness LSMO electrode was exposed to a standard cleaning process. It consists on a multiple sonication on acetone, isopropanol and subsequently on distillated water, of approximately 10 minutes in each case. After the last sonication, the LSMO was dried with an N_2 gas flow and exposed to a UV-ozone lamp during other ten minutes in order to complete the cleaning procedure. This process was applied for removing any organic residue on the surface of the electrode. In this way, it is avoided the appearance of defects that could lead to shortcuts or anomalous growing of the top layers in the device. Subsequently, and once the LSMO surface was cleaned, a monolayer of the N965 Ru complex was deposited on top of the magnetic oxide cathode by means of LB according to the process previously described.

The fabrication process of the other layers in the device is identical to the one described for the spin-OLED of chapter 7.After the deposition of the N965 monolayer, a 45 nm thickness film of the light emitting polymer F8BT was deposited by spin-coating from a chlorobenzene solution. This layer was subsequently annealed in the glove box at 100 °C for completing the fabrication of the active medium. This conjugated polymer, extensively described in the previous chapter, showed a good performance for acting both as the emissive layer and spin collector medium. Thus, this material was kept in the fabrication of the new spin-OLED structure with LSMO and Co electrodes, regarding to its ability for transporting both electrons and holes[11,38–41]. This property allows the fabrication of light emitting spintronic devices presenting a bipolar charge transport regime. In addition, the point of using a unique material for transporting both types of charge carriers makes possible to remove one interface in the spintronic structure. This is also very important considering the critical role of interfaces in the performance of the OSVs[32,42]. The thickness of the emissive layer was controlled by profillometry measurements.

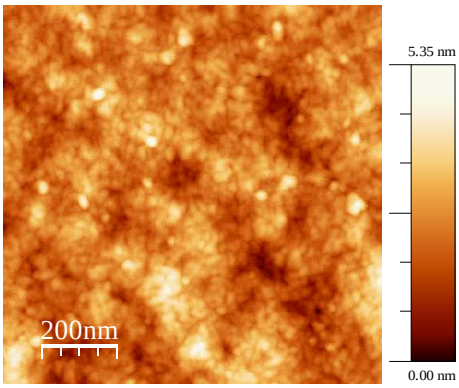

Figure 8.8- AFM topography image in tapping mode of 1μm² scan size of the 45 nm F8BT layer deposited on top of the functionalized LSMO substrate with a monolayer of N965.

The morphological quality of the LEP layer deposited onto the N965 monolayer was tested by means of AFM (figure 8.8). The topography image of 1μm² scan size shows a homogenous covering with an RMS roughness of 0.6 nm. The low surface roughness of the polymeric layer establishes good conditions for the fabrication of a smooth and high quality interface with the HIL deposited on top.

After the polymer deposition, the sample was transferred to a thermal evaporator where 3 nm MoO_3 layer was evaporated (base pressure < 10^{-6} mbar) on top of the whole substrate, acting as the HIL in the spin-OLED. The evaporation was performed with a speed of 0.1Å/s to minimize the impact on the OSC avoiding possible interpenetrations. The 3 nm thickness was maintained respect to the spin-OLED prototype described in the previous chapter. This thickness has been demonstrated to be a good compromise for the correct optoelectronic performance of the device as well as from the spintronic point of view. The AFM image of the MoO_3 surface onto the F8BT layer (figure 8.9), shows a RMS roughness of 0.6 nm. The unaltered RMS value respect to the one found for the F8BT onto the N965 monolayer, before the deposition of this oxide barrier, can be considered as an indication of a homogenous growing of this HIL.

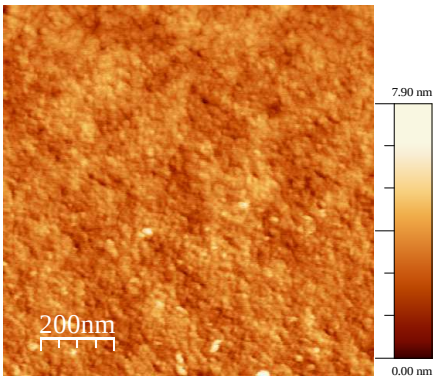

Figure 8.9- AFM topography image in tapping mode of 1μm² scan size of 3 nm MoO_3 on top of 45 nm thickness F8BT layer, just as prepared in the device.

A new shadow mask in a cross-bar configuration respect to the LSMO, was used for the deposition of 20 nm of Co by thermal evaporation (base pressure < 10^{-6} mbar). Without breaking the vacuum, a final gold layer of 35 nm thickness of Au was prepared (base pressure < 10^{-6} mbar). This last layer, as done in the device of chapter 7, was included for preventing the oxidation of the ferromagnetic electrode acting as the anode of the spin-OLED. The evaporation of these two layers was again done with a low rate of 0.1Å/s avoiding in this way any physical damaging of the 3 nm MoO_3barrier.

The good quality of all the interfaces was evaluated by means of an HRTEM study at the Advanced Microscopy Laboratory-INA. A lamella of the device was fabricated by means of focus ion beam technique (FIB). This process was done under cryogenic conditions for preventing the damage of the OSC, which in terms could alter the real morphology of the interfaces.

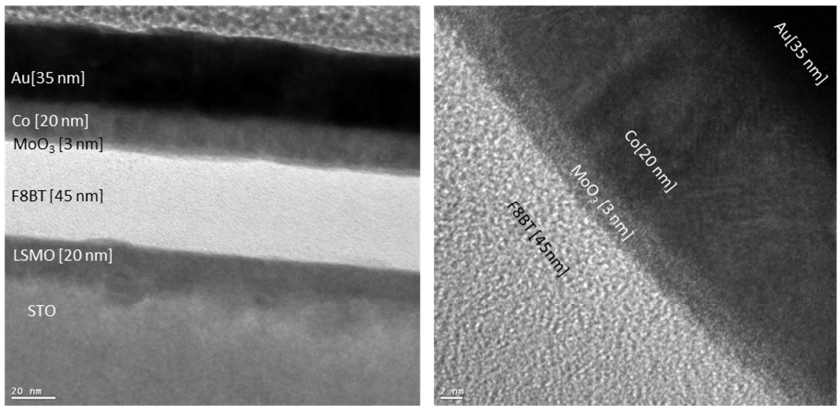

Figure 8.10- *Left*: HRTEM image of the cross section of the device. The thicknesses of the different layers were determined to be: LSMO 20nm, F8BT 45 nm, Co 18nm, Au 35 nm. *Right*: HRTEM image of the F8BT/MoO3/Co interface showing no interpenetration of Co atoms in the organic layer.

From a representative image of the lamella, shown in figure 8.10, it is possible to get a detailed view of all the layers composing the spin-OLED and particularly from the F8BT/MoO_3/Co interface. By this study the interpenetration of Co atoms in the organic material is discarded. This point demonstrates the effective prevention against Co inclusions, established by the presence of the MoO_3 barrier and the evaporation conditions. Thus, the formation of an "ill-defined" layer in the F8BT during the spin-OLED fabrication can be ruled out based on this information.

After depositing all the layers, the design of the masks and the technical conditions of fabrication, allowed us to obtain two cells per device with an effective area of 0.5 mm^2.The 3D sketch of all the layers composing the spin-OLED device is shown in figure 8.11., being: STO/LSMO(20nm)/(N965) /F8BT(45nm)/MoO_3(3nm)/Co(18nm)/Au(35nm)

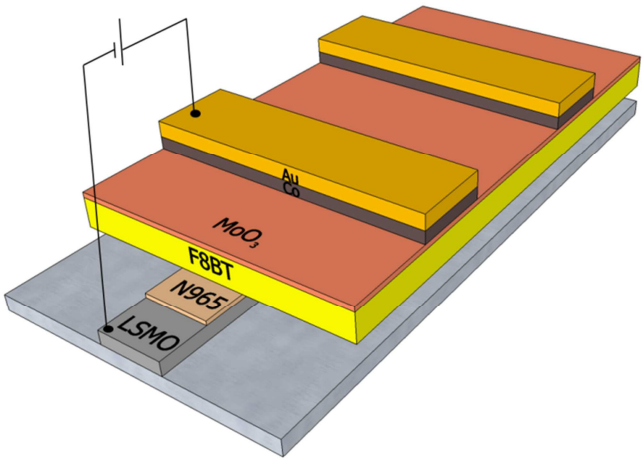

Figure 8.11- 3D sketch of the spin-OLED structure with an indication of the voltage biasing for the EL and spin transport measurements.

As it was explained in chapter 8, in order to have a correct OSV performance in the device, the ferromagnetic anode and cathode have to present a sufficient difference in the coercive fields. This point guarantees the stabilization of parallel and antiparallel relative orientations of the electrode magnetizations under the sweeping of the external magnetic field. The longitudinal hysteresis loops of the electrodes in the spin-OLED were measured with MOKE magnetometry at 14 K as depicted in figure 8.12.

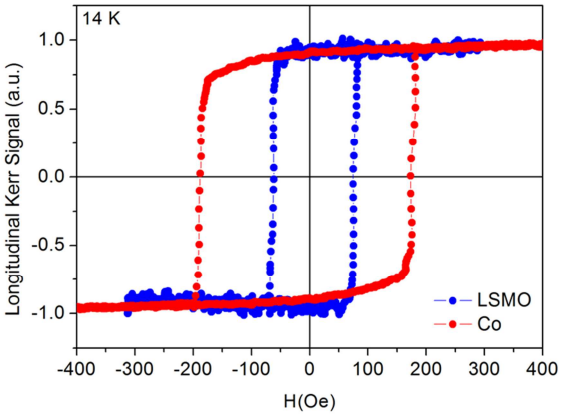

Figure 8.12- Longitudinal MOKE signal at low temperature of the LSMO (blue curve) and Co (red curve) in the spin-OLED.

The MOKE characterization shows coercive fields of 75 Oe and 180 Oe for the LSMO and Co electrodes respectively. This difference is enough to guarantee the stabilization of the antiparallel state in the OSV performance of the spin-OLED.

The next step in the study was the characterization of the EL performance as well as the spin transport properties of this light emitting spintronic device. The strategy on this spin-OLED has been based on the interface engineering by the inclusion of a molecular monolayer as EIL onto an air stable magnetic cathode. Thus in order to check the effect of this molecular ionic junction on the performance of the spin-OLED, a reference device without the N965 monolayer was prepared following exactly the same procedure previously described in this section. The EL and spin transport properties of the structures were evaluated simultaneously for each temperature from the minimum at 14 K to progressively higher temperatures. It is fundamental to remark that this measurement protocol has been possible thanks to the outstanding advantage provided by the availability of the MEL set-up described in chapter 6. The discussion of these results is going to be presented in the following section.

8.2.2 Electroluminescence properties

The comparison of the current density-voltage (J-V) and luminance-voltage(Lum-V) curves at 14 K for the device with the molecular ionic junction of N965 and the device without this EIL is shown in figure 8.13. As it was already done in chapter 7, both J-V and Lum-V curves are represented in logarithmic scale. The measurements shown in figure 8.13 were performed in forward bias, by applying a positive bias voltage at the Co/Au anode terminal as it is indicated in the inset of figure 14.The J-V curve for the spin-OLED with the monolayer of N965 as EIL shows a rapid increase, after overcoming a threshold voltage (~0.4 V), to values considerably higher than those detected for the spin-OLED without EIL. In addition, from the Lum-V curve of the device with the N965 monolayer, a turn on voltage (V_{on}) for light emission of 7 V, supposing a reduction of 3V is determined. This light emission V_{on} increases up to 10 V for the spin-OLED without the molecular ionic junction. A maximum luminance of 40 Cd/m^2 is detected at 12 V for the device with N965 being approximately one

order of magnitude higher compared to the reference device without the nanofuctionalizated LSMO cathode.

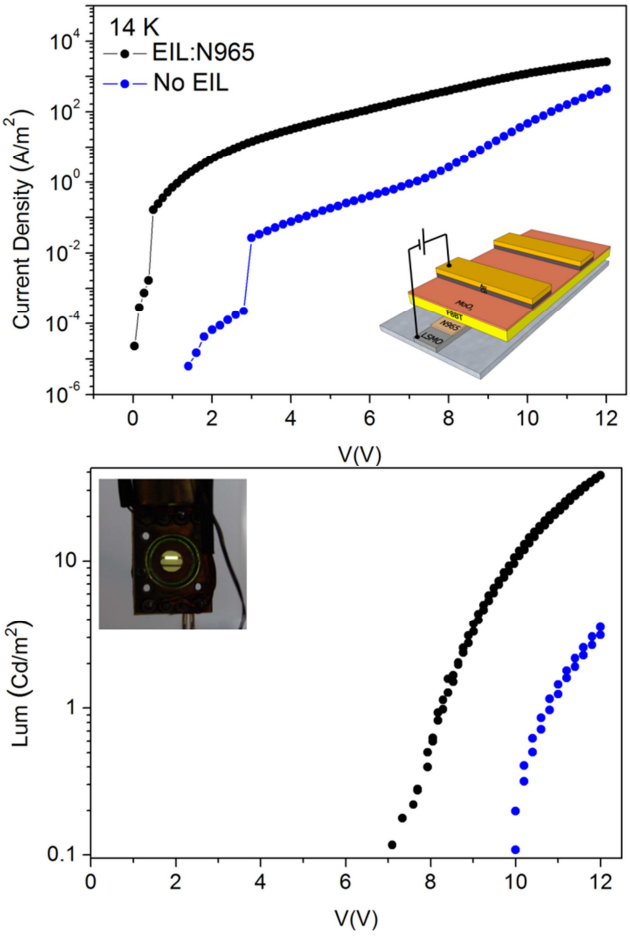

Figure 8.13- *Top*: Current density vs voltage (*inset*: biasing protocol) and *bottom*: luminance versus voltage (*inset*: light emission of the device) at 14 K.

Taking into account this information, it is clear that the insertion of the molecular monolayer improves the injection of electrons into the F8BT. In addition, the presence of the EIL produces a more efficiently hole blocking interface in the electron injecting interface of the device.

In principle, the current flowing through the device without the N965 monolayer is mainly composed by holes, just as the spin-OLED described in the previous chapter. This is due to the fact that the holes are more efficiently injected from the Co through the deep conduction band of the MoO_3 into the HOMO of the F8BT. On the contrary, there is an important energetic barrier for the injection of electrons from the non-functionalized LSMO cathode to the LUMO of the F8BT. When the molecular ionic junction of N965 is inserted, the electron injection is considerably improved, as mentioned before, reducing the injection barrier as it was demonstrated by the J-V and Lum-V curves of the device. Despite the fact that the inclusion of the N965 monolayer improves the electron injection, it is likely that the current flowing through the spin-OLED is still mainly determined by holes. This situation is assumed below the light emission V_{on}, as it has been described in the majority of HyLED devices[11,38].In fact, the delay between the turn on voltage for current and light in this type of devices can be considered as the evolution from a mainly unipolar to a proper bipolar charge transport regime[43]. Thus we conjecture that the current flowing through the device would be controlled by holes and the electroluminescence would be regulated by the injected electrons which are the minority charge carriers in this spin-OLED.

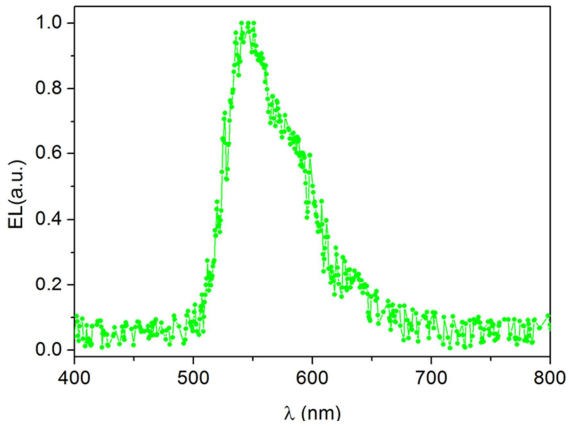

Figure 8.14- Electroluminescence spectrum of the spin-OLED with LSMO and Co electrodes.

Both active areas of the spin-OLED exhibited a homogenous yellow-green light emission. The measured electroluminescence spectrum depicted in figure 8.14 exhibits a maximum at a wavelength of around 560 nm. This value matches properly with the emission spectrum of the F8BT.

The improvement in the EL performance of the device with the N965 monolayer as EIL can be understood by the analysis of the electron injection processes in the system. As mentioned many times along the discussion of this thesis, the electron injection is considered the bottleneck in the performance of HyLED structures[11,38]. In the particular spin-OLED under discussion the electron injection is promoted by two processes: 1) the effect of the molecular ionic junction of N965, 2) the effect of hole accumulation at the electron injecting interface. The role of the molecular ionic junction of N965acting as EIL has been explained by a phenomenological model in the work of H.J. Bolink et al.[19](figure 8.15).

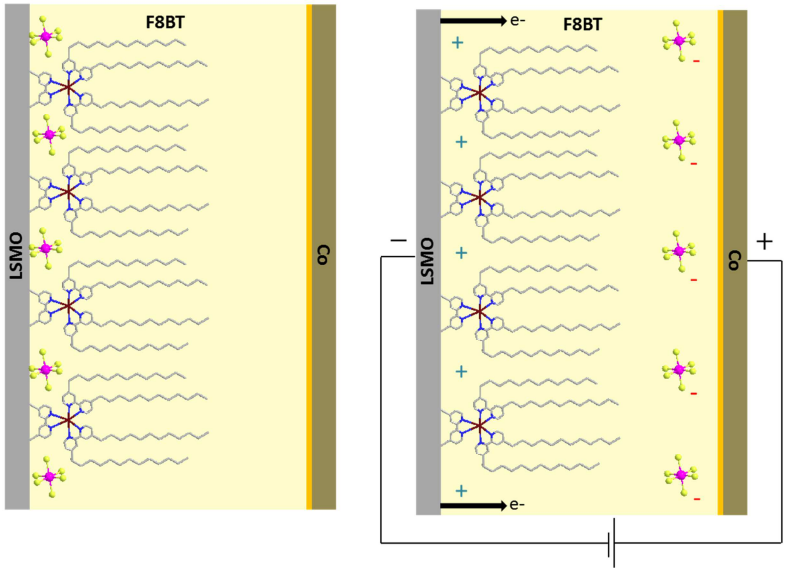

Figure 8.15- Phenomenological model explaining the formation of the charge double layer by the ionic movement enhancing the electron injection. Image adapted from reference [31]

When a bias is applied in the device, a redistribution of ions is generated with the consequent appearance of an ionic space charge at the interface. The established conditions promote the electron injection from the cathode to the LUMO of the F8BT. In this context, at the equilibrium state before applying any voltage, the cationic N965 molecule is bonded to the LSMO cathode and the hexafluorophosphate anions (PF_6^-) are located close to the magnetic oxide surface. This is a result of the electrostatic interaction of the anions with the cationic Ru complex. When the spin-OLED is forward biased, the anions start to separate from the cationic Ru complex and move in the direction of the Co anode. This process promotes the formation of a charge double layer close to the surface of the LSMO. In consequence, a strong interfacial field is generated in the LSMO/F8BT interface which in terms reduces the energy difference between the workfunction of the LSMO and the LUMO of the F8BT, favoring the electron injection.

The second process assisting the electron injection in the OSC from the LSMO is the same as explained for the spin-OLED prototype in chapter 7. The holes injected from the ohmic contact, established by the MoO_3 barrier, migrate across the organic semiconductor as a response of the external biasing. This migration takes place until they reach the interface of LSMO/N965 which will block the holes .As a consequence, a hole accumulation in a very thin region in the F8BT will be produced, inducing an interfacial field which promotes the injection of electrons trough the N965 monolayer[11,38]. In addition, an increase of the current density is produced as a result of a lowering of the space charge limitation for the hole current. In this context, a bipolar charge transport regime can be established by the injection of electrons from the LSMO cathode promoted by the N965 monolayer and holes from the Co anode through the CB of the MoO_3. In this way, electron-hole pairs or polaron pairs (PPs) are generated in the F8BT as a result of the mutual Coulomb attraction[44]. Once the PPs are located in the same monomer of the F8BT a rapid relaxation into a tightly bound exciton state takes place[31]. Two types of excitons will be formed in this way in the active medium, either singlet or triplet. Only singlet excitons will recombine in a radiative way thus being the responsible of light emission in our

spin-OLED. This phenomenology will be described with more details in the section corresponding to the MEL effect detected in the device.

The thermal evolution of the turn on voltage (V_{on}) for light emission was evaluated when heating up the system during the complete characterization. As it was expected, a reduction of the V_{on} for the EL was detected for progressively higher temperatures (figure 8.16). The explanation for this behavior has been discussed in the previous chapter. The thermal dependence of the injection process and mobilities of charge carriers was ascribed as the determining factors on this thermal response of the light emission V_{on}.

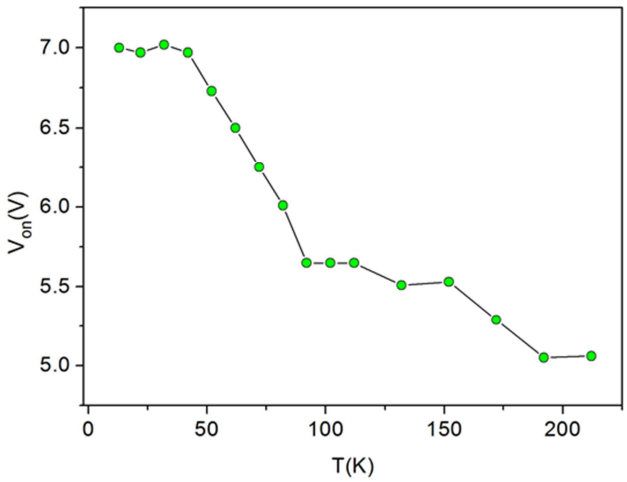

Figure 8.16- Thermal evolution of the V_{on} for light emission in the spin-OLED with LSMO and Co as cathode and anode respectively and a molecular ionic junction of N965 as EIL.

At this point, it is important to remark that the EL performance of the spin-OLED under study has demonstrated to be quite robust, taking into account that after many days of continuous measurements the J-V and Lum-V curves remain unaltered.

8.2.3 Spin transport properties

Several reported works have discussed experimental criteria for distinguishing the conductive mechanisms in OSVs[45–48]. These criteria are mainly based on the characteristics of the I-V curves measured in the device. If a spin injection takes place followed by a carrier hopping in the OSC, the I-V traces should present a highly temperature dependence. In addition, considering that organic materials possess mobilities which are dependent on the applied electric fields, the I-V curves are expected to exhibit a highly non-linear behavior. Both criteria are accomplished in our spin-OLED as depicted in figure 8.17, where the I-V curves at 3 different temperatures are compared.

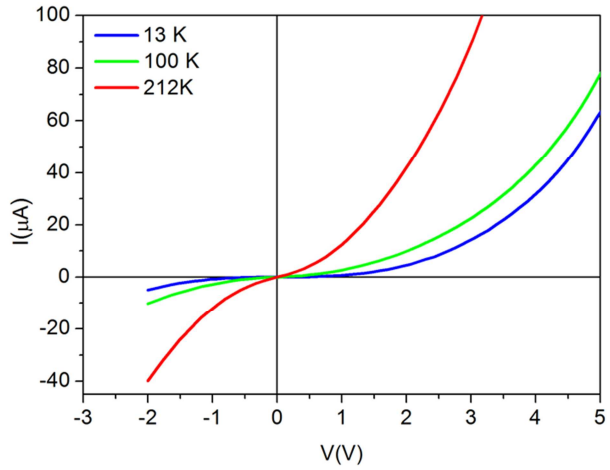

Figure 8.17- Thermal evolution the IV-curves of the spin-OLED. The highly temperature dependence and non-linearity of the traces confirms the spin injection with a subsequent hopping in the OSC as the conductive mechanism in the device.

As expected, the spin-OLED presents I-V curves of an OLED-type structure, in which an onset voltage can be detected below which any current can hardly flow through the device. In OLEDs the conduction mechanism is well known to take place by a carrier-injection followed by carrier hopping[49]. Thus, the same mechanism can be considered for the spin transport through the F8BT in our device. The I-V traces in OLED devices are usually explained by means of a space-charge limited current model[49] or by modelling the system with Monte-

Carlo simulations[50] considering a hopping mechanism between neighboring sites located in a disordered density of states. Nevertheless, the most determining proof of charge injection and transport in the F8BT in our spin-OLED is the presence of light emission for all the temperature range under study. This can be occurring only under an effective charge injection of electrons and holes into the LUMO and HOMO of the OSC, respectively. As it was previously mentioned, in the hopping process across the F8BT, the charge carriers will be able to form polaron pairs (PPs) the precursors of excitons in the material. The EL will arise from the decaying of the singlet excitons formed in the emissive layer of the spin-OLED[31].

With the mechanism of charge conduction in the spin-OLED explained, the next step is the analysis of the spin injection and spin transport processes in the F8BT. As it has been highlighted many times along the discussion, for getting a proper modulation of the EL by spin valve effect, the presence of a spin-polarized (SP) current in the device is essential. This SP current will be the responsible of the appearance of a giant magneto-resistance (GMR) in the spin-OLED. Magnetoresistance (MR) curves of the device were acquired in a wide range of voltages and temperatures when sweeping an external in-plane magnetic field. Just as done in the previous chapter, the MR ratio was calculated respect to the resistance in the antiparallel relative orientation of the ferromagnetic electrode magnetizations, by the formula:

$$\frac{\Delta R}{R_{ap}} = \left[\frac{\left(R_p - R_{ap}\right)}{R_{ap}}\right] \cdot 100 \ (\%) \qquad (eq.\ 8.2)$$

The MR signals measured on the device showed a non-hysteretic background, attributed to the LSMO, which was subtracted in order to obtain the net spin-valve response of the spin-OLED. This was done in the same way as Z.V. Vardeny and coworkers[51] for the magneto-conductance curves of their spin-OLED structure. In figure 8.18 are shown two representative MR curves at low temperature, at bias voltages of 3V and 5V. This set of measurements were performed under a forward biasing of the device, *i.e.*, with a positive bias for the

Co/Au anode. This procedure is exactly the same as the one applied for obtaining the J-V and Lum-V curves of the spin-OLED (figure 8.13) .

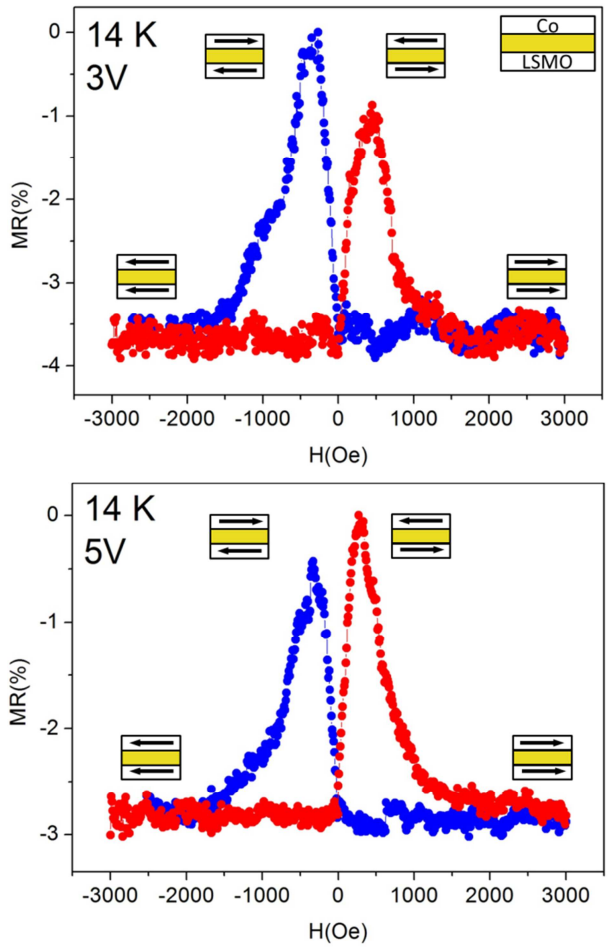

Figure 8.18- MR curves at 3V (top) and 5V (bottom) measured at 14K. The red and blue curves are indicating the up- and down-sweeping magnetic field respectively.

These MR curves correspond to bias voltages below the V_{on} for light emission in the spin-OLED. As it was previously mentioned, for voltages below light emission the charge transport is dominated by the majority charge carrier in the device, being holes in this case. According to this, the MR curves at 3V and 5V are likely arising from a current density dominated by holes and, in consequence, mainly corresponding to a homopolar charge transport regime in

the spin-OLED. The first striking result from our spintronic structure is the presence of MR signals at high bias voltages. This is a remarkable property of the device considering that most of the OSVs reported so far, show a total degradation of their MR signal for voltages above 1-2 V[5–8,27,29,31–33,52]. In addition, this spin-OLED presents the outstanding property of exhibiting a sizeable MR signal up to light emission voltages.

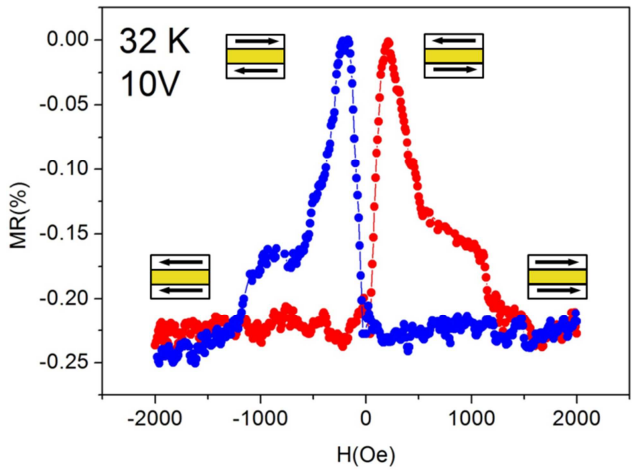

Figure 8.19- MR curve of the spin-OLED measured at 10 V and 32 K. The red and blue curves are indicating the up- and down-sweeping magnetic field respectively.

In figure 8.19 it is shown the MR curve measured at 10 V and 32 K where the light emission of the device is already considerable. The set of MR curves obtained for $V>V_{on}$ can be mainly associated to a bipolar regime in the device with a current density dominated by the holes being the majority charge carriers, and the electroluminescence limited by electrons.

The outstanding OSV performance of our light emitting spintronic device, up to unprecedented bias voltages, motivated the analysis of the possible artifacts that may resemble the presence of a spin-polarized current in the structure. In OSVs the MR of the electrodes can be shown, with their sign reversed, as the MR of the device, generating in this way an artifact in the measurement[53]. In order to discard that the MR signals registered in our spin-OLED are arising from an artifact induced by the effect of the electrodes, the sample was modelled

with a simple 1D resistor model[53].This modelling was performed in collaboration with Dr. A. Riminucci from ISMN-CNR (Bologna).In the context of this model, the measured R in the device is given by:

$$R = R_s \frac{\sqrt{\frac{R_t + R_b}{R_s}}}{\sinh\left(\sqrt{\frac{R_t + R_b}{R_s}}\right)} \qquad (eq\ 8.3)$$

where R_s is the resistance of the OSC , R_t is the resistance of the top electrode on the active area and R_b is the resistance of the bottom electrode on the active area. R, R_b and $R_t$can be directly measured, and $R_s$can be obtained numerically from equation 8.3. As a particular case of analysis, the MR curve measured at 32 K under a bias voltage of 10 V (figure 8.19) was modelled. In this case, R_s = 8.54 kΩ and R_t =1.3Ω. The R of the top Co electrode has been neglected since its contribution is negligible. A MR of 0.4% was measured for the bottom LSMO electrode which means that R_b ranges from 380 Ω to 382 Ω. By plugging these values into equation 8.3, a MR~3.5×10^{-3} % could be calculated for the device. This demonstrates that this effect cannot account for the measured MR in the spin-OLED of 0.23 %. This result rules out the possibility that the MR measured in our spin-OLED arises from an artifact originated on MR of the electrodes. Thus, it is demonstrated by this modelling way that this signal is coming from the OSV performance of the structure with the presence of a spin-polarized current through the spin-OLED.

Another important proof of the spin transport across the entire junction is the coincidence of the magnetic fields at which the changes from low to high resistance states in the OSV take place, with the coercive fields of the ferromagnetic electrodes present in the structure[54]. In general the coercive fields of the electrodes in OSVs are measured by means of MOKE magnetometry relying on the surface and spatial resolution of the technique as described in chapter 7. In section 8.2.1 it was described the longitudinal MOKE measurement at 14 K for LSMO and Co electrodes in the device, exhibiting values of 75 Oe and 180 Oe respectively.

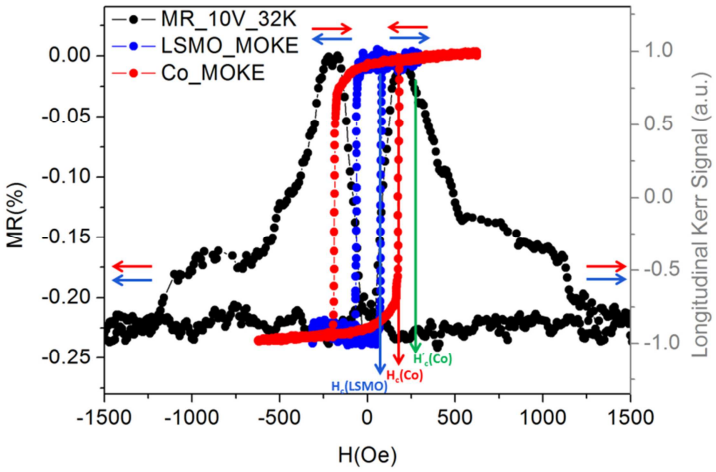

Figure 8.20- Comparative between the switching fields from low to high resistance states of the MR at 10V and 32 K with the coercive fields of the electrodes in the device measured with MOKE.

The grade of matching between the coercivity of the electrodes determined by MOKE and the switching fields for the transition from low to high resistance states has been analyzed. With this aim the MR curve of the spin-OLED at 10 V and 32K has been compared with the MOKE hysteresis as depicted in figure 8.20. This comparison is possible thanks to the slow thermal evolution of the coercive fields of the electrodes, which allows a direct comparison between the data at 14 K and 32 K without adding any error in the discussion. It is clear from figure 8.20 that the first switching of the MR curve matches perfectly with the coercive field of the LSMO, H_c (LSMO)=75 Oe, determined by MOKE magnetometry. On the other hand, the second switching of the MR curve from the high to the low resistance states is not taking place at the coercive field measured with MOKE for Co, H_c(Co)= 180 Oe. Instead of this, the switching is detected at a higher magnetic field, H_c' (Co), of around 260 Oe.

The same effect was detected for the spin-OLED employing Fe and Co as ferromagnetic electrodes and described in chapter 7. In that case it was also found a good coincidence between the first switching field in the MR curve and the MOKE coercive field for the Fe electrode. Nevertheless, the switching from high to low resistance states corresponding to Co was higher than the value

extracted from the longitudinal hysteresis loops measured by MOKE. From this information it is clear that the magnetization reversal process of the Co anode evaporated on top of the MoO_3 HIL has a special magnetization reversal dynamics which is being not reflected by the MOKE measurements. The same discrepancy in the switching of the MR curve with respect to the coercive field of the electrodes measured by MOKE has been reported for other OSVs[46,47,55]. In all these works, the hypothesis for explaining this point is articulated around the idea of a different magnetization reversal process occurring at the interface between the ferromagnetic electrode and the OSC, with respect to the one taking place at the top layers. Precisely the reversal process taking place in the latter case would be the one registered by MOKE. Based on this, it seems that some special physical process is taking place at the interface generated by the MoO_3 and the Co anode. This interface has been studied in previous reported works[56], in which by means of photoemission spectroscopy it was possible to detect the presence of a chemical reaction between these two materials. This reaction was identified as an oxidation process of the ferromagnetic electrode, leading to the appearance of a CoO phase in the interface with the MoO_3. Thus, considering this information, it is not possible to discard the appearance of such CoO phase in the F8BT/MoO_3/Co interface in our spintronic structure. The presence of an antiferromagnetic CoO at the interface induces a pinning effect on the magnetization reversal of the Co electrode. This process would be promoted by an exchange coupling between the CoO antiferromagnetic phase and the ferromagnetic layers close to the interface. As a consequence, a higher external magnetic field is necessary for reverting the magnetization of the Co electrode which is directly translated into an enhancement of its coercive field[57,58]. On the contrary, when going progressively away from the interface with the CoO, the successive layers of Co would be more free to reverse their magnetization in presence of the external magnetic field. Thus, a lower coercivity for these top layers will be present (figure 8.21).

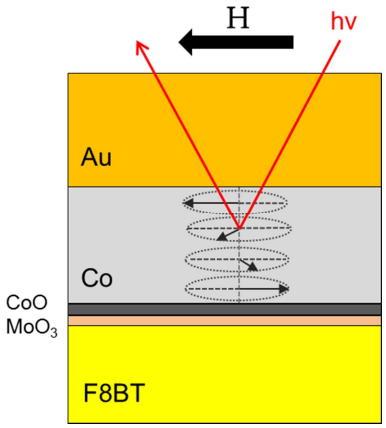

Figure 8.21- Schematic representation of the effect of the CoO phase on the magnetization reversal process of the Co anode. An effective pining of the layers close to the interface with the CoO phase is produced. As depicted in an illustrative way, the penetration of the MOKE laser is limited by the protective gold layer thus not reaching the interface with the CoO/MoO_3.

As shown in figure 8.21, the surface characteristics of the MOKE measurement restrict the analysis to the top layers. This situation is even more accentuated by the presence of the top Au protective layer which reduces the penetration depth of the laser. This inaccessibility of MOKE for probing the interfacial region has been mentioned in other reported OSVs[46].

For confirming this complex magnetization reversal process due to the presence of the CoO phase at the interface between the MoO_3 and Co, a bulk characterization of the magnetic properties of the electrodes in the device was done by means of SQUID. With this purpose, the magnetic signal of the spin-OLED was registered by introducing the system in the SQUID sample holder. Hysteresis loops were acquired at 2 K applying a magnetic field parallel to the surface (perpendicular to the current), just as in the spin transport characterization. From this measurement a two-step hysteresis loop was registered (figure 8.22) reflecting the switching of each ferromagnetic layer in the device. The same trend has been observed in the magnetic characterization of the magnetization reversal process for other spin valve structures reported in literature[59,60].

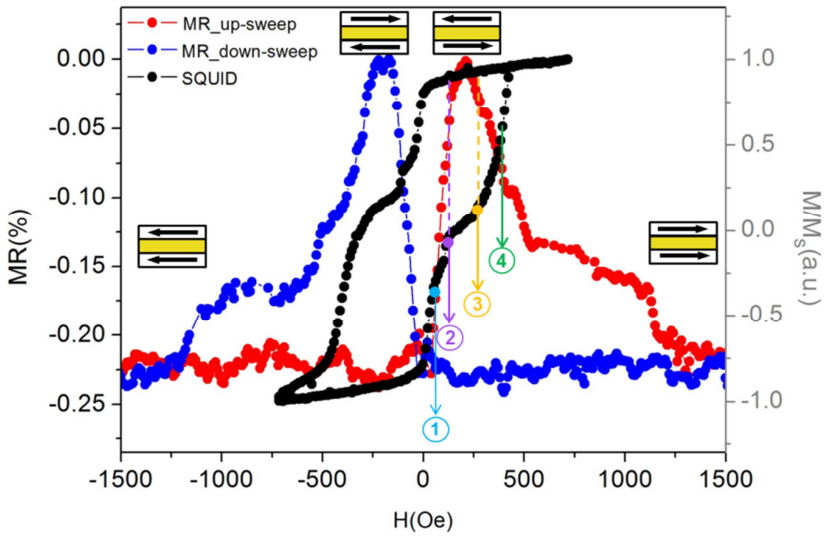

Figure 8.22- Comparative of the SQUID hysteresis loop of the spin-OLED with the switching fields of the MR curve of the device measured at 10 V and 32 K. The bulk hysteresis loop reflects the complexity of the magnetization reversal process in the Co anode:1) approximately 70 Oe, corresponds to the coercive field of the LSMO electrode ; between point 2) and 3), located at around 120 Oe and 270 Oe respectively, an antiparallel state between both ferromagnetic electrodes is stabilize;. 3)at 270 Oe the switching of the Co layer starts, and progressively the whole layer is reversed which is reflected in point 4) with the value of the coercive field for the anode, being approximately 385 Oe.

In figure 8.22, in which the MR curve at 10V and 32 K is compared with the SQUID magnetic characterization. The various magnetization reversal processes of the ferromagnetic electrodes in the device are pointed out. Point 1, at approximately at 70 Oe, corresponds to the coercive field of the LSMO electrode matching very well with the value obtained by MOKE magnetometry. Between points 2 and 3, located at around 120 Oe and 270 Oe respectively, an antiparallel state between both ferromagnetic electrodes is stabilized. When reaching point 3, at 270 Oe, the switching of the Co layer starts, and progressively the whole layer is reversed which is reflected in point 4 with the value of the coercive field for the anode, being approximately 385 Oe. This hysteresis loop exhibits the complexity of the magnetization reversal process related to the Co anode. The switching is not produced in a sharp way but

instead of that it is shown as a softer transition indicating successive magnetization reversal processes. Compared to the coercivity measured by MOKE for the Co anode, which was determined to be 180 Oe, a clear enhancement of this value is registered from the bulk characterization likely due to the exchange coupling with the CoO phase. In this sense, the SQUID measurement has been able to probe the magnetic properties of the electrode not only at the top layers as MOKE, but also at the interface with the MoO_3. The study of latter region has been shown to be critical for understand the switching fields in the MR curve of the spin-OLED.

As explained by Lin et al.[46]the progressively not-sharp switching in the MR curve, when passing from high to low resistance states, could be indicating the presence of certain imperfections at the interface between the Co and the F8BT. Precisely with all the information described previously, this extra CoO phase generated by the MoO_3 could be ascribed as the responsible of this feature. In the same way, the kind of "double switching" observed at around 1000 Oe would be also reflecting the complexity of the magnetization reversal process established at this interface with the F8BT. The same discussion can be extended for the rest of the MR curves obtained with other bias voltages for this spin-OLED.

According to the information presented so far, the presence of a spin polarized current in the spin-OLED for voltages above and below the light emission V_{on} can be considered. For all the bias voltages tested in the spin-OLED a positive spin valve effect has been observed. It means that a higher resistance is established for the antiparallel relative orientation of the electrode magnetizations. As it was discussed in chapter 7, the terminology "positive spin valve effect" it is not related to the sign of the MR as it depends on how is defined by the formula for calculating the MR ratio. In our case, as defined in equation 8.3, the reference for calculating the MR ratio is the resistance at the antiparallel state. According to this, in the parallel configuration the resistance is lower and the sign of the MR is negative, exhibiting in this way a positive spin valve effect. In most of the reported OSVs with LSMO/Alq_3/Co, independently of the material combination at the top interface, an inversion of the spin valve effect has been detected[32]. This negative spin valve effect

determined for Alq_3, seriously contradicts the knowledgement regarding to the spin polarization at both interfaces. By means of spin-sign-sensitive experiments on Zeeman effects in superconductor/barrier/Co structures it has been reported an injection of majority (up) spins at interfaces Co/Alq_3 and Co/Al_2O_3/Alq_3.[61] In addition, manganites such as LSMO are widely accepted as injectors of majority spins (spin up)[32].Considering all this information in the parallel configuration of the OSV, the resistance should be lower. This is precisely what we observe in the OSV performance of our spin-OLED. Thus, in our device no inversion of the spin valve effect, as the one registered in the systems employing the small molecule Alq_3 as the spin collector structure, has been detected at any of the bias voltages under study.

In figure 8.23, it is depicted the bias dependence of the MR signal for four representative temperatures, corresponding to the situation of forward biasing of the sample under which the light emission of the spin-OLED takes place.

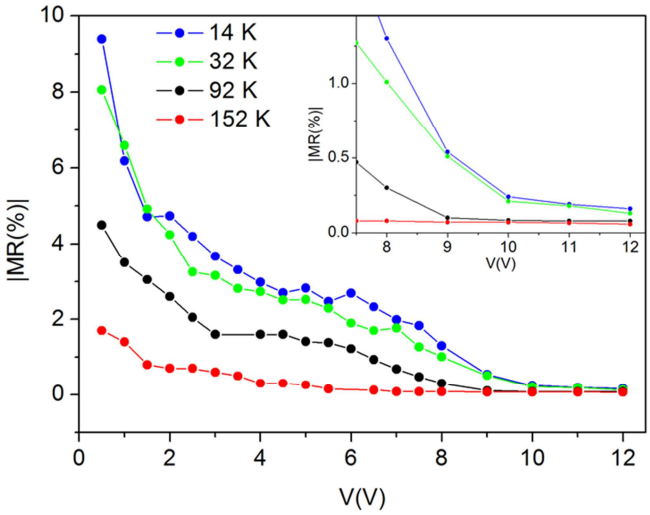

Figure 8.23- Thermal evolution of the V_{on} for light emission in the spin-OLED

The most noteworthy feature observed from the measurement displayed in figure 8.23 is the extreme robustness of the MR signal as a function of the bias voltage for all the tested spin-OLEDs. From this figure, it is interesting to remark that for bias voltages below the light emission V_{on} (7 V), corresponding

mainly to a homopolar OSV performance of the spin-OLED, a progressive decrease of the MR is detected but still with a sizeable signal for all the range.

This is the general tendency reported for the homopolar OSVs which can be found in literature[5–8,27–33,52]. On the other hand, for bias voltages above V_{on}, when a detectable EL is being registered by our photodiode, a clear stabilization of the MR values is achieved for all the temperatures. This tendency is more clearly reflected in the inset of figure 8.23, in which a zoom-in for the voltage windows of light emission is shown. A major stabilization in the OSV performance is taking place in the range of voltages where mainly a bipolar charge transport regime in the spin-OLED can be considered. The same stabilization in the MR, for the light emission voltage range, was also reported by Z.V. Vardeny in their bipolar spin-OLED[51]. It is interesting to highlight that an important stabilization of the MR is achieved for progressively lower voltages as the temperature is increased (inset of figure 8.23). This observation can be directly correlated to the evolution of V_{on} towards lower values when heating up the system as shown in figure 8.16. This is a confirmation that charge carrier annihilation, with a consequent light emission, is playing an important role in the stabilization of the spin-OLED performance at high bias voltages.

The bias voltage dependence of the MR in OSVs is still not a completely understood phenomenon. An open debate is still present with many proposed scenarios explaining this feature[29,31,51,62]. As it was previously mentioned, for the reported OSVs that can be found in literature, a degradation of the MR ratio with an increasing bias voltage has been observed being totally extinguished for voltages above 1-2V. Until now, two possible mechanisms have been in general proposed as responsible of this behavior[29,31,51,62] : i) a decrease of the spin polarization of the electrodes for high voltages affecting the spin injection into the OSC and ii) effects originated in the bulk of the OSC.

In view of the behavior observed in the MR signal for high bias voltages, it seems very likely that the mechanisms regulating the MR in our case are related to voltage-dependent processes in the bulk of the F8BT. It is fundamental to remark, that under the high bias voltages at which our study is being performed, the charge transport mechanisms are considerably different with

respect to the operation of the OSVs reported in literature[63] (taking place at small bias). For the high voltage range, a strong band bending is produced ,enabling a space charge limited current (SCLC) operation. Thus a bipolar SCLC model for conduction[64] can be considered for understanding the MR at such high bias voltages in our spin-OLED. This consideration has been also taken into account for the bipolar light emitting OSV reported by Vardeny et al., being the only precedent in the literature of a device with such characteristics[29,51]. In that particular work, Z.V. Vardeny and coworkers, modify the classical bipolar Parmenter-Ruppel (PR) model to include the presence of ferromagnetic electrodes in the structure, with an injection under unbalanced current densities for electrons and holes. In this case the holes were also the majority charge carriers. From this model they could obtain a magneto-conductance expression for the homopolar charge transport regime in their device below the light emission voltage. In addition, an expression for the magneto-conductance corresponding to the bipolar operation mode was presented. In the last case, they included in the formula a Langevin-type bimolecular recombination coefficient of the polaron pairs formed in the OSC. Thus this coefficient takes into account the charge annihilation under light emission conditions.

The stabilization by charge annihilation can be correlated to a decrease in the charge carrier density, either holes or electrons. How the reduction of charge carrier density can affect positively to the spin transport in the OSC has been discussed by S. Sanvito *et al*[54]. The charge transport in disordered OSCs, such as the F8BT, is a result of an incoherent hopping of charge carriers taking place between localized sites distributed according to a Gaussian density of states(DOS) for the energy states[31]. Within this model, when a spin-polarized electron (or hole) falls into an unoccupied state in the OSC, the charge carrier preserves the spin information when hopping to a neighboring empty state[54]. The spin relaxation process, and in consequence the loss of spin information in the charge carrier, is produced when the hopping is produced to an already occupied state. In this sense, if an electron (hole) with spin-up hops into a localized site already occupied by a spin-down electron (hole), the charge carrier when leaving this site for hopping into a new neighboring one, can have either direction with a consequent destruction of the spin polarization.

This mechanism is at the origin of spin relaxation in the OSC[54]. In this line of thought, S. Majumdar *et al.*[65] proposed recently that the increase of charge carrier density in the OSC could be an explanation for the degradation of MR with temperature and voltage for homopolar OSVs. Thus, when increasing the voltage in the OSV, more charge carriers are activated inside the OSC. This increase in charge carrier density produces greater occupation of the disordered energy states. Thus, when the carriers are driven across the OSC by the application of a voltage in the device, due to the Pauli Exclusion Principle, each hopping site can accommodate two carriers with different spin orientations. When a spin-polarized electron (hole) hops into a single-occupied hopping site, when leaving this state after certain time of residence, the spin of the carrier can acquire any random spin orientation leading to a 50 % of probability of a spin-flip[65]. According to all the explained so far, the process of bimolecular recombination with a consequent reduction of charge carrier density, may contribute to control the "spin-spin scattering" process leading to a reduction of this spin relaxation mechanism.

It is important to indicate that below the light emission voltage, in the range between 2-7 V, the spin-OLED is also presenting a good OSV performance with a sizeable MR. The fact of having this behavior, for still much higher voltages than those reported in literature, is an indication that the MR stabilization scenario presented before needs to be extended. Along the discussion of this section, it was mentioned that the light emission turn on voltage, V_{on}, can be mainly considered as the evolution from a homopolar charge transport regime to a regime which can be mainly associated to a bipolar charge transport regime. The term "mainly" is included because, in principle, it would not be that straightforward to relate this evolution of the charge transport regime from unipolar to bipolar just by the point in which there is a sizeable amount of light that we can register with the photodiode of our set-up. This last point is very important, because in fact we could have electron injection and, in consequence, charge annihilation by bimolecular recombination of the Langevin-type without light emission. This would be explained by the presence of non-radiative recombination processes occurring at the OSC which in terms do not contribute to the EL of the system. Among all these processes one of the

most studied in OLED devices is the trap-assisted recombination. It has been demonstrated by many works that the trap-assisted recombination is the dominant recombination mechanism in OLEDs at low driving voltages[66,67]. In the case of PPV OLEDs the trap-assisted recombination produces a radiation in the near infrared which is not detected by standard photodiodes as the one employed in our set-up[66].Thus, the possibility of non-radiative recombination processes of electro-hole pairs in the F8BT, makes difficult a direct establishment of the limit voltage for the bipolar charge transport regime, based uniquely on the light emission in the device.

According to all this information, at this point we propose the charge annihilation of the polaron pairs formed by the carrier injection in the OSC as one of the possible mechanisms regulating the spin relaxation processes in the F8BT. This would allow the OSV performance of the spin-OLED up to higher voltages than those reported in literature for homopolar OSVs. However, a theoretical framework for supporting all these assumptions is still needed, with a modelling of the system accompanied by extra experimental characterization in order to confirm or discard the stabilization mechanisms previously proposed. In this sense, the understanding of the trap effects on the conduction mechanisms in the OSC can play an important role. It is fundamental to take into account that after more than one decade, the field of organic spintronics is still looking for definitive answers to questions such as the effects of voltage and temperature on the performance degradation of homopolar OSVs[29,31,32]. Considering so far the existence of only one reported bipolar OSV with light emission[51] we are dealing with a total new physical scenario in organic spintronics.

The last point to treat is the effect of the temperature on the OSV performance. In chapter 7, the spin-OLED prototype with Fe and Co ferromagnetic electrodes showed an OSV performance with a drastic degradation when heating up the system. This degradation with temperature was so important that a proper characterization

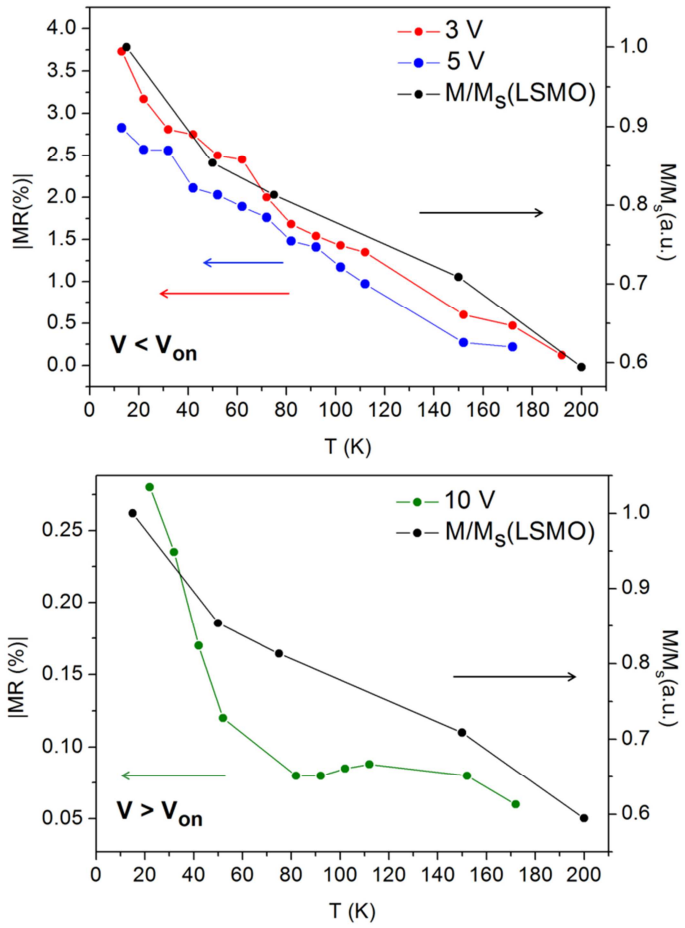

Figure 8.24- Thermal evolution of the absolute value of the MR signal for the LSMO-Co spin-OLED for voltages below (*top*) and above (*bottom*) the light emission V_{on}. The evolution of the MR for 3V, 5V and 10 V represented by the red, blue and green curves respectively are compared with the thermal evolution of the M/M_s of the LSMO determined by SQUID in the temperature range of the MR detection (black curve).

of the thermal effects on the spin transport properties of this family of spin-OLEDs could not be performed. In that case, a possible damaging of the spin injection properties of the ferromagnetic cathode, due to the fabrication conditions of the device, was proposed as a hypothesis for the limited thermal robustness of the spin transport performance. The substitution of the

ferromagnetic transition metal cathode by an air stable electrode such as the LSMO was described as an alternative route for solving this limitation.

In figure 8.24 it is depicted the thermal evolution of the MR signal for the spin-OLED with a LSMO cathode functionalized with a monolayer of the Ru complex N965. Three bias voltages located, below and above V_{on}, have been presented in this case. The first point to remark is the important improvement of the spin transport properties for this spin-OLED when heating up the system, compared to the Fe one presented in chapter 7. From figure 8.24 it is possible to observe, for voltages below the light emission, a sizeable MR signal up to 200 K for 3V and 180 K for 5V. Above these temperatures the signal-to-noise ratio of the measurements is extremely low, and prevents of getting a sizeable value for the MR. In the case of 10 V, above V_{on}, the MR signal is maintained up to approximately 180 K as the upper temperature limit, above which the spin transport is totally degraded.

A degradation of the MR when increasing the temperature has been reported in many other OSVs with LSMO as the spin injector electrode[6,7,68]. In these systems, the reduction of the MR with temperature is much steeper than in our spin-OLED. This feature is directly ascribed to a degradation of the surface magnetism of the LSMO and in consequence to the spin injection efficiency with temperature[6,7,32]. In these works, the impact on the MR of the thermal evolution of the bulk magnetization of the LSMO, M(T), is discarded assuming that the thermal degradation of this property follows a slower ratio in comparison with the evolution of the MR[6,7,32]. On contrary, the thermal degradation of the MR for our spin-OLED at voltages below the light emission, matches quite well with the decreasing ratio of the LSMO bulk magnetization ($M(T)/M_s$) (figure 8.24). The same feature was described in the bipolar OSV of Z.V. Vardeny et al.[51] in which the spin transport degradation with temperature resembled very well the thermal evolution of the bulk magnetization of the LSMO. On the other hand, the MR(T) at 10 V in our spin OLED follows the same general trend that the thermal evolution of the bulk magnetization of the LSMO, but with a certain deviation. This characteristic could be an indication of other extra mechanisms affecting the MR. This is not unexpected as at this range of voltages an important bimolecular charge recombination is taking place with a detectable

light emission. Thus, at this point, it could be proposed that in general the thermal degradation of the bulk magnetization of the LSMO is having an effect on the MR (T) of the spin-OLED. Other extra mechanisms seem to play a role in this dependence for the light emission voltage range that at this stage of the study could not be determined with the available information.

The influence of the monolayer of N965 on the spin transport properties of the spin-OLED was evaluated in a reference device without this molecular ionic junction. For the devices without the monolayer of the ruthenium complex as EIL, the thermal degradation of the MR is steeper with a signal that vanishes for temperatures above 90 K as observed from figure 8.25.

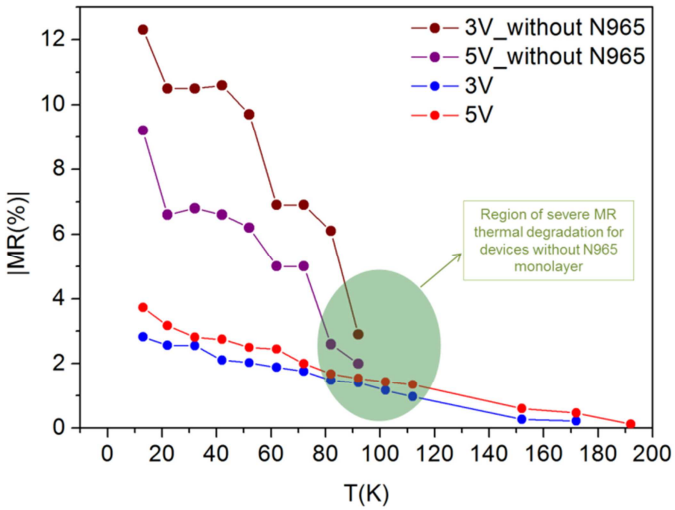

Figure 8.25- Comparison of the thermal evolution of the absolute value of the MR for the spin-OLED presenting the N965 monolayer and devices without this barrier.

In addition, for these structures the MR signal is severally damage for bias voltages well below the light emission V_{on}. This information is indicating that part of the stability of the spin-OLED performance, related to the spin transport properties, can be associated to the presence of the molecular ionic junction. It is interesting to highlight that the measured MR ratio for a device without the molecular ionic junction is higher than the one containing this molecular monolayer. This could be in principle, an indication of the fact that the presence

of the N965 monolayer induces a certain grade of spin depolarization on the charge carriers injected from the LSMO to the F8BT. However, the total understanding of the influence of the molecular ionic junction on the spin injection and spin transport in this light emitting spintronic structure needs a deeper analysis. Extra characterization techniques, such as an UPS study of the energetics at the interface arising from the presence of the N965 monolayer on top of the LSMO, would provide a more complete understanding of the influence of this barrier on the performance of the device. In addition, as it was done for the MoO_3 barrier, spin-resolved UPS studies are needed for quantifying the grade of possible spin depolarization that this molecular barrier induces at the interface with the OSC.

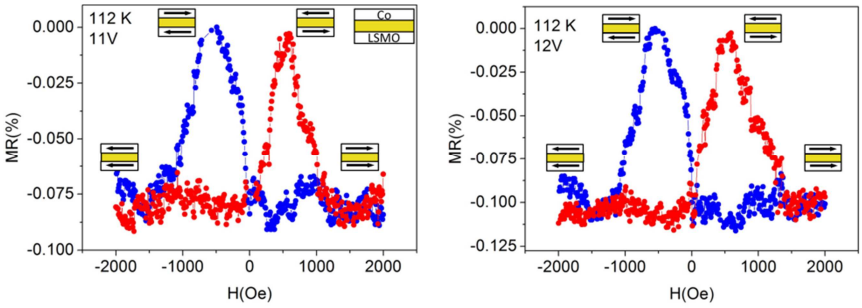

Figure 8.26- MR signals of the spin-OLED measured at 11 V (left) and 12 V (right) at 112 K. The red and blue curves are indication of the up- and down-sweeping fields.

According to all the information presented in this section, we have designed and fabricated a spin-OLED structure with a bipolar OSV performance, exhibiting an effective spin-polarized current through the device which is preserved up to high temperatures. As it was mentioned before, in the OSVs reported so far in literature, the MR signal of the device vanishes at voltages above 1-2V. In our spin OLED, the OSV performance remains up to bias voltages of 11-12 V which supposes an outstanding response for a spintronic structure (figure 8.26). By the proposed approach it has been possible to drive the OSV of the spin-OLED to bias voltages at which the device has a measurable light emission. In this sense, it is straightforward to evaluate the possible modulation of the electroluminescence of the structure by a spin valve MEL effect. The description of this characterization will be developed in the next section.

8.2.4 Spin valve magneto-electroluminescence (MEL) effect

The experimental magneto-electroluminescence (MEL) effect on the spin-OLED structure was evaluated by comparing the amount of light registered by the photodiode when sweeping the external magnetic field, using as reference the electroluminescence (EL) in the antiparallel state. This lead to the equation for the MEL:

$$MEL = \frac{\Delta EL}{EL_{ap}} = \left(\frac{EL_p - EL_{ap}}{EL_{ap}}\right) \times 100\ (\%) \qquad (eq.8.4)$$

EL_p and EL_{ap} is the electroluminescence, just as read from the photodiode of the set-up, when sweeping the external magnetic field from parallel (P) to antiparallel (AP) configurations of the electrode magnetizations respectively.

By performing this characterization, we have been able to detect a modulation of light with a hysteretic behavior that follows the coercive fields of the electrodes. The experimental magneto-electroluminescence, MEL_{exp}, presents two contributions: a) the hysteretic behavior assigned to the spin valve effect in the spin-OLED, b) a non-hysteretic signal arising from the influence of the LSMO, with a monotonic variation with the applied magnetic field, which is mainly evident in the saturation region. As it was done for the MR curves in the previous section, the LSMO influence was subtracted in order to get the net signal of the light modulation by a spin valve effect. The same procedure was applied by Z.V Vardeny and coworkers in their reported spin-OLED[51]. In figure 8.27 it is shown the MEL_{exp} just as measured at 10 V and 42 K and the net MEL signal coming from the modulation of the light under the external magnetic field after the removal of the LSMO influence.

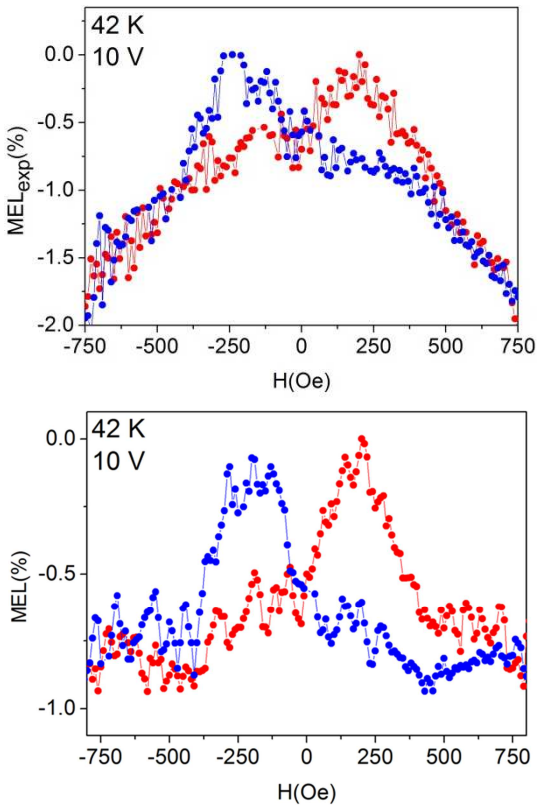

Figure 8.27- *Top*: MEL_{exp} signal just as it is directly measured at 42 K and 10V. *Bottom*: Subtraction of the LSMO non-hysteretic signal from the MEL signal in order to get the net light modulation under the external magnetic field.

In this study it was found that only samples presenting the monolayer of the Ru complex N965 deposited by LB exhibited a MEL effect. This feature is due to the outstanding OSV performance of the device which is preserved up to 12 V, with a light emission for the same range of bias voltages when this molecular ionic layer is included.

In the spin-OLED without the molecular ionic junction, which has been employed as a reference device, the important degradation of the OSV performance well below the light emission V_{on} supposes a definitive limitation for detecting the light modulation in the system.

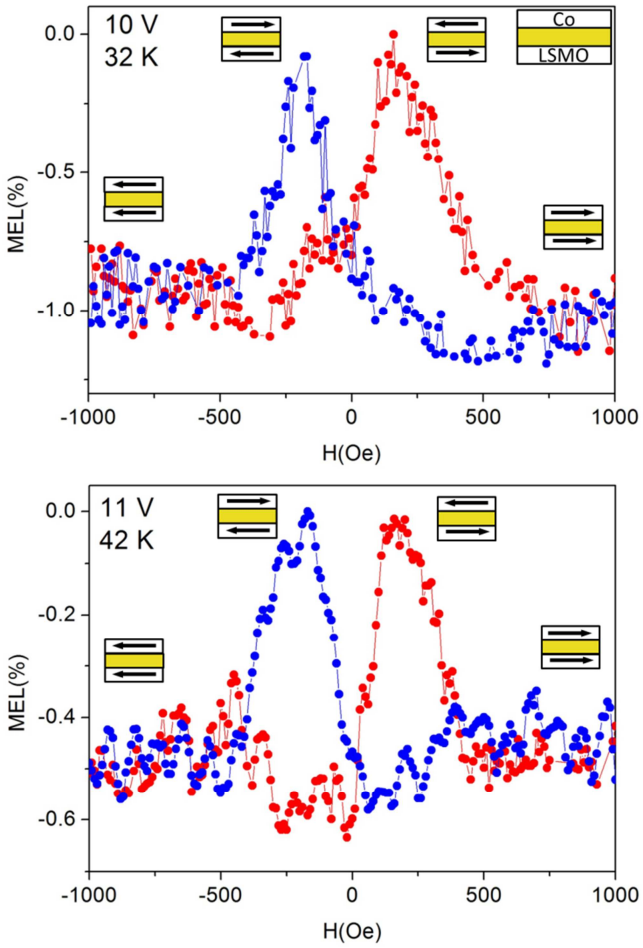

Figure 8.28- *Top*: Maximum MEL response in our spin-OLED measured at 10 V and 32 K, with an enhancement of light emission of 1% in the antiparallel state of magnetizations. *Bottom:* MEL signal of the spin-OLED obtained at 11V and 42 K.

In figure 8.28 it is shown some representative MEL curves obtained at low temperature in the device with functionalized LSMO cathode. A maximum modulation of the emitted light of around 1% has been detected at 32 K under a bias voltage of 10 V. This modulation is manifested as an enhancement of the EL for the AP configuration of the electrode magnetizations (figure 8.28). In the spin- OLED, it was only possible to detect a MEL signal for voltages of 10 V, 11 V and 12 V. At these bias voltages the amount of light emitted was enough to make possible a good detection of the effect with a proper signal-to-noise ratio.

We propose that this light modulation is due the presence of a spin-polarized (SP) current through the structure. By injecting spin-polarized carriers in the F8BT, the singlet:triplet ratio of excitons in the device can be modulated by the external magnetic field, inducing in consequence a modulation of the EL[32]. This point will be described more extensively in the following pages of this section. Thus, this MEL response would be directly related to the spin valve performance of our spin-OLED. Nevertheless, in order to confirm this affirmation, a deep analysis of the data has been performed for ruling out the presence of any kind of artifacts in the measurements artifacts. These artifacts could influence the light emission under external magnetic fields without being related to the effects of spin-polarized carrier injection in the F8BT.

The first point for relating the MEL signal to the presence of a spin-polarized current in the spin-OLED is the matching of the switching fields in the MEL curves with the coercive fields of the ferromagnetic electrodes in the device. In figure 8.29 it is depicted the comparison of the maximum MEL signal measured at 32 K and 10 V with the hysteresis loop of the device measured with SQUID in the same way as done in figure 8.22 for the MR signal at the same voltage and temperature. The first switching of the MEL curve located in point 1, at approximately 70 Oe, matches perfectly with the coercive field of the LSMO electrode, H_c (LSMO). Again it is clear how an AP state is stabilized in the device between points 2 and 3 with magnetic fields of 120 Oe and 270 Oe respectively, where a maximum EL is registered. The crossing from high- to low-EL states in the MEL curve starts at point 3 located at around 270 Oe. This value is coincident with the switching field of the magnetization reversal on the Co electrode as determined from the SQUID hysteresis loop. The progressive evolution of the MEL curve, with the absence of a sharp jump towards the P state, is clearly reflected by the magnetization reversal characteristics of the Co electrode. The tail of the MEL curve is quite coincident with the coercive field (385 Oe) assigned to this Co electrode and indicated as point 4. The same comparison has been made for the rest of MEL curves registered in the spin-OLED, exhibiting in all the cases a good matching. According to all this information, the MEL effect in the spin-OLED has been demonstrated to follow the coercive fields of the electrodes in the device. This is the first clear evidence

of an EL modulation originated from the spin polarized carriers in the F8BT responding to OSV behavior of the light emitting spintronic structure.

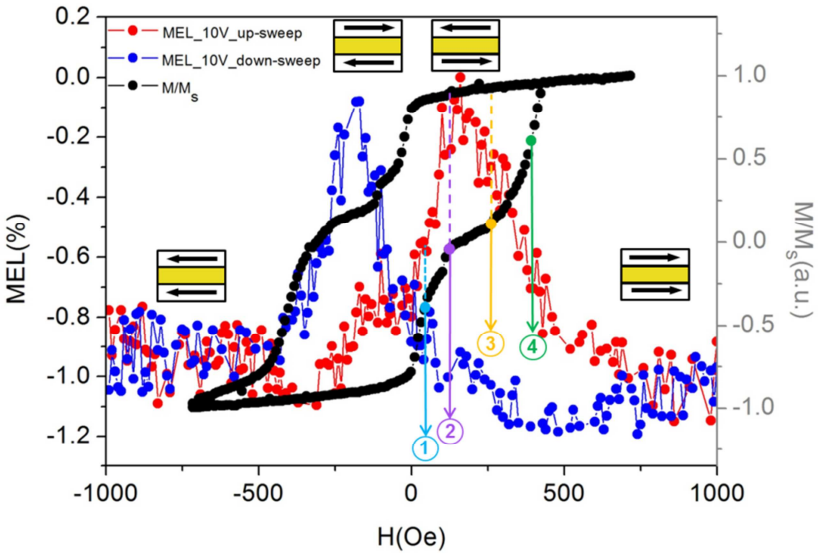

Figure 8.29- Comparative of the MEL signal at 10 V and 32 K with the hysteresis curve of the device measured with SQUID.1) at approximately 70 Oe, corresponds to the coercive field of the LSMO electrode ; between point 2) and 3), located at around 120 Oe and 270 Oe respectively, an antiparallel state between both ferromagnetic electrodes is stabilized;. 3) at 270 Oe the switching of the Co layer starts, and progressively the whole layer is reversed which is reflected in point 4) with the value of the coercive field for the anode, of approximately 385 Oe.

On the other hand, a systematic study has been performed in order to discard a light emission modulation arising from an effect induced by the ferromagnetic electrodes without being related to the spin-polarized carrier injection. The magnetic field effects on the EL of an OLED containing electrodes of Py and Ni were studied by G. Salis and coworkes[69]. In that case, it was analyzed the influence of the stray fields of the ferromagnetic electrodes on the EL response of the light emitting device. One of the main conclusions of this work was that the stray fields of the electrodes can induce a hysteretic response of the EL, which would not be related to the spin valve effect of the device. Thus, the stray fields of the electrodes could mimic a spin injection process inducing a false

relation between light modulation and presence of SP current through the structure. In order to discard the effect of the electrode stray fields on the detected MEL signal, reference HyLED structures were prepared employing the same layers but modifying the electrodes. Three types of devices were obtained: 1) HyLED with no ferromagnetic electrodes, where ITO is employed as the cathode and Au as the anode, 2) HyLED with only one ferromagnetic electrode, being LSMO the cathode and Au the anode, 3) HyLED with only one ferromagnetic electrode with an ITO electrode as the cathode and Co as the anode. These structures were evaluated under the same experimental conditions of the spin-OLED in order to compare the possible MEL responses.

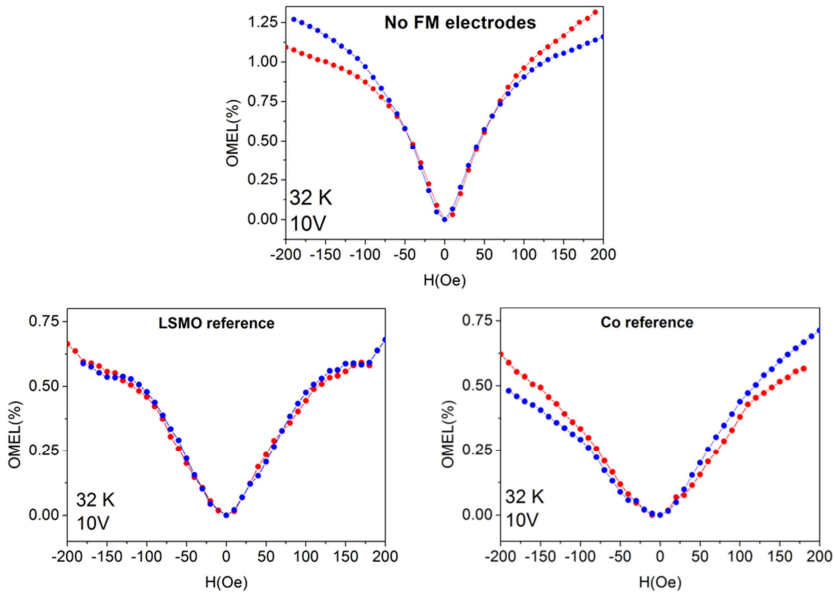

Figure 8.30- Light emission response of the reference devices under sweeping of an external magnetic field. These curves reflect the OMEL response of the F8BT.

In figure 8.30 it is depicted the three MEL effects on these reference devices, being their response clearly different to the light emission modulation in the spin-OLED. The response in the three cases has no hysteretic features, with a decrease of the EL when sweeping to magnetic fields in which an AP configuration would be obtained in the spin-OLED. The completely different

characteristics of these curves, with a light emission modulation opposite in sign to the one obtained for the MEL response in the spin-OLED, makes possible to discard the influence of the electrode stray fields in MEL effect for our light emitting spintronic device. As indicated in figure 8.30, the magnetic field effect on these reference devices has been denoted as OMEL (organic magneto-electroluminescence) which can be directly related to the intrinsic response of the F8BT light emission under a variable external magnetic field. There are many models trying to explain the OMAR (organic magneto-resistance) and OMEL phenomena in organic semiconductors.

In the particular case of OLEDs, there are several experiments and theoretical models addressing the magnetic field effects on this type of devices without ferromagnetic electrodes[70–74]. In general, it has been reported the influence of variations in the local magnetic field over the recombination and transport processes of the injected carriers in the OSC. In this context, the hyperfine nuclear field is the major responsible, playing a key role on the OMAR and OMEL effects[31]. In the reference devices, the absence of spin-polarized carrier injection from both electrodes, suppressed the hysteretic MEL effect observed in the spin-OLED structure. The EL modulation under these conditions is responding to the intrinsic properties of the polymer not being related in any case to the OSV performance detected in our light emitting device.

Another possible artifact to discard, related to the effects of the electrodes on the MEL signal, is the existence of voltage redistribution. Voltage redistribution on the electrodes can take place when the device switches between AP and P states. This is due to the fact that, while the device resistance changes, the electrodes resistance does not. This means that any voltage drop along the electrodes would be different in the AP and P state, which could cause a change in the light emission of the device when sweeping an external magnetic field. For being more precise, the decrease in device resistance in the P state causes a greater voltage drop along the electrodes. This situation could result in a decrease of the detected EL, which is what we observe. In order to rule out this artifact, a quantitative estimate of the effect is warranted. The 1D resistor model[53], applied in the previous section to evaluate the impact of the electrode

response on the MR of the spin-OLED, predicts the following voltage profile across one electrode:

$$V(x) = V \cdot e^{\frac{x}{L}\sqrt{\frac{R_t+R_b}{R_s}}} \qquad (eq\ 8.5)$$

where V is the measurement voltage, L is the length of the electrode and x is the distance from where the voltage is measured. Again by using equation 8.3, R_s can be calculated numerically from the measured resistance for R in the AP and P states. In this context, whether the device MR occurs on the bulk of the OSC or at the interface with the electrodes is immaterial in this analysis. The difference in the voltage profile between the two states is therefore:

$$\Delta V(x) = V \cdot \left(e^{\frac{x}{L}\sqrt{\frac{R_t+R_b}{R_{s,P}}}} - e^{\frac{x}{L}\sqrt{\frac{R_t+R_b}{R_{s,AP}}}} \right) \qquad (eq.\ \ 8.6)$$

where $R_{s,AP}$ is R_s calculated for the AP state and $R_{s,P}$ is R_s calculated for the P state. Since the device MR occurs in a narrow interval of applied magnetic field, R_t and R_b can be taken as constant in this case. Figure 8.31 shows $\Delta V(x)$ for a 1 mm size device, with R_t= 1.3 Ω, R_b= 380 Ω , $R_{s,AP}$= 8.56 kΩ and $R_{s,P}$= 8.54 kΩ, for a measured voltage of 10 V. The maximum deviation from the measured voltage is 3.2×10^{-2} %, with a nearly linear increase with position. The average voltage deviation is then ΔV_{AVG} $\sim 1.6 \times 10^{-2}$ %. To calculate the effect on the MEL, one has to consider the EL as a function of the applied voltage, given in figure 8.13. The relative change in voltage is very small and the EL can be taken as linearly dependent on the applied voltage in this range.

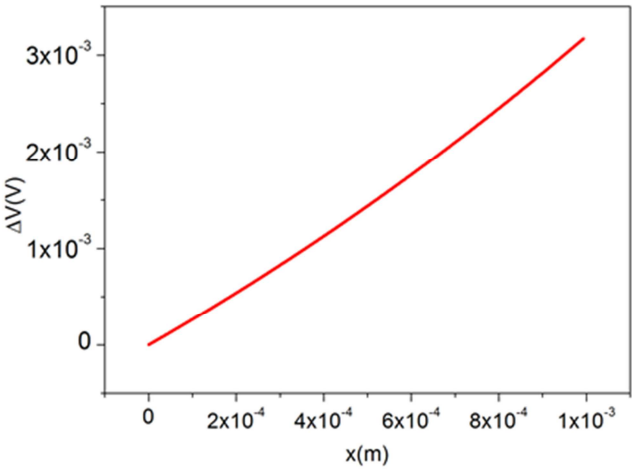

Figure 8.31- $\Delta V(x)$ for a 1 mm size device, with R_t= 1.3Ω, R_b=380Ω , $R_{s,AP}$=8.56 kΩ and $R_{s,P}$=8.54kΩ, for a measured voltage of 10 V in the spin-OLED.

The expected MEL due to the voltage redistribution at bias voltage of 10 V, as calculated from the data in figure 8.31, is $\Delta EL/EL$ ~0.16%, which is well below the MEL effect of 1% registered experimentally in our device. According to all this information, it is possible to completely discard a voltage redistribution in the electrodes of the spin-OLED when sweeping the external magnetic field, as the responsible of the EL modulation.

The last artifact to be treated regarding the MEL effect in our spin-OLED, and probably the most important one, is the possibility of having a light emission response directly coupled to the modulation of the current by the MR effect in the device. In an OLED type device the intensity of the light emission is directly related to the current density through the structure[75]. In this sense, at a fixed voltage an increase in resistance due to the MR response would cause a decrease in the current through the structure. This process would be translated into a decrease in the EL of the device. In the spin-OLED reported by Z.V. Vardeny et al.[51], the modulation of light follows the same behavior than the magneto-conductance response. In that case, when in the AP state there is a decrease in the current, due to the evolution of the resistance following the MR behavior, the electroluminescence suffers the same decrease as well. According to this, the MEL effect in the spin-OLED of Z.V. Vardeny and co-workers[51] could

be related to an artifact in the EL induced by changes of current density, instead of an effect due to the injection of spin-polarized charge carriers in the structure allowing a modulation of the singlet:triplet ratio in the system. It is interesting to notice that this response of the EL to the current density has been recently employed by Z.V. Vardeny et al.[75] for building up a hybrid device that couples an inorganic magnetic tunnel junction (MTJ), with large room temperature MR, with an OLED structure without ferromagnetic electrodes. In that hybrid system, the current density to the OLED is provided by the MTJ. Thus a modulation of the current density by the changes of resistance in the MTJ under an external magnetic field allows a direct modulation of the EL of the OLED which follows exactly the same behavior. This is a clear example of the application of this coupling between current density and EL in an OLED, illustrating quite well the artifact that has to be ruled out in a spin-OLED device. In our particular system, the EL and the current density follow two totally different channels. Under the sweeping of an external magnetic field, when the AP state is stabilized, an increase of the resistance in the structure is produced. This process is accompanied by a decrease in the amount of current through the device. On the contrary, when the AP state is established, the EL of our spin-OLED is enhanced thus having a totally opposite response respect to the current. This effect is illustrated in figure 8.32 by showing the current and EL just as measured in our spin-OLED at 10 V and 32 K with an opposite effect between both properties.

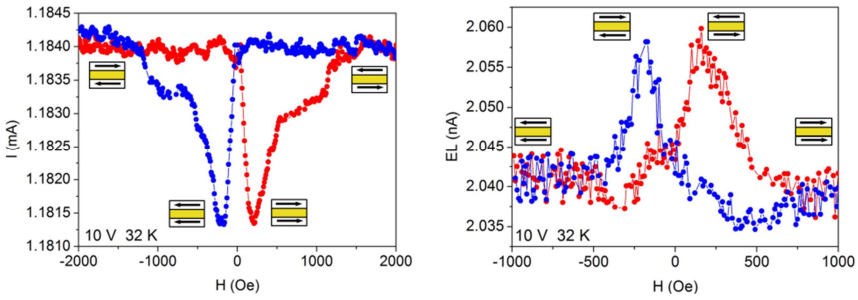

Figure 8.32- Comparative of the opposite behavior of current and EL in the antiparallel state of magnetizations. The current and EL (in nA as the detected by the photodiode) follow two totally opposite behaviors when responding to the external magnetic field.

According to all the studies discussed so far, we have ruled out many possible artifacts that could induce a MEL effect in the spin-OLED based on mechanisms that are not directly related to the control over the excitons statistics by the application of an external magnetic field. With all this information in hand, it is possible to assume that the MEL effect in our spin-OLED could be directly related with the spin valve effect in the device. Thus, the light emission modulation is established by the injection of spin-polarized charge carriers from the ferromagnetic cathode and anode into the F8BT.

A simple phenomenological model, based on fundamental concepts, allows the understanding of the mechanisms behind the MEL effect in our spin-OLED[32,44,76]. In our device, the injection of carriers with a controlled spin state, inducing the appearance of a spin-polarized current, would promote the control over the exciton populations. In this way, an enhancement of light emission in the AP state would be induced [32].Once the spin-polarized electrons and holes are injected from the LSMO and Co respectively into the F8BT, they move across the OSC until they form local polaron pairs (PPs) due to their mutual Coulomb attraction. As a consequence of the interaction with nuclear spins or additional scattering process related to the spin-orbit coupling in the F8BT, these spin-polarized charge carriers can suffer a spin flipping. Nevertheless, as the hyperfine interaction and spin-orbit coupling are considered to be weak in OSC, this spin flip scattering is assumed not to be important in the emissive layer. When the PPs are sharing a particular monomer of the F8BT, they become precursors of highly bounded exciton states. These exciton states can be either singlets or triplets with spin values of S = 0 or S = 1 respectively. The light emission in the F8BT will be mediated by a bimolecular recombination process of Langevin type, when the decaying of the excitons takes place. As mentioned many times along this thesis, only singlet excitons can decay radiatively and contribute to the light emission of the spin-OLED. On the contrary, the decaying dynamics of triplet excitons are much slower, being defined by non-radiative recombination processes. In this sense, the EL quantum efficiency of a device is determined by the fraction of singlet excitons generated in the light emitting layer, χ_s[31,44]. In a simple picture, the singlet:triplet ratio established by quantum statistics is determined to be 1:3 under the consideration of a similar

formation for one singlet and three triplet states[32]. According to this, the maximum quantum efficiency in the spin-OLED should be less than 25%. The application of an external magnetic field is able to influence the spin injection charge carrier process, affecting directly to the singlet:triplet ratio. Let us analyze this point with more detail. As mentioned previously, the PPs can lead to singlet or triplet excitons according to the spin of the charge carriers involved in the process. An electron-hole pair with antiparallel spins may generate either a singlet or a triplet state, but when all electron-hole pairs are in parallel state only triplet can be produced as depicted in an illustrative way in figure 8.33.

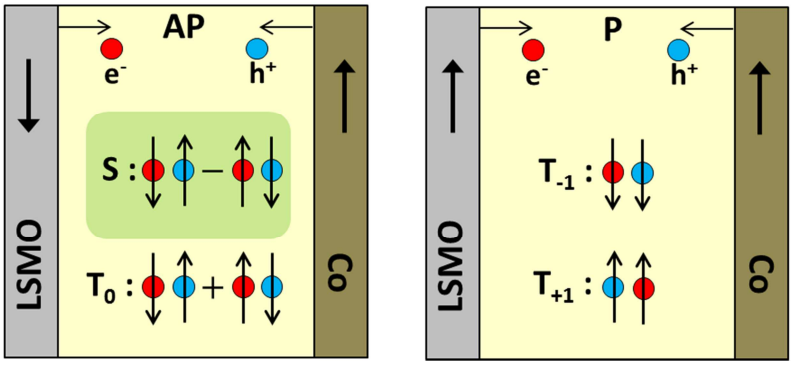

Figure 8.33- Exciton type formation according to the relative orientation of the electrode magnetization. An electron-hole pair with AP spins may generate either a singlet (S) or one of the three triplet components (T_0). On the contrary, when all electron-hole pairs are in parallel state only triplet (T_{-1},T_{+1}) excitons can be generated in the OSC. Only S excitons (highlighted in green) decay in a radiative way leading to light emission in the device.

Based on figure 8.33, name the singlet exciton state as S, and each of the three possible triplet states (T_{-1}, T_0, T_{+1}) as T. When sweeping the external magnetic field, the relative magnetization orientations of the ferromagnetic cathode and anode can be switched from P to AP. In first approximation, when the P state is established, the parallel combinations of spin-polarized charge carriers do not contribute to the emission of light taking into account that they can only lead to triplet excitations. In contrast, the antiparallel pair contains the singlet state, which will be the responsible of light emission. In this conceptual framework, in a HyLED with no SP electrodes, the charge injection will introduce in the OSC

electrons and holes with all possible values of spin, $M_S = 1/2$ and $M_S = -1/2$. This situation can lead to four possible PPs: $e^{\uparrow}h^{\uparrow}$,$e^{\uparrow}h^{\downarrow}$,$e^{\downarrow}h^{\uparrow}$,$e^{\downarrow}h^{\downarrow}$, which give rise to a singlet spin state, $S = \frac{1}{\sqrt{2}}\left(e^{\downarrow}h^{\uparrow} - e^{\uparrow}h^{\downarrow}\right)$, and a triplet state formed by three components, $T_{+1} = e^{\uparrow}h^{\uparrow}$; $T_{-1} = e^{\downarrow}h^{\downarrow}$; $T_0 = \frac{1}{\sqrt{2}}\left(e^{\downarrow}h^{\uparrow} + e^{\uparrow}h^{\downarrow}\right)$. Thus, in the particular case of no spin-polarized electrodes, the singlet spin state and the three components of the triplet one can be present. This possible scenario resembles the ratio 1:3 for singlets and triplets that lead to a maximum efficiency of 25 % in an OLED device as previously explained.

Now we can consider the situation of spin polarized electrodes (figure 8.34), just as in our spin-OLED, where the LSMO cathode is responsible of injecting spin-polarized electrons, being the spin-polarized holes introduced in the F8BT by the Co anode. An ideal situation in which both electrodes are 100 % spin polarized will be assumed, being far from reality but resulting useful for the qualitative understanding of the process. When sweeping an external magnetic field, both electrodes can be set in an antiparallel (AP) magnetization configuration, thus the LSMO and Co will introduce electrons and holes respectively of only one type, for example $e^{\uparrow}$ and $h^{\downarrow}$.[76] In this scenario, the formation of the triplet type exciton components with T_{+1} and T_{-1} will be forbidden and only the T_0 and excitons S will be formed. This will change the ration singlet:triplet to 1:1, enhancing the emission of light in the spintronic structure. In contrast, when the external magnetic field induces a parallel magnetization configuration in the electrodes, assuming a perfect spin alignment, triplet states will be exclusively formed with a correspondent reduction of light emission[76]. The phenomenological model detailed above is able to explain the MEL effect in our spin-OLED where an enhancement of the EL is detected when the AP magnetization state is stabilized in the OSV performance

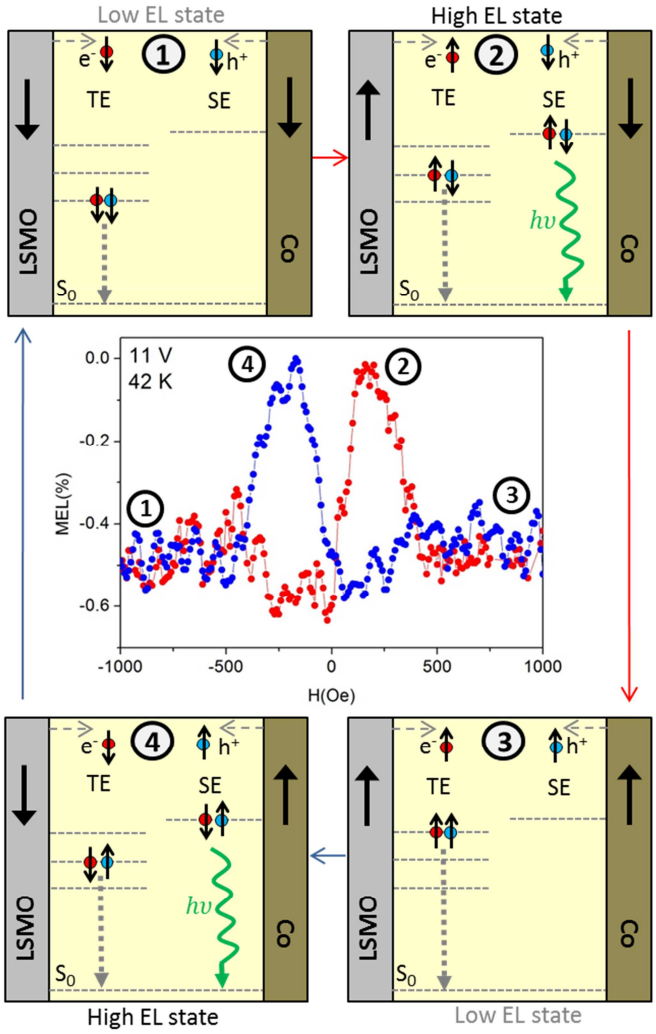

Figure 8.34- Illustration of the mechanism underlying the control of the exciton statistics in the device and its impact on the EL signal registered from the system. Points 2 and 4 corresponds to AP magnetization sates in which singlet excitons will be formed, decaying radiatively to the fundamental state with a consequent enhancement of the EL. On the contrary, points 1 and 3 correspond to a P magnetization state in which only triplet excitons can be formed decaying to the fundamental state via non-emissive pathways. This leads to a reduction of light emission at these points in the MEL curve. Blue and red arrows indicate the up- and down- sweeping fields respectively.

We can relate the MEL response in the spin-OLED with a proper spin valve effect in the device which allows, in the bipolar charge transport regime, the injection of spin-polarized electrons and holes. The spin-polarized injection in the system increases the formation of singlet excitons when the AP state is stabilized by an external magnetic field. By this process an enhancement of the EL in the AP state of the device is produced, with a maximum light modulation of around 1% at 32 K and 10 V. However, it is clear that a more sophisticated theoretical model needs to be developed for explaining in a quantitative way the phenomenology of the MEL response in our spin-OLED structure. This theoretical framework would allow confirming the grade of accuracy of the hypothesis that we have proposed over the discussion.

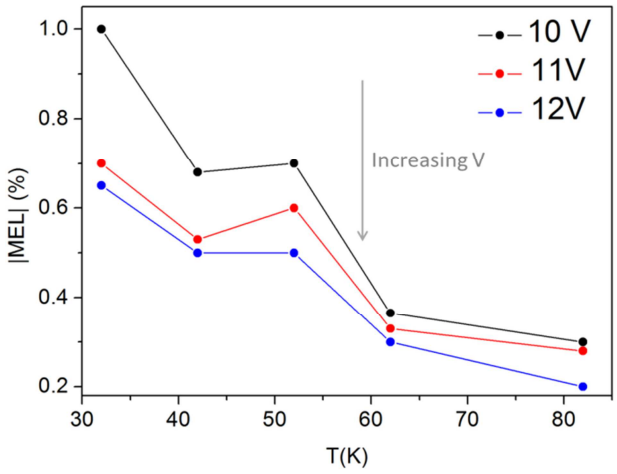

Figure 8.35- Thermal evolution of the MEL response in the spin-OLED for 10 V, 11 V and 12V. The tendency with increasing voltage is also indicated in the graph by the grey arrow.

The last point to treat is the thermal dependence. In figure 8.35 it is depicted the thermal evolution of the absolute value of the MEL response measured at 10 V, 11 V and 12 V. For the spin-OLED containing the molecular ionic junction of the ruthenium complex N965, the MEL effect associated to the injection of spin-polarized charge carriers in the F8BT is observed up to 82 K. By comparing figure 8.24 and 8.35, it is possible to observe that the signal associated to the MEL effect vanishes at lower temperatures respect to the MR signal of the spin-

OLED. This difference is not due to the thermal response of the spin injection processes, but it is related to the appearance of a measurable intrinsic OMEL effect in the F8BT. As the temperature is progressively increased, the OMEL effect is enhanced leading to a screening of the MEL signal related to the spin valve performance of the device.

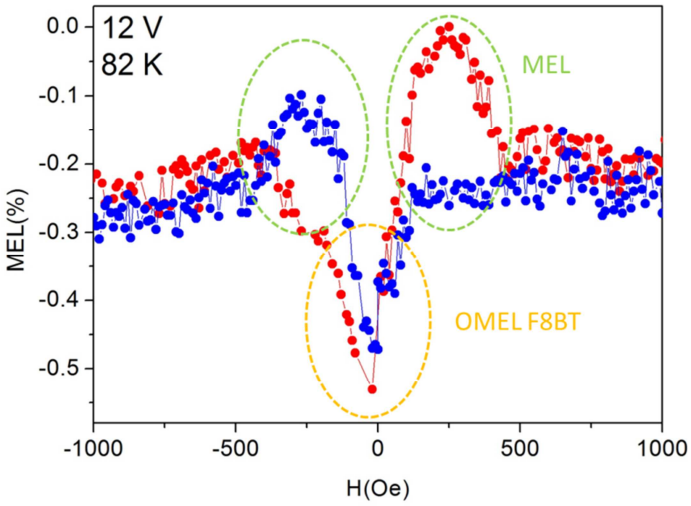

Figure 8.36- Magnetic field modulation of EL in the spin-OLED at 12 V and 82 K showing the appearance of an important intrinsic OMEL signal related to the F8BT. At higher temperatures this OMEL component produces a screening of the MEL effect associated to the injection of spin-polarized charge carriers in the F8BT.

From figure 8.36 it is possible to observe that the OMEL at 82 K starts to be important compared to the MEL signal, presenting an inverse sign response respect to the external magnetic field. At higher temperatures the EL modulation under external magnetic fields in the spin-OLED is dominated by this OMEL response in the F8BT.

It is also possible to extract a tendency for the MEL effect with respect to the bias voltage applied to the spin-OLED from figure 8.35. A slight reduction in the amplitude of the MEL response, when increasing the bias voltage from 10-12 V, is detected. However, the values are maintained in the same order of magnitude in all the cases. Thus, at these high voltages the outstanding stabilization of the

spin transport properties in the device seems to preserve the MEL effect from severe damage in the range of bias voltages under study. Still, it is necessary to improve the performance of the spin-OLED for having the presence of MEL effect associated to the spin valve performance in a wider range of voltages. This would allow extracting a more accurate bias voltage dependence, as done for the MR response.

8.3 Conclusions and perspectives

In this chapter we have described the successful designing and fabrication of a spin-OLED, based on a HyLED configuration, exhibiting a MEL effect related to the control of the exciton densities in the OSCs. This process is promoted by the injection of spin-polarized charge carriers in the device. The inclusion of an air stable ferromagnetic cathode as the LSMO has allowed a major improvement in the performance of the device. By the functionalization of the LSMO, through the deposition of a molecular ionic junction of a ruthenium complex named N965, it has been possible to drive the light emission and the OSV performance of the spin-OLED to the same range of temperatures and voltages. This was the main bottleneck in the field of molecular spintronics for the obtaining of a spin-OLED structure presenting a spin valve MEL effect. This is ascribed to the fact that the bias voltage operation of the OSVs reported so far has been always much lower than the voltages for light emission in optoelectronic devices. Thus, the incorporation of this Ru complex as an electron injection layer (EIL) has promoted an outstanding stabilization of the performance of the spin-OLED in terms of electroluminescence and OSV response.

The presence of the N965 as EIL had a direct impact on the light emission of the spin-OLED, in such a way that the light emission turn-on-voltage (V_{on}) light is reduced in approximately three volts respect to the device without this EIL. Under these conditions a detectable light emission takes place above 7 V at 14 K. When a bias voltage is applied in the device, the molecular ionic junction promotes the appearance of an ionic space charge at the interface by means of an ion redistribution, with a consequent formation of an ionic space charge at the interface. This process reduces the energy barrier for electron injection into

the LUMO of the F8BT, leading to the described decrease in the light emission V_{on}.

On the other hand, our spin-OLED presents an outstanding performance as a bipolar OSV, preserving a spin-polarized current through the structure up to 12 V at temperatures of 180-200 K. This is the first report of a spintronic structure preserving a MR signal up to such high voltages, taking into account that the OSVs described so far in literature suffer a total degradation of their spin transport for voltages above 1-2 V. We have related this outstanding stabilization of the MR to processes of charge annihilation taking place in the emissive layer of the device. These processes would be the responsible of reducing the spin relaxation mechanisms in the OSC. Nevertheless, it is important to consider that nowadays in the field of molecular spintronics there is no satisfactory explanation to the MR degradation in OSVs when increasing the bias voltage above 2V. In consequence, it is not straightforward to give a definitive explanation to the high bias voltage performance of our spin-OLED. It is fundamental to keep in mind that, in addition to our system, only one reported result of a spin-OLED working in a bipolar regime at high voltages can be found in literature[51]. Thus, we are in front of a new phenomenology in the field of spintronics that need of several more experiments and a solid theoretical framework to predict and confirm the described mechanisms that have been proposed. In the perspective article of V. A. Dediu et al.[32] it is written: "*In parallel with spin-transport studies, simpler charge transport in organic spintronic devices (OSPDs) also needs a deeper understanding. The study of charge transport in organic electronic or optoelectronic devices usually involves detailed investigations of the role of shallow and/or deep trap levels, transitions from injection-limited to space-charge-limited current and other standard models. A similar analysis for OSPDs is still lacking. This absence is probably motivated by the small voltage range in which spin effects usually take place (± 1 V), and this reduced part of the I–V curves does not provide enough information to explain the transport mechanism involved. At present it is difficult to determine whether and how spin injection and transport are related to very relevant parameters, such as natural defects of the OSC or traps".* In this sense, our spin-OLED could provide

the proper scenario for addressing many of the open questions in the field of molecular spintronics related to spin injection and spin transport.

Regarding to the thermal evolution of the MR in the spin-OLED, it has been detected a crucial improvement respect to the spin-OLED prototype containing an Fe electrode as the ferromagnetic cathode and described in chapter 7. In that case it was proposed the substitution of this transition metal ferromagnetic electrode by other air stable cathode which could preserve the spin injection properties despite the conditions under which the device is fabricated. This statement has been proved by the fact that a spin polarized current is detected up to 180-200K in the spin-OLED employing the functionalized LSMO cathode.

The presence of a spin-polarized current in the device in the same range of voltages and temperature for light emission, has allowed the detection of a MEL effect, which can be related with the spin valve performance of the system. A maximum modulation of light emission of 1 % has been detected at 10 V and 32 K with an enhancement of the EL for the antiparallel configuration of the electrode magnetizations. This effect has been registered at voltages of 10-12V, where a sufficient amount of light can be detected guaranteeing a good signal-to-noise ratio in the measurement. Only the spin-OLED containing the monolayer of N965 exhibited this successful MEL effect. In absence of the molecular ionic junction, at the bias voltages at which it is possible to register a sufficient intensity of light, the OSV performance is totally degraded. This situation highlights the importance of the inclusion of an efficient electron injection layer in the structure.

A detailed analysis of the data has been performed in order to rule out any possible artifact that could mimic a modulation of the light by spin injection processes. Effects related to the ferromagnetic electrodes and light emission mechanisms in the spin-OLED performance have been discarded as responsible of the described behavior. With this work we have proposed a protocol to test the performance of a spin-OLED device. By this means it can be demonstrated that the light modulation is produced by an effective control of the exciton statistics promoted by the injection of spin-polarized charge carries in the OSC. This quality test is missing in the reported work of Z.V. Vardeny and co-

workers[51] claiming to have a spin-OLED with a proper spin valve MEL effect in the structure. Nevertheless, the fact that the EL and the current follow the same behavior in this device is indicating that the claim of a real control of the exciton statistics leading to a light emission modulation has to be carefully evaluated and reproduced by other laboratories.

One major advantage of the spin-OLED proposed in this chapter is the application of a commercial light emitting polymer that is used just as received from the provider. This is translated into a cheaper and more accessible device in terms of fabrication. Thus, by our strategy we have been able to obtain an effective light modulation in a spintronic structure whose main components are deposited from wet solution methods. It supposes several advantages from the point of view of a scalable, low-cost and large area deposition.

There are many possible strategies to improve the performance of the described spin-OLED. The electron injection from the LSMO cathode into the LUMO of the F8BT is one of the most important bottlenecks in the operation of this device. In this sense, the efficient hole injection mediated by the MoO_3 HIL has been extensively demonstrated. Thus, the electron injection interface has to be the center of attention in the future improvements of this system. It is important to study the impact of the application of other molecules as the EIL in this light emitting spintronic devices. The functionalization of the LSMO cathode can be done by growing self-assembling monolayers of a wide variety of functional molecules, as well as the deposition by means of Langmuir-Blodgett of other molecular barriers. From this interface engineering approach a more efficient charge carrier injection in the OSC would be obtained, by a reduction of the energy barrier for electron injection, leading to a decrease in the turn on voltage for light emission. Driving the threshold voltages for EL to lower values will promote the appearance of the MEL effect at lower bias voltages in the device. In addition, by introducing these improvements, is expected to enhance the magnitude of the MEL effect above the 1 %, which is the upper limit in the present situation. Increasing the magnitude of the MEL would reduce the impact of the “screening effect” introduced by the intrinsic OMEL signal of the F8BT. In this sense, it would be possible to increase the upper limit of thermal degradation on the spin valve MEL response above 82 K. In conclusion, these

improvements in the design and fabrication of the spin-OLED will drive the performance of the system to higher temperatures and lower bias voltages, increasing at the same time the magnitude of the MEL effect. This will provide a new generation of molecular spintronic devices with tunable optoelectronic properties.

8.4 Bibliography

(1) Park, J. -H., Vescovo, E., Kim, H.-J., Kwon, C., Ramesh, R., Venkatesan, T. *Nature* **1998**, *392*, 794.

(2) Bowen, M.; Maurice, J.-L.; Barthélémy, a; Bibes, M.; Imhoff, D.; Bellini, V.; Bertacco, R.; Wortmann, D.; Seneor, P.; Jacquet, E.; Vaurès, a; Humbert, J.; Contour, J.-P.; Colliex, C.; Blügel, S.; Dederichs, P. H. *J. Phys. Condens. Matter* **2007**, *19*, 315208.

(3) Mercone, S.; Perroni, C.; Cataudella, V.; Adamo, C.; Angeloni, M.; Aruta, C.; De Filippis, G.; Miletto, F.; Oropallo, a.; Perna, P.; Petrov, a.; Scotti di Uccio, U.; Maritato, L. *Phys. Rev. B* **2005**, *71*, 064415.

(4) Dediu, V.; Murgia, M.; Matacotta, F. C.; Taliani, C.; Barbanera, S. *Solid State Commun.* **2002**, *122*, 181.

(5) Xiong, Z. H.; Wu, D.; Vardeny, Z. V.; Shi, J. *Nature* **2004**, *427*, 821.

(6) Wang, F.; Yang, C.; Vardeny, Z.; Li, X. *Phys. Rev. B* **2007**, *75*, 245324.

(7) Dediu, V.; Hueso, L.; Bergenti, I.; Riminucci, a.; Borgatti, F.; Graziosi, P.; Newby, C.; Casoli, F.; De Jong, M.; Taliani, C.; Zhan, Y. *Phys. Rev. B* **2008**, *78*, 115203.

(8) Barraud, C.; Seneor, P.; Mattana, R.; Fusil, S.; Bouzehouane, K.; Deranlot, C.; Graziosi, P.; Hueso, L.; Bergenti, I.; Dediu, V.; Petroff, F.; Fert, A. *Nat. Phys.* **2010**, *6*, 615.

(9) Galbiati, M.; Barraud, C.; Tatay, S.; Bouzehouane, K.; Deranlot, C.; Jacquet, E.; Fert, A.; Seneor, P.; Mattana, R.; Petroff, F. *Adv. Mater.* **2012**, *24*, 6429.

(10) Galbiati, M.; Seneor, P.; Mattana, R.; Tatay, S.; Bouzehouane, K.; Deranlot, C.; Jacquet, E.; Forment-aliaga, A.; Jegou, P. *ACS Nano* **2012**, *6*, 8753.

(11) Sessolo, M.; Bolink, H. J. *Adv. Mater.* **2011**, *23*, 1829.

(12) Meyer, J.; Shu, a.; Kröger, M.; Kahn, a. *Appl. Phys. Lett.* **2010**, *96*, 133308.

(13) Michaelson, H. B. *J. Appl. Phys.* **1977**, *48*, 4729.

(14) Graziosi, P.; Prezioso, M.; Gambardella, a.; Kitts, C.; Rakshit, R. K.; Riminucci, a.; Bergenti, I.; Borgatti, F.; Pernechele, C.; Solzi, M.; Pullini, D.; Busquets-Mataix, D.; Dediu, V. a. *Thin Solid Films* **2013**, *534*, 83.

(15) Prellier, W.; Lecoeur, P.; Mercey, B. *J. physics. Condens. matter* **2001**, *13*, R915.

(16) Li, K.-S.; Chang, Y.-M.; Agilan, S.; Hong, J.-Y.; Tai, J.-C.; Chiang, W.-C.; Fukutani, K.; Dowben, P. a.; Lin, M.-T. *Phys. Rev. B* **2011**, *83*, 172404.

(17) Schmidt, G.; Ferrand, D.; Molenkamp, L.; Filip, a.; van Wees, B. *Phys. Rev. B* **2000**, *62*, R4790.

(18) Djeghloul, F.; Ibrahim, F.; Cantoni, M.; Bowen, M.; Joly, L.; Boukari, S.; Ohresser, P.; Bertran, F.; Le Fèvre, P.; Thakur, P.; Scheurer, F.; Miyamachi, T.; Mattana, R.; Seneor, P.; Jaafar, a; Rinaldi, C.; Javaid, S.; Arabski, J.; Kappler, J.-P.; Wulfhekel, W.; Brookes, N. B.; Bertacco, R.; Taleb-Ibrahimi, a; Alouani, M.; Beaurepaire, E.; Weber, W. *Sci. Rep.* **2013**, *3*, 1272.

(19) Bolink, H. J.; Baranoff, E.; Clemente-León, M.; Coronado, E.; Lopéz-Muñoz, A.; Repetto, D.; Sessolo, M.; Nazeeruddin, M. K. *Langmuir* **2009**, *25*, 79.

(20) Nuesch, F, Rotzinger, F., Si-Ahmed, L., Zuppiroli, L. *Chem. Phys. Lett.* **1998**, *288*, 861.

(21) Zuppiroli, L., Si-Ahmed, L., Kamaras, K., Bussac, M.N., Ades, D., Siove, A., Moons, E., Grätzel, M. *Eur. Phys. J. B* **1999**, *11*, 505.

(22) Besbes, S.; Ltaief, a.; Reybier, K.; Ponsonnet, L.; Jaffrezic, N.; Davenas, J.; Ben Ouada, H. *Synth. Met.* **2003**, *138*, 197.

(23) Malinsky, B. J. E.; Jabbour, G. E.; Shaheen, S. E.; Anderson, J. D.; Richter, A. G.; Marks, T. J.; Armstrong, N. R.; Kippelen, B. *Adv. Mater.* **1999**, *11*, 227.

(24) De Boer, B.; Hadipour, a.; Mandoc, M. M.; van Woudenbergh, T.; Blom, P. W. M. *Adv. Mater.* **2005**, *17*, 621.

(25) Petta, J.; Slater, S.; Ralph, D. *Phys. Rev. Lett.* **2004**, *93*, 136601.

(26) Wang, W.; Richter, C. a. *Appl. Phys. Lett.* **2006**, *89*, 153105.

(27) Nguyen, T. D.; Hukic-Markosian, G.; Wang, F.; Wojcik, L.; Li, X.-G.; Ehrenfreund, E.; Vardeny, Z. V. *Nat. Mater.* **2010**, *9*, 345.

(28) Gobbi, M.; Golmar, F.; Llopis, R.; Casanova, F.; Hueso, L. E. *Adv. Mater.* **2011**, *23*, 1609.

(29) Ehrenfreund, E.; Valy Vardeny, Z. *Phys. Chem. Chem. Phys.* **2013**, *15*, 7967.

(30) Zhang, X.; Mizukami, S.; Ma, Q.; Kubota, T.; Oogane, M.; Naganuma, H.; Ando, Y.; Miyazaki, T. *J. Appl. Phys.* **2014**, *115*, 172608.

(31) Vardeny, Z. V. *Organic Spintronics*; Taylor & Francis Group: Boca Raton-Florida, 2010.

(32) Dediu, V. A.; Hueso, L. E.; Bergenti, I.; Taliani, C. *Nat. Mater.* **2009**, *8*, 707.

(33) Zhang, X.; Mizukami, S.; Kubota, T.; Ma, Q.; Oogane, M.; Naganuma, H.; Ando, Y.; Miyazaki, T. *Nat. Commun.* **2013**, *4*, 1392.

(34) Schwartz, D. K.; Garnaes, J.; Viswanathan, R.; Zasadzinski, J. A. N. *Science (80-.).* **1992**, *257*, 508.

(35) Mcgovern, M. E.; Kallury, K. M. R.; Thompson, M. *Langmuir* **1994**, *10*, 3607.

(36) Biebuyck, H. A.; Whitesides, G. M. *Langmuir* **1995**, *11*, 4371.

(37) Frederick, E.; Dickerson, P. N.; Zhong, Y. L.; Bernasek, S. L. *Langmuir* **2014**, *30*, 7687.

(38) Sessolo, M. *Hybrid organic-inorganic Light Emitting Diodes. PhD Thesis*; University of Valencia, 2010.

(39) Zhang, Y.; Blom, P. W. M. *Appl. Phys. Lett.* **2011**, *98*, 143504.

(40) Zaumseil, J.; Donley, C. L.; Kim, J.-S.; Friend, R. H.; Sirringhaus, H. *Adv. Mater.* **2006**, *18*, 2708.

(41) Chua, L.; Zaumseil, J.; Chang, J.; Ou, E. C. *Nature* **2005**, *434*, 194.

(42) Wang, F. J.; Xiong, Z. H.; Wu, D.; Shi, J.; Vardeny, Z. V. *Synth. Met.* **2005**, *155*, 172.

(43) Bolink, H. J.; Coronado, E.; Repetto, D.; Sessolo, M.; Barea, E. M.; Bisquert, J.; Garcia-Belmonte, G.; Prochazka, J.; Kavan, L. *Adv. Funct. Mater.* **2008**, *18*, 145.

(44) Yunus, M.; Ruden, P. P.; Smith, D. L. *Appl. Phys. Lett.* **2008**, *93*, 123312.

(45) Yoo, J.-W.; Jang, H. W.; Prigodin, V. N.; Kao, C.; Eom, C. B.; Epstein, a. J. *Phys. Rev. B* **2009**, *80*, 205207.

(46) Lin, R.; Wang, F.; Rybicki, J.; Wohlgenannt, M.; Hutchinson, K. a. *Phys. Rev. B* **2010**, *81*, 195214.

(47) Wohlgenannt, M. *Phys. status solidi - Rapid Res. Lett.* **2012**, *6*, 229.

(48) Sun, X.; Gobbi, M.; Bedoya-Pinto, A.; Txoperena, O.; Golmar, F.; Llopis, R.; Chuvilin, A.; Casanova, F.; Hueso, L. E. *Nat. Commun.* **2013**, *4*, 2794.

(49) Blom, P. W. M.; Vissenberg, M. C. J. M. *Mater. Sci. Eng. R-Rep* **2000**, *27*, 53.

(50) Bassler, H. *Pshysica Status Solidi B* **1993**, *175*, 15.

(51) Nguyen, T. D.; Ehrenfreund, E.; Vardeny, Z. V. *Science* **2012**, *337*, 204.

(52) Sun, D.; Yin, L.; Sun, C.; Guo, H.; Gai, Z.; Zhang, X.-G.; Ward, T. Z.; Cheng, Z.; Shen, J. *Phys. Rev. Lett.* **2010**, *104*, 236602.

(53) Riminucci, A.; Prezioso, M.; Graziosi, P.; Newby, C. *Appl. Phys. Lett.* **2010**, *96*, 112505.

(54) Szulczewski, G.; Sanvito, S.; Coey, M. *Nat. Mater.* **2009**, *8*, 693.

(55) Riminucci, A.; Bergenti, I.; Hueso, L. E.; Murgia, M.; Taliani, C.; Zhan, Y.; Casoli, F. <*http://arxiv.org/abs/cond-mat/0701603*> **2007**.

(56) Wang, Y.-Z.; Yang, M.; Qi, D.-C.; Chen, S.; Chen, W.; Wee, A. T. S.; Gao, X.-Y. *J. Chem. Phys.* **2011**, *134*, 034706.

(57) Nogués, J.; Sort, J.; Langlais, V.; Skumryev, V.; Suriñach, S.; Muñoz, J. S.; Baró, M. D. *Phys. Rep.* **2005**, *422*, 65.

(58) Gredig, T.; Krivorotov, I. N.; Eames, P.; Dahlberg, E. D. *Appl. Phys. Lett.* **2002**, *81*, 1270.

(59) Lee, W. Y.; Samad, a.; Moore, T. a.; Bland, J. a. C.; Choi, B. C. *J. Appl. Phys.* **2000**, *87*, 6600.

(60) Mooser, S.; Cooper, J. F. K.; Banger, K. K.; Wunderlich, J.; Sirringhaus, H. *Phys. Rev. B* **2012**, *85*, 235202.

(61) Santos, T.; Lee, J.; Migdal, P.; Lekshmi, I.; Satpati, B.; Moodera, J. *Phys. Rev. Lett.* **2007**, *98*, 016601.

(62) Bobbert, P.; Wagemans, W.; van Oost, F.; Koopmans, B.; Wohlgenannt, M. *Phys. Rev. Lett.* **2009**, *102*, 156604.

(63) Yu, Z. G. *Nat. Commun.* **2014**, *5*, 4842.

(64) Parmenter, R.H., Ruppel, W. *J. Appl. Phys.* **1959**, *30*, 1548.

(65) Majumdar, S.; Majumdar, H. S. *Org. Electron.* **2012**, *13*, 2653.

(66) Kuik, M.; Koster, L. J. a.; Dijkstra, a. G.; Wetzelaer, G. a. H.; Blom, P. W. M. *Org. Electron.* **2012**, *13*, 969.

(67) Wetzelaer, G. a. H.; Kuik, M.; Nicolai, H. T.; Blom, P. W. M. *Phys. Rev. B* **2011**, *83*, 165204.

(68) Majumdar, S.; Majumdar, H. S.; Laiho, R.; Österbacka, R. *J. Alloys Compd.* **2006**, *423*, 169.

(69) Salis, G.; Alvarado, S.; Tschudy, M.; Brunschwiler, T.; Allenspach, R. *Phys. Rev. B* **2004**, *70*, 085203.

(70) Francis, T. L.; Mermer, Ö.; Veeraraghavan, G.; Wohlgenannt, M. *New J. Phys.* **2004**, *6*, 185.

(71) Bobbert, P.; Nguyen, T.; van Oost, F.; Koopmans, B.; Wohlgenannt, M. *Phys. Rev. Lett.* **2007**, *99*, 216801.

(72) Kalinowski, J.; Cocchi, M.; Virgili, D.; Di Marco, P.; Fattori, V. *Chem. Phys. Lett.* **2003**, *380*, 710.

(73) Desai, P.; Shakya, P.; Kreouzis, T.; Gillin, W.; Morley, N.; Gibbs, M. *Phys. Rev. B* **2007**, *75*, 094423.

(74) Wang, J.; Chepelianskii, A.; Gao, F.; Greenham, N. C. *Nat. Commun.* **2012**, *3*, 1191.

(75) Sun, D.; Basel, T. P.; Gautam, B. R.; Han, W.; Jiang, X.; Parkin, S. S. P.; Valy Vardeny, Z. *Appl. Phys. Lett.* **2013**, *103*, 042411.

(76) Bergenti, I.; Dediu, V.; Arisi, E.; Mertelj, T.; Murgia, M.; Riminucci, a.; Ruani, G.; Solzi, M.; Taliani, C. *Org. Electron.* **2004**, *5*, 309.

RESUMEN

En el campo de la electrónica tradicional de semiconductores, la detección de cambios en la corriente eléctrica bajo la influencia de estímulos externos es el principio operacional de los dispositivos fabricados. La manipulación activa del grado de libertad de espín de los portadores de carga, sumado al control sobre la carga eléctrica, es el tema central que concierne a un campo de investigación relativamente joven denominado espintrónica. En el área de la nanotecnología, la espintrónica es una de los campos de investigación más emergentes, suponiendo una rama muy activa dentro del nanomagnetismo. El origen de esta área de conocimiento se puede situar en 1982 con el trabajo de Albert Fert y Peter Grünberg referido a la magnetoresistencia gigante (GMR) de multicapas metálicas. Por esta razón dichos investigadores fueron galardonados con el premio Nobel de física en 2007. La espintrónica ha supuesto un gran impacto en nuestro día a día mediante el desarrollo de sistemas de hardware para el almacenamiento de información y sensores magnéticos, entre otras aplicaciones. Hasta la fecha, este campo de investigación ha usado principalmente metales y semiconductores inorgánicos. Sin embargo, el rápido desarrollo experimentado en los campos de la electrónica molecular y el magnetismo molecular en la última década, junto con el progresivo desplazamiento hacia un escenario en la escala nanométrica, han propiciado las condiciones adecuadas para el surgimiento de una nueva área: la Espintrónica Molecular.

De la misma manera que se hizo para la electrónica molecular, este nuevo campo de investigación se ha dividido en dos áreas principales: i) espintrónica basada en moléculas o espintrónica orgánica más comúnmente denominada por la comunidad física, ii) espintrónica unimolecular. Los temas tratados en la presente tesis se centran en la primera área de conocimiento. En este contexto, el principal objetivo es el diseño y fabricación de dispositivos espintrónicos innovadores y de menor coste mediante la utilización de materiales moleculares (más comúnmente denominados materiales orgánicos).

El manuscrito de la tesis se encuentra dividido en dos partes.

- **Parte I**:

La primera parte de este manuscrito versa sobre la caracterización física de películas delgadas de análogos de azul de Prusia (PBA). Estos materiales basados en moléculas presentan un gran interés desde el punto de vista del control de sus propiedades por dos razones principales. En primer lugar, los PBAs son preparados mediante procesos sintéticos de baja complejidad. En segunda instancia, el diseño de sus propiedades magnéticas, tales como su ordenamiento ferromagnético, puede ser fácilmente alcanzado mediante la correcta selección de las fuentes de espín.

Dos tipos de estructuras cristalinas pueden ser descritas para los PBA: i) $A^{I}M_{A}^{II}[M_{B}^{III}(CN)_{6}]$ siendo M_A y M_B iones de metales de transición y A un cation alcalino ocupando de forma alterna sitios intersticiales de la red; ii) $A^{I}M_{A}^{II}[M_{B}^{III}(CN)_{6}]_{2/3}\cdot zH_2O$ conteniendo moléculas de agua coordinadas y sin coordinar. Cada tipo de estructura va a proveer de diferentes funcionalidades magnéticas y ópticas al material. En este sentido, es larga la lista de multifuncionalidades reportadas en los PBAs entre las cuales pueden destacarse: i) transición de fase por transferencia de carga, ii) fotomagnetismo, iii) piezomagnetismo, iv) second harmonic generation (SHG) y magnetization induced SHG (MSHG), v) coexistencia de ferroelectricidad y ferromagnetismo, vi) magnetismo sensible a la humedad, vii) Spin-iónica.

Estos materiales magnéticos basados en moléculas pueden considerarse como potenciales candidatos para su aplicación en estructuras espintrónicas moleculares. En este sentido, el objetivo de esta tesis es desarrollar un amplio marco de conocimiento referido a las propiedades de los PBA al ser depositados en forma de películas delgadas, para lo cual se empleó la deposición electroquímica. La motivación para emplear esta técnica de crecimiento frente a otras, tales como el layer by layer (LbL), está suficientemente argumentada. A diferencia del método electroquímico, el LbL no necesita de sustratos conductores para el crecimiento de las capas delgadas. A pesar de esta ventaja, la técnica de LbL presenta una importante cantidad de inconvenientes. Para la fabricación de capas homogéneas se requiere un proceso secuencial caracterizado por un número elevado de ciclos de crecimiento. Esto deriva en

un consumo importante de tiempo para la obtención del sistema final, lo cual dificulta el control sobre las condiciones de crecimiento. A su vez muchos parámetros deben de ser fijados para la obtención de películas delgadas reproducibles en términos de morfología y composición (y en consecuencia, propiedades magnéticas). Por el contrario, la deposición electroquímica es un método rápido y reproducible para la fabricación de capas delgadas homogéneas de PBAs sobre sustratos con áreas grandes. Mediante esta estrategia, un alto grado de control puede ser alcanzado en la referente la morfología, composición y propiedades magnéticas.

El estudio llevado a cabo sobre los sistemas de PBA en esta primera parte de la tesis, está reflejado en cinco capítulos. El primero de ellos presenta una introducción a los conceptos fundamentales y técnicas experimentales correspondientes a esta parte de la tesis.

En el capítulo 2 del manuscrito, se presentó una caracterización física completa de películas delgadas del PBA $Cr_{5.5}(CN)_{12} \cdot 11.5\ H_2O$ en función del grosor de la capa. Cuatro grosores fueron elegidos para este estudio siendo de 1500 nm, 450nm, 250 nm y 80 nm. Este rango de grosores permitió evaluar de una manera completa posibles variaciones en las propiedades del material a medida que el proceso de fabricación evolucionaba hacia valores de este parámetro con interés para posibles aplicaciones. El estudio de IR-ATR llevado a cabo sobre estos sistemas muestra que, independientemente del grosor, estas películas delgadas sufren una oxidación completa como consecuencia de la exposición al aire. Dicho material se ha designado como CrCr a lo largo de toda la discusión de esta tesis con el fin de simplificar la notación. Este sistema presenta un comportamiento ferrimagnético, con una alta temperatura crítica (T_c) de 240 K, exhibiendo una alta estabilidad química y propiedades magnéticas controlables. En consecuencia, este PBA se plantea como uno de los candidatos más prometedores para su aplicación en espintrónica molecular. Es interesante remarcar que en este estudio se ha podido comprobar que al reducir el grosor de las capas, las propiedades magnéticas se ven considerablemente mejoradas (ciclos de histéresis con mayores campos coercitivos y forma cuadrada definida). En este capítulo de la tesis, el primer estudio de efecto Kerr magneto-óptico (MOKE) sobre películas delgadas de este PBA ha sido extensamente descrito. En

este sentido, se ha demostrado que la magnetometría MOKE es una técnica potente para el estudio de las propiedades magnéticas de capas delgadas de estos materiales magnéticos basados en moléculas. Dichos materiales ofrecen una respuesta magneto-óptica excepcional debido a la alta intensidad de luz reflejada por su superficie transparente, aportando evidencias claras de efectos de tamaño de grano en el registro de la medida. En este capítulo, se introdujo un modelo para entender el origen de la sensibilidad superficial del MOKE en estos materiales transparentes. Dicho modelo fue formulado en base a consideraciones ópticas en el contexto de estudios elipsométricos. La naturaleza superficial de la información magnética adquirida mediante MOKE permitió el registro de los procesos de reversión de la magnetización que tienen lugar en las capas superiores de estas películas delgadas de CrCr. Esta región interfacial es de gran interés, teniendo en cuenta su posible uso como electrodos inyectores de espín, puesto que dicha región definirá la calidad de las interfases en el dispositivo espintrónico resultante. Un estudio de Microscopía de Fuerza Magnética a baja temperatura (LT-MFM) se ha realizado sobre los films de CrCr de 80 nm de grosor. Los resultados de esta caracterización indican que el alto valor de campo coercitivo determinado por MOKE para las capas delgadas de este PBA son debidas a un efecto de tamaño de las nanopartículas en la superficie. Esta información no pudo ser obtenida mediante SQUID, siendo esta una caracterización referida al volumen completo del material, sin la posibilidad de alcanzar una sensibilidad superficial. Sumado a todo lo descrito hasta ahora, se pudo comprobar que la magnetometría MOKE permite el registro de ciclos de histéresis del CrCr a temperaturas relativamente altas (justo por debajo de la T_c), lo cual resulta de gran interés en términos de futuras aplicaciones. De hecho, el estudio desarrollado en este capítulo, mostró la capacidad de obtener ciclos de histéresis a temperaturas próximas a la T_c para capas delgadas de este PBA ferrimagnético con grosores ultra-delgados de 40 nm. Con el fin de evaluar la validez de las conclusiones extraídas de las medidas MOKE sobre el CrCr, se abordó un estudio paralelo sobre otra familia de PBA constituida por el sistema ternario $(Fe^{II}_xCr^{II}_{1-x})_3\,[Cr^{III}(CN)_6]_2{\cdot}z\,H_2O$, al que se denominó FeCrCr a lo largo de la discusión del manuscrito. Los estudios realizados, confirmaron las propiedades determinadas mediante MOKE para las capas delgadas de CrCr y

su relación con respecto a la información proporcionada por el SQUID, otorgando universalidad a las conclusiones extraídas.

Las habilidades únicas del MOKE para estudiar las propiedades magnéticas de PBAs, se testó de igual forma sobre capas delgadas de la familia del PBA $Fe_3[Cr(CN)_6]_2 \cdot 15\ H_2O$, denominado FeCr a lo largo de la discusión. Este trabajo se encuentra extensamente descrito en el capítulo 3 de este texto. En películas delgadas de FeCr se detectó una discrepancia entre la temperatura crítica determinada mediante MOKE (T_c=60-70 K) y la hallada mediante SQUID (T_c=20 K) siendo esta última la habitualmente reportada en literatura para este material. Esta anomalía en la determinación de la T_c se explicó en base a la presencia de una fase de óxido de hierro amorfa. Dicha fase aparecería en el entorno del electrolito e introduciéndose en la estructura del PBA durante el proceso de electrodeposición de las capas. Los estudios de Raman sobre las películas delgadas de este material descartaron cualquier tipo de fenómeno fotomagnético como responsable de esta anomalía en la T_c. Esta información llevó a considerar un origen externo de esta anomalía, resultado de la incorporación de una fase química extra, la cual podía ser detectada por el MOKE pero no por medio de SQUID. Observando la evolución del electrolito, fue posible determinar la aparición de un material precipitado que se aisló y caracterizó tanto morfológicamente como en sus propiedades magnéticas. De esta manera se pudo identificar como una fase amorfa de óxido de hierro. A partir del análisis de TEM de alícuotas del electrolito, las mismas estructuras amorfas fueron detectadas. Con esta información fue posible concluir que en el entorno químico, en el cual la electropolimerización de las capas delgadas tiene lugar, estructuras basadas en hierro aparecen espontáneamente. Estas impurezas son incluidas en la estructura del PBA durante la electrodeposición, acumulándose principalmente en la superficie de la película delgada. Esta es la razón por la cual la señal magnética de dicha fase extra es sólo detectada mediante MOKE. Esta fase extra sólo pudo ser medida para tiempos de deposición altos (1000 segundos). Para tiempos menores (<100 segundos), la formación de las estructuras de óxido de hierro no llega a completarse, no pudiendo ser ya detectadas. El estudio desarrollado en este capítulo mostró la enorme capacidad del MOKE para actuar como una técnica de magnetometría

complementaria al SQUID en el estudio de las propiedades magnéticas de películas delgadas de PBA.

En el capítulo 4, películas delgadas de los dos PBA's CrCr y FeCr caracterizados extensamente en los capítulos 2 y 3, fueron puestas en contacto directo. El primer de los materiales es un ferrimagneto blando y el segundo de ellos presenta un comportamiento de ferromagneto duro. De esta manera se pudieron fabricar estructuras de bicapa en el rango nanométrico mediante una aproximación electroquímica. Las medidas de espectroscopía IR-ATR de dichas bicapas de PBAs, como así mismo las medidas de evolución térmica de la susceptibilidad magnética, permitieron mostrar la preservación de las identidades químicas tanto del CrCr como del FeCr durante la fabricación del sistema. Esto se consiguió tras una correcta selección del orden de electrodeposición en base a los potenciales de reducción para la síntesis de cada material. De este modo, se depositó una primera capa de CrCr (V=-0.88 V) para acto seguido ser recubierto por una segunda película de FeCr (V=-0.5 V), con grosores de 175 nm y 60 nm respectivamente. Mediante la caracterización STEM de una lamela de dicha bicapa fue posible generar perfiles químicos del sistema con el fin de establecer la región asociada a cada PBA. A través de esta técnica se determinó la presencia de una interface clara contenida en una región de 10 nm, demostrando la ausencia de interpenetración de una capa en la otra. Por otro lado, a través de una detallada caracterización mediante SQUID de la bicapa de PBA fue posible evidenciar la aparición de un acoplamiento magnético entre ambos materiales. Dependiendo del rango de campos magnéticos bajo estudio fue posible determinar una variada fenomenología magnética fruto de dicho acoplamiento. En este sentido, cuando ambos PBAs fueron puestos en íntimo contacto, se pudo detectar un claro incremento de sus campos coercitivos con respecto a cada caso aislado. Mediante la medida de ciclos menores de la bicapa, en rangos de campo magnético correspondientes a la saturación de la magnetización de la capa ferrimagnética de CrCr, se pudo determinar un comportamiento histerético reversible para la dinámica de magnetización de este material. Estos ciclos menores mostraron la presencia de una respuesta de "exchange-bias" con un crecimiento del campo coercitivo y un desplazamiento positivo en la histéresis

del CrCr. Este comportamiento fue asociado a la presencia de un proceso de "exchange-spring" en los mecanismos de reversión de la magnetización de la capa de CrCr inducido por la interacción magnética en la interfase con el ferromagneto duro FeCr. El bajo valor del campo de "exchange bias" (16.5 Oe) y el comportamiento histerético de la señal del CrCr fueron asociados a la naturaleza no epitaxial del crecimiento de ambas capas de PBAs. Al incrementar el campo magnético hasta valores correspondientes al proceso de reversión magnética del FeCr, la influencia del ferrimagneto CrCr en esta capa magnética dura pudo ser detectada. Una interacción antiferromagnética entre el FeCr y el CrCr en la interfase de ambos materiales fue propuesta como explicación. A partir de esta interacción, tiene lugar un efecto de anclaje en la reversión de la magnetización del FeCr. Dicho efecto quedó reflejado en un incremento del campo coercitivo del ferrimagneto duro en la bicapa, en comparación con la situación aislada. En consecuencia, la caracterización magnética de esta bicapa permitió detectar un interesante efecto de "cross-talk" en términos de interacción magnética. Los resultados descritos en este capítulo suponen la primera descripción de una fenomenología de este tipo en una heteroestrcutura magnética formada completamente por materiales basados en moléculas.

Tal como se indicó previamente el CrCr constituye uno de los mejores candidatos para su aplicación en estructuras espintrónicas moleculares. Motivados por este aspecto, una completa caracterización de la magnetoresistencia (MR) de capas delgadas de 80 nm de espesor de este PBA fue llevada a cabo, cuya explicación detallada se encuentra contenida en el capítulo 5 de este manuscrito. Con el fin de llevar a cabo dicho estudio, en este capítulo se describió un procedimiento para electrodepositar películas ultra-delgadas de CrCr en sustratos de área reducida. El diseño y fabricación de un adaptador para muestras de tamaño reducido permitió la fabricación de capas de 80 nm de espesor de este cianuro de cromo mediante la configuración de celda electroquímica utilizada habitualmente para sustratos de área grande. Dispositivos con áreas activas de 0.0025 cm^2 fueron fabricados mediante la deposición de la capa de CrCr entre dos electrodos de oro. Mediante el estudio de estas estructuras se logró reportar por primera vez las propiedades de MR de una película delgada poli-cristalina de PBA. Una MR positiva aproximadamente

2.2 % a 60 kOe y 200 K pudo ser registrada, con un comportamiento lineal hasta campos de 15 kOe, con una contribución cuadrática para el rango de altos campos magnéticos. Se indicó la necesidad de desarrollar un modelo capaz de incluir las características de los orbitales moleculares del PBA, conjuntamente con la influencia del ordenamiento magnético en el "hopping" de los portadores de carga entre centros de CrCr. De esta manera se podrían sentar las bases de un modelo capaz de explicar el comportamiento lineal de la MR en este PBA. En este contexto, la visión molecular aplicada para el desarrollo del modelo de MR en el ferrimagneto basado en moléculas $V[TCNE]_x$ podría ser considerada como una referencia con tal propósito. Por otra parte, la contribución cuadrática de la MR en altos campo fue explicada a través de un término de MR ordinaria en el material. Basado en las interesantes propiedades de MR detectadas en el CrCr, se procedió a la fabricación de un prototipo de válvula de espín. Para ello se efectuó una estimación de los niveles de energía en el CrCr mediante voltametría cíclica. Con esta información, una estructura de válvula de espín con el CrCr como electrodo inyector de espín y el Co como electrodo analizador de espín fue fabricada empleando el polímero electroluminiscente F8BT como medio colector de espín. En la caracterización de dicho dispositivo no se detectó una MR asociada a la válvula de espín. Por el contrario, una importante influencia de la respuesta de MR del electrodo de CrCr en el comportamiento de la estructura completa fue detectada. En este sentido, un proceso de "apantallamiento" por parte de la resistividad "bulk" del CrCr al enfriar el sistema fue propuesto como posible explicación para la ausencia del efecto de válvula de espín en el dispositivo prototipo. La razón de elegir un colector de espín basado en un semiconductor orgánico depositado por "spin-coating" residió en la necesidad de fabricar futuras estructuras espintrónicas obtenidas íntegramente mediante métodos en disolución.

- **Parte II**:

La segunda parte de esta tesis se centró en la fabricación de dispositivos espintrónicos moleculares emisores de luz capaces de exhibir una modulación de la emisión de luz bajo la aplicación de campos magnéticos externos. La obtención de este tipo de dispositivos supone el surgimiento de una nueva generación de tecnologías optoelectrónicas. La fabricación de estas estructuras multifuncionales puede conseguirse a través de la sinergia de dos áreas de investigación ampliamente estudiadas en la última década: la electrónica molecular y la espintrónica molecular. La estrategia elegida en esta tesis para la fabricación de estos dispositivos se centró en el diseño y fabricación de estructuras en las cuales la electroluminiscencia (EL) es sensible a la polarización de espín de los portadores de carga inyectados en la capa orgánica emisora de luz. Estos dispositivos reciben el nombre de spin-OLEDs. El punto fundamental de esta estrategia reside en la presencia de una corriente polarizada en espín en el dispositivo, capaz de derivar en un efecto de magneto-electroluminiscencia (MEL) bajo la aplicación de campos magnéticos externos. El control de la estadística de excitones singletes y tripletes en la capa orgánica emisora puede permitir una modulación de la emisión de luz del sistema. Para este propósito, la espintrónica molecular provee de la estructura adecuada denominada válvula de espín orgánica (OSV). Dicha estructura se encuentra constituida por un semiconductor orgánico (OSC) ubicado entre dos electrodos polarizados en espín que actúan como inyector y analizadores de espín. El OSC actuando como colector de espín posee una longitud de difusión de espín grande, gracias al débil acoplamiento espín-órbita, como así mismo una baja interacción hiperfina. Ambas propiedades permiten la preservación de la información de espín de las cargas inyectadas entre ambos electrodos. Es de vital importancia remarcar, que con el fin de obtener un efecto MEL de válvula de espín, es mandatorio el establecimiento de las condiciones adecuadas de trabajo para el dispositivo en términos de voltaje de operación como así mismo en lo referente a la temperatura. Esto permitirá la coexistencia de EL y de una corriente polarizada en espín en el OSC del dispositivo. En base a todo esto, con el fin de fabricar un spin-OLED es necesario la coordinación de los esfuerzos realizados tanto desde el punto de vista de la electrónica molecular como de la

espintrónica molecular. En el capítulo 6 de este manuscrito se introdujeron todos los conceptos fundamentales relacionados con el trabajo de esta segunda parte, junto con los detalles de la aproximación experimental.

En el capítulo 7 se ha describió el diseño y fabricación de un prototipo de spin-OLED utilizando electrodos ferromagnéticos de Fe y Co. Se propuso por primera vez la implementación de una estructura de Organic Light Emitting Diode (OLED) invertida, HyLED, para fabricar dicho dispositivo multifuncional. Esta aproximación de trabajo permitió la obtención de estructuras robustas y estables. En esta estrategia, materiales comerciales y de bajo coste fueron empleados tal cual recibidos desde el fabricante, sin procesos químicos adicionales. A raíz de este trabajo, se emplearon por primera vez en el campo de la espintrónica el polímero electroluminiscente poly(9,9-dioctylfluorene-*co*-benzothidiazole) (F8BT) y el óxido de molibdeno, MoO_3, extensamente empleados en el campo de la optoelectrónica. Tal como se citó previamente, existe una condición indispensable para la modulación de la luz bajo campos magnéticos a través de un efecto MEL de válvula de espín. Esta consiste en la coexistencia de electroluminiscencia (EL) y corriente polarizada de espín en la capa orgánica emisora del dispositivo, para el mismo rango de temperaturas y voltajes. En este prototipo de spin-OLED se registró una buena EL para todo el rango de temperaturas estudiadas. Adicionalmente, su funcionamiento como OSV fue registrado en el rango de bajas temperaturas, lo cual sirvió como indicativo de la presencia de una corriente polarizada en espín. Sin embargo, ambas funcionalidades fueron detectadas en rangos diferentes de temperatura y voltaje. A pesar de este inconveniente, el sistema propuesto, supuso el establecimiento de interesante prototipo para el desarrollo de dispositivos espintrónicos electroluminiscentes fabricados con materiales comerciales. De hecho, este trabajo permitió la creación de una patente nacional número 201300083: “Dispositivo opto-espintrónico y método para su fabricación”.

En este punto del trabajo se entendió claramente que para tener una modulación efectiva de la luz por efecto MEL de válvula de espín, en nuestro spin-OLED era necesario llevar la EL y el funcionamiento de OSV al mismo rango de voltajes y temperaturas. Una rápida degradación de las propiedades de MR con la temperatura fue detectada este dispositivo con electrodos de Fe y Co.

Se planteó como hipótesis una degradación de las propiedades de inyección de espín del electrodo de Fe, fruto de las condiciones de fabricación. Este aspecto sentó las bases para una posible mejora del funcionamiento del spin-OLED, proponiéndose la sustitución de este electrodo constituido por un metal de transición por otro más estable. En esta línea, la inclusión de un óxido magnético, tal como el $La_{1-x}Sr_xMnO_3$ (LSMO), se planteó como una opción a considerar. Esto se hizo teniendo en cuenta la importante estabilidad química de este material frente a la oxidación, como así mismo, sus propiedades excepcionales como electrodo inyector de espín. Con esta idea en mente se abordó el trabajo del último capítulo de esta tesis.

En el capítulo 8 se diseñó y fabricó un spin-OLED manteniendo una estructura HyLED que presentó un efecto MEL relacionado con la inyección de portadores de carga polarizados en espín en la capa emisora de luz del dispositivo. Se mantuvieron todos los elementos del prototipo planteado en el capítulo anterior y se procedió a la inclusión de un cátodo de LSMO. A través de la funcionalización de la LSMO mediante la deposición de una capa molecular iónica del complejo de rutenio bis(4,4'-tridecyl-2,2'-bipyridine)-(4,4'-dicarboxy-2,2'-bipyridine)ruthenium(II)-bis(chloride), denominado N965, mediante la técnica de Langmuir-Blodgett, fue posible llevar las condiciones de EL y funcionamiento de OSV al mismo rango de voltajes y temperaturas. Dicha situación ha sido el mayor obstáculo en el campo de la espintrónica molecular para la fabricación de dispositivos emisores de luz con presencia de un efecto de MEL de válvula de espín. Esto reside en el hecho de que los voltajes de operación de las OSVs reportadas en literatura han sido siempre mucho menores que los voltajes necesarios para la emisión de luz en dispositivos opto-electrónicos. La incorporación del complejo de rutenio como capa inyectora de electrones (EIL) promovió una excepcional estabilización del comportamiento del spin-OLED en términos de EL y respuesta de OSV.

La presencia de la molécula dipolar N965 como EIL tuvo un impacto directo en las propiedades de emisión de luz del spin-OLED, de tal forma que el voltaje de emisión (V_{on}) se redujo en aproximadamente 3 V respecto al dispositivo sin este EIL. Bajo estas condiciones se detectó EL por encima de 7V a 14 K. Por otro lado, nuestro spin-OLED presentó un excepcional funcionamiento como OSV

bipolar, preservando una corriente polarizada en espín a través de la estructura hasta voltajes de 12 V en el rango de temperaturas 180-200 K. Este resultado constituye el primer ejemplo de una estructura espintrónica con preservación de la señal de MR hasta tan altos voltajes. Hay que mantener presente, que las OSVs descritas hasta ahora en la literatura sufren una degradación total en su funcionamiento para voltajes por encima de 1-2 V. Se relacionó esta excepcional estabilización de OSV a un proceso de aniquilación de carga en la capa orgánica emisora de luz a través de diversos mecanismos. Estos procesos serían los responsables de reducir los fenómenos de relajación de espín en el F8BT. Sin embargo, es importante tener en cuenta que hoy en día, en el campo de la espintrónica molecular no existe una explicación satisfactoria para la degradación de la MR a voltajes por encima de 2 V. En consecuencia, no es posible dar una explicación certera para el funcionamiento de nuestro spin-OLED a voltajes tan altos. Es importante considerar, que además de nuestro sistema sólo existe un artículo en literatura reportando la fabricación de un spin-OLED que funciona en el régimen bipolar a altos voltajes. Dicho trabajo se corresponde a la publicación de Z.V. Vardeny et al., Science 337, 204, 2012. Por tanto, estamos ante una nueva fenomenología en el capo de la espintrónica que requiere de más experimentos y un marco teórico sólido para predecir y confirmar los mecanismos que fueron propuestos en el trabajo descrito en este capítulo. Con respecto a la respuesta térmica de la MR en el spin-OLED, se pudo detectar una mejora crucial respecto al prototipo conteniendo el cátodo de Fe descrito en el capítulo 7. La inclusión de un electrodo estable a la oxidación como el LSMO al que se le efectuó una nanofuncionalización mediante la molécula N965 permitió la preservación de una corriente polarizada en espín hasta el rango de temperaturas de 180-200 K.

La presencia de una corriente polarizada en espín para el mismo rango de voltajes y temperaturas que la EL, permitió la detección de un efecto MEL directamente relacionado con el funcionamiento de válvula de espín del dispositivo. Una modulación máxima de la emisión de luz de un 1 % fue registrada a 10 V y 32 K con un incremento de la EL para la configuración anti-paralela de las magnetizaciones de los electrodos ferromagnéticos. Este efecto fue detectado para voltajes de 10-12 V, donde se produce una suficiente

cantidad de luz garantizando un buen ratio señal-ruido en la medida. Sólo el spin-OLED conteniendo la monocapa de N965 exhibió un efecto MEL. En ausencia de esta capa molecular iónica, los voltajes en los que es posible detectar un nivel adecuado de EL fueron tan elevados que derivaron en una degradación del funcionamiento de OSV del spin-OLED. Esta situación resaltó la importancia de incluir una EIL eficiente en el dispositivo.

Un análisis detallado de los datos registrados fue llevado a cabo con el fin de descartar cualquier posible artefacto que pudiera imitar una modulación de luz por procesos de inyección de espín. Efectos relacionados con los electrodos ferromagnéticos y con los mecanismos de emisión de luz fueron descartados como responsables del efecto MEL en el sistema. Con este trabajo propuso un protocolo para testar el funcionamiento de las estructuras de tipo spin-OLED. Por este medio, hemos podido demostrar que la modulación de la luz bajo campos magnéticos en nuestro dispositivo se produce fruto de un control en la estadística de los excitones en la capa emisora, promovido por la inyección de cargas polarizadas en espín. Este protocolo de control no se aplicó en el caso del spin-OLED reportado por Z.V. Vardeny et al. En dicho sistema, el hecho de tener una EL y una corriente eléctrica que siguen exactamente el mismo comportamiento, es un indicativo de que el efecto MEL de válvula de espín que dicho autores proponen podría ser un artefacto y por tanto necesita ser revisado con detenimiento y reproducido por otros laboratorios. Una de las mayores ventajas del spin-OLED, extensamente descrito en este capítulo 8, es la utilización de un polímero emisor de luz comercial que se empleado tal como se recibe desde el proveedor. Esto se traduce en la posibilidad de fabricar dispositivos más baratos y accesibles. Por tanto, mediante nuestra estrategia hemos sido capaces de obtener una modulación de luz por efecto MEL de válvula de espín en una estructura espintrónica cuyos principales componentes han sido depositados desde disolución. Esto supone una gran ventaja en lo que se refiere a la posibilidad de acceder a una producción en grandes áreas, de bajo coste y escalable.